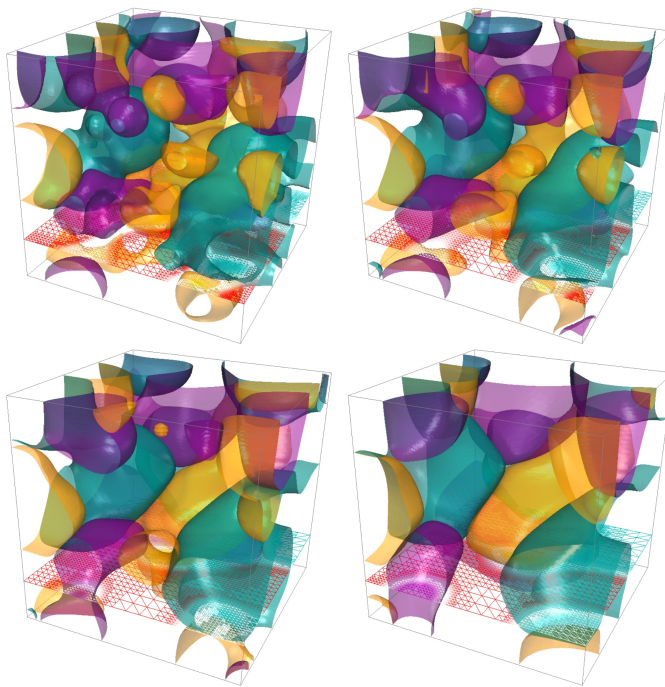# Numerical Simulation of Phase Separation in Binary and Multicomponent Systems

Inauguraldissertation
zur Erlangung des Grades eines
Doktors der Naturwissenschaften
am Fachbereich Mathematik und Informatik
der Freien Universität Berlin

vorgelegt von
Uli Sack

Berlin 2014

Betreuer: Prof. Dr. Ralf Kornhuber   (Freie Universität Berlin)

Erstgutachter: **Prof. Dr. Ralf Kornhuber**   (Freie Universität Berlin)
Zweitgutachter: **Prof. Dr. Harald Garcke**   (Universität Regensburg)

Tag der Disputation: 3. September 2014

Contents

Contents

Introduction

With the banishment of lead (Pb) solders from use in most electronics equipment by the EU directives WEEE [107, 109] and RoHS [106, 108] taking effect in 2006, the necessity arose to develop lead-free substitutes with comparable life-span and processing properties. From amongst a number of binary, ternary, and higher alloy candidates SnAgCu variants have emerged as the most widely used lead-free solder alloy. However, in addition to higher cost due to the high silver content, it is widely accepted that current lead-free solder-joints may be less reliable. The development of cheaper and more reliable solder materials involves lengthy experiments and testing. Numerical simulations may help to focus development by identifying promising candidates.

One of the principle causes for electronics failures is thermomechanically accelerated phase separation and coarsening and the related derating of macroscopic properties. Crack formation induced by thermal and mechanical stresses is facilitated by a coarser microstructure of the solder and occurs typically along phase interfaces. The coarseness of the microstructure is hence a useful indicator for the aging of the material and reliable simulations of the microstructure evolution yield lifespan predictions for the considered material. In this thesis the numerical tools for the robust and reliable microstructure simulation are developed and presented.

We focus on the Cahn–Larché model of phase separation under mechanical stress [32, 20] which couples the the equation of elastostatic equilibrium to the Cahn–Hilliard model of phase separation in solids [31]. The latter is an instance of the so-called *phase-field models* and allows a derivation as a gradient flow of a free energy that typically involves an interfacial energy term and a nonconvex mixing energy. While the mixing energy drives the phase separation, the interfacial energy penalizes large interfaces and thus drives coarsening. In natura microstructural inclusions
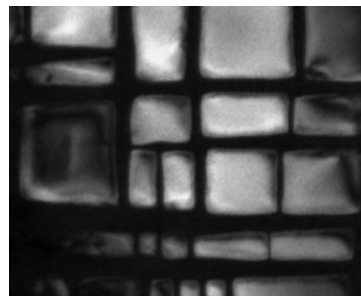

Figure 0.1 – Anisotropic phase shapes (image taken from [120]).

may exhibit anisotropy (cf. Figure 0.1). In the Cahn–Larché model anisotropy may be accounted for by an anisotropic interface energy and/or an anisotropic elasticity tensor (cf. e.g. [12, 121]). Both options find some consideration in this thesis. The temperature dependent mixing energy or *Gibbs free energy* in models for phase separation is typically of logarithmic type (cf. [56, 57]) with singular derivative and nondifferentiable in the limit case for temperature $\theta \longrightarrow 0$. In the N-component case we have an additional constraint that forces solutions onto the N-dimensional unit simplex.

While there are the robust and efficient Nonsmooth Schur–Newton Multigrid (NSNMG) methods [66, 61] for the solution of the scalar Cahn–Hilliard equation with logarithmic potential, existing numerical solvers for Cahn–Larché equations are either limited to smooth approximations of the Gibbs free energy density [121, 95] or to periodic domains and uniform computational meshes [42, 43, 20]. Smooth approximations of the Gibbs free energy density, however, may severely affect the computed coarsening dynamics (cf. Chapter 3).

For the multicomponent Cahn–Hilliard equation existing solvers typically suffer from severe mesh dependance [16, 5, 6] or again rely on smooth approximations of the free energy [80, 26]. To the author's best knowledge, efficient, reliable and robust solvers for multicomponent Cahn–Hilliard systems with logarithmic free energy are previously unknown.

The main contribution of this thesis is threefold:

1. The NSNMG methods are extended to the multicomponent case in Chapter 4.

2. A complete numerical framework for the robust and reliable simulation of microstructure evolution in binary alloys was implemented and applied to a eutectic AgCu alloy in Chapter 3. The framework includes adaptive space discretization for evolution problems, a quantification scheme for the coarseness of microstructures, and a quotient space multigrid method for indefinite linear elasticity problems.

3. A novel existence and uniqueness proof for the anisotropic Allen–Cahn equation is given in Chapter 2 relying on the theory of maximal monotone operators [27].

The thesis is organized as follows. After some preliminary remarks on phase diagrams, phase separation, and phase-field models in Chapter 1 we firstly focus on anisotropic Allen–Cahn equations in Chapter 2. Apart from being of interest in their own right Allen–Cahn-type problems arise as subproblems in the NSNMG method for the solution

of discrete Cahn–Hilliard equations in Chapters 3 and 4 which is the main reason to treat them in this thesis. Existence and uniqueness of solutions is proved employing the theory of maximal monotone operators using lower semicontinuity results for the anisotropic interface energy and the Gibbs free energy. We go on to introduce an adaptive mesh refinement cycle for evolution problems based on hierarchical error estimators and address some issues that arise from temporally varying grids. Furthermore several variants of Euler time discretization are introduced, proven to be stable and investigated numerically.

Chapter 3 gathers and integrates existing and newly developed numerical tools to a framework for efficient and robust microstructure evolution simulations and applies it to a eutectic AgCu alloy. The framework includes the adaptive mesh refinement cycle introduced in Chapter 2, the NSNMG solver, a quotient space multigrid solver for the Neumann problem of linear elastostatics, and a coarseness quantification algorithm. The numerical experiments indicate that in the setting considered the mechanical influence on the coarsening behaviour is marginal while substitution of the logarithmic Gibbs free energy by a quartic polynomial interpolant alters the coarsening dynamics considerably. The final chapter treats multicomponent Cahn–Hilliard equations. A unified formulation for all temperatures $\theta \geqslant 0$ of the discretized problem is given that incorporates a weak version of the affine constraints and existence and uniqueness of solutions is proved. This formulation allows the straightforward application of NSNMG methods. Numerical examples illustrate the robustness of the method with respect to temperature and the number of components.

1. Preliminaries

1.1. Phase Transformations, Phase Separation and Phase Diagrams

In materials science the term *phase* describes a variety of different states of a material, for example different states of aggregation, crystal structure, stoichiometric relations, concentrations etc. (as e.g. in liquid phase, cubic phase). At times domains of the same state are also termed phases (as e.g. in mean phase radius, phase shape).

Under changing conditions these phases can transform one into the other (e.g. solidification of a melt) in which case one speaks of *phase transformations* or *phase transitions*. Some materials may also exhibit multiple distinct phases coexisting in equilibrium under which circumstances *phase separation* occurs. For binary mixtures the equilibrium phases and phase transformations can be read from concentration-temperature *phase diagrams* as in Figure 1.1 left. The lines in the diagram partition the c-θ–plane in areas of different
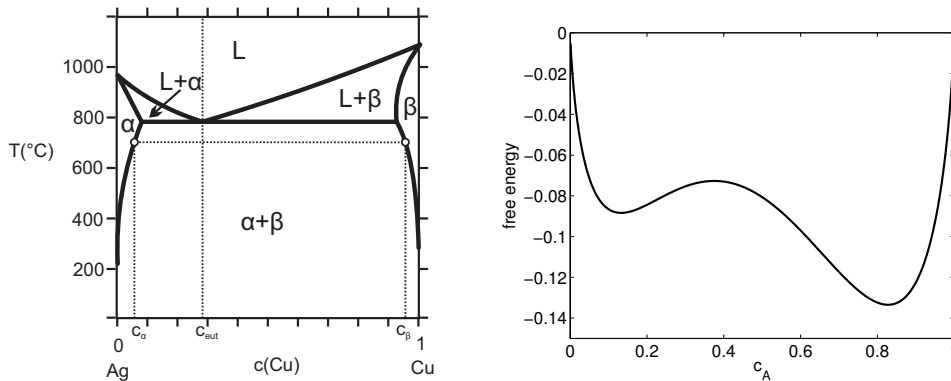
Figure 1.1 – Left: Phase diagram for a AgCu alloy (modified from [99]). Right: free energy of a hypothetic binary mixture with a miscibility gap at a given temperature

phases or phase mixtures, in this case the liquid phase (L), a Ag-rich solid phase (α), a Cu-rich solid phase (β) and mixtures thereof. Across lines phase transformations will occur, for example when cooling a melt with given composition c_0. A special feature of this particular phase diagram is the *eutectic point* where the liquid phase solidifies instantaneously into two coexistent solid phases. Also a eutectic material of composition c_{eut} will exhibit the lowest possible melting point for mixtures of these two constituents - two properties sought after in solder alloys. The area of coexisting solid phases ($\alpha + \beta$) in equilibrium represents a so-called *miscibility gap* meaning that the constituents at the given composition and temperature do not form a heterogeneous mixture since the free energy develops a concave zone (cf. Figure 1.1 right). The equilibrium concentrations of the coexisting α- and β-phases may be determined from the phase diagram by following the isothermal line to where it intersects the diagram lines of the respective pure phase regions (cf. Figure 1.1 left). This splitting in two distinct coexisting solid phases is known as *phase separation.*

In the present work we will not so much be concerned with the actual equilibria but the dynamics of attaining equilibrium which esp. in the case of phase separation require diffusion in solids.

1.2. Phase-field modelling

Phase-field models are so called diffuse interface models, that is they postulate a continuous transition from one phase to another in an interface region of finite width as opposed to sharp interface models which assume a jump from one phase to the next across a hypersurface. In consequence phase-field models involve computations in a higher dimension because they need to resolve the finite width interface. Sharp interfaces are often described by parametric curves or graphs which for computations require the discretization of only $d-1$ dimensional objects but lack the ability to represent topological changes such as pinch-offs, unions, or vanishing. Another d-dimensional approach that may account for such changes is by level-set functions. For a good overview over the different interface formulations in the setting of mean curvature flow we refer to [37]. Phase-field models also accomodate for topological changes and naturally occur in thermodynamical modelling (see for example [20]). For N-phase systems they consider the phase-field $\boldsymbol{c} = (c_1, \ldots, c_N) : \mathbb{R}^d \supset \Omega \to [0,1]^N$, where the components fulfill the pointwise constraint $\sum_{i=1}^{N} c_i = 1$. In the case of phase separation in metallic alloys we

may think of the c_i as concentrations of the constituents. For binary systems the sum constraint is usually exploited to eliminate one component and obtain a scalar order parameter $c = c_2 - c_1 \in [-1, 1]$.

Phase-field equations are usually formulated as gradient flows for some energy functional that take into account the mixing energy as for example described in the previous section and the surface tension or interfacial energy and may be augmented by additional terms that establish a coupling to other equations, e.g. elasticity or heat equations:

$$\mathcal{E}(\boldsymbol{c}, b) = \int_\Omega G(x, c, \nabla \boldsymbol{c}) + \Psi(\boldsymbol{c}) \, dx + W(\boldsymbol{c}, b),$$

where G is the interfacial energy density, Ψ the mixing energy density, and W sums up possible coupling terms. Anisotropy may enter in the interfacial energy and/or the coupling terms. Examples of phase-field models include the L^2-gradient flow for $\mathcal{E}$ without further coupling which results in the Allen–Cahn model for phase transition considered in Chapter 2, the H^{-1}-gradient flow without coupling that comprises the Cahn–Hilliard model for phase separation which is the subject of Chapter 4, and the H^{-1}-gradient flow coupled to linear elasticity leading to the Cahn–Larché equations of mechanically stressed solids under consideration in Chapter 3.

2. Anisotropic Allen–Cahn Equations

Originally established as a model for isothermal phase transition dynamics in [2] Allen–Cahn equations now appear in a number of contexts and applications are widely varied. They range from thermodynamics over image processing (cf. [79, 13]) and geoscience (cf. [122]) to geometric PDEs (cf. [37]). The main reason we consider Allen–Cahn equations in this work, however, is that the Schur-Newton solver for the Cahn–Hilliard model of phase separation employed in subsequent chapters requires the solution of many Allen–Cahn-type problems. Hence, while being of interest in their own right, Allen–Cahn equations in this context are seen more as a means to hone our algorithmic tools than as an end.

2.1. Continuous Problem

Considering the thermodynamic origin of Allen–Cahn equations and bearing in mind the applications in the following chapters we follow common practice and use thermodynamics inspired terminology albeit the presented results are more general. Here and in the following Ω will always denote an open, bounded domain in $\mathbb{R}^d$, $d \in \{1, 2, 3\}$ with Lipschitz boundary. In this chapter we focus on binary systems, i.e. we consider transitions between two distinct phases only. We therefore consider an order parameter c taking values in $[-1, 1] \subset \mathbb{R}$ on Ω (cf. Section 1.2).

2.1.1. Ginzburg-Landau free energy

For a given interface parameter $\varepsilon > 0$ the Ginzburg-Landau free energy functional is here defined as

$$\mathcal{E}(c) = \int_\Omega \frac{\varepsilon}{2} G(x, \nabla c(x)) + \frac{1}{\varepsilon} \Psi(c(x)) \, dx \tag{2.1}$$

This energy functional splits into two parts - the interfacial energy and the Gibbs free energy with densities G and Ψ respectively.

Gibbs free energy

When considering scalar Allen–Cahn equations the Gibbs free enrgy density Ψ typically takes a double-well shape, i.e. it has two local minima, and drives uphill diffusion and thus the formation of the two corresponding phases (see also Section 1.1). We assume it allows a splitting

$$\Psi(r) = \Phi(r) + \Upsilon(r) \tag{2.2}$$

where $\Phi : \mathbb{R} \to \mathbb{R} \cup \{+\infty\}$ is such that

(A1) $\exists_{k \in \mathbb{R}} \forall_{r \in \mathbb{R}} : \ \Phi(r) \geqslant k$ (for simplicity we will assume $k = 0$) and

(A2) the functional $\phi : L^2(\Omega) \to \mathbb{R} \cup \{+\infty\}$ defined by $\phi(v) = \int_\Omega \Phi(v(x)) \, dx$ is proper convex and lower semicontinuous (lsc) in $L^2(\Omega)$,

and

(A3) the functional $\gamma(v) = \int_\Omega \Upsilon(v) \, dx$ is differentiable and its derivative $D\gamma$ is Lipschitz continuous.

The following lemma states sufficient conditions such that Assumption (A2) is satisfied.

Lemma 2.1. *Let $\Phi : \mathbb{R}^N \to \mathbb{R} \cup \{+\infty\}$ be a proper convex function with closed effective domain* $\mathrm{dom}(\Phi)$ *and* $\Phi|_{\mathrm{dom}(\Phi)}$ *be continuous and satisfy*

$$|\Phi(r)| \leqslant c_0 \, |r|^2 + c_1 \quad \forall r \in \mathrm{dom}(\Phi). \tag{2.3}$$

The functional $\phi : L^2(\Omega)^N \to \mathbb{R}$ given by

$$\phi(v) = \int_\Omega \Phi(v(x)) \, dx$$

is then proper convex and lsc in $L^2(\Omega)^N$ and continuous on its domain. The domain of ϕ is given by the non-empty, convex, and closed set

$$\mathcal{K} = \left\{ v \in L^2(\Omega) \mid v(x) \in \mathrm{dom}(\Phi) \ a.e. \ in \ \Omega \right\}.$$

Proof. We first note that convexity of $\mathrm{dom}(\Phi)$, ϕ, and $\mathrm{dom}(\phi)$ follows immediately from the convexity of Φ.

We can extend Φ continuously to all of $\mathbb{R}^N$ by

$$\hat{\Phi}(r) = \Phi(Pr) + |r - Pr|$$

where P denotes the (uniquely defined) orthogonal projection onto $\mathrm{dom}(\Phi)$. Continuity of $\hat{\Phi}$ follows from the continuity of the projection P, of the norm, and of Φ on $\mathrm{dom}(\Phi)$ respectively. We know that $|Pr - Ps| \leqslant |r - s|$ for any $r, s \in \mathbb{R}^N$ from which by choosing $s = 0$ we may readily deduce

$$|Pr| \leqslant |r| + |P0|.$$

It follows that for all $r \in \mathbb{R}^N$

$$
\begin{aligned}
\left| \hat{\Phi}(r) \right| = |\Phi(Pr) + |r - Pr|| &\leqslant |\Phi(Pr)| + |r - Pr| \\
&\leqslant c_0 |Pr|^2 + c_1 + |r| + |Pr| \\
&\leqslant c_0 \left(|r| + |P0| \right)^2 + 2 |r| + |P0| + c_1 \\
&= c_0 |r|^2 + (2 + 2c_0 |P0|) |r| + c_1 + c_0 |P0|^2 + |P0| \\
&\leqslant c_2 |r|^2 + c_3
\end{aligned}
$$

for some constants $c_2, c_3 \in \mathbb{R}$ depending only on $\mathrm{dom}(\Phi)$. Now Theorem A.10 implies that the superposition operator induced by $\hat{\Phi}$ maps $L^2(\Omega)^N$ continuously into $L^1(\Omega)$.

We now show the claims concerning $\mathcal{K}$. Let $v \in \mathcal{K}$. Then we have $v(x) \in \mathrm{dom}(\Phi)$ a.e. in Ω and may deduce

$$\Phi(v(x)) = \hat{\Phi}(v(x)) \quad \text{for a.e. } x \in \Omega$$

and since by the above result $\hat{\Phi}(v(\cdot)) \in L^1(\Omega)$ we have

$$|\phi(v)| \leqslant \int_\Omega |\Phi(v(x))| \, dx = \int_\Omega \left| \hat{\Phi}(v(x)) \right| \, dx < \infty.$$

Therefore $v \in \mathrm{dom}(\phi)$.

Now let $v \notin \mathcal{K}$. Then there exists a subset $A \subset \Omega$ with positive measure such that $v(a) \notin \mathrm{dom}(\Phi)$, i.e. $\Phi(v(a)) = +\infty$, for every $a \in A$. Without loss of generality we may

assume that $x \notin A \Rightarrow v(x) \in \mathrm{dom}(\Phi)$. We can conclude that

$$\phi(v) = \int_\Omega \Phi(v(x))\, dx = \int_{\Omega \setminus A} \Phi(v(x))\, dx + \int_A \Phi(v(x))\, dx = \int_{\Omega \setminus A} \hat{\Phi}(v(x))\, dx + \infty = +\infty$$

holds. Hence $v \notin \mathrm{dom}(\phi)$ and $\mathrm{dom}(\phi) = \mathcal{K}$.

As the domain of a convex functional $\mathcal{K}$ is convex. The closedness of $\mathcal{K}$ is proven as follows. Consider an $L^2(\Omega)^N$-convergent sequence $(v_n) \subset \mathcal{K}$ with $v_n \longrightarrow v$. By Theorem A.9 there is a subsequence (v_{n_k}) such that

$$v_{n_k}(x) \longrightarrow v(x) \quad \text{for a.e. } x \in \Omega.$$

As $v_{n_k} \in \mathcal{K}$ it follows that $v_{n_k}(x) \in \mathrm{dom}(\Phi)$ for every n_k and a.e. $x \in \Omega$. Closedness of $\mathrm{dom}(\Phi)$ then implies $v(x) \in \mathrm{dom}(\Phi)$ a.e., which in turn is equivalent to $v \in \mathcal{K}$. Finally the properness of Φ implies the existence of some $r \in \mathbb{R}^N$ such that $|\Phi(r)| < \infty$. Choose $v \in L^2(\Omega)^N$ such that $v \equiv r$. Then by the boundedness of Ω we have $v \in \mathrm{dom}(\phi)$, i.e. $\mathcal{K} \neq \varnothing$:

$$\phi(v) = \int_\Omega \Phi(v(x))\, dx = \int_\Omega \Phi(r)\, dx = |\Omega|\, \Phi(r) < \infty$$

The arguments above also prove the properness of ϕ.

Defining $\hat{\phi}(v) = \int_\Omega \hat{\Phi}(v(x))\, dx$ we easily see that $\hat{\phi}|_{\mathcal{K}} = \phi|_{\mathcal{K}}$. Exploiting the continuity of the superposition operator induced by $\hat{\Phi}$ from $L^2(\Omega)^N$ to $L^1(\Omega)$ we find that $\phi|_{\mathcal{K}}$ is continuous. Let v_n now be a sequence in $L^2(\Omega)^N$ converging towards v. If $\liminf_{n \to \infty} \phi(v_n) = \infty$ we trivially find $\phi(v) \leqslant \liminf_{n \to \infty} \phi(v_n)$. Let's therefore assume $\liminf_{n \to \infty} \phi(v_n) = J < \infty$. Without loss of generality we may assume $v_n \in \mathcal{K}$ for al n. Closedness of $\mathcal{K}$ implies $v \in \mathcal{K}$ and continuity of $\phi|_{\mathcal{K}}$ implies

$$\liminf_{n \to \infty} \phi(v_n) = \lim_{n \to \infty} \phi(v_n) = \phi(v).$$

This concludes the proof. $\qquad\square$

Remark 2.1. *By virtue of the compact embedding $H^1(\Omega) \hookrightarrow L^2(\Omega)$ any weakly convergent sequence in $H^1(\Omega)$ is strongly convergent in $L^2(\Omega)$. Therefore the set $\mathcal{K}$ and the functional ϕ in Lemma 2.1 are weakly closed and weakly lsc in $H^1(\Omega)$ respectively.*

Remark 2.2. *A stronger condition for lower semicontinuity is found in [84, Subsection*

1.2.1], where condition (2.3) is replaced by the condition that

$$|\Phi(r) - \Phi(s)| \leqslant G(|r| + |s|)\,|r - s| \quad \forall r, s \in \mathrm{dom}(\Phi)$$

holds for some affine function $G : \mathbb{R} \to \mathbb{R}$. This condition implies (2.3). The logarithmic potential considered below does not satisfy this stronger condition while it does satisfy (2.3) (see Lemma 2.3).

In a thermodynamic context $\Psi = \Psi_\theta$ is the Gibbs free energy of a binary system frequently given by

$$\Upsilon(r) = \frac{1}{2}(1 - r^2) \tag{2.4}$$

and Φ of logarithmic form (cf. [56, 57]):

$$\Phi(r) = \Phi_\theta(r) = \begin{cases} \frac{\theta}{2}\left((1 + r)\log(1 + r) + (1 - r)\log(1 - r)\right) & r \in (-1, 1) \\ \theta \log(2) & |r| = 1 \\ +\infty & \text{else} \end{cases} \tag{2.5}$$

with θ denoting dimensionless (normalized) temperature. In many phase-field publications quartic polynomial approximations to Ψ_θ are used which are appropriate in the case of *shallow quench*, i.e. for (normalized) temperatures close to but less than 1 (e.g. [124, 121, 55, 50]). This simplifies analytical and numerical issues enormously because the singular nonlinearity is replaced by a well behaved polynomial which allows the use of classic Newton methods for numerics (e.g. [55, 95]) - but may, however, yield nonphysical order parameter values outside $[-1, 1]$. The *deep quench limit*, i.e. $\theta = 0$, leads to the so-called (double) obstacle potential opening stage for primal-dual active set strategies (cf. [15]). We will stick to the original logarithmic potential and apply solvers that work robustly for all $\theta \in [0, 1)$ including the double obstacle case (cf. [68, 66]).

In the following we state some properties of the logarithmic potential ([66, Proposition 2.1])

Lemma 2.2. *For $\theta > 0$ the logarithmic potential Φ_θ (2.5) has the following properties:*

   (i) $\Phi_\theta(r) = \Phi_\theta(-r)$, *i.e. Φ_θ is symmetric*
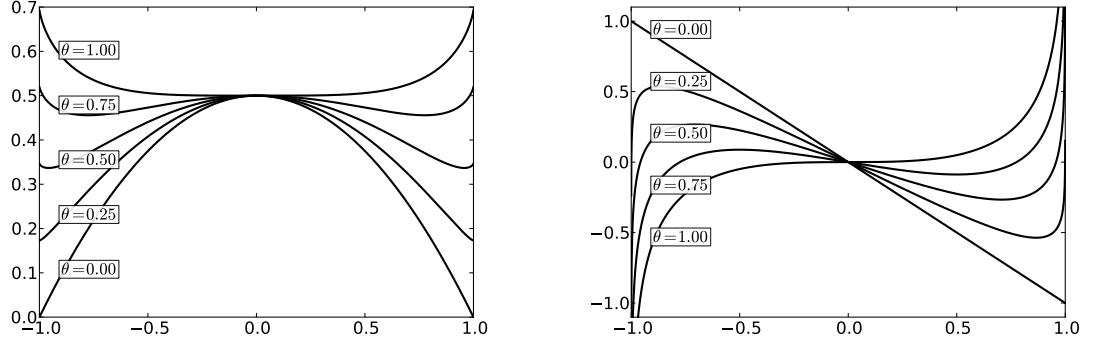
Figure 2.1 – The logarithmic potential Ψ_θ (left) and its derivative (right) for various values of θ

(ii) $\Phi_\theta|_{(-1,1)} \in \mathcal{C}^\infty(-1,1)$ *and*

$$\Phi_\theta'(r) = \frac{\theta}{2} \log\left(\frac{1+r}{1-r}\right) \qquad\qquad \Phi_\theta''(r) = \frac{\theta}{1-r^2}$$

(iii) $\Phi_\theta(0) = 0$ *and* $\arg\min_{r\in\mathbb{R}} \Phi_\theta(r) = 0$

(iv) *for* $|r| \nearrow 1$

$$\Phi_\theta(r) \longrightarrow \theta\log(2) \qquad \Phi_\theta'(r) \longrightarrow \pm\infty \ (\textit{for } r \longrightarrow \pm 1) \qquad \Phi_\theta''(r) \longrightarrow \infty$$

Note that the first statement together with (ii). implies continuity of Φ_θ on $[-1,1] = \mathrm{dom}(\Phi_\theta)$.

(v) Φ_θ *is convex and strictly convex on* $[-1,1]$ *for all* $\theta > 0$

Lemma 2.3. *The functional ϕ_θ defined by $\phi_\theta(v) = \int_\Omega \Phi_\theta(v(x))\, dx$ with Φ_θ as defined in (2.5) is lsc in $L^2(\Omega)$.*

Proof. Φ_θ is proper by construction, and convex by Lemma 2.2(v). Furthermore it is continuous on its effective domain which is the closed interval $[-1,1]$ (Lemma 2.2(iv)). Φ_θ is bounded by $\theta\log(2)$ on its domain and thus satisfies the condition (2.3). Applying Lemma 2.1 yields the claim. $\qquad\square$

Lemma 2.4. *The functional γ with Υ as defined in (2.4) is differentiable in $L^2(\Omega)$ and $D\gamma$ is Lipschitz continuous.*

Proof. An easy computation yields $\gamma(v+w) = \gamma(v) - (v,w) - \|w\|_0^2$ for all $v, w \in L^2(\Omega)$. Hence γ is Fréchet differentiable on $L^2(\Omega)$ with $D\gamma(v) = -(v,\cdot)$. Therefore we have for every $v, w \in L^2(\Omega)$

$$\|D\gamma(v) - D\gamma(w)\|_{L^2(\Omega)'} = \sup_{\substack{u \in L^2(\Omega) \\ \|u\|_0 = 1}} |(v,u) - (w,u)| = \sup_{\substack{u \in L^2(\Omega) \\ \|u\|_0 = 1}} |(v-w,u)|$$

$$\leqslant \sup_{\substack{u \in L^2(\Omega) \\ \|u\|_0 = 1}} \|v-w\|_0 \|u\|_0 = \|v-w\|_0$$

$\square$

Corollary 2.5. *The logarithmic Gibbs free energy $\psi_\theta = \phi_\theta + \gamma$ given by (2.5),(2.4) satisfies assumptions (A1),(A2),(A3).*

Interfacial free energy

The interfacial energy is a generalization of the isotropic version $\int_\Omega |\nabla u|^2\, dx$ which is recovered by choosing $G(x,\xi) = |\xi|^2$. Other ℓ^p-norms ($2 \leqslant p < \infty$) also yield examples for homogeneous anisotropic interface energies (see Example 2.3). In general we may think of $G^{\frac{1}{2}}$ as a norm in a generalized sense (namely a Finsler metric; see e.g. [12]). For our treatment of anisotropic Allen–Cahn equations we focus on homogeneous anisotropy functions $G(x,\xi) = \gamma^2(\xi)$ and make the following assumptions on γ.

(A4) $\gamma : \mathbb{R}^d \to \mathbb{R}$ is

    i. continuous on $\mathbb{R}^d$ and twice continuously differentiable on $\mathbb{R}^d \setminus \{0\}$,

    ii. positively 1-homogeneous, i.e. $\gamma(x) \geqslant 0$ and

$$\gamma(\lambda x) = \lambda \gamma(x) \quad \forall x \in \mathbb{R}^d,\ \lambda > 0$$

    iii. γ is definite, i.e. $\gamma(x) = 0 \Rightarrow x = 0$.

(A5) There is a positive constant γ_0 such that for the Hessian $\gamma''(x)$ holds

$$\langle \gamma''(x) y, y \rangle \geqslant \gamma_0 |y|^2, \quad \forall x, y \in \mathbb{R}^d \text{ with } |x| = 1 \wedge \langle y, x \rangle = 0$$

2. Anisotropic Allen–Cahn Equations

Note that, in contrast to a norm, γ is not necessarily symmetric to the origin as Example 2.5 illustrates. We state some consequences of Assumptions (A4) and (A5) which will be needed later on. Proofs may be found in [70, 66].

Lemma 2.6. *For $x \in \mathbb{R}^d \setminus \{0\}$ and $\alpha > 0$ there hold*

$$\gamma'(\alpha x) = \gamma'(x), \qquad\qquad \gamma''(\alpha x) = \frac{1}{\alpha}\gamma''(x),$$

$$\langle \gamma'(x), x \rangle = \gamma(x), \qquad\qquad \gamma''(x)\, x = 0,$$

implying convexity:

$$\langle \gamma''(x)y, y \rangle \geqslant 0 \qquad \forall y \in \mathbb{R}^d, x \in \mathbb{R}^d \setminus \{0\}.$$

For our analysis we are of course rather interested in properties on γ^2.

Lemma 2.7. *The functional $\gamma^2 : \mathbb{R}^d \to \mathbb{R}$ is continuously differentiable on $\mathbb{R}^d$ and twice continuously differentiable on $\mathbb{R}^d \setminus \{0\}$ and the Hessian $(\gamma^2)''(x)$ of γ^2 is positive definite for $x \in \mathbb{R}^d \setminus \{0\}$.*

Under Assumption (A4) positive definiteness of $(\gamma^2)''(x)$ is actually equivalent to Assumption (A5) (see [58, Remark 1.7.5]). The Hessian of γ^2 for any $x \in \mathbb{R}^d \setminus \{0\}$ thus induces a norm on $\mathbb{R}^d$ which is of course equivalent to the Euclidean norm. What is more the constants witnessing equivalence are independent of x:

Lemma 2.8. *There are constants $\mu, L > 0$ such that the Hessian of γ^2 satisfies*

$$\mu \, |y|^2 \leqslant \langle (\gamma^2)''(x)y, y \rangle \leqslant L \, |y|^2 \qquad \forall x \in \mathbb{R}^d \setminus \{0\}, y \in \mathbb{R}^d.$$

A particular choice of μ, L for which the preceding inequalities hold is

$$L = \sup_{x,y \in S^{d-1}} \langle (\gamma^2)''(x)y, y \rangle, \qquad\qquad \mu = \inf_{x,y \in S^{d-1}} \langle (\gamma^2)''(x)y, y \rangle > 0 \qquad (2.6)$$

These bounds also have a direct implication on the gradient $(\gamma^2)'$.

Lemma 2.9. *The gradient $(\gamma^2)' : \mathbb{R}^d \to \mathbb{R}^d$ is Lipschitz continuous with Lipschitz*

constant L and strongly monotone. More precisely we have

$$\left|(\gamma^2)'(y) - (\gamma^2)'(x)\right| \leqslant L\,|y - x| \qquad \forall x, y \in \mathbb{R}^d \ and$$
$$\left\langle(\gamma^2)'(y) - (\gamma^2)'(x), y - x\right\rangle \geqslant \mu\,|y - x|^2 \qquad \forall x, y \in \mathbb{R}^d.$$

As a direct consequence we get the strong convexity of γ^2.

Corollary 2.10. *The function $\gamma^2 : \mathbb{R}^d \to \mathbb{R}$ is strongly convex. More precisely we have*

$$\gamma^2(x) - \gamma^2(y) \geqslant \left\langle(\gamma^2)'(y), x - y\right\rangle + \frac{\mu}{2}\,|x - y|^2 \qquad \forall x, y \in \mathbb{R}^d.$$

Note that strong convexity implies coercivity.

Due to homogeneity, anisotropy functions are characterized by their sublevelsets and the sublevelsets of their polar functions which are the subjects of the following definition.

Definition 2.1 (Frank diagram, Wulff shape)**:**   Let γ be an anisotropy function satisfying Assumption (A4). The 1-sublevel set of γ

$$F_\gamma = \{x \in \mathbb{R}^d \mid \gamma(x) \leqslant 1\}$$

is called the *Frank diagram* of γ.
The 1-sublevelset of the polar function $\gamma^*(x) = \sup_{y \in S^{d-1}} \frac{\langle x, y\rangle}{\gamma(y)}$

$$W_\gamma = \{x \in \mathbb{R}^d \mid \gamma^*(x) \leqslant 1\} = \{x \in \mathbb{R}^d \mid \langle x, y\rangle \leqslant \gamma(y)\ \forall y \in S^{d-1}\}$$

is called the *Wulff shape* (also *Wulff crystal* or *Wulff region*) of γ. $\qquad\qquad \triangle$

It turns out that, while the Frank diagram illustrates energetic deviations from the isotropic case, the Wulff shape is the energetically favored phase shape as stated by Wulff's Theorem (Theorem 2.16).

Example 2.3 (ℓ^p-norms)**.** *A first example for anisotropy functions γ is given by the ℓ^p-norms*

$$\gamma_p(x) = \|x\|_p = \left(\sum_i |x_i|^p\right)^{\frac{1}{p}} \tag{2.7}$$

A straightforward computation verifies assumptions (A4) and (A5). The choice $p = 2$, i.e. the Euclidean norm, recovers the isotropic case. Frank diagram and Wulff shape coincide

in this case with the Euclidean unitsphere. Figure 2.2 illustrates the Frank diagram and the Wulff shape of γ_p for $p = 3$ and $p = 16$.

Example 2.4 (Regularized ℓ^1-norm)**.** *Another example is a smooth approximation of the ℓ^1-norm given by*

$$\gamma_{\mathtt{E}}(x) = \sum_i \sqrt{x_i^2 + \mathtt{E}|x|^2} \tag{2.8}$$

for $\mathtt{E} > 0$. Verification of (A4) and (A5) is straightforward. Figure 2.2 illustrates the Frank diagram and the Wulff shape of $\gamma_{\mathtt{E}}$ for $\mathtt{E} = 10^{-1}$ and $\mathtt{E} = 10^{-3}$.

Example 2.5 (Kobayashi)**.** *In his pioneering paper on modelling and simulation of anisotropic crystal growth Kobayashi [81] introduces the anisotropy*

$$\gamma_{k,\bar{a}} : \mathbb{R}^2 \to \mathbb{R}, \qquad \gamma_{k,\bar{a}}(x) = \begin{cases} (1 + \bar{a} \cos(k\beta(x))) \, |x| & , \ x \neq 0 \\ 0 & , \ x = 0 \end{cases} \tag{2.9}$$

where $k \in \mathbb{N}$, $\bar{a} > 0$ and $\beta(x) \in [0, 2\pi]$ is the angle between x and the (positive) horizontal axis. Assumption (A4) is obviously satisfied. Moreover, $(\gamma_{k,\bar{a}}^2)''$ is positive definite for $\bar{a} < \bar{a}_c := \frac{1}{k^2-1}$ (see [29]) so that (A5) again follows from [58, Remark 1.7.5]. Figure 2.2 illustrates the Frank diagram and the Wulff shape of $\gamma_{5,0.041}$ and $\gamma_{3,0.124}$.

Important properties like strong convexity, Fréchet-differentiability and Lipschitz continuity of the derivative of γ^2 carry over to the interface energy part $\mathcal{E}_0 : H^1(\Omega) \to \mathbb{R}$ of the Ginzburg-Landau energy $\mathcal{E}$ (2.1) given by

$$\mathcal{E}_0(c) = \int_\Omega \frac{\varepsilon}{2} \gamma^2(\nabla c) \, dx. \tag{2.10}$$

Lemma 2.11. *The interface energy $\mathcal{E}_0$ (2.10) is Fréchet-differentiable on $H^1(\Omega)$. The derivative $D\mathcal{E}_0(v) \in H^1(\Omega)'$ at $v \in H^1(\Omega)$ is given by*

$$\langle D\mathcal{E}_0(v), w \rangle = \int_\Omega \frac{\varepsilon}{2} \left\langle (\gamma^2)'(\nabla v), \nabla w \right\rangle dx = \varepsilon \left(\gamma(\nabla v)\gamma'(\nabla v), \nabla w \right) \quad \forall w \in H^1(\Omega)$$

and it is Lipschitz continuous in the following sense

$$\sup_{\substack{u \in H^1(\Omega) \\ \|\nabla u\|_0 = 1}} |\langle D\mathcal{E}_0(v) - D\mathcal{E}_0(w), u \rangle| \leqslant \frac{\varepsilon L}{2} \|\nabla v - \nabla w\|_0 \qquad \forall v, w \in H^1(\Omega).$$
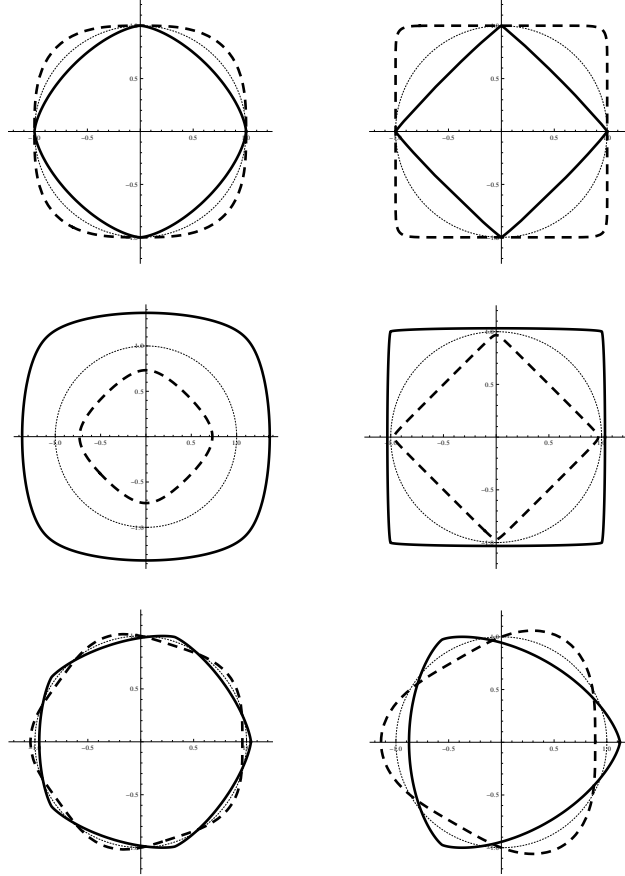
Figure 2.2 – Frank diagram (thick dashed), Wulff shape (thick) and Euclidean unitsphere (thin dashed) for γ_p (top) with $p = 3$ (left) and $p = 16$ (right), $\gamma_{\texttt{E}}$ (middle) with $\texttt{E} = 10^{-1}$ (left) and $\texttt{E} = 10^{-3}$ (right), and $\gamma_{k,\bar{a}}$ (bottom) with $k = 5$, $\bar{a} = 0.041$ (left) and $k = 3$, $\bar{a} = 0.124$ (right).

Furthermore $\mathcal{E}_0$ is strongly convex wrt to the H^1-seminorm $\|\nabla \cdot\|_0$, i.e.

$$\mathcal{E}_0(v) - \mathcal{E}_0(w) \geqslant \langle D\mathcal{E}_0(w), v - w \rangle + \frac{\varepsilon\mu}{4} \|\nabla v - \nabla w\|_0^2 \qquad \forall v, w \in H^1(\Omega).$$

We may extend $\mathcal{E}_0$ to $L^2(\Omega)$ with the value $+\infty$ and find that the extended functional is lower semicontinuous in $L^2(\Omega)$. We will use this result in our existence and uniqueness proof in subsection 2.1.3.

Lemma 2.12. *The extended functional* $\mathcal{E}_0 : L^2(\Omega) \to \mathbb{R} \cup \{+\infty\}$ *is proper convex and lower semicontinuous in* $L^2(\Omega)$.

In the proof we will employ the following result.

2. Anisotropic Allen–Cahn Equations

Lemma 2.13. *Consider a function $G : \Omega \times \mathbb{R}^d \to \mathbb{R} \cup \{+\infty\}$ such that $G(\cdot, \xi) \in L^1(\Omega)$ for all $\xi \in \mathbb{R}^d$, $G(x, \cdot)$ is continuous and proper convex for a.e. $x \in \Omega$, and satisfies the growth condition*

$$G(x, \xi) \geqslant \alpha_0 \|\xi\|^2 - \alpha_1 \quad \forall \xi \in \mathbb{R}^d, \ a.e. \ x \in \Omega \tag{2.11}$$

with some positive constants α_0, α_1. For some closed (wrt $\|\cdot\|_{H^1(\Omega)}$) convex set $\mathcal{K} \subset H^1(\Omega)$ the functional $\phi : L^2(\Omega) \to \mathbb{R}$

$$\phi(v) = \begin{cases} \int_\Omega G(x, \nabla v(x)) \, dx & v \in \mathcal{K} \\ \infty & otherwise \end{cases}$$

is then proper convex and lsc in $L^2(\Omega)$.

Proof. ϕ proper. As G is proper in the second argument we find a $\xi \in \mathbb{R}^d$ such that $G(x, \xi) < +\infty$ (and not $-\infty$) for a.e. $x \in \Omega$. If we choose $v(x) = \langle \xi, x \rangle$ then we have $\phi(v) = \int_\Omega G(x, \xi) \, dx < +\infty$ by the assumption $G(\cdot, \xi) \in L^1(\Omega)$. Hence $\phi \neq +\infty$. From the growth condition (2.11) follows for bounded Ω and any $v \in \text{dom}(\phi)$ that

$$\phi(v) = \int_\Omega G(x, \nabla v(x)) \, dx \geqslant \int_\Omega \left(\alpha_0 \|\nabla v(x)\|^2 - \alpha_1 \right) \, dx \geqslant -\alpha_1 |\Omega| > -\infty.$$

Convexity. Convexity follows immediately from the convexity of $G(\xi, \cdot)$ and $\mathcal{K}$.

Lower semicontinuity in $L^2(\Omega)$. We start by showing weak lower semicontinuity in $H^1(\Omega)$. Since ϕ is convex it is weakly lsc if it is lsc in norm. Consider therefore some (strongly) convergent sequence $v_n \longrightarrow v \in H^1(\Omega)$. Let's assume $I = \liminf \phi(v_n) < \phi(v)$. It follows immediately that $I < +\infty$ and without loss of generality we can assume that $v_n \in \mathcal{K}$ and $\phi(v_n) \longrightarrow I < \phi(v)$ because otherwise we could consider a corresponding subsequence v_{n_k} without changing the limes inferior. Closedness of $\mathcal{K}$ implies $v \in \mathcal{K}$.

On the other hand we know that $\nabla v_n \longrightarrow \nabla v$ in $L^2(\Omega; \mathbb{R}^d)$ and therefore we can extract a subsequence v_{n_k} such that $\nabla v_{n_k}(x) \longrightarrow \nabla v(x)$ almost everywhere. Hence the (lower semi-) continuity of $G(x, \cdot)$ yields for a.e. $x \in \Omega$

$$\liminf_{n_k \longrightarrow \infty} G(x, \nabla v_{n_k}(x)) \geqslant G(x, \nabla v(x)).$$

Bearing in mind that $v_n, v \in \mathcal{K}$ and applying Fatou's lemma (Lemma A.8) we may

20

compute upon integration over Ω

$$\liminf_{n_k \longrightarrow \infty} \phi(v_{n_k}) = \liminf_{n_k \longrightarrow \infty} \int_\Omega G(x, \nabla v_{n_k}(x)) \geqslant \int_\Omega \liminf_{n \longrightarrow \infty} G(x, \nabla v_{n_k}(x))$$
$$\geqslant \int_\Omega G(x, \nabla v(x)) = \phi(v)$$

which is a contradiction to the assumption.

Now let $w_n \longrightarrow w$ be an arbitrary sequence converging in $L^2(\Omega)$. We need to ascertain that $\liminf_{n \longrightarrow \infty} \phi(w_n) \geqslant \phi(w)$. If $\liminf_{n \longrightarrow \infty} \phi(w_n) = +\infty$, there's nothing to prove. Hence let's assume that
$$\liminf_{n \longrightarrow \infty} \phi(w_n) = I < +\infty$$

Again we can extract a subsequence in $\mathcal{K}$ (also denoted by w_n) such that $\phi(w_n) \longrightarrow I$. Therefore $\phi(w_n)$ is bounded. Together with the growth condition (2.11) we deduce

$$c \geqslant \phi(w_n) \geqslant \int_\Omega (\alpha_0 |\nabla w_n(x)|^2 - \alpha_1) \, dx \quad \forall n$$

and therefore

$$\int_\Omega |\nabla w_n(x)|^2 \, dx \leqslant \frac{c + \alpha_1}{\alpha_0}$$

whence it follows that w_n is not only bounded in $L^2(\Omega)$ but also in $H^1(\Omega)$. Thus we can extract a weakly convergent (in $H^1(\Omega)$) subsequence w_{n_k} that by virtue of the compact embedding $H^1 \hookrightarrow L^2$ has w as its weak limit. Finally we use the $H^1(\Omega)$-weak lower semicontinuity of ϕ to attain

$$\liminf_{n_k \longrightarrow \infty} \phi(w_{n_k}) \geqslant \phi(w).$$

The same indirect argument as above ensures that this inequality holds for the whole sequence w_n. $\qquad \square$

Proof of Lemma 2.12. By Assumption (A4) γ^2 is continuous and proper on $\mathbb{R}^d$ and strongly convex and coercive by Corollary 2.10 with

$$\gamma^2(x) \geqslant \frac{\mu}{2} |x|^2 \qquad \forall x \in \mathbb{R}^d.$$

Hence Lemma 2.13 applies and we have the claim. $\qquad \square$

2.1.2. Allen–Cahn Equation

The anisotropic Allen–Cahn equation is postulated as the (scaled) L^2-gradient flow for the Ginzburg–Landau energy $\mathcal{E}$ as given in (2.1). Considering the splitting

$$\mathcal{E}(c) = \mathcal{E}_0(c) + \frac{1}{\varepsilon}\phi(c) + \frac{1}{\varepsilon}\Upsilon(c) := \int_\Omega \frac{\varepsilon}{2}\gamma(\nabla c)^2\,dx + \int_\Omega \frac{1}{\varepsilon}\Phi(c)\,dx + \int_\Omega \frac{1}{\varepsilon}\Upsilon(c)\,dx$$

into a smooth convex, a nonsmooth convex, and a smooth possibly nonconvex part we have for some final time $T > 0$

$$-\varepsilon\frac{dc}{dt}(t) - \frac{1}{\varepsilon}D\Upsilon(c(t)) \in \partial\left(\mathcal{E}_0(c(t)) + \frac{1}{\varepsilon}\phi(c(t))\right) \qquad a.e.\ t \in (0,T] \qquad (2.12)$$

where D,∂ denote the Fréchet differential and the convex subdifferential (see e.g. [45]) respectively. With natural boundary conditions, $n(x)$ being the outer unit normal of Ω at $x \in \partial\Omega$,

$$\gamma(\nabla c(x))\langle n(x), (\nabla\gamma)(\nabla c(x))\rangle = 0 \quad \forall x \in \partial\Omega,\ a.e\ t > 0 \qquad (2.13)$$

and exploiting the definition of the subdifferential we have the variational inequality formulation of the anisotropic Allen-Cahn equation

$$0 \leqslant \varepsilon\langle\frac{dc}{dt}, v - c\rangle + \langle D(\mathcal{E}_0 + \frac{1}{\varepsilon}\Upsilon)(c), v - c\rangle + \frac{1}{\varepsilon}\phi(v) - \frac{1}{\varepsilon}\phi(c) \quad \forall v \in H^1(\Omega),\ a.e.\ t \in (0,T]$$
$$(2.14)$$

Note that from (A5) follow convexity, continuity and Fréchet–differentiability of $\mathcal{E}_0$ in $H^1(\Omega)$.

2.1.3. Analytic properties

Existence and uniqueness of solutions

We will base our existence and uniqueness proof on an abstract result from the theory of maximal monotone operators. It is stated together with the definition, basic properties, and some examples of maximal monotone operators in the appendix A.1; we refer to the monograph [27] for a thorough treatment of the subject. However we shall stress at this point, that the subdifferential of a proper convex and lower semicontinuous (lsc) functional is maximal monotone (see Theorem A.3).

Theorem 2.14 (Existence and uniqueness). *For every $c_0 \in \overline{\mathrm{dom}(\mathcal{E})} = \mathrm{dom}(\phi)$ there is a unique solution to the anisotropic Allen–Cahn equation (2.12) in the sense of definition A.3, i.e. it exists $c \in \mathcal{C}(0, T; L^2(\Omega))$ such that*

1. *c is locally absolutely continuous*

2. *$c(t) \in \mathrm{dom}(\partial\mathcal{E})$ a.e. in $(0, T)$*

3. *$0 \in \varepsilon \frac{dc}{dt}(t) + \partial\mathcal{E}(c(t))$ a.e. in $(0, T)$*

It is $\sqrt{t}\frac{dc}{dt} \in L^2(0, T; H^1(\Omega))$ and iff $c_0 \in \mathrm{dom}(\mathcal{E}) = H^1(\Omega) \cap \mathrm{dom}(\phi)$ $\frac{dc}{dt} \in L^2(0, T; H^1(\Omega))$.

Proof. In order to apply Theorem A.7 with $\mathcal{H} = L^2(\Omega)$ we need to show

1. that $\mathcal{E}_0 + \frac{1}{\varepsilon}\phi$ is proper convex and $L^2(\Omega)$-lsc

2. that $D\gamma$ is Lipschitz continuous on $\mathrm{dom}(\mathcal{E}_0 + \phi)$

The latter is satisfied by Assumption (A3) or in the special case of (2.4) by Lemma 2.4. Concerning the former we first note that the sum of convex functions is always convex and the sum of proper functions is again proper iff the intersection of the effective domains, i.e. the sets where they take finite values, is nonempty. Furthermore the sum of lsc functions is lsc. Properness, convexity and lower semicontinuity in $L^2(\Omega)$ of $\mathcal{E}_0$ and ϕ are ensured by Lemma 2.12 and Assumption (A2) (or Lemma 2.1 for the particular choice of the logarithmic potential) respectively. It remains to be shown, that $\mathrm{dom}(\mathcal{E}_0 + \phi) = \mathrm{dom}(\mathcal{E}_0) \cap \mathrm{dom}(\phi)$ is nonempty. However, since $\mathcal{E}_0$ is finite for all $v \in H^1(\Omega)$, $\mathrm{dom}(\mathcal{E}_0 + \phi)$ is simply the domain of ϕ which is nonempty since the functional is proper.

Applying Theorem A.7 yields the claim. $\qquad\square$

Sharp interface-limit and asymptotic phase shapes

Many phase-field models may also be regarded as approximations of lower dimensional models for the evolution of a closed hypersurface $\Gamma(t)$. As these models are limit models in a certain sense for $\varepsilon \longrightarrow 0$ (see Theorem 2.15 below) they are usually termed the corresponding *sharp-interface limit*. In the case of the isotropic Allen–Cahn equation the sharp-interface limit is known to be given by mean curvature flow (also curve shortening

2. Anisotropic Allen–Cahn Equations

flow) (cf. [49]).

$$V_n = -\kappa \qquad \text{on } \Gamma(t),$$

where n, V_n, and κ denote the outer normal, normal velocity and mean curvature respectively. In the context of Finsler geometry the anisotropic mean curvature flow for an anisotropy function γ can be written analogously as

$$V_{n_\gamma} = -\kappa_\gamma \qquad \text{on } \Gamma(t), \tag{2.15}$$

with n_γ, V_{n_γ}, κ_γ being the anisotropic pendants to n, V_n, and κ. This is the gradient flow with respect to the Finsler metric induced by γ for the surface energy functional

$$\mathcal{S}(\Gamma) = \int_\Gamma \gamma(n)\, d\gamma \tag{2.16}$$

For precise definitions and further detail we refer to [12, 1]. Bellettini and Paolini [12] argue formally that the sharp-interface limit to the anisotropic Allen–Cahn equation is given by anisotropic mean curvature flow. The following result has been rigorously proven by Alfaro et al in [1].

Theorem 2.15. *Choose initial data $c_0 \in H^1(\Omega) \cap L^\infty(\Omega)$ and $\Gamma_0 = \{x \in \Omega \mid c_0(x) = 0\}$ and let $c_\varepsilon(x,t)$ and $\Gamma(t)$ be the corresponding solutions to the anisotropic Allen–Cahn equation (2.14) and anisotropic mean curvature flow (2.15) respectively. Furthermore let Ω_t^- denote the part of Ω enclosed by $\Gamma(t)$, $\Omega_t^+ = \Omega \setminus \Omega_t^-$, and $\bar{c}(x,t) = \chi_{\Omega_t^+}(x) - \chi_{\Omega_t^-}(x)$ with*

$$\chi_A(x) = \begin{cases} 1 & \text{if } x \in A \\ 0 & \text{else.} \end{cases}$$

Then c_ε converges to $\bar{c}$ almost everywhere in $\Omega \times (0,T)$.

Note that this result was proven under the assumption of smooth potentials Ψ (at least $\mathcal{C}^2$) but virtually arbitrary initial data. Elliott and Schätzle [46, 47] proved a similar result in the double obstacle case, but with stronger restrictions on the initial data.

While in under isotropic mean curvature flow all particles are asymptotically spherical (cf. [77]) the analogous anisotropic equilibrium shape is given by the Wulff shape (see Definition 2.1) as is stated by Wulff's Theorem (cf. [123, 75, 33]).

Theorem 2.16 (Wulff)**.** *The boundary of a scaled Wulff shape is the unique minimizer of*

the surface energy functional (2.16) *among all closed hypersurfaces enclosing a prescribed d-dimensional volume.*

Hence, taking the boundary of a scaled Wulff shape W_γ as initial value, one might expect $\Gamma(t)$ to be self-similarly shrinking under anisotropic mean curvature flow. The following theorem states that this is indeed the case (cf. [114, 58]).

Theorem 2.17. *Let* $\Gamma_0 = \{x \in \mathbb{R}^d \mid \gamma^*(x) = r_0\}$ *evolve under mean curvature flow. Then the solution is given by*

$$\Gamma(t) = \left\{ x \in \mathbb{R}^d \mid \gamma^*(x) = \sqrt{r_0^2 - 2t} \right\} \qquad , \ 0 \leqslant t \leqslant \frac{r_0^2}{2}$$

2.2. Numerical Solution

For the numerical approximation of the Allen-Cahn equation (2.14) we apply ROTHE*'s method* (or horizontal method of lines) (cf. [23]), i.e. we treat the PDE as an ODE in function space and first discretize in time resulting in a series of nonlinear stationary problems, the so-called spatial problems. The advantage of this approach over the (vertical) *method of lines* is that it allows for evolving locally refined spatial meshes. Since solutions to phase-field models after decomposition typically show areas of largely constant value separated by thin transitional layers which have to be resolved, adaptivity in space strongly recommends itself.

This section is organized as follows: Firstly we discuss several Euler time discretizations differing in the treatment of the nonlinearities Ψ and γ for which we give existence and stability results. Following is a description of our adaptive space discretization by P1 finite elements and the hierarchical error estimators it is based on. Some implementational issues arising from evolving grids are adressed in the notes on implementation (Sec. 2.2.4) after going into some detail about the solution of the algebraic (discretized spatial) problems by means of the Truncated Nonsmooth Newton Multigrid method (TNNMG). A number of numerical experiments conclude the section.

2.2.1. Euler Time Discretizations

We will present four Euler time discretizations differing in the way they treat the nonlinearities ψ and γ respectively. Starting out from a fully implicit nonlinear scheme we discuss a semi-implicit (wrt. ψ) scheme and a linearized (wrt. γ) time discretization. The schematic in Table 2.1 gives an overview of the considered time discretizations and the names employed in the following.

In the isotropic and anisotropic case with quartic potential exist convergence results for

$\psi \setminus \gamma$	nonlinear	linearized
fully implicit	NONLIN	LIN(λ)
semi implicit	NONLINSEMI	LINSEMI(λ)

Table 2.1 – Overview of Euler time discretization schemes for anisotropic Allen–Cahn equations

the implicit Euler discretization proved in [50] and [28] respectively. For the anisotropic case with logarithmic potential convergence of time discretizations remains largely open. Nevertheless the stability results for each considered scheme comprise an important step towards a convergence proof. Furthermore the results show that the discrete flows retain the Lyapunov property for the Ginzburg-Landau energy.

NONLIN

First we consider the fully implicit, nonlinear Euler method for some $T > 0$, some uniform time step $\tau = T/M$ and some consistent initial condition $c^0 \in L^\infty(\Omega)$

$$c^m \in H^1(\Omega): \quad \left(c^m - c^{m-1}, v - c^m\right) + \frac{\tau}{\varepsilon} \left\langle D\mathcal{E}_0(c^m), v - c^m \right\rangle$$
$$+ \frac{\tau}{\varepsilon^2}\left(\phi(v) - \phi(c^m) + \left\langle D\Upsilon(c^m), v - c^m \right\rangle\right) \geqslant 0 \qquad \forall v \in H^1(\Omega) \quad (2.17)$$

Let L^* be the Lipschitz constant of $D\Upsilon$. Then, under the assumption $\tau \cdot L^* \leqslant \varepsilon^2$ this variational inequality may be reformulated as an equivalent minimization problem

$$c^m \in H^1(\Omega): \quad \mathcal{J}^m(c^m) \leqslant \mathcal{J}^m(v) \qquad \forall v \in H^1(\Omega) \qquad (2.18)$$

for the energy functional

$$\mathcal{J}^m(v) := \frac{\tau}{\varepsilon}\mathcal{E}_0(v) + \frac{\tau}{\varepsilon^2}\phi(v) + \frac{1}{2}\|v\|_0^2 + \frac{\tau}{\varepsilon^2}\Upsilon(v) - \left(c^{m-1}, v\right).$$

Defining $\mathcal{J}_*(v) = \frac{1}{2}\|v\|_0^2 + \frac{\tau}{\varepsilon^2}\Upsilon(v)$ by Lipschitz continuity of $D\Upsilon$ we may infer monotonicity of $D\mathcal{J}_*$ as follows

$$
\begin{aligned}
\langle D\mathcal{J}_*(v) - D\mathcal{J}_*(w), v - w\rangle &= (v, v - w) - (w, v - w) + \frac{\tau}{\varepsilon^2}\langle D\Upsilon(v) - D\Upsilon(w), v - w\rangle \\
&\geq (v - w, v - w) - \frac{\tau}{\varepsilon^2}|\langle D\Upsilon(v) - D\Upsilon(w), v - w\rangle| \\
&\geq \|v - w\|_0^2 - \frac{\tau}{\varepsilon^2}\|D\Upsilon(v) - D\Upsilon(w)\|_{L^2(\Omega)'}\|v - w\|_0 \\
&\geq \left(1 - \frac{\tau}{\varepsilon^2}L^*\right)\|v - w\|_0^2 \geq 0 \quad \text{if } \tau \leq \frac{\varepsilon^2}{L^*},
\end{aligned}
$$

and hence convexity of $\mathcal{J}_*$. From Lemma 2.11 and Assumption (A2) the convexity of $\mathcal{J}^m$ then follows immediately; strict convexity holds for $\tau \cdot L^* < \varepsilon^2$, which gives

Proposition 2.18. *Let* $\tau \cdot L^* < \varepsilon^2$. *Then the spatial problem* (2.18) *and equivalently* (2.17) *allow a unique solution for all* $m \leq M$.

Proof. As $\mathcal{J}^m$ under the given assumptions is strictly convex and by Assumption (A2) and Lemma 2.12 lsc., by [45, Prop. 1.2, Ch. II] all that is left to show is the coercivity of $\mathcal{J}^m$. Exploiting Assumption (A1) we have

$$\mathcal{J}^m(v) - \mathcal{J}_*(v) \geq \frac{\tau}{2}\left(\inf_{|x|=1}\gamma(x)\right)^2\|\nabla v\|_0^2 - \left(c^{m-1}, v\right)$$

and exploiting Lemma A.11 arrive at

$$
\begin{aligned}
\mathcal{J}_*(v) &\geq \frac{1}{2}\|v\|_0^2 - \frac{\tau}{\varepsilon^2}|\Upsilon(v)| \\
&\geq \frac{1}{2}\|v\|_0^2 - \frac{\tau}{\varepsilon^2}\left(\frac{L^*}{2}\|v\|_0^2 + \|D\Upsilon(0)\|_{L^2(\Omega)'}\|v\|_0 + |\Upsilon(0)|\right) \\
&= \frac{1}{2}\left(1 - \frac{\tau}{\varepsilon^2}L^*\right)\|v\|_0^2 - \|D\Upsilon(0)\|_{L^2(\Omega)'}\|v\|_0 - |\Upsilon(0)|
\end{aligned}
$$

$\square$

We now state stability results for the given time discretization whose short proofs are given in [70] and repeated here slightly modified to accomodate for a more general γ. In

the following μ, L are those of Lemma 2.8.

Theorem 2.19. *Let $\tau \cdot L^* < \varepsilon^2$. Then the Ginzburg–Landau free energy $\mathcal{E}$ defined in (2.1) is a Lyapunov functional for (2.17) satisfying*

$$\frac{\varepsilon}{2\tau}\|c^m - c^{m-1}\|_0^2 + \frac{\varepsilon\mu}{4}\|\nabla c^m - \nabla c^{m-1}\|_0^2 + \mathcal{E}(c^m) \leqslant \mathcal{E}(c^{m-1}). \tag{2.19}$$

The fully implicit Euler method NONLIN (2.17) is conditionally stable in the sense that

$$\frac{\varepsilon}{2\tau}\sum_{m=1}^M \|c^m - c^{m-1}\|_0^2 + \frac{\varepsilon\mu}{4}\sum_{m=1}^M \|\nabla c^m - \nabla c^{m-1}\|_0^2 \leqslant \mathcal{E}(c^0). \tag{2.20}$$

holds for all $\tau < \varepsilon^2$.

Proof. Substitution of $v = c^{m-1}$ and $\psi(v) = \phi(v) + \Upsilon(v)$ in (2.17) and again application of Lemma A.11 yields

$$
\begin{aligned}
\|c^m - c^{m-1}\|_0^2 \leqslant{}& \frac{\tau}{\varepsilon}\left\langle D\mathcal{E}_0(c^m), c^{m-1} - c^m \right\rangle \\
&+ \frac{\tau}{\varepsilon^2}\left(\psi(c^{m-1}) - \psi(c^m)\right) - \frac{\tau}{\varepsilon^2}\left(\Upsilon(c^{m-1}) - \Upsilon(c^m) - \left\langle D\Upsilon(c^m), c^{m-1} - c^m\right\rangle\right) \\
\leqslant{}& \frac{\tau}{\varepsilon}\left\langle D\mathcal{E}_0(c^m), c^{m-1} - c^m \right\rangle \\
&+ \frac{\tau}{\varepsilon^2}\left(\psi(c^{m-1}) - \psi(c^m)\right) + \frac{\tau}{\varepsilon^2}\left|\Upsilon(c^{m-1}) - \Upsilon(c^m) - \left\langle D\Upsilon(c^m), c^{m-1} - c^m\right\rangle\right| \\
\leqslant{}& \frac{\tau}{\varepsilon}\left\langle D\mathcal{E}_0(c^m), c^{m-1} - c^m \right\rangle \\
&+ \frac{\tau}{\varepsilon^2}\left(\psi(c^{m-1}) - \psi(c^m)\right) + \frac{\tau}{2\varepsilon^2}L^*\|c^m - c^{m-1}\|_0^2
\end{aligned}
$$

Exploiting the strong convexity of $\mathcal{E}_0$ as stated in Lemma 2.11 we conclude that

$$
\begin{aligned}
(1 - \frac{\tau}{2\varepsilon^2}L^*)\|c^m - c^{m-1}\|_0^2 \leqslant{}& \frac{\tau}{\varepsilon}\left(\mathcal{E}_0(c^{m-1}) - \mathcal{E}_0(c^m) - \frac{\varepsilon\mu}{4}\|\nabla c^m - \nabla c^{m-1}\|_0^2\right) \\
&+ \frac{\tau}{\varepsilon^2}\left(\psi(c^{m-1}) - \psi(c^m)\right)
\end{aligned}
$$

Finally we use the assumption $\tau \cdot L^* < \varepsilon^2$ and $\mathcal{E} = \mathcal{E}_0 + \frac{1}{\varepsilon}\psi$ to arrive at the assertion (2.19) after multiplication by ε/τ and some rearranging of terms.

The estimate (2.20) then follows immediately by recursive application of (2.19) bearing in mind that $\mathcal{E}(v) \geqslant 0$, $\forall v \in H^1(\Omega)$ (by (A1)). $\qquad\square$

NONLINSEMI

Assuming additionally that γ is concave we may exploit the splitting $\psi = \phi + \gamma$ (cf. equation (2.2)) to overcome the stability constraints on τ in the previously described scheme. Discretizing the expanding part explicitely leads to the semi-implicit nonlinear Euler discretization (NONLINSEMI):

$$c^m \in H^1(\Omega): \quad \left(c^m - c^{m-1}, v - c^m\right) + \frac{\tau}{\varepsilon}\left\langle D\mathcal{E}_0(c^m), v - c^m\right\rangle$$
$$+ \frac{\tau}{\varepsilon^2}\left(\phi(v) - \phi(c^m)\right) \geqslant -\frac{\tau}{\varepsilon^2}\left\langle D\gamma(c^{m-1}), v - c^m\right\rangle \qquad \forall v \in H^1(\Omega) \quad (2.21)$$

Again we can formulate an equivalent minimization problem, this time for the energy functional

$$\mathcal{J}^m(v) := \frac{\tau}{\varepsilon}\mathcal{E}_0(v) + \frac{\tau}{\varepsilon^2}\phi(v) + \frac{1}{2}\|v\|_0^2 - \left(\left(c^{m-1}, v\right) + \frac{\tau}{\varepsilon^2}\left\langle D\gamma(c^{m-1}), v\right\rangle\right)$$

Note that $\mathcal{J}^m$ is strictly convex for all $\tau > 0$. Existence and uniqueness of solutions follows as before. The semi-implict nonlinear Euler method is unconditionally stable as stated by the following

Theorem 2.20. *For all $\tau > 0$ the Ginzburg–Landau free energy $\mathcal{E}$ defined in (2.1) is a Lyapunov functional for (2.21) satisfying*

$$\frac{\varepsilon}{\tau}\|c^m - c^{m-1}\|_0^2 + \frac{\varepsilon\mu}{4}\|\nabla c^m - \nabla c^{m-1}\|_0^2 + \mathcal{E}(c^m) \leqslant \mathcal{E}(c^{m-1}). \qquad (2.22)$$

The semi-implicit Euler method NONLINSEMI (2.21) is unconditionally stable in the sense that

$$\frac{\varepsilon}{\tau}\sum_{m=1}^{M}\|c^m - c^{m-1}\|_0^2 + \frac{\varepsilon\mu}{4}\sum_{m=1}^{M}\|\nabla c^m - \nabla c^{m-1}\|_0^2 \leqslant \mathcal{E}(c^0) \qquad (2.23)$$

holds for all $\tau > 0$.

Proof. From the assumption that γ is concave we can deduce by a straightforward computation

$$(-\gamma)(c^m) - (-\gamma)(c^{m-1}) - \left\langle D(-\gamma)(c^{m-1}), c^m - c^{m-1}\right\rangle \geqslant 0.$$

This is sometimes called *gradient inequality (for convex funcions)*.

2. Anisotropic Allen–Cahn Equations

The rest of the proof is very similar to that of Theorem 2.19 and therefore not repeated. $\quad\square$

Remark 2.6. *For the special choice given in (2.4) the inequalities in Theorem 2.20 are stronger in the sense that they hold also for $\left(\frac{\varepsilon}{\tau} + \frac{1}{2\varepsilon}\right)$ instead of $\frac{\varepsilon}{\tau}$ (cf. [70, Thm. 3.2]).*

LIN(λ)

To circumvent the costly inversion of the nonlinear operator induced by γ^2 we replace the corresponding term in the spatial problem (2.17) by the linear approximation

$$\langle D\mathcal{E}_0(c^m), v - c^m \rangle \approx \langle D\mathcal{E}_0(c^{m-1}), v - c^m \rangle + \lambda\varepsilon \left(\nabla c^m - \nabla c^{m-1}, v - c^m\right)$$

resulting in the fully implicit linearized Euler discretization (LIN(λ)):

$$c^m \in H^1(\Omega):$$
$$\left(c^m - c^{m-1}, v - c^m\right) + \tau\lambda\left(\nabla c^m, \nabla(v - c^m)\right) + \frac{\tau}{\varepsilon^2}\left(\phi(v) - \phi(c^m) + \langle D\Upsilon(c^m), v - c^m\rangle\right)$$
$$\geqslant \tau\lambda\left(\nabla c^{m-1}, \nabla(v - c^m)\right) - \frac{\tau}{\varepsilon}\langle D\mathcal{E}_0(c^{m-1}), v - c^m\rangle \qquad \forall v \in H^1(\Omega) \quad (2.24)$$

For $\lambda > 0$, $\tau < \varepsilon^2$ and $c^0 \in H^1(\Omega)$ existence and uniqueness follows as for NONLIN considering the minimization problem for the functional

$$\mathcal{J}^m(v) := \frac{\tau\lambda}{2}\left(\nabla v, \nabla v\right) + \frac{\tau}{\varepsilon^2}\phi(v) + \frac{1}{2}\|v\|_0^2 + \frac{\tau}{\varepsilon^2}\Upsilon(v)$$
$$+ \frac{\tau}{\varepsilon}\langle\mathcal{E}_0(c^{m-1}), v\rangle - \tau\lambda\left(\nabla c^{m-1}, \nabla v\right) - \left(c^{m-1}, v\right)$$
$$= \frac{\tau}{\varepsilon}\widehat{\mathcal{E}}_0(v) + \frac{\tau}{\varepsilon^2}\phi(v) + \frac{1}{2}\|v\|_0^2 + \frac{\tau}{\varepsilon^2}\Upsilon(v) - \langle f^{m-1}, v\rangle$$

where $\widehat{\mathcal{E}}_0$ is defined as in (2.10) with $\gamma = \hat{\gamma} := \sqrt{\lambda}\,|\cdot|$ and $f^{m-1} \in H^1(\Omega)'$ is a functional collecting the linear terms. In order for LIN(λ) to be stable, apart from $\tau < \varepsilon^2$, we expect λ has to be sufficiently large wrt. γ such that $\frac{\tau}{\varepsilon}\langle\mathcal{E}_0(c^{m-1}), v\rangle - \tau\lambda\left(\nabla c^{m-1}, \nabla v\right) < 0$ and indeed we find (cf. [70])

Theorem 2.21. *Let $\tau < \varepsilon^2$ and choose $\lambda \geqslant L/2$. Then the Ginzburg–Landau free energy $\mathcal{E}$ defined in (2.1) is a Lyapunov functional for (2.24) satisfying*

$$\frac{\varepsilon}{2\tau}\|c^m - c^{m-1}\|_0^2 + \frac{\varepsilon\mu}{4}\|\nabla c^m - \nabla c^{m-1}\|_0^2 + \mathcal{E}(c^m) \leqslant \mathcal{E}(c^{m-1}). \qquad (2.25)$$

The linearized fully implicit Euler method (2.24) is conditionally stable in the sense that

$$\frac{\varepsilon}{2\tau} \sum_{m=1}^{M} \left\| c^m - c^{m-1} \right\|_0^2 + \frac{\varepsilon\mu}{4} \sum_{m=1}^{M} \left\| \nabla c^m - \nabla c^{m-1} \right\|_0^2 \leqslant \mathcal{E}(c^0) \tag{2.26}$$

holds under the above assumptions.

Proof. Following the first steps of the proof for Theorem 2.19 we find the inequality

$$\left(1 - \frac{\tau}{2\varepsilon^2}\right) \left\| c^m - c^{m-1} \right\|_0^2 + \tau\lambda \left\| \nabla c^m - \nabla c^{m-1} \right\|_0^2$$
$$\leqslant \frac{\tau}{\varepsilon^2} \left(\psi(c^{m-1}) - \psi(c^m) \right) + \frac{\tau}{\varepsilon} \left\langle D\mathcal{E}_0(c^{m-1}), c^{m-1} - c^m \right\rangle$$

Adding zero and exploiting Lipschitz continuity of $D\mathcal{E}_0$ (cf. 2.11) yields the following upper bound for the rightmost term

$$\frac{\tau}{\varepsilon} \left\langle D\mathcal{E}_0(c^{m-1}), c^{m-1} - c^m \right\rangle \leqslant \frac{\tau L}{2} \left\| \nabla c^m - \nabla c^{m-1} \right\|_0^2 + \frac{\tau}{\varepsilon} \left\langle D\mathcal{E}_0(c^m), c^{m-1} - c^m \right\rangle.$$

Continuing as in the proof for Theorem 2.19 yields the assertion (2.25).
The second estimate (2.26) follows as before. $\qquad\square$

LINSEMI(λ)

Our final scheme combines the two approaches to ψ and γ giving rise to the semi-implicit linearized Euler method. As for NONLINSEMI we assume γ to be concave.

$$c^m \in H^1(\Omega):$$
$$\left(c^m - c^{m-1}, v - c^m \right) + \tau\lambda \left(\nabla c^m, \nabla(v - c^m) \right) + \frac{\tau}{\varepsilon^2} \left(\phi(v) - \phi(c^m) \right)$$
$$\geqslant \tau\lambda \left(\nabla c^{m-1}, \nabla(v - c^m) \right) - \frac{\tau}{\varepsilon} \left\langle D\mathcal{E}_0(c^{m-1}), v - c^m \right\rangle$$
$$- \frac{\tau}{\varepsilon^2} \left\langle D\gamma(c^{m-1}), v - c^m \right\rangle \quad \forall v \in H^1(\Omega) \quad (2.27)$$

Existence and uniqueness follow for $\lambda > 0$, $\tau > 0$ and $c^0 \in H^1(\Omega)$ as before. The energy functional for the equivalent minimization problem is

$$
\begin{aligned}
\mathcal{J}^m(v) := {} & \frac{\tau\lambda}{2}\left(\nabla v, \nabla v\right) + \frac{\tau}{\varepsilon^2}\phi(v) + \frac{1}{2}\left\|v\right\|_0^2 \\
& + \frac{\tau}{\varepsilon}\left\langle \mathcal{E}_0(c^{m-1}), v\right\rangle - \tau\lambda\left(\nabla c^{m-1}, \nabla v\right) - \left(c^{m-1}, v\right) + \frac{\tau}{\varepsilon^2}\left\langle D\Upsilon(c^{m-1}), v\right\rangle \\
= {} & \frac{\tau}{\varepsilon}\widehat{\mathcal{E}}_0(v) + \frac{\tau}{\varepsilon^2}\phi(v) + \frac{1}{2}\left\|v\right\|_0^2 - \left\langle f^{m-1}, v\right\rangle
\end{aligned}
$$

with $\widehat{\mathcal{E}}_0$ defined as for LIN(λ) and $f^{m-1} \in H^1(\Omega)'$ collects the linear terms. Again the semi-implicit time discretization is unconditionally stable with respect to τ but same as for LIN(λ) the parameter λ has to be chosen suffiently large (cf. [70])

Theorem 2.22. *Let $\tau > 0$ and choose $\lambda \geqslant L/2$. Then the Ginzburg–Landau free energy $\mathcal{E}$ defined in (2.1) is a Lyapunov functional for (2.27) satisfying*

$$
\frac{\varepsilon}{\tau}\|c^m - c^{m-1}\|_0^2 + \frac{\varepsilon\mu}{4}\|\nabla c^m - \nabla c^{m-1}\|_0^2 + \mathcal{E}(c^m) \leqslant \mathcal{E}(c^{m-1}). \tag{2.28}
$$

The semi-implicit linearized Euler method (2.27) is unconditionally stable in the sense that

$$
\frac{\varepsilon}{\tau}\sum_{m=1}^{M}\|c^m - c^{m-1}\|_0^2 + \frac{\varepsilon\mu}{4}\sum_{m=1}^{M}\|\nabla c^m - \nabla c^{m-1}\|_0^2 \leqslant \mathcal{E}(c^0) \tag{2.29}
$$

holds for all $\tau > 0$.

The proof (cf. [70]) follows closely the proofs given above and is omitted here. Again the result is slightly stronger in the case of Υ as in (2.4) exchanging $\frac{\varepsilon}{\tau}$ for $\frac{\varepsilon}{\tau} + \frac{1}{2\varepsilon}$.

2.2.2. Adaptive Space Discretization for Evolution Problems

For simplicity we assume from now on Υ to be given by (2.4). The spatial problems of all considered time discretizations may be unifyingly written as the variational inequality

$$
c^m \in H^1(\Omega): \quad \frac{\tau}{\varepsilon}\left\langle D\widetilde{\mathcal{E}}_0(c^m), v - c^m\right\rangle + \frac{\tau}{\varepsilon^2}\left(\phi(v) - \phi(c^m)\right) + \alpha\left(c^m, v - c^m\right)
$$
$$
\geqslant \left\langle f^{m-1}, v - c^m\right\rangle \qquad \forall v \in H^1(\Omega) \tag{2.30}
$$

or equivalently as the minimization problem

$$c^m \in H^1(\Omega): \qquad \mathcal{J}^m(c^m) \leqslant \mathcal{J}^m(v) \qquad \forall v \in H^1(\Omega)$$
$$\mathcal{J}^m(v) := \frac{\tau}{\varepsilon}\widetilde{\mathcal{E}}_0(v) + \frac{\tau}{\varepsilon^2}\phi(v) + \alpha \|v\|_0^2 - \langle f^{m-1}, v \rangle, \tag{2.31}$$

where α is some positive constant, $f^{m-1} \in H^1(\Omega)'$ collects the explicit (linear) terms, and $\widetilde{\mathcal{E}}_0 = \mathcal{E}_0$ for the nonlinear schemes, whereas $\widetilde{\mathcal{E}}_0 = \widehat{\mathcal{E}}_0$ for the linearized ones. From here on the tilde will be dropped for notational convenience.

In the following, for simplicity, we assume Ω to be a nonempty, bounded, open polyhedral subset of $\mathbb{R}^d$, $1 \leqslant d \leqslant 3$.

From the use of locally refined grids for the solution of the sequence of discrete spatial problems arise several issues to be adressed. Firstly, we not only need an adaptive refinement scheme but also a coarsening scheme from one time step to the next in order to avoid an accumulation of unnecessary degrees of freedom over time. This coarsening scheme amounts to choosing an initial grid for the refinement process which ensures that no features of the previous (in time) solution are overlooked by the error estimator. A heuristic coarsening scheme designed for the present problems is described in the following. Secondly, we need to ensure that no information is lost from one timestep to the next - even in case of local coarsening. We approach this issue by keeping a grid that resolves the leaf grids of both, the current and the previous timestep. More details are found in the paragraph "The Subgrid Approach for Evolving Grids".

P1-Finite Element Discretization on Nonconforming Grids

Before giving the space discretized problem we define admissible grids and piecewise affine finite elements on such grids.

Definition 2.2 (Simplicial Partition)**:** We call a finite set $\mathfrak{T} \in 2^\Omega$ a *simplicial partition* of Ω if each $\mathfrak{t} \in \mathfrak{T}$ is a nondegenerate closed d-dimensional simplex and

$$\overline{\Omega} = \bigcup_{\mathfrak{t} \in \mathfrak{T}} \mathfrak{t} \quad \wedge \quad \forall_{\mathfrak{t}_1, \mathfrak{t}_2 \in \mathfrak{T}} : \mathfrak{t}_1 \neq \mathfrak{t}_2 \Rightarrow \mathring{\mathfrak{t}}_1 \cap \mathring{\mathfrak{t}}_2 = \varnothing$$

Furthermore we denote the set of (closed) k-faces of some $\mathfrak{t} \in \mathfrak{T}$ by $\mathfrak{F}_k(\mathfrak{t})$ and for some $\mathfrak{A} \subset \mathfrak{T}$ $\mathfrak{F}_k(\mathfrak{A}) = \bigcup_{\mathfrak{t} \in \mathfrak{A}} \mathfrak{F}_k(\mathfrak{t})$. Hence the set of vertices of $\mathfrak{T}$ is $\mathfrak{F}_0(\mathfrak{T})$ and so on. $\triangle$

Therefore the vertices $\mathfrak{p} = \{p\} \in \mathfrak{F}_0(\mathfrak{T}) \subset 2^\Omega$ are singletons of points $p \in \mathbb{R}^d$. To simplify

notation by $\mathfrak{p}$ we will denote a vertex (i.e. element of $\mathfrak{F}_0$) or the corresponding point in $\mathbb{R}^d$ as fitting the context.

Definition 2.3 (Simplicial Grid)**:** A simplicial partition $\mathfrak{T}$ is called a *simplicial grid* if

$$\forall_{\mathfrak{t}_1,\mathfrak{t}_2 \in \mathfrak{T}} : \; \mathfrak{t}_1 \cap \mathfrak{t}_2 = \varnothing \; \vee \; \exists_{0 \leqslant k \leqslant d} : \; \mathfrak{t}_1 \cap \mathfrak{t}_2 \in \mathfrak{F}_k(\mathfrak{t}_1) \cup \mathfrak{F}_k(\mathfrak{t}_2)$$

A simplicial grid is called *conforming* if the assertion holds also for the intersection of the $\mathfrak{F}_k(\mathfrak{t}_i)$. $\triangle$

Note that the general definition requires the intersection of two simplices to be a subentity (k-face) of *at least* one of the simplices and therefore allows for hanging nodes, whereas in conforming grids hanging nodes are forbidden. The reason why we allow hanging nodes will be made clear in the paragraph on "The Subgrid Approach for Evolving Grids" below. Figure 2.3 gives some examples and counterexamples of simplicial grids.

Definition 2.4 (Hanging Node)**:** A vertex $\mathfrak{p} \in \mathfrak{F}_0(\mathfrak{T})$ is called a *hanging node* if for some $\mathfrak{t} \in \mathfrak{T}$ and some k-face $\mathfrak{f} \in \mathfrak{F}_k(\mathfrak{t})$ with $0 < k < d$ holds $\mathfrak{p} \subset \mathfrak{f} \wedge \mathfrak{p} \notin \mathfrak{F}_0(\mathfrak{t})$. The set of hanging nodes is denoted by $\mathfrak{F}_0^\circ(\mathfrak{T})$; its complement in the set of vertices, i.e. the non-hanging nodes by $\mathfrak{F}_0^\bullet(\mathfrak{T})$. $\triangle$
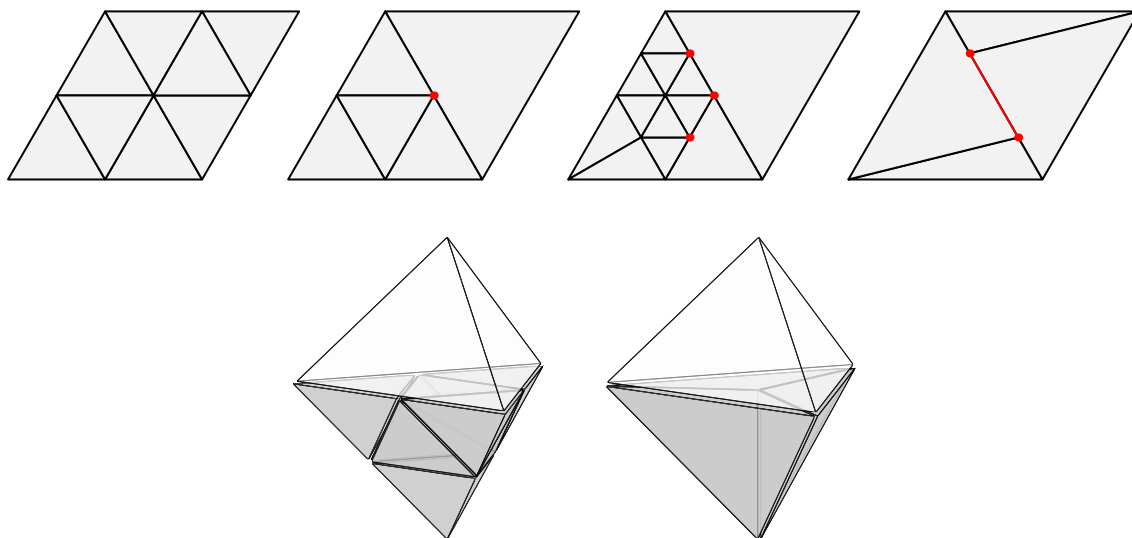

Figure 2.3 – Examples of simplicial partitions in 2D and 3D that are simplicial grids (a-c, e-f) and one that is not (d). Hanging nodes are marked by red dots in the 2D grids; in the counterexample the intersection that is not a face of either intersecting simplex is highlighted in red

We approximate the spatial problems (2.30) by piecewise affine elements on a simplicial grid $\mathfrak{T}$

$$\mathcal{S}_\mathfrak{T} := \left\{ v \in \mathcal{C}(\overline{\Omega}) \mid \forall_{\mathfrak{t} \in \mathfrak{T}} : v|_\mathfrak{t} \in \mathcal{P}^1(\mathfrak{t}) \right\} \tag{2.32}$$

and the discretized nonlinearity

$$\phi_\mathfrak{T}(v) := \phi_{\mathcal{S}_\mathfrak{T}}(v) := \int_\Omega I_\mathfrak{T}\big(\Phi(v)\big)\, dx = \sum_{\mathfrak{p} \in \mathfrak{F}_0^\bullet(\mathfrak{T})} \Phi\big(v(\mathfrak{p})\big) \int_\Omega b_\mathfrak{p}(x)\, dx \tag{2.33}$$

as obtained by replacing exact integration by a quadrature rule based on linear nodal interpolation. Here $I_\mathfrak{T}$ stands for the interpolation operator $I_\mathfrak{T} : \mathcal{C}(\Omega) \to \mathcal{S}_\mathfrak{T}$ and the $b_\mathfrak{p}$ denote the conforming nodal basis functions

$$\mathcal{B} := \left\{ b_\mathfrak{p} \in \mathcal{S}_\mathfrak{T} \mid \forall_{\mathfrak{q} \in \mathfrak{F}_0^\bullet(\mathfrak{T})} : b_\mathfrak{p}(\mathfrak{q}) = \delta_{\mathfrak{p}\mathfrak{q}} \right\}.$$

We note that by the requirement of continuity the hanging nodes do not contribute to the number of unknowns because function values must be interpolated linearly from those of surrounding (nonhanging) vertices. Proof of these claims can be found in [66, Sect. 3.1]. For practical reasons we restrict ourselves in all our computations to hanging nodes $\mathfrak{p}$ that satisfy

$$\exists_{\mathfrak{e} \in \mathfrak{F}_1(\mathfrak{T})} \forall_{\mathfrak{q} \in \mathfrak{F}_0^\circ(\mathfrak{T}) \setminus \{\mathfrak{p}\}} : \mathfrak{p} \subset \mathring{\mathfrak{e}} \wedge \mathfrak{e} \cap \mathfrak{q} = \varnothing, \tag{2.34}$$

that is we allow nodes only to be hanging on edges and only one hanging node per edge. The example of a simplicial grid in Figure 2.3 would thus be excluded.

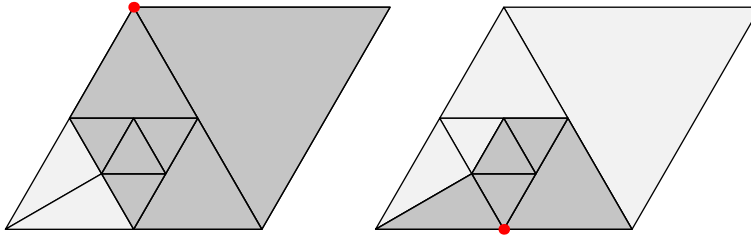Dropping the index m for readability, the discrete spatial problems are now given by

Figure 2.4 – The support of some examples of conforming nodal basis functions on nonconforming 2D simplicial grids. The vertex corresponding to the respective basis function is marked red.

2. Anisotropic Allen–Cahn Equations

$$c_{\mathfrak{T}} \in \mathcal{S}_{\mathfrak{T}} : \qquad \frac{\tau}{\varepsilon} \left\langle D\widetilde{\mathcal{E}}_0(c_{\mathfrak{T}}), v - c_{\mathfrak{T}} \right\rangle + \frac{\tau}{\varepsilon^2} \left(\phi_{\mathfrak{T}}(v) - \phi_{\mathfrak{T}}(c_{\mathfrak{T}}) \right) + \alpha \left(c_{\mathfrak{T}}, v - c_{\mathfrak{T}} \right)$$

$$\geqslant \langle f_{\mathfrak{T}}, v - c_{\mathfrak{T}} \rangle \qquad \forall v \in \mathcal{S}_{\mathfrak{T}} \quad (2.35)$$

or alternatively

$$c_{\mathfrak{T}} \in \mathcal{S}_{\mathfrak{T}} : \qquad \mathcal{J}_{\mathfrak{T}}(c_{\mathfrak{T}}) \leqslant \mathcal{J}_{\mathfrak{T}}(v) \qquad \forall v \in \mathcal{S}_{\mathfrak{T}}$$

$$\mathcal{J}_{\mathfrak{T}}(v) := \frac{\tau}{\varepsilon} \widetilde{\mathcal{E}}_0(v) + \frac{\tau}{\varepsilon^2} \phi_{\mathfrak{T}}(v) + \alpha \left\| v \right\|_0^2 - \langle f_{\mathfrak{T}}, v \rangle , \qquad (2.36)$$

where $f_{\mathfrak{T}} = f_{\mathfrak{T}}^{m-1}$ results from using the (spatially) discrete solution of the previous timestep.

Note that $\mathcal{J}_{\mathfrak{T}} : \mathcal{S}_{\mathfrak{T}} \to \mathbb{R} \cup +\infty$ inherits strict convexity, properness and coercivity of $\mathcal{E}_0$ and ϕ. Lower semicontinuity of $\mathcal{J}_{\mathfrak{T}}$ boils down to lower semicontinuity of $\phi_{\mathfrak{T}}$ which may be shown analogously to Lemma 2.1.

We identify $\mathcal{S}_{\mathfrak{T}}$ with $\mathbb{R}^n$ via $i_{\mathcal{B}} : v = \sum_j \mathrm{v}_j b_{\mathfrak{p}_j} \mapsto \mathrm{v}$ for some fixed enumeration of the nonhanging nodes and may also write

$$\mathrm{c} \in \mathbb{R}^n : \qquad J(\mathrm{c}) \leqslant J(\mathrm{v}) \qquad \forall \mathrm{v} \in \mathbb{R}^n \qquad (2.37)$$

with J such that the following diagram commutes or more precisely

$$
\begin{array}{ccc}
\mathcal{S}_{\mathfrak{T}} & \xrightarrow{\ \mathcal{J}_{\mathfrak{T}}\ } & \mathbb{R} \\
{\scriptstyle i_{\mathcal{B}}} \searrow & & \nearrow {\scriptstyle J} \\
& \mathbb{R}^n &
\end{array}
$$

$$J(\mathrm{v}) = \mathcal{J}_{\mathfrak{T}} \circ (i_{\mathcal{B}})^{-1}(\mathrm{v})$$

$$= \frac{\tau}{2} \sum_{i=1}^m |\mathfrak{t}_i| \, \gamma^2 \left(\sum_{j=1}^n \mathrm{v}_j \nabla b_{\mathfrak{p}_j}|_{\mathfrak{t}_i} \right) + \frac{\tau}{\varepsilon^2} \sum_{j=1}^n \Phi(\mathrm{v}_j) \int_\Omega b_{\mathfrak{p}_j(x)} \, dx + c \langle B\mathrm{v}, \mathrm{v} \rangle - \langle f_{\mathfrak{T}}, \mathrm{v} \rangle . \qquad (2.38)$$

Here we used $n = |\mathfrak{F}_0^\bullet(\mathfrak{T})|$, $m = |\mathfrak{F}_1(\mathfrak{T})|$, and the mass matrix $B = \left((b_{\mathfrak{p}_i}, b_{\mathfrak{p}_j}) \right)_{i,j \in \{1 \dots n\}}$.

Adaptive Mesh Refinement

Adapting a grid to resolve local features of the solution requires local refinements of the grid. We make the following

Definition 2.5 (Refinement)**:**   Let $\mathfrak{T}, \mathfrak{S}$ be simplicial grids on Ω. $\mathfrak{T}$ is called a *refinement* of $\mathfrak{S}$, in symbols $\mathfrak{S} \prec \mathfrak{T}$, if for all $\mathfrak{s} \in \mathfrak{S}$ the set $\{\mathfrak{t} \in \mathfrak{T} \mid \mathfrak{t} \subset \mathfrak{s}\}$ is a simplicial grid on $\mathfrak{s}$. The refinement is called *global* if $\mathfrak{T} \cap \mathfrak{S} = \varnothing$; otherwise it's called *local*. It is called *conforming* if $\mathfrak{T} \setminus \mathfrak{S}$ is a conforming grid on its covered domain and we write $\mathfrak{S} \prec\!\!\prec \mathfrak{T}$. If $\mathfrak{T}$ results from multiple successive refinements of $\mathfrak{S}$, we use the notation $\mathfrak{S} \prec\!\!\prec \mathfrak{T}$ resp. $\mathfrak{S} \prec\!\!\!\prec\!\!\!\prec \mathfrak{T}$. $\triangle$

Note that successive conforming local refinements can result in a nonconforming grid and may be represented by a hierarchy of grids.

Definition 2.6 (Grid Hierarchy)**:** $(\mathfrak{T}_0, \ldots, \mathfrak{T}_j)$ is called a *grid hierarchy* on Ω if the following conditions are satisfied.

  a) $\mathfrak{T}_0$ is a conforming simplicial grid on Ω.

  b) $\forall_i \mathfrak{T}_i \succ \mathfrak{A} \subset \mathfrak{T}_{i-1}$, i.e. $\mathfrak{T}_i$ is a conforming refinement of some subset $\mathfrak{A}$ of $\mathfrak{T}_{i-1}$.

$\mathfrak{T}_i$ is called the *i*-th *level grid*. $\triangle$

Definition 2.7 (Leaf Grid)**:**   Let $(\mathfrak{T}_0, \ldots, \mathfrak{T}_j)$ be a grid hierarchy. We define the *leaf grid* of the hierarchy to be

$$\mathfrak{L} = \mathfrak{L}(\mathfrak{T}_0, \ldots, \mathfrak{T}_j) := \mathfrak{T}_j \cup \bigcup_{i=0}^{j-1} \left\{ \mathfrak{t} \in \mathfrak{T}_i \mid \forall_{\mathfrak{s} \in \mathfrak{T}_{i+1}} : \mathring{\mathfrak{t}} \cap \mathring{\mathfrak{s}} = \varnothing \right\}$$
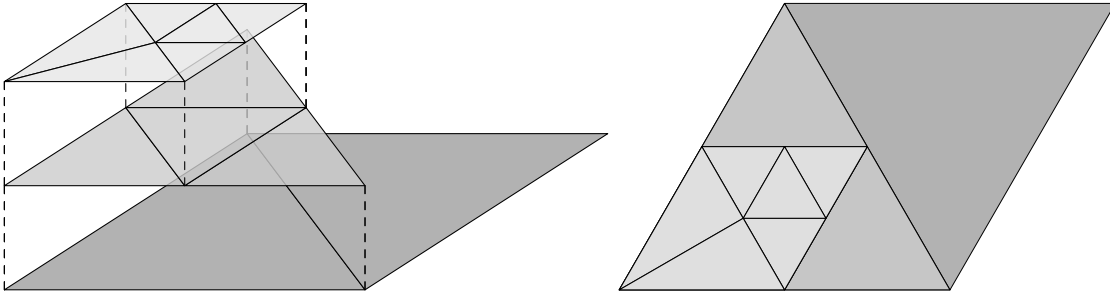
$\triangle$

Figure 2.5 – Illustration of a grid hierarchy (left) and its leaf grid (right). Note that each level grid is conforming.

Our computational grids will be such leaf grids of grid hierarchies on Ω and it is straightforward to show that they are simplicial grids on Ω.

2. Anisotropic Allen–Cahn Equations

In order to obtain an adaptive mesh we firstly select an intial grid for the refinement cycle. The grid is then repeatedly refined according to an error fraction marking strategy using local error indicators based on hierarchical error estimation. The refinement process is stopped once the relative estimated error drops below a given tolerance ϑ_{adapt}

$$\eta \leqslant \vartheta_{\text{adapt}} \, \|c\| \, . \tag{2.39}$$

In all our computations we will use so-called *red refinement*, i.e. each simplex is refined by introducing vertices at each edge midpoint resulting in four congruent triangles in the 2D case. Red refinement of tetrahedra is slightly more intricate and is illustrated in lower tetrahedron of Figure 2.3e. The selection of the initial grid, hierarchical error estimation, and the marking strategy are treated in the following paragraphs.

Selection of the Initial Grid   For the refinement process in each timestep we need to determine an initial grid. While with an overly coarse initial mesh the extended space Q for the error estimation might not be rich enough to detect all particles present in the solution of the previous timestep (cf. Figure 2.6 left), a very fine initial mesh will lead to many unnecessary degrees of freedom and thus compromise overall efficiency.

In order to obtain an initial grid fine enough to resolve all relevant features of the previous solution and coarse enough to avoid accumulation of unnecessary degrees of freedom, we apply successive derefinement to the grid $\mathfrak{T}^{\text{old}}$ of the preceding timestep. In the first time step $\mathfrak{T}^{\text{old}}$ is chosen to be a uniformly refined grid which is sufficiently fine to resolve all relevant features of the initial value c_0. In each of the m derefinement steps, we mark all simplices $\mathfrak{t}$ of $\mathfrak{T}^{\text{old}}$ on level $j \geqslant \mathsf{minLevel}$ for derefinement that satisfy either the condition (i) $\left|\nabla(I_{\mathfrak{t}} c^{\text{old}})|_{\mathfrak{t}}\right| < \vartheta_{\text{coarsen}}$ or the condition (ii) $\left|\nabla(I_{\mathfrak{t}'} c^{\text{old}})|_{\mathfrak{t}'}\right| \geqslant \vartheta_{\text{coarsen}}$ with $\mathfrak{t}'$ chosen such that $\mathfrak{t}$ is obtained by refinement of $\mathfrak{t}'$. Here, $I_{\mathfrak{t}}$ and $I_{\mathfrak{t}'}$ denote the linear interpolation on $\mathfrak{t}$ and $\mathfrak{t}'$, respectively. The reasoning behind this choice is purely heuristic and relies heavily on the assumption that the solutions show large areas of nearly constant value (the phases) and small interfacial areas with large gradients in between, i.e. that we have clearly separated phases. The first condition marks all elements that lie completely in one phase and therefore do not contain any relevant information that would be lost by coarsening. In the case that $\left|\nabla(I_{\mathfrak{t}} c^{\text{old}})|_{\mathfrak{t}}\right| > \vartheta_{\text{coarsen}}$ the second condition ensures that elements lying in or across phase interfaces are kept unless their father element also 'sees' the interface (cf. Figure 2.6 middle). The middle and righthand images in Figure 2.6 illustrate the derefinement process for a hypothetical grid $\mathfrak{T}^{\text{old}}$. Note that that marked

elements are not abandoned unless all 'sibling' elements are marked as well nor when it would lead to multiple hanging nodes on the same edge (cf. Equation (2.34)).
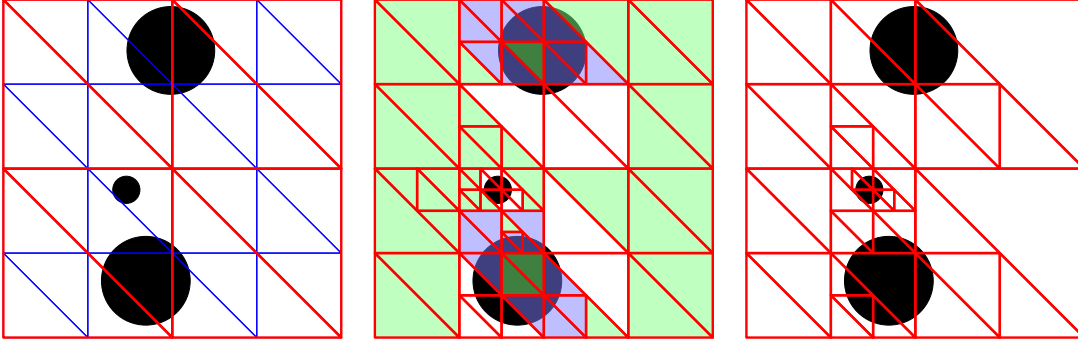
Figure 2.6 – Left: A too coarse initial grid (red). The extended space - P1 elements on a uniformly refined grid (blue) - will not detect the smallest particle. Middle: A hypothetical grid $\mathfrak{T}^{\text{old}}$ (red) and the derefinement marks corresponding to conditions (i) (green) and (ii) (blue). Right: The grid from the picture in the middle after one derefinement step.

Hierarchical Error Estimators   Hierarchical error estimators are based on the approximation of the error in an extended discrete space and its subsequent hierarchical splitting. Early works investigate the linear elliptic self-adjoint case [103, 39, 24] while elliptic variational inequalities and elliptic obstacle problems in particular have been considered in [83, 125, 87]. Hierarchical error estimators have been successfully applied to time-discretized phase-field models in [68, 66]. Here we will shortly recall the procedure for variational inequalities before applying it to the problem at hand.

Consider the variational inequality

$$c \in H : \quad a(c, v - c) + \phi(v) - \phi(c) \geqslant \langle \ell, v - c \rangle \qquad \forall v \in H$$

in a Hilbert space H and its finite element discretization

$$c_{\mathcal{S}} \in \mathcal{S} : \quad a(c_{\mathcal{S}}, v - c_{\mathcal{S}}) + \phi_{\mathcal{S}}(v) - \phi_{\mathcal{S}}(c_{\mathcal{S}}) \geqslant \langle \ell, v - c_{\mathcal{S}} \rangle \qquad \forall v \in \mathcal{S}.$$

We assume $a(\cdot, \cdot)$, ϕ, $\phi_{\mathcal{S}}$, and ℓ to be a symmteric H-elliptic bilinear form, a proper, lsc, convex functional, some discretization thereof, and a bounded linear functional respectively, such that the existence of unique solutions to the continuous and the discrete problems is ensured. The discretization error $e := c - c_{\mathcal{S}}$ is then the unique

solution to the *defect problem*

$$e \in H : \quad a(e, v - e) + \hat{\phi}(v) - \hat{\phi}(e) \geqslant \langle r, v - e \rangle \qquad \forall v \in H \qquad (2.40)$$

where the residual r and the shifted nonlinearity $\hat{\phi}$ are defined by

$$\langle r, v \rangle = \langle \ell, v \rangle - a(c_{\mathcal{S}}, v) \qquad \hat{\phi}(v) = \phi(v + c_{\mathcal{S}}).$$

We approximate (2.40) in an extended finite element space $\mathcal{Q} \supset \mathcal{S}$ such that for some $\mathcal{V} \subset \mathcal{Q}$ we have

$$\mathcal{Q} = \mathcal{S} \oplus \mathcal{V} \quad \text{and} \quad \mathcal{S} \cap \mathcal{V} = \{0\}$$

to obtain the *discrete defect problem*

$$e_{\mathcal{Q}} \in \mathcal{Q} : \quad a(e_{\mathcal{Q}}, v - e_{\mathcal{Q}}) + \hat{\phi}_{\mathcal{Q}}(v) - \hat{\phi}_{\mathcal{Q}}(e_{\mathcal{Q}}) \geqslant \langle r, v - e_{\mathcal{Q}} \rangle \qquad \forall v \in \mathcal{Q} \qquad (2.41)$$

Furthermore we assume that there is a direct splitting of the extension space $\mathcal{V} = \mathcal{V}_1 \oplus \ldots \oplus \mathcal{V}_k$ such that the discretized nonlinearity decomposes on $\mathcal{V}$

$$\hat{\phi}_{\mathcal{Q}}(v) = \sum_{i=1}^{k} \hat{\phi}_{\mathcal{Q}}^{i}(v_i) \qquad \forall v = \sum_{i=1}^{k} v_i, \ v_i \in \mathcal{V}_i \qquad (2.42)$$

into convex functionals $\hat{\phi}_{\mathcal{Q}}^{i} : \mathcal{V}_i \to \mathbb{R} \cup \{+\infty\}$. In order to avoid the computational effort of solving (2.41) we perform a localization by firstly replacing the bilinear form with the hierarchical preconditioner

$$b(v, w) = a(v_{\mathcal{S}}, w_{\mathcal{S}}) + \sum_{i=1}^{k} a(v_i, w_i) \qquad v, w \in \mathcal{Q} \qquad (2.43)$$

and secondly by *assuming* that the low frequency contributions $e_{\mathcal{S}}$ may be neglected. Note that we cannot expect $e_{\mathcal{S}}$ to be zero since it is still coupled to $e_{\mathcal{V}}$ by the nonlinearity $\hat{\phi}_{\mathcal{Q}}$. Thereby we arrive at the *localized discrete defect problem*

$$\tilde{e} \in \mathcal{V} : \quad b(\tilde{e}, v - \tilde{e}) + \hat{\phi}_{\mathcal{Q}}(v) - \hat{\phi}_{\mathcal{Q}}(\tilde{e}) \geqslant \langle r, v - \tilde{e} \rangle \qquad \forall v \in \mathcal{V} \qquad (2.44)$$

which by virtue of the decomposition assumption (2.42) splits into k independent sub-problems

$$\tilde{e}_i \in \mathcal{V}_i : \quad a(\tilde{e}_i, v - \tilde{e}_i) + \hat{\phi}_Q^i(v) - \hat{\phi}_Q^i(\tilde{e}_i) \geqslant \langle r, v - \tilde{e}_i \rangle \qquad \forall v \in \mathcal{V}_i \qquad (2.45)$$

The error estimate then is given by

$$\eta := \|\tilde{e}\|_b = \left(\sum_{i=1}^k \|\tilde{e}_i\|_a^2 \right)^{\frac{1}{2}} \qquad (2.46)$$

The local contributions $\eta_i := \|\tilde{e}_i\|_a$ may be used as error indicators for adaptive mesh refinement.

One aims at approximations $\tilde{e} \approx e$ that yield *efficient* and *reliable* error estimates, i.e.

$$C_0 \|\tilde{e}\|_b \leqslant \|e\|_a \leqslant C_1 \|\tilde{e}\|_b$$

where the left estimate manifests *efficiency* whereas the right estimate constitutes *reliability*. While for linear self-adjoint problems efficiency is obtained without unknown constants and reliability is implied by the saturation assumption, for general nonlinear problems of the discussed form a proof is beyond reach. For obstacle problems, however, augmentation of the estimator by a higher order term recovers efficiency and reliability (cf. [87, 125]).

We will now describe our approach to hierarchical a posteriori error estimation for the spatial problems of the time-discrete anisotropic Allen–Cahn equation. A typical choice for the extended space Q is a higher order finite element space such as the piecewise quadratic finite elements. In the case of obstacle problems, however, this might lead to instabilities [59, 87]. For the sake of robustness we therefore chose Q to be the piecewise affine conforming FE-space on a once uniformly refined grid. So if $\mathcal{S} = \mathcal{S}_\mathfrak{T}$ and $\mathfrak{T}' \succ \mathfrak{T}$ is a global refinement of $\mathfrak{T}$ we choose $Q = \mathcal{S}_{\mathfrak{T}'}$. Recall that we use red refinement such that new nodes are introduced solely at the edge midpoints. Hence we have $Q = \mathcal{S}_{\mathfrak{T}'} = \mathcal{S}_\mathfrak{T} \oplus \mathcal{V}$ where $\mathcal{V}$ is spanned by the "linear edge bubbles" or more precisely by the fine grid nodal basis functions associated to vertices $\mathfrak{F}_0^{\mathcal{V}} := \mathfrak{F}_0^\bullet(\mathfrak{T}') \setminus \mathfrak{F}_0^\bullet(\mathfrak{T})$, i.e. the nonhanging nodes of $\mathfrak{T}'$ that were not nonhanging nodes in $\mathfrak{T}$ (cf. [66, Theorem 6.1]). Therefore each $v \in Q$ has a unique splitting $v = v_\mathcal{S} + v_\mathcal{V}$.

Stating the localized discrete defect problem requires a little more care in case of the

nonlinear time discretizations, due to the nonlinear anisotropic operator replacing the Laplacian of the isotropic case. For this end we introduce the shifted diagonalized anisotropic operator

$$\left\langle \widehat{\mathcal{A}}_Q(v), w \right\rangle := \sum_{\mathfrak{p} \in \mathfrak{F}_0^{\mathcal{V}}} \langle \mathcal{A}(c_{\mathfrak{T}} + v(\mathfrak{p})b_{\mathfrak{p}}), b_{\mathfrak{p}} \rangle \, w(\mathfrak{p}) + \langle \mathcal{A}(c_{\mathfrak{T}} + v_S), w_S \rangle \quad v, w \in Q \quad (2.47)$$

with $\mathcal{A} = D\widehat{\mathcal{E}}_0$. For the linearized time-discretizations and in the isotropic case this essentially reduces to the hierarchical splitting (2.43) of the scaled Laplace operator.The localized dicrete defect problem now reads

$$\tilde{e} \in \mathcal{V}: \qquad \left\langle \widehat{\mathcal{A}}_Q(\tilde{e}), v - \tilde{e} \right\rangle + \alpha\,(\tilde{e}, v - \tilde{e})_{\mathcal{S} \oplus \mathcal{V}} + \frac{\tau}{\varepsilon^2}\left(\hat{\phi}_Q(v) - \hat{\phi}_Q(\tilde{e}) \right) \geqslant \langle r, v - \tilde{e} \rangle \quad (2.48)$$

where $(\cdot, \cdot)_{\mathcal{S} \oplus \mathcal{V}}$ denotes the hierarchical splitting of the L^2-scalar product. Again the error estimate is computed as the sum of local contributions

$$\eta := \left(\sum_{i=1}^{k} \|\tilde{e}_i\|_{\text{iso}}^2 \right)^{\frac{1}{2}} \tag{2.49}$$

which are used as local edge based error indicators. For computational simplicity we use the energynorm of the corresponding isotropic problem here, i.e.

$$\|v\|_{\text{iso}}^2 := \tau\,(\nabla v, \nabla v) + \alpha\,(v, v)$$

Error Fraction Marking Strategy Based on the edge based local error indicators η_i we decide which edges to refine following the marking strategy described in [40]. The aim is to find a minimal set of edges $\mathfrak{E}$ such that for some prescribed $\kappa \in (0, 1]$

$$\sum_{\mathfrak{e} \in \mathfrak{E}} \eta_{\mathfrak{e}}^2 \geqslant \kappa \cdot \eta^2$$

holds. Then all elements sharing these edges are marked for refinement. In order to obtain such a minimal set we order the set of local indicators and sum up starting from the largest until the criterion is met. In case the error estimate barely misses the termination criterion (2.39), we may reduce κ such that severe overrefinement is avoided.

Clearly, we expect the error estimate on successive grids to decrease according to

$$\eta_{j+1}^2 = (1 - \kappa)\eta_j^2 + \kappa\omega\eta_j^2 \qquad , \omega \in (0, 1).$$

Of course ω may be computed from the expected order of convergence p as $\omega = 1/2^{2p}$. This might however be overly optimistic in some situations. Therefore we use the error reduction actually achieved in the previous refinement $\rho_j = \frac{\eta_j}{\eta_{\text{older}}}$ to determine ω by

$$\rho_j^2 = 1 - (1 - \omega)\kappa$$

which yields

$$\omega = 1 - \left(\frac{1 - \rho_j^2}{\kappa}\right).$$

Thus $\rho(\tilde{\kappa}) = \sqrt{1 - \frac{1-\rho_j^2}{\kappa}\tilde{\kappa}}$ acts as a predictor for the error reduction depending on the marked error fraction $\tilde{\kappa}$ in the following refinement step. With this we can now compute an optimal $\tilde{\kappa}$ from the termination criterion (2.39)

$$\tilde{\kappa} = \frac{\eta_j^2 - \vartheta_{\text{adapt}}^2\,\|c\|^2}{\eta_j^2 - \rho_j^2\eta_j^2}\kappa.$$

Note that in relevant situations, i.e. the termination criterion (2.39) is not yet met but expected to be fulfilled in the following refinement step, we will always have $0 < \tilde{\kappa} \leqslant \kappa$. This involves a saturation assumption, namely $\rho_j < 1$. In order to ensure that we don't fall short of the termination criterion we finally introduce a safety factor $\beta \in (0, 1]$ such that in the j-th refinement step we choose

$$\lambda = \frac{\eta_j^2 - (\beta\vartheta_{\text{adapt}})^2\,\|c\|^2}{\eta_j^2 - \rho_j^2\eta_j^2} \qquad\qquad \kappa_j = \begin{cases} \lambda\kappa_{j-1} & , \text{if } 0 < \lambda \leqslant 1 \\ \kappa_{j-1} & , \text{otherwise} \end{cases} \qquad (2.50)$$

for a given $\kappa_0 \in (0, 1]$.

The Subgrid Approach for Evolving Grids

In order to use different locally refined grids in two successive timesteps without loss of information we will make use of a grid that resolves both computational grids. Such a grid we will call *hostgrid* which is defined below.

Definition 2.8 (Hostgrid)**:** Let $\mathfrak{S} = \mathfrak{L}(\mathfrak{S}_0, \ldots, \mathfrak{S}_j)$ and $\mathfrak{T} = \mathfrak{L}(\mathfrak{T}_0, \ldots, \mathfrak{T}_k)$, $k \geqslant j$ be two grids such that for all $i \in \{0 \ldots, j\}$ $\mathfrak{S}_i \cup \mathfrak{T}_i$ is a conforming simplicial grid on its domain. Then we can consider the grid $\mathfrak{H} = \mathfrak{H}(\mathfrak{S}, \mathfrak{T}) = \mathfrak{L}(\mathfrak{S}_0 \cup \mathfrak{T}_0, \ldots, \mathfrak{S}_j \cup \mathfrak{T}_j, \mathfrak{T}_{j+1} \ldots, \mathfrak{T}_k)$. We call this grid the *hostgrid* of $\mathfrak{S}$ and $\mathfrak{T}$. Relaxing this definition slightly we may call any conforming refinement $\tilde{\mathfrak{H}} \twoheadrightarrow \mathfrak{H}$ of $\mathfrak{H}$ a hostgrid of $\mathfrak{S}$ and $\mathfrak{T}$. $\triangle$

Now consider the differing leaf grids of two subsequent time steps namely $\mathfrak{T}^{\text{old}}$ and $\mathfrak{T}$ and each results from successive refinements of a common coarse grid using red refinement. Then the hostgrid $\mathfrak{H}(\mathfrak{T}^{\text{old}}, \mathfrak{T})$ is defined. Note that in the presence of green closures this might not be the case. The reason for this definition is that such grids will induce nested finite element spaces, $\mathcal{S}_{\mathfrak{T}^{\text{old}}} \subset \mathcal{S}_{\mathfrak{H}}$ and $\mathcal{S}_{\mathfrak{T}} \subset \mathcal{S}_{\mathfrak{H}}$, which again might not be the case in the presence of green closures, and which in turn is the reason we allow nonconforming leaf grids, i.e. hanging nodes.

Now consider the discrete spatial problem (2.35). The right hand side is given by the functional $f_{\mathfrak{T}} \in \mathcal{S}'_{\mathfrak{T}}$ induced by the discrete solution in the previous time step $c^{\text{old}} \in \mathcal{S}_{\mathfrak{T}^{\text{old}}}$ which due to $\mathcal{S}_{\mathfrak{T}^{\text{old}}} \subset \mathcal{S}_{\mathfrak{H}}$ finds an exact representation in $i_{\mathcal{B}}(\mathcal{S}_{\mathfrak{H}})$. Hence the right hand side may be evaluated exactly for test functions in $\mathcal{S}_{\mathfrak{H}}$ using quadrature rules that are exact on $\mathcal{S}_{\mathfrak{H}}$. Because of $\mathcal{S}_{\mathfrak{T}} \subset \mathcal{S}_{\mathfrak{H}}$ we also have $\mathcal{S}'_{\mathfrak{H}} \subset \mathcal{S}'_{\mathfrak{T}}$ and the restriction of the right hand side (functional) to $\mathcal{S}_{\mathfrak{T}}$ is again exact.

2.2.3. Algebraic Solution of Discrete Spatial Problems

The discrete spatial problems (2.37) to be solved in each time step are minimization problems

$$\mathrm{c} \in \mathbb{R}^n: \quad J(\mathrm{c}) \leqslant J(\mathrm{v}) \quad \forall \mathrm{v} \in \mathbb{R}^n$$

for the proper, strictly convex, lsc energy functional (2.38) which splits into a smooth convex and a nonsmooth strictly convex part:

$$J = J_0 + \varphi.$$

Note that for the functional under consideration the nonsmooth part φ decomposes with respect to the canonical directions:

$$\varphi(\mathrm{v}) = \sum_{i=1}^{n} \varphi_i(\mathrm{v}_i), \text{ with } \varphi_i(\mathrm{v}_i) = \frac{\tau}{\varepsilon^2} \Phi(\mathrm{v}_i) \int_\Omega b_{\mathrm{p}_i}(x) \, dx$$

being twice continuously differentiable on $(-1, 1) = \overset{\circ}{\mathrm{dom}}(\varphi_i)$ (cf. Lemma 2.2). The smooth part is of the form

$$J_0(v) = \alpha \langle Bv, v \rangle - \langle f, v \rangle + \sum_{j=1}^{m} \gamma_j(D_j v),$$

where $\gamma_j^2 = |\mathfrak{t}_j| \cdot \gamma^2$ and D_j is the $d \times n$-matrix computing the gradient on $\mathfrak{t}_j$ of a P1-finite element function. Recall that by assumption γ_j^2 is twice continuously differentiable except in zero and that by Lemma 2.9 $(\gamma_j^2)'$ is Lipschitz continuous. Hence we may define a suitable generalized Hessian of γ_j^2 by setting $\partial^2 \gamma_j^2(0) = \|\mathfrak{t}_j\| \mathsf{Id}_d \in \partial_C \gamma_i^2(0)$ (Clarke's generalized Jacobian [35]) and thus construct a generalized Hessian for J_0: $\partial^2 J_0(v) = \alpha B + D^\mathsf{T} \partial^2 \gamma^2(Du) D$. For details we refer to [66, Sect. 4.1].

In order to solve these highly nonlinear, nonsmooth convex minimization problems we will apply the Truncated Nonsmooth Newton Multigrid method (TNNMG). Here we will give a short overview and refer to [62, 65, 66] for details.

The TNNMG method for the problems at hand is employed as a two-step algorithm consisting of nonlinear smoothing $\mathcal{F}$ and a subsequent linear correction $\mathcal{C}$ for acceleration:

$$c^{\nu+\frac{1}{2}} = c^\nu \quad + \mathcal{F}(c^\nu) \tag{2.51}$$

$$c^{\nu+1} = c^{\nu+\frac{1}{2}} + \mathcal{C}(c^{\nu+\frac{1}{2}}) \tag{2.52}$$

For the given energy functional such a method is known to be convergent if the operators $\mathcal{F}, \mathcal{C} : \mathrm{dom}\, J \to \mathbb{R}^n$ are monotone with respect to J, i.e. $J(c + \mathcal{F}(c)) \leqslant J(c), \forall c \in \mathrm{dom}\, J$ and analogously for $\mathcal{C}$, and if for any convergent sequence $(c^\nu)_\nu \subset \mathrm{dom}\, J$ $J(c^{\nu+1}) \leqslant J(c^\nu + \mathcal{F}(c^\nu)), \forall \nu \in \mathbb{N}$ implies $\arg\min_{v \in \mathrm{dom}\, J} J(v) = \lim_{\nu \to \infty} c^\nu$ (cf. [66, Theorem 4.1]). This condition is met by the nonlinear Gauss–Seidel method given by successive minimization in the coordinate directions

$$\mathcal{F}(v)_i = \arg\min_{\rho \in \mathbb{R}} J(v + \sum_{j=1}^{i-1} \mathcal{F}(v)_j e_j + \rho e_i)$$

and even its inexact counterpart

$$\mathcal{F}_\star(v)_i = \omega(v, i) \cdot \arg\min_{\rho \in \mathbb{R}} J(v + \sum_{j=1}^{i-1} \mathcal{F}_\star(v)_j e_j + \rho e_i), \qquad \omega(v, i) \in [\omega_0, 1] \tag{2.53}$$

for some fixed $\omega_0 \in (0, 1]$ ([66, Theorem 4.2]). The latter is relevant as the minimizer may not be readily available. Convergence of a Gauss-Seidel iteration for energy functionals that also cover the vector-valued case was proven in [86] and further generalized in [74]. As secondary correction $\mathcal{C}$ we apply one Newton step on a subspace reduced to components where J is sufficiently smooth. For this end we introduce the index sets

$$\mathcal{I}(v) = \{i \in \mathbb{N} \mid \partial\varphi_i(v_i) \text{ is single-valued}\}$$

$$\mathcal{I}'(v) = \left\{i \in \mathcal{I}(v) \mid \max\{\lim_{w \nearrow v_i} \varphi_i''(w), \lim_{w \searrow v_i} \varphi_i''(w)\} < \infty\right\},$$

the reduced space

$$V_{\mathcal{I}} = \text{span}\{e_i \mid i \in \mathcal{I}\} \subset \mathbb{R}^n,$$

and the truncated matrix resp. vector

$$(M_{\mathcal{I},\mathcal{J}})_{ij} = ((i \in \mathcal{I} \wedge j \in \mathcal{J}) \cdot M_{ij})_{ij}, \qquad (v_{\mathcal{I}})_i = ((i \in \mathcal{I}) \cdot v_i)_i \qquad (2.54)$$

for some matrix $M \in \mathbb{R}^{m \times n}$ resp. vector $v \in \mathbb{R}^n$ and index sets $\mathcal{I}$ and $\mathcal{J}$. Abbreviating notation we also write $M_{\mathcal{I}}$ for $M_{\mathcal{I},\mathcal{I}}$.

For a symmetric positive definite matrix M the truncated matrix $M_{\mathcal{I}}$ is still spd on the reduced space $V_{\mathcal{I}}$ and thus would be invertible if we deleted the corresponding rows and columns instead of truncating them. This inspires the definition

$$(M_{\mathcal{I}})^+ = \left((M_{\mathcal{I}} + \mathsf{Id} - \mathsf{Id}_{\mathcal{I}})^{-1}\right)_{\mathcal{I}},$$

which is the inverse of $M_{\mathcal{I}}$ on the reduced space in the sense that $(M_{\mathcal{I}})^+ M_{\mathcal{I}} = \mathsf{Id}_{\mathcal{I}}$ (cf. [66, Appendix A.6, Lemma A.5]).

With the definitions $\nabla J(v)_{\mathcal{J}} = (\nabla J_0(v + \varphi'(v))_{\mathcal{J}}$ and $\partial^2 J(v)_{\mathcal{J}} = (\partial^2 J_0(v) + \varphi''(v))_{\mathcal{J}}$ a Newton step on the reduced space as secondary correction $\mathcal{C}$ is given by

$$\mathcal{C}(v) = -\left(\partial^2 J(c)_{\mathcal{I}'(v)}\right)^+ \nabla J(v)_{\mathcal{I}'(v)}. \qquad (2.55)$$

In the case of quadratic J_0, i.e. in the isotropic case or for the linearized time discretizations in our context, the two-step method (2.51), (2.52) finds an equivalent reformulation as a Newton-like method for finding the zeros of the nonlinear smoother

$$c \in \mathbb{R}^n : \quad \mathcal{F}(c) = 0,$$

(cf. [65, 66]).

Note that entries φ_i'' in the reduced Newton linearization (2.55) might get arbitrarily large, albeit the restriction to a subspace where φ is smooth. In order to avoid the resulting ill-conditioned linear systems we restrict the linearization further to

$$\mathcal{I}''(\mathrm{v}) = \left\{ i \in \mathcal{I}'(\mathrm{v}) \mid \varphi_i''(\mathrm{v}_i) < (C_\varphi)_{i_i} \right\}$$

for some positive definite diagonal matrix C_φ.

Bearing in mind the general convergence result we notice that we cannot expect the correction $\mathcal{C}(\mathrm{c}^{\nu+\frac{1}{2}})$ to be monotone or even feasible, i.e. $\mathrm{c}^{\nu+1} \in \mathrm{dom}\, J$. To enforce monotonicity while retaining the possibility for substantial descent in case $\mathrm{c}^{\nu+\frac{1}{2}}$ is close to $\partial \mathrm{dom}\, J$ we apply a simple line search for minimal energy in direction of $\mathcal{C}(\mathrm{c}^{\nu+\frac{1}{2}})$ orthogonally projected to $\mathrm{dom}\, J - \mathrm{c}^{\nu+\frac{1}{2}}$. Using the inexact Gauss-Seidel method (2.53) and some approximation of the linear correction $\mathcal{C}(\mathrm{c}^{\nu+\frac{1}{2}}) + \varepsilon^\nu$ the overall method is thus given by

$$\mathrm{c}^{\nu+\frac{1}{2}} = \mathrm{c}^\nu + \mathcal{F}_\star(\mathrm{c}^\nu) \tag{2.56}$$
$$\mathrm{c}^{\nu+1} = \mathrm{c}^{\nu+\frac{1}{2}} + \rho^\nu P^\nu(\mathcal{C}(\mathrm{c}^{\nu+\frac{1}{2}}) + \varepsilon^\nu) \tag{2.57}$$

where ρ^ν has simply to ensure monotonicity, and P^ν is the Euclidean orthogonal projection to $\mathrm{dom}\, J - \mathrm{c}^{\nu+\frac{1}{2}}$ (cf. [66, Section 4.2.5]). In practice we determine ρ^ν by a bisection iteration. Finally we apply one step of a truncated multigrid to the linear system in (2.57) in order to compute the inexact correction $\mathcal{C}(\mathrm{c}^{\nu+\frac{1}{2}}) + \varepsilon^\nu$ (cf. [62, 65, 66]).

2.2.4. Notes on Implementation

Employed Software

Computations   All computational implementations in this and the following chapters were realized on the basis of the Distributed and Unified Numerics Environment - DUNE (cf. [10, 11, 117]) which provides a common grid interface for various grid managers such as for instance ALUGrid [30, 116] employed here, a linear algebra backend, a collection of linear solvers, local finite element function and more in the core modules `dune-common`, `dune-grid`, `dune-istl`, `dune-geometry`, and `dune-localfunctions`. Further DUNE

modules used in the present work include `dune-subgrid` [73, 72], `dune-solvers` [71], `dune-fufem` [44], and `dune-tnnmg` developed jointly by the Computational PDEs group at Freie Universität Berlin. They provide a meta-grid, a solver framework including a linear multigrid solver, global finite element bases and assemblers, and the TNNMG solver respectively. While the first two are publicly available and the third module is available on request, the latter mentioned has so far not been published.

Visualization and illustration For the visualization of numerical solutions we used Amira® [3] and ParaView [105]. The plots were realized in part with Matlab® [93] and with the Python library `matplotlib` [78, 94] for the rest. The illustrations of grids and basis functions were done with the help of `asymptote` [25, 4]. The illustrations of Wulff shapes were realized with Mathematica® [92].

Implementation of the Subgrid Approach

The implementation of what we termed the subgrid approach above was carried out using the `dune-subgrid` module [73, 72]. It provides a so-called meta-grid building upon an existing grid manager. Within the subgrid module we can mark a subset of a given grid managed by some external grid manager and treat it as a grid of its own. We will refer to this externally managed grid as the *hostgrid* and to the marked subset as *subgrid*. Refinement of the subgrid amounts to adding additional hostgrid elements to the subgrid with prior refinement of the hostgrid if required. The term hostgrid is thus used a little differently here than before but as we use the hostgrid here as the implementational representation of the conceptual hostgrid above, there will be no ambiguities.

Starting out with the computational grid $\mathfrak{T}^{\text{old}}$ of the previous timestep we choose the initial hostgrid $\mathfrak{H}_0$ as small as the external grid manager allows such that $\mathfrak{T}^{\text{old}} \lll \mathfrak{H}_0$. The computational grid $\mathfrak{T}$ of the current timestep is kept as a subgrid on the hostgrid such that each refinement of $\mathfrak{T}$ will be reflected in the hostgrid. Hence the hostgrid will really be a hostgrid of $\mathfrak{T}^{\text{old}}$ and $\mathfrak{T}$ in the sense of Definition 2.8.

Efficient Evaluation of Anisotropies of Kobayashi Type

In his pioneering paper [81] KOBAYASHI used smooth anisotropies in 2D with an arbitrary number of preference directions in the shape of

$$\gamma : \mathbb{R}^2 \to \mathbb{R} : \quad \gamma(\xi) = 1 + \bar{a} \cos(nx), \tag{2.58}$$

where x is the angle between ξ and the positive x-axis, n the number of preference directions and $\bar{a}$ a parameter of anisotropic "intensity" (cf. Example 2.5).
The implementation of the evaluation of γ (and its derivatives) is critical as especially in the nonlinear discretizations (2.17), (2.21) the solution of the spatial problems requires many $(\gamma^2)'$- resp. $(\gamma^2)''$-evaluations. For efficient evaluation of the trigonometric functions $\cos nx$ and $\sin nx$ we make use of the summation formulae

$$\cos nx = \sum_{i=0}^{\lfloor \frac{n}{2} \rfloor} (-1)^i \binom{n}{2i} \sin^{2i} x \ \cos^{n-2i} x$$

$$\sin nx = \sum_{i=1}^{\lceil \frac{n}{2} \rceil} (-1)^{i+1} \binom{n}{2i-1} \sin^{2i-1} x \ \cos^{n-2i+1} x$$

Thus we are left with evaluation of powers of basic trigonometric functions. Since we never need the angle x explicitly and the sine and cosine are given by the input argument ξ through

$$\cos x = \frac{\xi_1}{\|\xi\|_2} \quad \text{and} \quad \sin x = \frac{\xi_2}{\|\xi\|_2}$$

all we ever need to calculate are basically sums and powers of reals - and of course the binomial coefficients. The computation of the binomials is probably the most costly part but since we only need small n ($n \leqslant 7$) in this context, we hard-wire the corresponding binomial coefficients into the code. As either $(\gamma^2)'$ and $(\gamma^2)''$ require the evaluation of both $\cos nx$ and $\sin nx$ it is favorable to compute the required powers only once and use them for both evaluations.
Table 2.2 compares CPU time for 10^8 $(\gamma^2)'$-evaluations at random locations for naïve computations using $x = \arctan(\xi_2/\xi_1)$ and our evaluation with and without caching of powers and binomial coefficients. All methods have been implemented in C++ compiled with gcc-4.3.2 and options -O3 -funroll-loops, $\bar{a}$ has been taken to be 1 for $n == 1$ and $1/(n^2 - 1)$ else. As might be expected computation time for the naïve evaluation is independent of n while it deteriorates for evaluatio schemes using the summation

n	naïve	w/o caching	caching binom.	caching powers & binom.
1	12.808801 (1.00)	6.108382 (2.1)	5.028314 (2.55)	3.952247 (3.24)
2	12.924808 (1.00)	8.904556 (1.45)	5.680355 (2.28)	4.380274 (2.95)
3	12.908807 (1.00)	12.708794 (1.02)	6.276392 (2.06)	4.756297 (2.71)
4	12.892806 (1.00)	17.889118 (0.721)	7.396462 (1.74)	5.148322 (2.5)
5	12.908807 (1.00)	26.72567 (0.483)	7.52447 (1.72)	5.404338 (2.39)
6	12.924808 (1.00)	42.778673 (0.302)	9.132571 (1.42)	5.776361 (2.24)
7	12.912807 (1.00)	72.388524 (0.178)	9.104569 (1.42)	6.24039 (2.07)

Table 2.2 – CPU time in seconds and speedup-factor vs the naïve variant for
various ways of evaluation of $(\gamma^2)'$

formula. The latter effect can largely be avoided, at least for small n, when one avoids recomputation of binomial coefficients and powers of ξ_i. Overall speedup for our evaluation scheme lies between 2 and 3 for $1 < n < 8$ compared to naïve evaluation.

2.2.5. Numerical Results

Our starting set of numerical experiments focusses on the accuracy of the various time discretizations NONLIN (2.17), NONLINSEMI (2.21), LIN(λ) (2.24), and LINSEMI(λ) (2.27) introduced in Section 2.2.1 applied to a 2D model problem. Measurements of computational effort and convergence rates of the spatial solver complete this experiment. The second experiment illustrates qualitative effects of anisotropy on the topology of the solution. We present an initial value whose orientation in space determines whether pinch off occurs or not.

2D Model Problem

In order to investigate and compare the accuracy and computational effort of the nonlinear time discretizations NONLIN and NONLINSEMI and their linearized counterparts LIN(λ) resp. LINSEMI((λ) we consider the mean curvature flow of a scaled Wulff shape $\Gamma(0) = \{x \in \mathbb{R}^2 \mid \gamma^*(x) = r_0\}$. Theorem 2.17 states that the solution is self-similarly shrinking.

Accuracy We assume the overall error is dominated by the discretization error and deviations due to the phase-field regularization may be neglected. The computed radii of

the shrinking Wulff shape are compared to the exact solution $r(t) = \sqrt{r_0^2 - 2t}$. First we choose the Kobayashi anisotropy $\gamma_{k,\bar{a}}$ (cf. Example 2.5) with $k = 3$, $\bar{a} = 0.124$ and initial radius $r_0 \approx 0.7958$. Note that for this choice of parameters we have $L/2 \approx 1.745$ and the extinction time is $t^* = r_0^2/2 \approx 0.3167$. The corresponding Wulff shape is depicted in Figure 2.2. We consider the anisotropic Allen–Cahn model (2.14) with obstacle potential Ψ_0 and $\varepsilon = 4 \cdot 10^{-2}$. A uniform time stepsize is selected to be $\tau = 10^{-4} < \varepsilon$. The spatial discretization is based on a uniform triangular grid with mesh size $h = \sqrt{2} \cdot 2^{-7}$. Note that this grid satisfies $\varepsilon/h \approx 3.6$ leading to 12-14 nodes across the interfacial region. Figure 2.7 shows the exact radius evolution (i.e. that of the sharp interface model) as
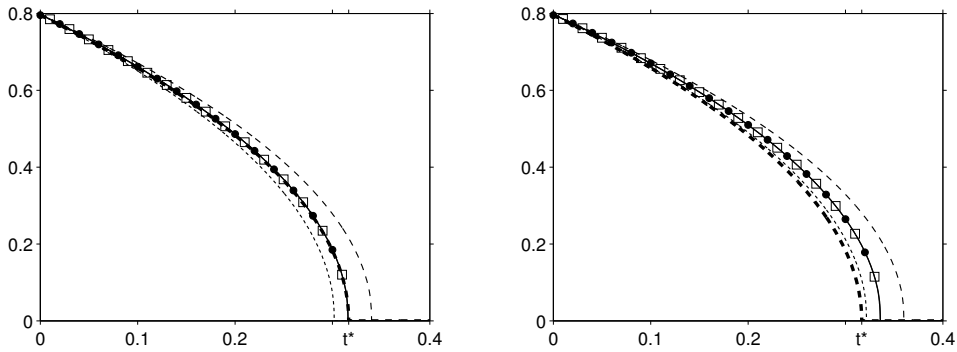
Figure 2.7 – Radius evolutions over t for $\gamma = \gamma_{k,\bar{a}}$, $k = 3$, $\bar{a} = 0.124$. by sharp interface model (thick dashed) and schemes left[right] NONLIN[SEMI] (–•–) and LIN[SEMI](λ) with λ=0.7 (dotted), 0.9 (–□–) and 2.0 (dashed)

well as its approximations over time t. We find that while NONLIN reproduces the radius dynamics very well the results of LIN(λ) depend heavily on the parameter λ. For $\lambda = 0.7 < L/4$ LIN(λ) produces unstable solutions with too fast dynamics; the radius dynamics are approximated well for $\lambda = 0.9 \approx L/4$ and are too slow for $\lambda > L/4$. The semi-implicit time discretizations all produce too slow dynamics and overestimate the extinction time t^* by a factor of roughly 1.06 as compared to their fully implicit counterparts. This factor reduces towards 1 for $\tau \longrightarrow 0$ as is illustrated by Figure 2.8.

Figure 2.9 illustrates the smoothing effect of the linearization by showing the difference of the approximations by NONLIN and LIN(0.9). Initially, large deviations occur at the vertices which are better resolved by the anisotropic nonlinearity than by the isotropic counterpart $\lambda(\nabla \cdot, \nabla \cdot)$. It seems that these differences are smeared out but uniformly remain bounded in course of the evolution.

Next we look at the smooth ℓ^1-norm γ_E as in example 2.4 with $E = 10^{-1}$ and $E = 10^{-3}$,
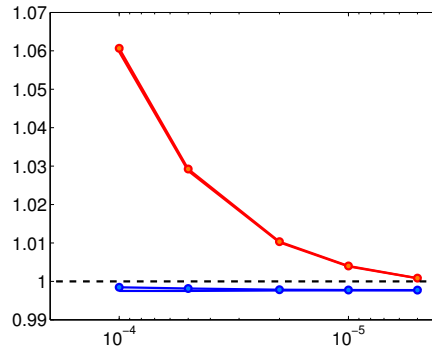
Figure 2.8 – extinction time over τ for schemes NONLIN (blue w/o markers), NONLINSEMI (red w/o markers), LIN(0.9) (blue w/markers) and LINSEMI(0.9) (red w/markers).
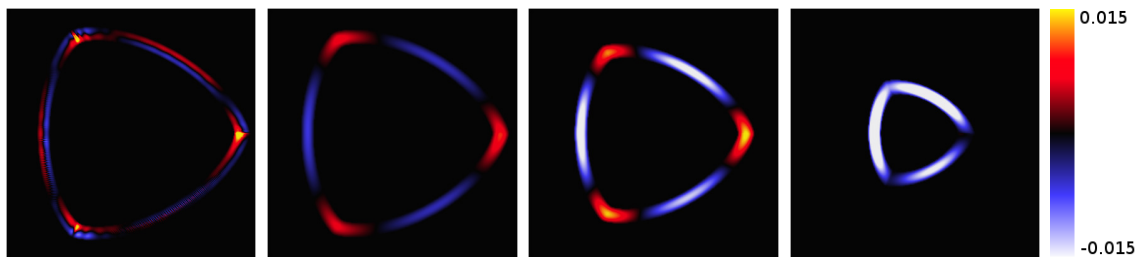
Figure 2.9 – Difference of approximations by NONLIN and LIN(0.9) at time $t = 10^{-3}$, $2 \cdot 10^{-2}$, 10^{-1}, $2.5 \cdot 10^{-1}$

$r_0 \approx 0.5008$ resp. $r_0 \approx 0.7002$ and $L/2 \approx 4.878$ resp. $L/2 \approx 32.6723$ (again the corresponding Wulff shapes are to be found in Figure 2.2). Considering $L/2$ as a quantification of anisotropy, these are stronger than the previously investigated Kobayashi anisotropy by a factor of about 3 resp. 20. This time only the fully implicit (wrt the potential Φ) schemes are taken into account. Again we find LIN(λ) to be unstable for $\lambda < L/4$ and stable but dynamically inaccurate for $\lambda > L/4$. In the moderate case $\mathtt{E} = 10^{-1}$ LIN($L/4$) produces satisfactory results whereas for $\mathtt{E} = 10^{-3}$ the dynamics are widely off the mark for all stable values of λ. NONLIN on the other hand still nicely reproduces the radius dynamics of the reference problem.

Computational Effort The nonlinear time stepping scheme is accurate independently of any tuning parameters whereas we expect the linearized version to to be cheaper in terms of computational effort. Again we consider the 2D model problem with mesh size $h = \sqrt{2} \cdot 10^{-10}$ and 4198401 degrees of freedom; other parameters as above. We report the
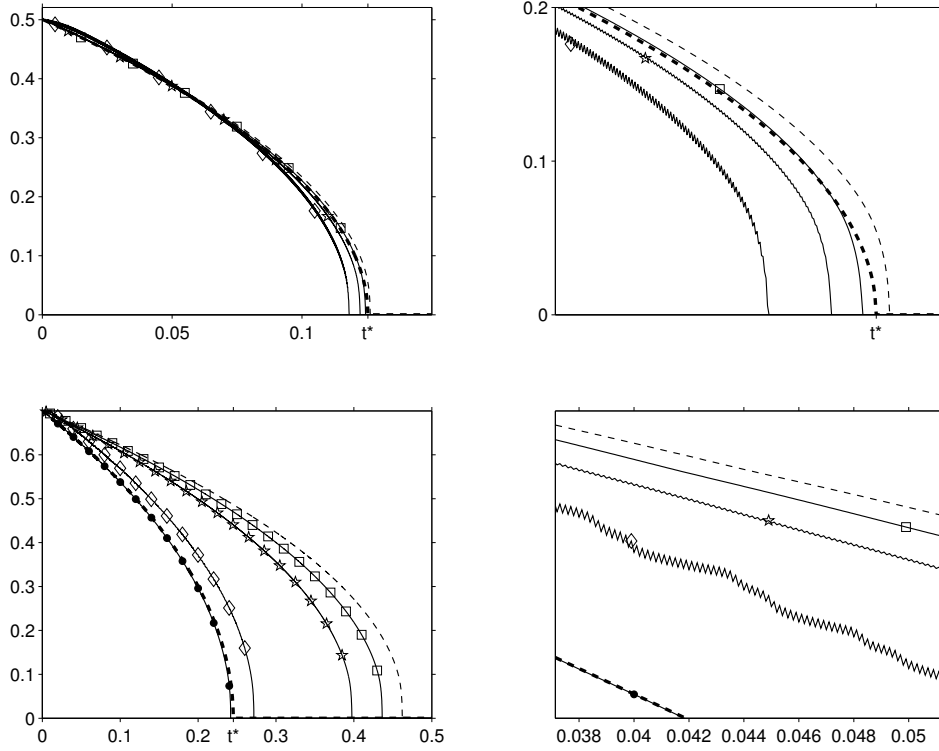
Figure 2.10 – Radius evolutions over t for $\gamma = \gamma_E$, $E = 10^{-1}$ (top) resp. $E = 10^{-3}$ (bottom). *left:* NOLIN ($-\bullet$), LIN(λ) with $\lambda = 1.5$ resp. 4.0 ($-\diamondsuit$), $\lambda = 2.0$ resp. 13.0 ($-\star$), $\lambda = 2.5$ resp. 16.0 ($-\boxminus$) and $\lambda = 3.0$ resp. 18.0 (dashed), and $r(t)$ (thick dashed). *right:* Zoom illustrating instability of LIN(λ) for $\lambda < L/4$.

number of TNNMG steps and measured CPU time necessary to reach a given tolerance of $tol = 10^{-13}$ when solving the spatial problem of the first time step. The results for NONLIN and LIN(λ) are summarized in Table 2.3. For completeness we performed all calculations with the obstacle potential and the logarithmic potential with $\theta = 0.1$. In the case of the obstacle potential we observe a reduction of number of iteration steps by the factor 6 for LIN as compared to NONLIN. Due to the much more expensive evaluation of $D\mathcal{E}_0$ in the nonlinear case the decrease in CPU time is even by a factor of 11.5. For the logarithmic potential case these gain factors reduce to about 1.5 and 4.4 respectively. As expected the nonlinear scheme requires considerably more CPU time due to a more costly fine grid smoothing as well as a larger number of TNNMG iterations. In case of the obstacle potential the difference is particularly striking: While the linearized scheme requires only one sixth of the TNNMG steps in comparison to NONLIN the gain in overall CPU time is by a factor of 11.

scheme	potential	iteration steps	cpu time [s]
NONLIN	obstacle	47	3444
	logarithmic	47	5017
LIN(0.9)	obstacle	8	298
	logarithmic	32	1140

Table 2.3 – Computational effort of TNNMG for a spatial problems arising from NONLIN and LIN(λ), $\lambda = 0.9$

3D pinchoff

Our final experiment illustrates the sensitivity of the anisotropic Allen–Cahn equation to the spatial orientation of the initial shape. To be more precise, we consider a dumbbell shape as initial values lying parallel or diagonal to the main anisotropic directions of the regularized ℓ^1-norm γ_{E} ($\mathsf{E} = 10^{-3}$) and compute their anisotropic Allen–Cahn flow with obstacle potential Φ_0 and $\varepsilon = 2 \cdot 10^{-2}$ with NONLIN time discretization and $\tau = 2 \cdot 10^{-4} < \varepsilon^2$. In this computation we employ spatially adaptive grids determined by using the schemes described above with parameters $\mathsf{minLevel} = 2$, $\vartheta_{\mathrm{coarsen}} = 1.7$ for the derefinement, $\kappa = 0.8$ in the marking strategy, and an error tolerance of $\vartheta_{\mathrm{adapt}} = 10^{-2}$ leading to minimal mesh size of $h_{min} = \sqrt{2} \cdot 2^{-7}$ concentrated in the diffuse interface. The number of unknowns varies between roughly 570000 and 14000 over the time intervals represented by Figures 2.11. A uniform grid of the same mesh size would contain almost 17 million nodes and be most unwieldy for sequential computations on desktop computers. In the present setting no pinch-off occurs if the initial dumbbell shape is oriented along one coordinate direction (cf. Figure 2.11). This is different, however, if the dumbell is oriented diagonally to the coordinate directions (Figure 2.12), where pinch off is enforced by the anisotropy.
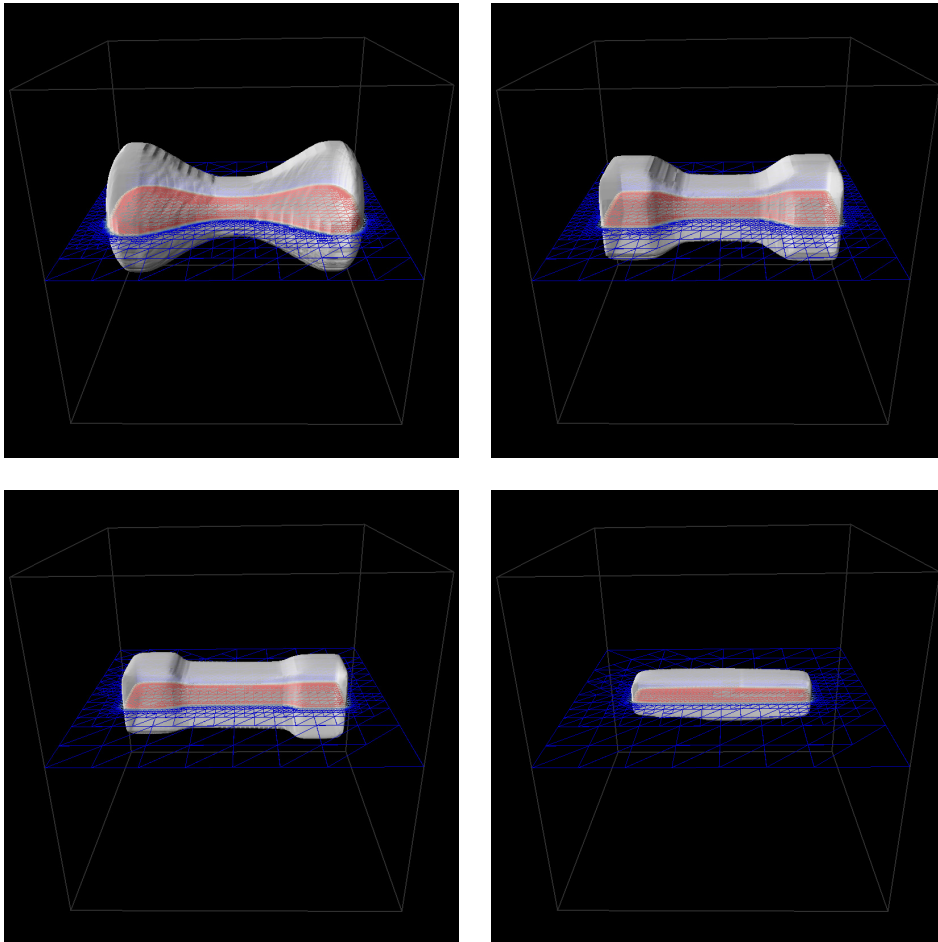
Figure 2.11 – Evolution of dumbbell shape under anisotropic Allen–Cahn flow with regularized ℓ^1 anisotropy at $t = 4 \cdot 10^{-4}$, $6 \cdot 10^{-3}$, $1.2 \cdot 10^{-2}$, $2 \cdot 10^{-2}$. Depicted is the 0-level set and a cross-section of the grid colored according to the phase-field
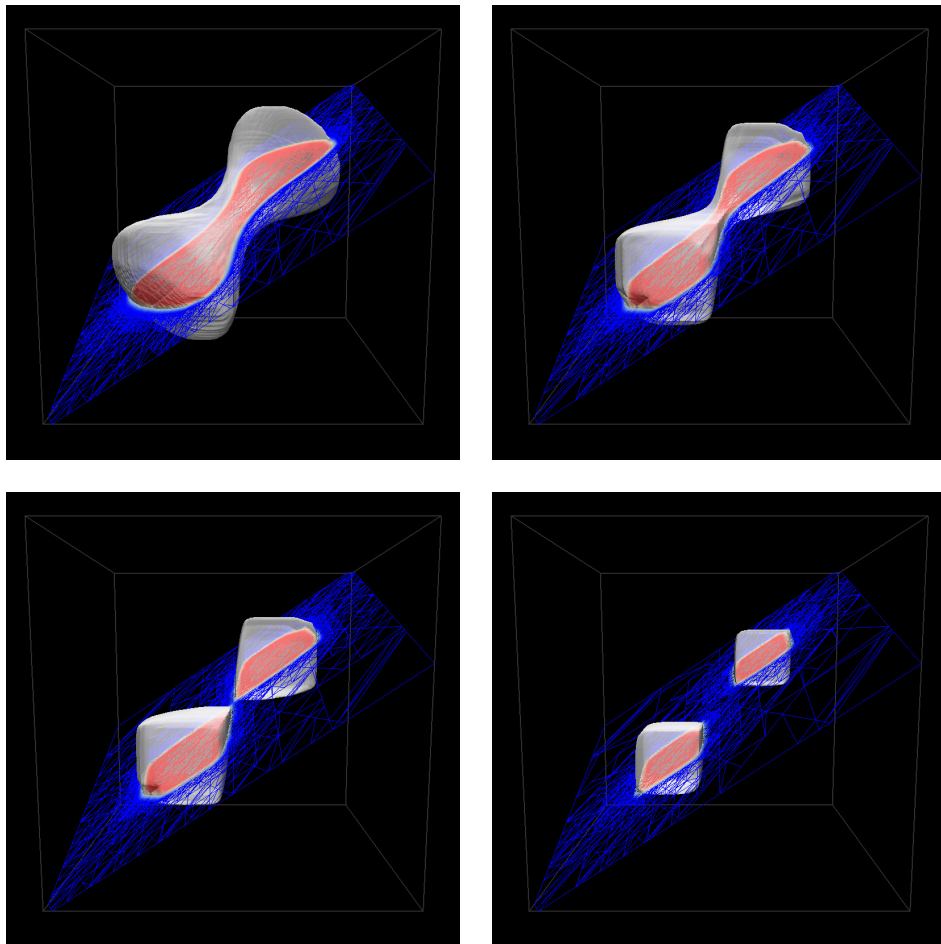
Figure 2.12 – Evolution of dumbbell shape under anisotropic Allen–Cahn flow with regularized ℓ^1 anisotropy at $t = 4 \cdot 10^{-4}$, $6 \cdot 10^{-3}$, $9 \cdot 10^{-3}$, $1.6 \cdot 10^{-2}$. Depicted is the 0-level set and a cross-section of the grid colored according to the phase-field

3. Cahn–Larché Equations and Simulation of a AgCu Brazing Alloy

In this chapter we are concerned with phase separation in binary alloys under thermo-mechanical stress. Solid-solid phase separation processes typically take place in two distinct regimes. Firstly, if the specimen is quenched, i.e. cooled down quickly, *spinodal decomposition* occurs, which is a global spontaneous decomposition of the homogeneous mixture (cf. Chapter 1) on a fast timescale as opposed to decomposition by nucleation and growth. Secondly, on a much slower time scale, the microstructure of the decomposed mixture coarsens which is known as *Ostwald ripening* or simply *coarsening*. A mathematical model that accounts for both regimes and incorporates mechanical effects was first proposed by Cahn and Larché [32] and subsequently generalized to concentration dependant surface tension, mobility and Hooke tensor (cf. [42, 43, 20]).

While the analysis of the Cahn–Larché model and some of its generalizations is well developed ([52, 95, 22]), existing numerical solution schemes are typically limited to smooth approximations of the logarithmic Gibbs free energy ([121, 53, 95]) or periodic domains and uniform meshes ([42, 43, 20]).

Here we present a numerical framework for the robust solution of Cahn–Larché equations with logarithmic potential and concentration dependant material data and apply it to simulate microstructure evolutions in a eutectic AgCu alloy focussing on the coarsening regime.

3.1. Continuous Problem

We consider a binary mixture of constituents A and B on an open and bounded polyhedral domain $\Omega \subset \mathbb{R}^d$, $d \in \{1, 2, 3\}$. The order parameter is taken to be the concentration $c = c_A$ of species A such that $c_A(x) \in [0, 1]$ almost everywhere. The concentration c_B of

constituent B is then determined by the constraint $c_A + c_B = 1$.

3.1.1. Ginzburg–Landau free energy

The Ginzburg–Landau free energy for the Cahn–Larché model is similar to the one we considered for the Allen–Cahn model (2.1), augmented by elastic contributions

$$\mathcal{E}(c, \boldsymbol{u}) = \int_\Omega \frac{1}{2} G(x, c, \nabla c(x)) + \Psi(c) + \mathcal{W}(c(x), \boldsymbol{\varepsilon}(\boldsymbol{u}(x))) \, dx - \int_{\partial\Omega} \boldsymbol{u} \cdot \boldsymbol{g} \, ds. \qquad (3.1)$$

Gibbs free energy

As in the previous chapter we consider Gibbs free energy densities of the form (2.2) satisfying Assumptions (A1)-(A3). More specifically we employ the Margules ansatz (cf. [20])

$$\begin{aligned} \Psi(c) = {}& \beta_0 R\theta \big(c \log(c) + (1 - c) \log(1 - c)\big) \\ & + \beta_1(1 - c) + \beta_2 c + c(1 - c)\big(\beta_3 c + \beta_4(1 - c)\big) \end{aligned} \qquad (3.2)$$

for a given temperature $\theta > 0$, the universal gas constant $R = 8.3144621 \, \mathrm{J(mol\,K)}^{-1}$, and material parameters β_i. The classical logarithmic potential as considered in Chapter 2 is recovered for the choices $\beta_0 = 1/R$, $\beta_1 = \beta_2 = 0$, and $\beta_3 = \beta_4 = \frac{1}{2}$.

Interfacial energy

The interfacial energy density is here taken to be of the form

$$G(x, c, \nabla c) = \Gamma(c) \nabla c \cdot \nabla c$$

(cf. [20]), with a concentration dependent positive definite matrix $\Gamma(c) \in \mathbb{R}^{d \times d}$. A very simple example is

$$\Gamma(c) = \gamma(c)\mathsf{Id}_d \qquad (3.3)$$

with Id_d being the $d \times d$ identity matrix and $\gamma(c)$ interpolating linearly between the values $\gamma_A = \gamma(1)$ and $\gamma_B = \gamma(0)$ corresponding to the pure constituents A and B respectively:

$$\gamma(c) = c\gamma_A + (1 - c)\gamma_B. \tag{3.4}$$

Elastic energy

The elastic energy density $\mathcal{W}$ takes the shape

$$\mathcal{W}(c, \boldsymbol{\varepsilon}(\boldsymbol{u})) = \frac{1}{2}\left(\boldsymbol{\varepsilon}(\boldsymbol{u}) - \bar{\boldsymbol{\varepsilon}}(c)\right) : \boldsymbol{\sigma}. \tag{3.5}$$

Postulating small displacements we consider the linearized strain $\boldsymbol{\varepsilon}(\boldsymbol{u}) = \frac{1}{2}(\nabla \boldsymbol{u} + \nabla \boldsymbol{u}^{\mathsf{T}})$ and assume Hooke's law $\boldsymbol{\sigma} = \mathcal{C}(c)\left(\boldsymbol{\varepsilon}(\boldsymbol{u}) - \bar{\boldsymbol{\varepsilon}}(c)\right)$ with a given, positive definite tensor $\mathcal{C}(c)$ that fulfills the usual symmetry conditions of linear elasticity [100] and given eigenstrains $\bar{\boldsymbol{\varepsilon}}(c)$. Both, Hooke's tensor $\mathcal{C}(c)$ and the eigenstrains $\bar{\boldsymbol{\varepsilon}}(c)$ are allowed to be concentration dependent, for example linearly as in (3.4). The boundary integral term $- \int_{\partial\Omega} \boldsymbol{u} \cdot \boldsymbol{g} \, ds$ accounts for the prescribed boundary stress $\boldsymbol{g}$.

3.1.2. Generalized Cahn–Larché equations

Assuming conservation of mass of each component of the alloy we base the model on the mass balance

$$\partial_t c = -\operatorname{div} F, \tag{3.6}$$

with some diffusional flux F which we assume to be

$$F = -\mathcal{M}(c)\nabla w,$$

with a concentration dependent mobility matrix $\mathcal{M}(c)$ and the chemical potential

$$w = \frac{\partial \mathcal{E}}{\partial c} = -\operatorname{div}\left(\Gamma(c)\nabla c\right) + \tfrac{1}{2}\nabla c^{\mathsf{T}}\Gamma'(c)\nabla c + \Psi'(c) + \tfrac{\partial}{\partial c}\mathcal{W}(c, \boldsymbol{\varepsilon}). \tag{3.7}$$

Since mechanical equilibrium is expected to be attained much faster than thermodynamical equilibrium, we assume that

$$\frac{\partial \mathcal{E}}{\partial \boldsymbol{u}} = \operatorname{div} \boldsymbol{\sigma} = 0 \tag{3.8}$$

holds throughout the evolution (cf. [95, Sect. 1.3.2]). Selecting some final time $T > 0$, the above equations constitute the generalized Cahn–Larché system

$$\partial_t c - \operatorname{div} \mathcal{M}(c) \nabla w = 0 \qquad \text{(3.9a)}$$

$$-\operatorname{div}\left(\Gamma(c)\nabla c\right) + \tfrac{1}{2}\nabla c^{\mathsf{T}}\Gamma'(c)\nabla c + \Psi'(c) + \tfrac{\partial}{\partial c}\mathcal{W}(c, \boldsymbol{\varepsilon}(\boldsymbol{u})) - w = 0 \qquad \text{(3.9b)}$$

$$\operatorname{div}\left(\mathcal{C}(c)\left(\boldsymbol{\varepsilon}(\boldsymbol{u}) - \bar{\boldsymbol{\varepsilon}}(c)\right)\right) = 0 \qquad \text{(3.9c)}$$

on $\Omega \times [0, T]$ for the unknown concentration c, chemical potential w, and displacement $\boldsymbol{u}$. We prescribe the Neumann boundary conditions

$$\Gamma(c)\nabla c \cdot \boldsymbol{n} = 0, \qquad \nabla w \cdot \boldsymbol{n} = 0, \qquad \boldsymbol{\sigma} \cdot \boldsymbol{n} = \boldsymbol{g} \qquad \text{on } \partial\Omega \times [0, T] \qquad \text{(3.10)}$$

with $\boldsymbol{n}$ denoting the outward unit normal to $\partial\Omega$ and given boundary stress $\boldsymbol{g}$. Finally, we impose the initial condition

$$c(\cdot, 0) = c^0 \qquad \text{on } \Omega. \qquad \text{(3.11)}$$

A thermodynamical derivation of the Cahn–Larché system (3.9) as a higher gradient theory of mixtures was carried out by Böhme et al. [19, 20].
An interpretation of the Cahn–Larché equations as an H^{-1}-gradient flow is given in [52]. Observe that the Cahn–Larché system (3.9) is invariant under infinitesimal rigid body motions

$$\ker(\boldsymbol{\varepsilon}) = \{v : \Omega \to \mathbb{R}^d \mid v(x) = Ax + b \text{ with a skew symmetric matrix } A\}$$

representing the kernel of the differential operator $\operatorname{div}\left(\mathcal{C}(c)\boldsymbol{\varepsilon}(\cdot)\right)$. As only the strain $\boldsymbol{\varepsilon}$ enters the phase field equations (3.9a) and (3.9b), the remaining elasticity equation (3.9c) can be considered in the corresponding quotient space

$$\mathbf{H} = (H^1(\Omega))^d / \ker(\boldsymbol{\varepsilon}).$$

The weak formulation of the Cahn–Larché equations is then given by

Find $c \in L^2(0, T; H^1(\Omega)) \cap H^1(0, T; H^1(\Omega)')$ with the property $c(\cdot, 0) = c^0$,

$w \in L^2(0, T; H^1(\Omega))$, and $\boldsymbol{u} \in L^2(0, T; \mathbf{H})$ such that

$$\langle c_t, v \rangle + (\mathcal{M}(c)\nabla w, \nabla v) = 0 \qquad \forall v \in H^1(\Omega), \qquad (3.12a)$$

$$\left.\begin{aligned}(\Gamma(c)\nabla c, \nabla(v - c)) - (w, v - c) \\ + \phi(v) - \phi(c) \geqslant (R(c, \boldsymbol{u}), v - c)\end{aligned}\right\} \qquad \forall v \in H^1(\Omega), \qquad (3.12b)$$

$$(\mathcal{C}(c)\,(\boldsymbol{\varepsilon}(\boldsymbol{u}) - \bar{\boldsymbol{\varepsilon}}(c))\,, \boldsymbol{\varepsilon}(\boldsymbol{v})) = \int_{\partial\Omega} \boldsymbol{g} \cdot \boldsymbol{v} \, ds \qquad \forall \boldsymbol{v} \in \mathbf{H} \qquad (3.12c)$$

with

$$R(c, \boldsymbol{u}) = -\Upsilon'(c) - \frac{1}{2}\left(\nabla c\right)^{\mathsf{T}} \Gamma'(c)\nabla c - \tfrac{\partial}{\partial c}\mathcal{W}(c,\, \boldsymbol{\varepsilon}(\boldsymbol{u}))$$

holds a.e. in $(0, T]$.

3.1.3. Analytic properties

First *existence and uniqueness* results are due to Garcke. In [52] he established existence of solutions to the Cahn–Larché system in the case of homogeneous interface tension Γ and constant mobility. Uniqueness was shown, if additionally one assumes a constant Hooke tensor and a linear dependance of the eigenstrains on concentration. More precisely he proved the following theorem.

Theorem 3.1. *Assume that $\Omega \subset \mathbb{R}^d$ is a bounded domain with Lipschitz boundary $\partial\Omega$, the interfacial energy tensor takes the shape $\Gamma(c) = \gamma\mathsf{Id}_d$ with $\gamma > 0$ independent of c, the double-well potential Ψ is given by (2.4),(2.5), the mobility $\mathcal{M}(c) = \mathcal{M}_0 > 0$ is independent of c, the boundary stress takes the form $\boldsymbol{g} = \sigma\boldsymbol{n}$ with constant stress tensor σ on $\partial\Omega \times (0, T]$, and $c^0 \in H^1(\Omega)$ satisfies $c \in (0, 1)$ almost everywhere.*
Then there exists a solution to the weak Cahn–Larché system (3.12).

Assume additionally that the Hooke tensor $\mathcal{C}(c) = \mathcal{C}_0$ is independent of c, and the eigenstrain takes the form $\bar{\boldsymbol{\varepsilon}}(c) = c\bar{\boldsymbol{\varepsilon}}_1 + (1 - c)\bar{\boldsymbol{\varepsilon}}_0$ with given $\bar{\boldsymbol{\varepsilon}}_1, \bar{\boldsymbol{\varepsilon}}_0 \in \mathbb{R}^{d \times d}$. Then the weak solution to the Cahn–Larché system is unique.

Note that originally this theorem was proven for a multicomponent phase-field equation and therefore includes the vector-valued setting following in Chapter 4. A generalization of this result has been given by Merkle [95] who considers concentration dependent Hooke

tensor and mobility and also allows more general eigenstrains. However, his result suffers from the restriction to globally smooth Gibbs free energy densities Ψ, which excludes the logarithmic potentials considered here.

Earlier existence results by Bonetti et al [22, 21] relying on the introduction of a smoothing viscosity term include concentration dependent interface coefficients of the form (3.3) and concentration dependent mobility but have to assume a homogeneous Hooke tensor. Note, however, that the system considered there does not allow a derivation as a gradient flow.

Another feature of the Cahn–Larché system (3.9) is *thermodynamical consistence* in the sense that the Ginzburg–Landau energy acts as a Lyapunov functional for (3.9) (cf. [52, Section 2]).

For the Cahn–Hilliard equation the *sharp interface limit* is well known to be the so-called Mullins–Sekerka or Hele–Shaw model (cf. e.g. [34]).

The sharp interface limit of the Cahn–Larché model has been derived by Kwak and Garcke in [54, 88] which is a suitably modified version of the Mullins–Sekerka model accounting for the elastic effects by introducing the so-called Eshelby tensor.

3.2. Numerical Solution

In this section we present a discretization of the weak formulation (3.12) of the generalized Cahn–Larché system by an Euler-type discretization in time and finite elements in space. Again we employ ROTHE's method, i.e. we first dicretize in time to obtain a sequence of static spatial problems which are then discretized in space (cf. Section 2.2).

Following is a description of the solvers employed to solve the arising algebraic problems.

3.2.1. Time Discretization

In order to avoid any time step restrictions, we apply an implicit Euler discretization to the second order term and the convex part ϕ of the double-well potential ψ in the phase field equation (3.12b). The remaining, often concave part γ of ψ is taken explicitly (cf., e.g., [17]). Assuming moderate variation of the solution-dependent coefficient functions Γ, $\mathcal{M}$ and $\mathcal{C}$, these are frozen at the preceding time step. Note that this leads to a

decoupling of the phase field equation (3.12b) and mechanics (3.12c), which will simplify the algebraic solution of the discretized spatial problems later on. Denoting

$$\mathcal{K} = \mathrm{dom}(\phi) = \{v \in H^1(\Omega) \mid v(x) \in [0,1] \text{ a.e. in } \Omega\}$$

this approach results in the scheme:

For $m = 1, \ldots,$ find $(c^m, w^m, \boldsymbol{u}^m) \in \mathcal{K} \times H^1(\Omega) \times \mathbf{H}$ such that

$$(c^m, v) + \tau \left(\mathcal{M}(c^{m-1})\nabla w^m, \nabla v \right) = \left(c^{m-1}, v \right) \qquad \forall v \in H^1(\Omega), \quad (3.13\text{a})$$

$$\left. \begin{aligned} \left(\Gamma(c^{m-1})\nabla c^m, \nabla(v - c^m) \right) - (w^m, v - c^m) \\ + \phi(v) - \phi(c^m) \geqslant \left(R(c^{m-1}, \boldsymbol{u}^{m-1}), v - c^m \right) \end{aligned} \right\} \qquad \forall v \in \mathcal{K}, \qquad (3.13\text{b})$$

$$\left(\mathcal{C}(c^m) \left(\boldsymbol{\varepsilon}(\boldsymbol{u}^m) - \bar{\boldsymbol{\varepsilon}}(c^m) \right), \boldsymbol{\varepsilon}(\boldsymbol{v}) \right) = \int_{\partial\Omega} \boldsymbol{g} \cdot \boldsymbol{v} \, ds \qquad \forall \boldsymbol{v} \in \mathbf{H}. \qquad (3.13\text{c})$$

with given initial value $c^0 \in \mathcal{K}$, the displacement $\boldsymbol{u}^0 \in \mathbf{H}$ obtained from

$$\boldsymbol{u}^0 \in \mathbf{H}: \qquad \left(\mathcal{C}(c^0) \left(\boldsymbol{\varepsilon}(\boldsymbol{u}^0) - \bar{\boldsymbol{\varepsilon}}(c^0) \right), \boldsymbol{\varepsilon}(\boldsymbol{v}) \right) = \int_{\partial\Omega} \boldsymbol{g} \cdot \boldsymbol{v} \, ds \qquad \forall \boldsymbol{v} \in \mathbf{H},$$

and suitable time step size $\tau > 0$.

To show existence and uniqueness of solutions we impose the following conditions on coefficient functions and the initial value.

(A6) $\mathcal{M}(\cdot)$, $\Gamma(\cdot)$, and $\mathcal{C}(\cdot)$ are uniformly bounded from below on $[0,1]$, i.e., there are constants $\lambda_{\mathcal{M}}, \lambda_\Gamma, \lambda_{\mathcal{C}} > 0$ such that

$$\begin{aligned} \lambda_{\mathcal{M}}|x|^2 &\leqslant \mathcal{M}(c)x \cdot x & \forall c \in [0,1], \ x \in \mathbb{R}^d, \\ \lambda_\Gamma|x|^2 &\leqslant \Gamma(c)x \cdot x & \forall c \in [0,1], \ x \in \mathbb{R}^d, \\ \lambda_{\mathcal{C}}|x|^2 &\leqslant \mathcal{C}(c)x \colon x & \forall c \in [0,1], \ x \in \mathbb{R}^{d \times d}. \end{aligned}$$

(A7) The norms of $\mathcal{M}(\cdot), \Gamma(\cdot), \mathcal{C}(\cdot), \bar{\boldsymbol{\varepsilon}}(\cdot), \Gamma'(\cdot), \mathcal{C}'(\cdot), \bar{\boldsymbol{\varepsilon}}'(\cdot)$ are uniformly bounded from above on $[0,1]$.

(A8) The initial value c^0 is nontrivial in the sense that $0 < (c^0, 1) < |\Omega|$.

Theorem 3.2. *Assume that conditions (A6)–(A8) hold and that for a fixed $m > 0$*

$c^{m-1} \in \mathcal{K}$, c^{m-1} *is nontrivial in the sense that* $0 < (c^{m-1}, 1) < |\Omega|$, *and* $\boldsymbol{u}^{m-1} \in \mathbf{H}$. *Then there is a solution* $(c^m, w^m, \boldsymbol{u}^m) \in \mathcal{K} \times H^1(\Omega) \times \mathbf{H}$ *of* (3.13) *and* $(c^m, \nabla w^m, \boldsymbol{u}^m)$ *is unique.*

For the proof of Theorem 3.2 the following continuity result will be helpful.

Lemma 3.3. *Let* $z \in L^1(\Omega)$. *Then the functional* $g(v) = (z, v)$ *is continuous on each* $L^\infty(\Omega)$-*bounded subset of* $L^p(\Omega)$, $1 \leqslant p \leqslant \infty$.

Proof. For $p = \infty$ the assertion follows from Hölders inequality. Let $1 \leqslant p < \infty$. Consider some $U \subset L^p(\Omega)$ such that there is $r > 0$ with $|v(x)| \leqslant r$ a.e. in Ω for all $v \in U$. We define the function $f : \Omega \times \mathbb{R} \to \mathbb{R}$ according to

$$
f(x, v) = \begin{cases}
z(x)v, & \text{if} \quad |v| \quad \leqslant \quad r, \\
z(x)r, & \text{if} \quad v \quad > \quad r, \\
-z(x)r, & \text{if} \quad v \quad < \quad -r.
\end{cases}
$$

Then the corresponding superposition operator F, given by $(F(v))(x) = f(x, v(x))$, satisfies $F(v) = zv$ for all $v \in U$. Moreover, $|F(v)| \leqslant r|z|$ holds for all $v \in L^p(\Omega)$ and therefore $F : L^p(\Omega) \to L^1(\Omega)$. As $f(x, \cdot)$ is continuous on $\mathbb{R}$ for all $x \in \Omega$ and $f(\cdot, v)$ is measurable on Ω for all $v \in \mathbb{R}$ Theorem A.10 implies that $F : L^p(\Omega) \to L^1(\Omega)$ is even continuous. Hence $U \ni v \mapsto \int_\Omega F(v) \, dx = (z, v)$ is continuous from U to $\mathbb{R}$ with respect to $\| \cdot \|_{L^p(\Omega)}$. $\square$

Note that the linear map g is Gâteaux differentiable on bounded functions but its Gâteaux derivative $g'(v) = g$ is in general not continuous on this space.

Lemma 3.4. *Let* $c^{m-1} \in \mathcal{K} = \{v \in H^1(\Omega) \mid v(x) \in [0, 1] \ a.e\}$ *and* $\boldsymbol{u}^{m-1} \in \mathbf{H}$. *Then the functional* $\mathcal{J}^m : H^1(\Omega) \to \mathbb{R} \cup \{\infty\}$ *given by*

$$
\mathcal{J}^m(c) = \int_\Omega \tfrac{1}{2}\Gamma(c^{m-1})\nabla c \cdot \nabla c \, dx + \tfrac{\gamma_0}{2}\left(c - c^{m-1}, 1\right)^2 + \phi(c) - \left(R^{m-1}, c\right)
$$

with some $\gamma_0 > 0$ *and* $R^{m-1} = R(c^{m-1}, \boldsymbol{u}^{m-1})$ *is proper, strongly convex, and lower semi-continuous on* $H^1(\Omega)$.

Proof. Utilizing the assumptions (A1), (A2) on Γ, the Poincaré inequality implies that the two quadratic terms in $\mathcal{J}^m$ are strongly convex and continuous on $H^1(\Omega)$. Furthermore ϕ is convex, proper, and lower semi-continuous on $H^1(\Omega)$ (cf. Lemma 2.3).

It remains to show that the linear functional $(R^{m-1}, \cdot)$ is lower semi-continuous. To this end, first note that $c^{m-1}(x) \in [0,1]$ a.e. in Ω together with smoothness of Υ implies $\Upsilon'(c^{m-1}) \in L^\infty(\Omega)$. Utilizing the boundedness of the coefficient functions occurring in R^{m-1}, $c^{m-1} \in H^1(\Omega)$, and $\boldsymbol{u}^{m-1} \in H^1(\Omega)^d$, we get

$$z = \tfrac{1}{2}\left(\nabla c^{m-1}\right)^T \Gamma'(c^{m-1})\nabla c^{m-1} + \tfrac{1}{2}\boldsymbol{\varepsilon}(\boldsymbol{u}^{m-1}) : \mathcal{C}'(c^{m-1})\boldsymbol{\varepsilon}(\boldsymbol{u}^{m-1}) \in L^1(\Omega)$$

and all other terms are in $L^2(\Omega)$. Lemma 3.3 implies that $v \mapsto g(v) := (z, v)$ is continuous on $\mathcal{K} = \mathsf{dom}(\mathcal{J}^m)$ with respect to $\|\cdot\|_{L^2(\Omega)}$, and all the more with respect to $\|\cdot\|_{H^1(\Omega)}$. Hence, the extension of g by infinity is lower semi-continuous on $H^1(\Omega)$. Thus $\mathcal{J}^m$ is lower semi-continuous on $H^1(\Omega)$. $\qquad\square$

Note that strong convexity implies strict convexity and coercivity.

Proof of Theorem 3.2. To show existence of a solution to (3.13a)–(3.13b) we can proceed as in [66, Theorem 3.8]: First we note that these equations are equivalent to a saddle point problem for the associated Lagrangian functional

$$\mathcal{L}^m(c, w) = \mathcal{J}^m(c) - \left(c - c^{m-1}, w\right)^2 - \frac{\tau}{2}\left(\mathcal{M}(c^{m-1})\nabla w, \nabla w\right). \tag{3.14}$$

Note that the additional integral term $(c - c^{m-1}, 1)$ in $\mathcal{J}^m$ vanishes if (3.13a) is satisfied. While $\mathcal{L}^m(c, \cdot)$ is trivially concave and upper semi-continuous, Lemma 3.4 provides convexity, coercivity, and lower semi-continuity of $\mathcal{L}^m(\cdot, w)$. Now existence follows from [45, Chapter VI, Proposition 2.4], if the dual functional

$$h(w) = -\inf_{v \in \mathcal{K}} \mathcal{L}^m(v, w)$$

is coercive on $H^1(\Omega)$. This can be shown as in [66, Theorem 3.8] by proving that

$$h(w) \geqslant -\mathcal{L}^m(c(w), w) \geqslant C\|w\|_{H^1(\Omega)} - C$$

holds with $c(w) = (1 + \mathsf{sgn}(w, 1))/2 = \mathsf{const} \in \{0, 0.5, 1\}$.

In order to prove uniqueness, assume that (c_1^m, w_1^m) and (c_2^m, w_2^m) are two solutions. Then testing (3.13a) for (c_i^m, w_i^m) with $w_i^m - w_j^m$, $j \neq i$, and adding the equations yields

$$\left(w_2^m - w_1^m, c_1^m - c_2^m\right) = \tau\left(\mathcal{M}(c^{m-1})\nabla(w_1^m - w_2^m), \nabla(w_1^m - w_2^m)\right). \tag{3.15}$$

Similarly testing (3.13b) for (c_i^m, w_i^m) with c_j^m, $j \neq i$, yields

$$\left(\Gamma(c^{m-1})\nabla(c_1^m - c_2^m), \nabla(c_1^m - c_2^m)\right) + (w_2^m - w_1^m, c_1^m - c_2^m) \leqslant 0. \qquad (3.16)$$

Inserting (3.15) into (3.16) provides uniqueness on ∇c^m and ∇w^m. Testing (3.13a) with $v = 1 = \mathsf{const}$ finally provides uniqueness of $(c^m, 1)$ and therefore of c^m.

For the remaining problem (3.13c) the assumptions (A1)–(A3) on the coefficient functions ensure that the right hand side is in $H^1(\Omega)'$ and therefore the bilinear form $(\mathcal{C}(c^m)\varepsilon(\cdot), \varepsilon(\cdot))$ is $(\varepsilon(\cdot), \varepsilon(\cdot))$-elliptic. Now Korn's inequality (see, e.g., [100, Theorem 3.5]) provides $H^1(\Omega)^d$-ellipticity on the quotient space $\mathbf{H}$ and thus the existence of a unique solution $\boldsymbol{u}^m \in \mathbf{H}$. $\qquad\qquad\square$

Note that (3.13a) yields $(c^m, 1) = (c^{m-1}, 1)$. Hence, Theorem 3.2, $c^0 \in \mathcal{K}$ and $0 < (c^0, 1) < |\Omega|$ inductively imply existence for all time steps.

Corollary 3.5. *Assume that conditions (A6)–(A8) hold. Then (3.13) has a solution* $(c^m, w^m, \boldsymbol{u}^m)_{m=1,\dots}$ *and* $(c^m, \nabla w^m, \boldsymbol{u}^m)_{m=1,\dots}$ *is unique.*

3.2.2. Adaptive Space Discretization

We will now consider the adaptive finite element discretization of the stationary problems (3.13) arising in each timestep. For that matter we will use the terminology and notation as introduced in Section 2.2.2.

As before the strongly local variation of the phase-field makes adaptive space discretization mandatory. To that end we again employ hierarchical error estimates in conjunction with the previously described marking strategy, choice of initial grid and the Subgrid approach (cf. Section 2.2.2).

Finite element discretization

As in the previous chapter, we assume that $\mathfrak{T}$ is the leaf grid of an underlying simplicial grid hierarchy $(\mathfrak{T}_0, \dots, \mathfrak{T}_j)$ with an intentionally coarse initial grid $\mathfrak{T}_0$. We will discretize the spatial problems (3.13) with respect to the finite element space $\mathcal{S}_{\mathfrak{T}}$ (see 2.32). The

induced subspace hierarchy will be denoted according to

$$\mathcal{S}_0 \subset \ldots \subset \mathcal{S}_j = \mathcal{S}_{\mathfrak{T}}$$
$$\mathcal{S}_k = \mathcal{S}_{\mathfrak{L}(\mathfrak{T}_0,\ldots,\mathfrak{T}_k)} \tag{3.17}$$

In particular, the discretization of (3.13c) is based on the discrete quotient space $\mathbf{H}_{\mathfrak{T}} = \mathcal{S}_{\mathfrak{T}}^d / \ker(\boldsymbol{\varepsilon}) = \mathcal{S}_{\mathfrak{T}}^d \cap \mathbf{H}$ which is well defined since $\ker(\boldsymbol{\varepsilon}) \subset \mathcal{S}_{\mathfrak{T}}^d$. Recalling the approximate nonsmooth nonlinear functional

$$\phi_{\mathfrak{T}}(v) := \sum_{\mathfrak{p} \in \mathfrak{F}_0^\bullet(\mathfrak{T})} \Phi(v(\mathfrak{p})) \int_\Omega b_{\mathfrak{p}}(x) \, dx$$

as defined in (2.33), assuming that $c^{\mathrm{old}} \in \mathcal{K}$ and $\boldsymbol{u}^{\mathrm{old}} \in \mathbf{H}$ are approximations of c^{m-1} and $\boldsymbol{u}^{m-1}$, denoting

$$\mathcal{K}_{\mathfrak{T}} = \mathcal{S}_{\mathfrak{T}} \cap \mathcal{K},$$

and again dropping the index m for readability, the discretized spatial problem in the m-th time step is given by

Find $(c_{\mathfrak{T}}, w_{\mathfrak{T}}, \boldsymbol{u}_{\mathfrak{T}}) \in \mathcal{K}_{\mathfrak{T}} \times \mathcal{S}_{\mathfrak{T}} \times \mathbf{H}_{\mathfrak{T}}$ such that

$$\left(c_{\mathfrak{T}}, v\right) + \tau \left(\mathcal{M}(c^{\mathrm{old}})\nabla w_{\mathfrak{T}}, \nabla v\right) = \left(c^{\mathrm{old}}, v\right) \qquad \forall v \in \mathcal{S}_{\mathfrak{T}}, \tag{3.18a}$$

$$\left.\begin{array}{r} \left(\Gamma(c^{\mathrm{old}})\nabla c_{\mathfrak{T}}, \nabla(v - c_{\mathfrak{T}})\right) - (w_{\mathfrak{T}}, v - c_{\mathfrak{T}}) \\[4pt] + \phi_{\mathfrak{T}}(v) - \phi_{\mathfrak{T}}(c_{\mathfrak{T}}) \geqslant \left(R(c^{\mathrm{old}}, \boldsymbol{u}^{\mathrm{old}}), v - c_{\mathfrak{T}}\right) \end{array}\right\} \qquad \forall v \in \mathcal{K}_{\mathfrak{T}}, \tag{3.18b}$$

$$\left(\mathcal{C}(c_{\mathfrak{T}})\left(\boldsymbol{\varepsilon}(\boldsymbol{u}_{\mathfrak{T}}) - \bar{\boldsymbol{\varepsilon}}(c_{\mathfrak{T}})\right), \boldsymbol{\varepsilon}(\boldsymbol{v})\right) = \int_{\partial\Omega} \boldsymbol{g} \cdot \boldsymbol{v} \, ds \qquad \forall \boldsymbol{v} \in \mathbf{H}_{\mathfrak{T}}. \tag{3.18c}$$

The algebraic solution of (3.18) will be considered in Section 3.2.3.

Theorem 3.6. *Assume that conditions (A6)–(A8) hold and that for a fixed $m > 0$ $c^{\mathrm{old}} \in \mathcal{K}$, c^{old} is nontrivial in the sense that $0 < \left(c^{\mathrm{old}}, 1\right) < |\Omega|$, and $\boldsymbol{u}^{\mathrm{old}} \in \mathbf{H}$. Then there is a solution $(c_{\mathfrak{T}}, w_{\mathfrak{T}}, \boldsymbol{u}_{\mathfrak{T}}) \in \mathcal{K}_{\mathfrak{T}} \times \mathcal{S}_{\mathfrak{T}} \times \mathbf{H}_{\mathfrak{T}}$ of (3.18) and $(c_{\mathfrak{T}}, \nabla w_{\mathfrak{T}}, \boldsymbol{u}_{\mathfrak{T}})$ is unique. If there is furthermore a vertex $\mathfrak{p} \in \mathfrak{F}_0^\bullet(\mathfrak{T})$ such that Φ is differentiable at $c_{\mathfrak{T}}(\mathfrak{p})$, then $w_{\mathfrak{T}}$ is unique.*

Proof. The existence of $(c_{\mathfrak{T}}, w_{\mathfrak{T}}, \boldsymbol{u}_{\mathfrak{T}})$ and uniqueness of $(c_{\mathfrak{T}}, \nabla w_{\mathfrak{T}}, \boldsymbol{u}_{\mathfrak{T}})$ follows by the same arguments as in the proof of Theorem 3.2.

To show uniqueness of $w_{\mathfrak{T}}$ let $\mathfrak{p} \in \mathfrak{F}_0^{\bullet}(\mathfrak{T})$ such that Φ is differentiable at $\xi = c_{\mathfrak{T}}(\mathfrak{p})$. Then $\xi \in (0,1)$ and we can use $v_{\pm} = c_{\mathfrak{T}} \pm \delta b_{\mathfrak{p}}$ for sufficiently small $\delta > 0$ in (3.18b). Testing (3.18b) with v_+ and v_- for two solutions $w_{\mathfrak{T},1}$ and $w_{\mathfrak{T},2}$, respectively, and adding both inequalities yields

$$(w_{\mathfrak{T},2} - w_{\mathfrak{T},1}, b_{\mathfrak{p}}) \geqslant \left(\frac{\Phi(\xi) - \Phi(\xi+\delta)}{\delta} - \frac{\Phi(\xi-\delta) - \Phi(\xi)}{\delta} \right) \int_{\Omega} b_{\mathfrak{p}}(x) \, dx.$$

Taking the limit $\delta \to 0$ and switching the role of $w_{\mathfrak{T},1}$ and $w_{\mathfrak{T},2}$ we get

$$0 = (w_{\mathfrak{T},2} - w_{\mathfrak{T},1}, b_{\mathfrak{p}}) = (w_{\mathfrak{T},2} - w_{\mathfrak{T},1}, 1) \frac{(b_{\mathfrak{p}}, 1)}{|\Omega|}.$$

The last equation holds because $w_{\mathfrak{T},2} - w_{\mathfrak{T},1}$ is constant and implies that this constant is zero. $\qquad \square$

Note that the condition for uniqueness of $w_{\mathfrak{T}}$ is always fulfilled for logarithmic potentials of the form (2.5), because $0 < c_{\mathfrak{T}} < 1$. For the obstacle potential the condition is satisfied, if there is at least one vertex $\mathfrak{p} \in \mathfrak{F}_0^{\bullet}(\mathfrak{T})$ in the discrete interfacial region.

Usually, c^{old} is a finite element function on a grid $\mathfrak{T}^{\mathrm{old}}$. In case of adaptive refinement, $\mathfrak{T}^{\mathrm{old}}$ is usually different from $\mathfrak{T}$. Desired properties as, e.g., mass conservation $(c_{\mathfrak{T}}, 1) = (c^{\mathrm{old}}, 1)$ then impose the following restrictions on the choice of possible approximations of the occurring L^2-inner products (cf. [66, Sect. 3.4.3],[73, Sect. 5]).

(i) To guarantee mass conservation, the approximate inner products used on the left and right hand side of (3.18a) should both be exact for $v \equiv 1$.

(ii) To guarantee that (3.18a) is equivalent to $c_{\mathfrak{T}} = c^{\mathrm{old}}$ for $\tau \to 0$, the approximate inner products on the left and right hand side of (3.18a) should be the same.

(iii) To preserve the symmetric saddle point structure (see proof of Theorem 3.6), the approximate inner products used on the left hand sides of (3.18a) and (3.18b) should be the same.

As a consequence of (i), lumping should be carried out with respect to the hostgrid that contains both $\mathfrak{T}$ and $\mathfrak{T}^{\mathrm{old}}$. In general, lumping then no longer provides a diagonal matrix and thus its main advantage is lost. Hence, lumping is avoided here and we resort to the standard L^2-inner product.

We emphasize that for affine parameter functions Γ, $\mathcal{C}$, $\bar{\varepsilon}$, and $\mathcal{M}$, e.g., of the form (3.4), and finite element functions c^{old} and $\boldsymbol{u}^{\text{old}}$, all integrals involved in (3.18) can be calculated exactly using suitable quadrature rules. To this end we also employ the Subgrid approach as described in Section 2.2.4. Numerical computations indicate that this is particularly important for the leading order terms.

Hierarchical a posteriori error estimation for discrete Cahn–Hilliard equations

Thermomechanical stress is caused by different thermal expansion coefficients and the lattice mismatch of the different constituents [42]. Hence, we assume that the accuracy of the finite element approximation (3.18c) is controlled by the resolution of the diffuse interface and thus concentrate on hierarchical error estimation of the phase-field variables $c_{\mathfrak{T}}$ and $w_{\mathfrak{T}}$. As the general idea has already been described in Section 2.2.2 we will only highlight the problem specific details following [68, 66, 69].

To this end, we note that the discrete spatial Cahn–Hilliard system (3.18a), (3.18b) is equivalent to a saddle point problem in $\mathcal{S}_{\mathfrak{T}} \times \mathcal{S}_{\mathfrak{T}}$ for a Lagrangian functional $\mathcal{L}_{\mathfrak{T}}$ similar to $\mathcal{L}^m$ given in 3.14. In fact, selecting $c^{m-1} = c^{\text{old}}$ and $\boldsymbol{u}^{m-1} = \boldsymbol{u}^{\text{old}}$, the Lagrangian $\mathcal{L}_{\mathfrak{T}}$ is obtained from $\mathcal{L}^m$ by replacing ϕ with the approximation $\phi_{\mathfrak{T}}$. Following [68, 66], we now derive an a posteriori error estimate by suitable approximation of the defect problem associated with the defect Lagrangian

$$\mathcal{D}(e_c, e_w) = \mathcal{L}^m(c_{\mathfrak{T}} + e_c, w_{\mathfrak{T}} + e_w) - \phi(c_{\mathfrak{T}} + e_c) + \phi_{\mathfrak{T}'}(c_{\mathfrak{T}} + e_c).$$

Again we first discretize the defect problem with respect to the extended space $Q \times Q$, where $Q = \mathcal{S}_{\mathfrak{T}'}$ and $\mathfrak{T}'$ is obtained by uniform refinement of $\mathfrak{T}$. Recall that we have $Q = \mathcal{S}_{\mathfrak{T}} \oplus \mathcal{V}$ with $\mathcal{V}$ denoting the incremental space

$$\mathcal{V} = \text{span}\{b_{\mathfrak{p}}^{\mathfrak{T}'} \mid \mathfrak{p} \in \mathfrak{F}_0^{\mathcal{V}}\}$$

and $\mathfrak{F}_0^{\mathcal{V}} = \mathfrak{F}_0^{\bullet}(\mathfrak{T}') \setminus \mathfrak{F}_0^{\bullet}(\mathfrak{T})$ being the set of non-hanging edge mid points in $\mathfrak{T}$. Here we use the grid as additional index for the basis functions to stress the fact, that they are nodal basis functions with respect to the refined grid $\mathfrak{T}'$.

In the second step, the discrete defect problem is localized by ignoring the coupling between $\mathcal{S}_{\mathfrak{T}}$ and $\mathcal{V}$ and also the coupling of the $b_{\mathfrak{p}}^{\mathfrak{T}'}$ for all $\mathfrak{p} \in \mathfrak{F}_0^{\mathcal{V}}$. Denoting $\mathcal{D}_{\mathfrak{p}}(r, s) =$

$\mathcal{D}(rb_{\mathfrak{p}}^{\mathfrak{T}'}, sb_{\mathfrak{p}}^{\mathfrak{T}'})$, this results in the local saddle point problems

$$(e_{c,\mathfrak{p}}, e_{w,\mathfrak{p}}) \in \mathbb{R}^2 : \qquad \mathcal{D}_{\mathfrak{p}}(e_{c,\mathfrak{p}}, s) \leqslant \mathcal{D}_{\mathfrak{p}}(e_{c,\mathfrak{p}}, e_{w,\mathfrak{p}}) \leqslant \mathcal{D}_{\mathfrak{p}}(r, e_{w,\mathfrak{p}}) \qquad \forall r, s \in \mathbb{R}$$

for all $\mathfrak{p} \in \mathfrak{F}_0^{\mathcal{V}}$ that give rise to the local error indicators and the hierarchical a posteriori error estimate

$$\eta_{\mathfrak{p}}^2 = \left\| e_{c,\mathfrak{p}} b_{\mathfrak{p}}^{\mathfrak{T}'} \right\|_{\mathrm{c}}^2 + \left\| e_{w,\mathfrak{p}} b_{\mathfrak{p}}^{\mathfrak{T}'} \right\|_{\mathrm{w}}^2, \quad \mathfrak{p} \in \mathfrak{F}_0^{\mathcal{V}}; \qquad \eta = \left(\sum_{\mathfrak{p} \in \mathfrak{F}_0^{\mathcal{V}}} \eta_{\mathfrak{p}}^2 \right)^{\frac{1}{2}} \tag{3.19}$$

for the norms

$$\begin{aligned} \|c\|_{\mathrm{c}}^2 &= \left(\Gamma(c^{\mathrm{old}}) \nabla c, \nabla c \right) + \gamma_0 \left(c, 1 \right)^2, \\ \|w\|_{\mathrm{w}}^2 &= \tau \left(\left(\mathcal{M}(c^{\mathrm{old}}) \nabla(w), \nabla w \right) + \|w\|_{0,\mathfrak{T}}^2 \right) \end{aligned}$$

and an averaged surface tension coefficient $\gamma_0 = \frac{1}{d} \sum_{i=1}^d \Gamma_{ii}(0)$.

After elimination of $e_{w,\mathfrak{p}}$, the local saddle point problems can be expressed in terms of scalar convex minimization problems which can be easily solved, e.g., by bisection. Numerical computations indicate efficiency and reliability of this error estimate [68], but theoretical justification is still open.

The mesh refinement cycle based on the estimate and local error indicators (3.19) then is executed exactly as in the previous chapter.

Algebraic reformulation

Assuming an ordering $b_{\mathfrak{p}_1}, \ldots, b_{\mathfrak{p}_n}$ of the basis of $\mathcal{S}_{\mathfrak{T}}$ with $n = \dim \mathcal{S}_{\mathfrak{T}} = |\mathfrak{F}_0^{\bullet}(\mathfrak{T})|$ we can represent $c_{\mathfrak{T}}$ and $w_{\mathfrak{T}}$ by coefficient vectors c, w $\in \mathbb{R}^n$. Following the proof of Theorem 3.2 we use an equivalent reformulation of (3.18a)–(3.18b) with $0 = \gamma_0 \left(c_{\mathfrak{T}} - c^{\mathrm{old}}, 1 \right) (1, v - c_{\mathfrak{T}})$ added to (3.18b) resulting in the discrete variational problem to find c, w $\in \mathbb{R}^n$ such that

$$\begin{aligned} \langle A\mathrm{c}, \mathrm{v} - \mathrm{c} \rangle - \langle B\mathrm{w}, \mathrm{v} - \mathrm{c} \rangle + \varphi(\mathrm{v}) - \varphi(\mathrm{c}) &\geqslant \langle \mathrm{f}, \mathrm{v} - \mathrm{c} \rangle \quad \forall \mathrm{v} \in \mathbb{R}^n \\ B\mathrm{c} + C\mathrm{w} &= -\mathrm{g} \end{aligned} \tag{3.20}$$

with $A, B, C \in \mathbb{R}^{n \times n}$, $\mathrm{f}, \mathrm{g} \in \mathbb{R}^n$, and the functional $\varphi : \mathbb{R}^n \to \mathbb{R} \cup \{+\infty\}$ given by

$$A_{ij} = \left(\Gamma(c^{\mathrm{old}})\nabla b_{\mathfrak{p}_i}, \nabla b_{\mathfrak{p}_j}\right) + \gamma_0 \, \mathrm{m}_i \mathrm{m}_j, \qquad \mathrm{m}_i = \int_\Omega b_{\mathfrak{p}_i}(x)\,dx,$$

$$B_{ij} = \left(b_{\mathfrak{p}_i}, b_{\mathfrak{p}_j}\right), \qquad\qquad\qquad \mathrm{f}_i = \left(R(c^{\mathrm{old}}, \boldsymbol{u}^{\mathrm{old}}), b_{\mathfrak{p}_i}\right) + \gamma_0 \left(c^{\mathrm{old}}, 1\right) \mathrm{m}_i$$

$$C_{ij} = \tau \left(\mathcal{M}(c^{\mathrm{old}})\nabla b_{\mathfrak{p}_i}, \nabla b_{\mathfrak{p}_j}\right), \qquad\qquad \mathrm{g}_i = -\left(c^{\mathrm{old}}, b_{\mathfrak{p}_i}\right)$$

and

$$\varphi(\mathrm{v}) = \sum_{i=1}^{n} \Phi(\mathrm{v}_i)\mathrm{m}_i.$$

Utilizing the subdifferential $\partial\varphi : \mathbb{R}^n \to 2^{\mathbb{R}^n}$ of φ the phase-field system can be written as the inclusion

$$\begin{pmatrix} A + \partial\varphi & -B \\ -B & -C \end{pmatrix} \begin{pmatrix} \mathrm{c} \\ \mathrm{w} \end{pmatrix} \ni \begin{pmatrix} \mathrm{f} \\ \mathrm{g} \end{pmatrix} \tag{3.21}$$

with symmetric positive semi-definite $C \in \mathbb{R}^{n \times n}$ and symmetric positive definite matrix $A \in \mathbb{R}^{n \times n}$. Notice that A is the sum of a sparse matrix of rank $(n-1)$ and a dense matrix of rank 1. The inclusion (3.21) is called a saddle point problem since its solutions are saddle points of

$$\mathcal{L}(\mathrm{c}, \mathrm{w}) = \frac{1}{2} \langle A\mathrm{c}, \mathrm{c} \rangle - \langle \mathrm{f}, \mathrm{c} \rangle + \varphi(\mathrm{c}) - \langle B\mathrm{c}, \mathrm{w} \rangle - \langle \mathrm{g}, \mathrm{w} \rangle - \frac{1}{2} \langle C\mathrm{w}, \mathrm{w} \rangle.$$

In case of a logarithmic potential (2.5), the inclusion (3.21) can as well be written as an equation, involving the derivative of Ψ. However, in the light of its singularities at $c = 0, 1$ and desired robustness of iterative solution with respect to temperature θ, we concentrate on the more general formulation (3.21).

3.2.3. Algebraic Solution of Discrete Spatial Problems

In this section we will discuss the efficient algebraic solution of the discrete problems (3.18) by iterative methods. In each time step this amounts to the solution of the nonsmooth nonlinear saddle point problem (3.18a)–(3.18b) and the linear equation (3.18c) in the quotient space $\mathbf{H}_{\mathfrak{T}}$.

Nonsmooth Schur–Newton methods

We solve the saddle point system (3.21) iteratively by so-called nonsmooth Schur–Newton multigrid methods, NSNMG methods in short. Here, it does not matter whether $\partial\varphi$ is set- or single-valued, because NSNMG relies on convexity rather than smoothness. While originally introduced for saddle point problems with obstacles [67, 63], NSNMG has been meanwhile extended to more general nonlinearities with nonsmooth convex energies [66, 61, 64]. Since the method and corresponding results are literally the same as for the vector-valued case (Section 4.2.2) we refer to the presentation there and the cited references for details and just give an overview of the basic ideas here.

The NSNMG approach relies on the equivalent minimization problem

$$\mathrm{w} \in \mathbb{R}^n: \qquad h(\mathrm{w}) \leqslant h(\mathrm{v}) \qquad \forall \mathrm{v} \in \mathbb{R}^n$$

for the dual energy functional

$$h(\mathrm{w}) = -\inf_{\mathrm{v} \in \mathbb{R}^n} L(\mathrm{v}, \mathrm{w}), \tag{3.22}$$

which was already used in the proofs of Theorems 3.2 and 3.6.

Now the main observation is that $h : \mathbb{R}^n \to \mathbb{R}$ is convex and differentiable with Lipschitz continuous derivative ∇h. Hence, the saddle point system (3.21) is equivalent to the equation

$$\nabla h(\mathrm{w}) = 0, \tag{3.23}$$

where the derivative ∇h is given by the nonlinear Schur-complement

$$\nabla h(\mathrm{w}) = B\Big((A + \partial\varphi)^{-1}(\mathrm{f} + B\mathrm{w})\Big) + C\mathrm{w} + \mathrm{g}.$$

Lipschitz continuity of ∇h allows to apply Newton-like gradient related descent methods

$$\mathrm{w}^{\nu+1} = \mathrm{w}^\nu - \rho_\nu \Big(\partial^2 h(\mathrm{w}^\nu)\Big)^{-1} \nabla h(\mathrm{w}^\nu) \tag{3.24}$$

with $\partial^2 h(\mathrm{w}^\nu)$ being a generalized linearization of ∇h at w^ν and ρ_ν a suitable damping parameter.

The associated primal iterate c^ν is then determined by

$$c^\nu = (A + \partial\varphi)^{-1}(f + B w^\nu).\tag{3.25}$$

Assuming existence and uniqueness of the solution $w_{\mathfrak{T}}$, it was shown in [66, 61] that the resulting algorithm is globally convergent, if the damping parameters ρ_ν are properly chosen, e.g., by bisection or by the Armijo rule. Global convergence is preserved by inexact evaluation of the directions $(\partial^2 h(w^\nu))^{-1}\nabla h(w)$ with increasing accuracy.

Each NSNMG iteration is stopped, if the norm of the actual correction of the dual iterate falls below a given threshold, i.e.,

$$\left\| w^{\nu+1} - w^\nu \right\|_{\mathrm{w}} \leqslant \vartheta_{\mathrm{NSNMG}}.\tag{3.26}$$

In the numerical experiments reported below $\vartheta_{\mathrm{NSNMG}} = 10^{-12}$ was chosen.

Each iteration step of NSNMG requires the (approximate) solution of the nonlinear Allen–Cahn-type problem (3.25) and the linear system (3.24) in order to obtain $\nabla h(w^\nu)$ and the new iterate $w^{\nu+1}$, respectively. In our numerical computations to be reported below, the nonlinear Allen–Cahn-type problem (3.25) is solved in an efficient and robust way by V(3,3) cycles of *Truncated Nonsmooth Newton Multigrid* (TNNMG) as described in Section 2.2.3. The linear system (3.24) is equivalent to a linear saddle point problem and can be solved by a multitude of direct or iterative solvers. We used the GMRES method [112] preconditioned with a multigrid method with block Gauß–Seidel smoother [113, 119, 126] in our numerical computations.

A multigrid method for singular elasticity problems

In order to describe the iterative solution of the elasticity problem (3.18c), we first consider the semi-definite problem on the whole finite element space

$$\tilde{\boldsymbol{u}}_{\mathfrak{T}} \in \mathcal{S}_{\mathfrak{T}}^d : \qquad a(\tilde{\boldsymbol{u}}_{\mathfrak{T}}, \boldsymbol{v}) = \ell(v) \qquad \forall \boldsymbol{v} \in \mathcal{S}_{\mathfrak{T}}^d\tag{3.27}$$

with a symmetric positive semi-definite bilinear form and a linear functional given by

$$a(\cdot,\cdot) = \left(\mathcal{C}(c_{\mathfrak{T}})\boldsymbol{\varepsilon}(\cdot), \boldsymbol{\varepsilon}(\cdot)\right), \qquad \ell(\cdot) = \int_{\partial\Omega} \boldsymbol{g} \cdot (\cdot)\, ds + \left(\mathcal{C}(c_{\mathfrak{T}})\bar{\boldsymbol{\varepsilon}}(c_{\mathfrak{T}}), \boldsymbol{\varepsilon}(\cdot)\right)$$

respectively. Without loss of generality we assume that $\boldsymbol{g}$ satisfies the compatibility condition

$$\int_{\partial\Omega} \boldsymbol{g} \cdot \boldsymbol{v} \, ds = 0 \qquad \forall \boldsymbol{v} \in \ker(\boldsymbol{\varepsilon}).$$

Then the solution space of (3.27) is given by $\boldsymbol{u}_{\mathfrak{T}} + \ker(\boldsymbol{\varepsilon})$.

For the solution of (3.27) we can now use a classical linear multigrid method with linear Gauß–Seidel smoother with respect to the hierarchy $\mathcal{S}_0^d \subset \cdots \subset \mathcal{S}_j^d = \mathcal{S}_{\mathfrak{T}}^d$ of subspaces, as introduced in (3.17). We emphasize that the Gauß–Seidel smoother is well-defined for all levels k because the vector valued nodal basis functions of $\mathcal{S}_k^d$ are not contained in the kernel $\ker(\boldsymbol{\varepsilon})$ of the bilinear form a.

It is easy to see that this multigrid method converges to the solution $\boldsymbol{u}_{\mathfrak{T}}$ with respect to the half-norm $a(\cdot, \cdot)^{1/2}$. For the Poisson problem with Neumann boundary conditions discretized with respect to a hierarchy of quasi-uniform grids, mesh independence of the convergence rates was shown in [90]. Mesh independence for classical multigrid applied to the present singular elasticity problem (3.27) can be shown using the same arguments.

Notice that only the projected iterates, i.e. projected onto to $\mathbf{H}$, converge to $\boldsymbol{u}_{\mathfrak{T}}$ with respect to the $H^1(\Omega)^d$-norm. This is due to the non-uniqueness of rigid body motions of solutions to (3.27).

3.2.4. Quantification of Coarsening

As macroscopic properties of alloys usually degrade with increasing coarseness of the microstructure, a main aspect of the simulation of microstructure evolutions is the quantification of coarsening. For that end we need to introduce a characteristic length scale of a given grain distribution. It is well-known that for the Cahn–Hilliard equation (without elasticity) such a length scale cannot grow faster than $t^{1/3}$ in a time averaged sense. (cf. [82, 36, 101, 102]). Obviously, there are no corresponding global lower bounds, as there are stable states that do not coarsen at all.

While the inverse of the Ginzburg–Landau energy has emerged as a convenient length scale in analysis and numerical computations (cf. [36, 55, 82, 101, 102, 121]), it suffers from inaccessibility in physical experiments. Hence, we choose the so-called *mean intercept length* $\bar{L}$ as characteristic length scale to maintain quantitative comparability

with material science experiments as for example in [19]. It gives the expected value of the length of a secant across a precipitate. If all precipitates are roughly spherical and of comparable size, the mean intercept length approximately translates to the *mean phase radius* by a simple multiplication. In order to determine $\bar{L}$ we follow standard procedure of quantitative stereology performing a lineal analysis (cf. [118]). The details of the applied procedure are given below.

For the following let's call the matrix and particle (or precipitate) phases β- resp. α-phase and assume that the phase field value c_α of the α-phase is greater than that of β-phase, c_β. In this context let Θ denote the set of secants of α-precipitates and $L(\omega)$ the length of $\omega \in \Theta$. The mean intercept length is then

$$\bar{L} = E(L)$$

the expected value of secant length assuming uniform distribution on Θ. In order to approximate $\bar{L}$ we lay an equidistant cube mesh with mesh size h over the computational domain and count the number of mesh edges $N_\mathcal{E}$ and the number of line segments N_L intersecting an α-precipitate, i.e. α-secants lying on mesh lines. Partially intersecting edges are counted as one half. Thus we have as an approximation

$$\bar{L} \approx N_\mathcal{E} \cdot h / N_L.$$

If no particles of diameter less than $\sqrt{2}h$ are present, counting the intersecting edges amounts to counting grid vertices inside α-regions and multiplying by the dimension of the computational domain (note that smaller particles might be overlooked this way, cf. Fig. 3.1 left). A vertex is counted as inside α-phase iff the value of the phase field at its coordinates is above a given threshold c_0. As intersecting line segments we count nonempty α-vertex sets which are discretely connected along single mesh lines (cf. Fig. 3.1 right). Under the assumption that the minimal distance of two neighboring precipitates is larger than h this is exactly the number N_L.

As the mean intercept length of a single spherical particle of radius r is $\nu_d \cdot r$ where $\nu_d = \frac{\pi}{2}$ in 2D and $\nu_d = \frac{4}{3}$ in 3D, we validate our algorithm with a set of grain distributions of equisized particles of known radius $r \in \{k \cdot 0.05\}_{k=1}^{10}$. We choose various mesh sizes for the algorithm and compute the relative error of our numerical measurement. The results are aggregated in Figure 3.2 where we plot the relative error of our mean radius measurement over the relative mesh size, i.e. h/r. We find that our method is exact up
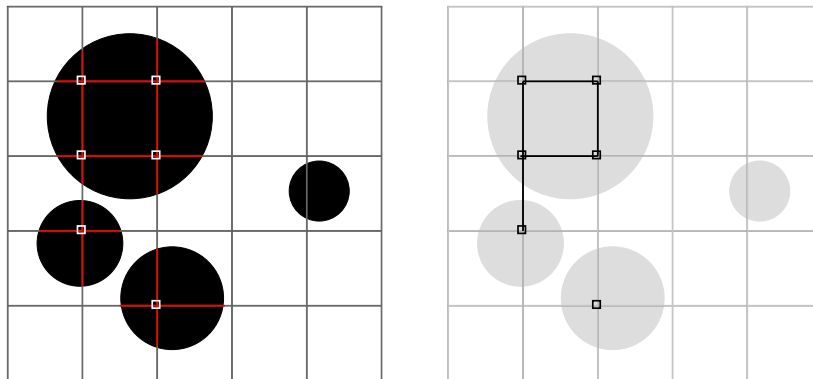
Figure 3.1 – Illustration of our lineal analysis. In this example we have $N_{\mathcal{E}} = 12;\ N_L = 7$

to an order of magnitude of 10^{-3} at $h/r = 0.02$ for all tested cases.

For conglomerates of (roughly) spherical particles of various radii, we define the *mean*
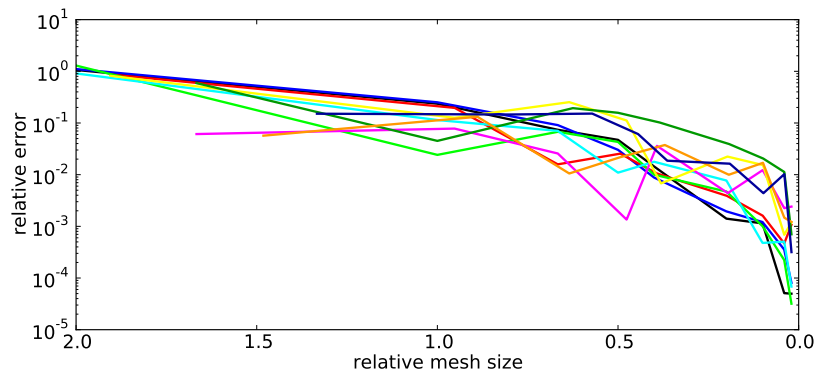
Figure 3.2 – The relative error of our mean radius measurement over relative meshsize, i.e. h/r, for $r \in \{k \cdot 0.05\}_{k=1}^{10}$. Plot colors relate to radii in ascending order by black, blue, red, green, cyan, magenta, yellow, darkgreen, orange, darkblue. Note the inverted horizontal axis.

phase radius $\bar{r}$ as

$$\bar{r} = \frac{\bar{L}}{\nu_d}.$$

Note that, in general, this differs from the arithmetic mean phase radius $\bar{r}_a = \frac{1}{N_A} \sum_{i=1}^{N_A} r_i$ where N_A and r_i are the number of particles and the radius of the i-th particle respectively. Consider the case of two spherical particles of roughly the same size under competitive growth. One will grow at the expense of the other until the latter one's annihilation as illustrated in Figure 3.3 top, while the total particle volume is conserved. While the

arithmetic mean phase radius even decreases and then jumps at the annihilation point, our mean phase radius as computed by the mean intercept length makes a continuous transition from the starting value to its double as seen in Figure 3.3 bottom. For conglomerates of equisized spherical particles $\bar{r} = \bar{r}_a$ holds, however.

For the competitive growth example we chose an initial configuration of two circles with radii $r_{1,2} = r_0 = 0.2$ centered at $(-0.3, 0)$ and $(0.3, 0)$ respectively with a smooth transition from value -1 to 1 according to a sine profile across an interface of width 10^{-13}. The radius refers to the zero level line. We then let one circle shrink according to $r_1(t) = \sqrt{r_0^2 - 2t}$ and the other inflate such that the overall particle volume is constant.
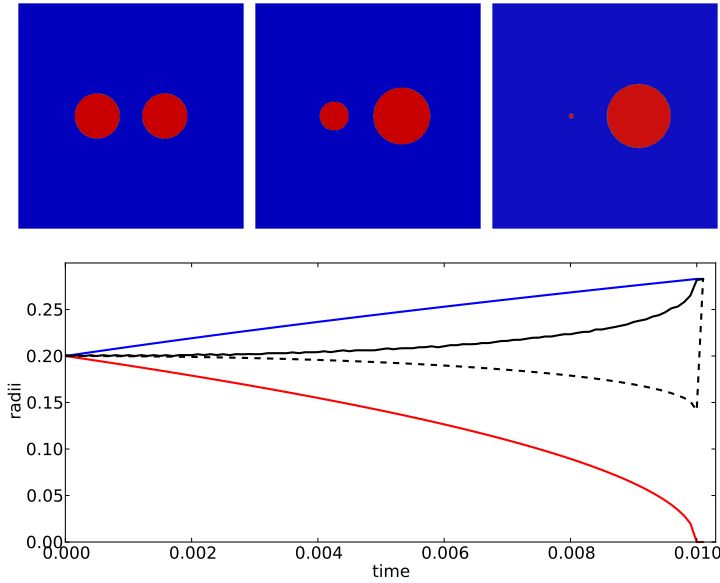
Figure 3.3 – Top: Two identical particles under competitive growth at various stages. Bottom: The radii r_1 (red) and r_2 (blue) of the two particles, their arithmetic mean $\bar{r}_a$ (dashed), and the mean phase radius $\bar{r}$ (solid black) over time

3.3. Coarsening of microstructure in a eutectic AgCu brazing alloy

In this section we simulate the microstructure evolution in a eutectic silver/copper (Ag71Cu29) brazing alloy utilizing the Cahn–Larché model (3.9) and its discretization (3.18). The presentation follows that of [69], while the results are recomputations that

differ in the following ways: Firstly, the temperature difference $\Delta\theta = 51$K was chosen as opposed to 1000K in [69] and, secondly, the norm for the dual quantity $\|\cdot\|_{\mathrm{w}}$ was chosen independently of $\mathfrak{T}$, i.e. in particular there was no mass-lumping.

3.3.1. Problem setting

The computations are carried out on the square $\Omega = [-L, L]^2$ with edge length $2L = 0.1\,\mu$m during the time interval from zero to $T = 375\,\mathrm{s} = 6.25\,\mathrm{min}$. We choose c to be the copper concentration such that $c = 0$ corresponds to pure silver and $c = 1$ corresponds to pure copper. Concerning the setting and material parameters, we closely follow [20], i.e., for the alloy in question the eigenstrains are assumed to result only from thermal expansion: $\bar{\varepsilon}(c) = \Delta\theta\mathcal{A}(c)$. In our computations we select $\Delta\theta = 51\,$K, which is the difference of the solidus temperature of eutectic Ag71Cu29 and $1000\,$K, the temperature we chose for our simulations. The surface tension, mobility, and thermal expansion in this setting reduce to scalar functions

$$\Gamma(c) = \gamma(c)\mathsf{Id}, \ \ \mathcal{M}(c) = m(c)\mathsf{Id}, \ \ \mathcal{A}(c) = a(c)\mathsf{Id}.$$

The corresponding quantities for the pure constituents, i.e. for $c \in \{0, 1\}$, are given in Table 3.1 (note that due to a different scaling in our equations, we need to rescale γ by a factor of 2 as compared to [20]). The entries of the Hooke tensors $\mathcal{C}_{\mathrm{Ag}}$ and $\mathcal{C}_{\mathrm{Cu}}$ for pure silver and copper are given in Table 3.2. In all 2D computations we assume plain strain conditions. As in (3.4), the values of the functions γ, m, a, and $\mathcal{C}$ at $c \in (0, 1)$ are obtained by linear interpolation. The chemical energy density Ψ takes the form (3.2)

$\gamma_{\mathrm{Ag}}[\mathrm{N}]$	$\gamma_{\mathrm{Cu}}[\mathrm{N}]$	$m_{\mathrm{Ag}}\left[\frac{\mathrm{m}^5}{\mathrm{Js}}\right]$	$m_{\mathrm{Cu}}\left[\frac{\mathrm{m}^5}{\mathrm{Js}}\right]$	$a_{\mathrm{Ag}}\left[\frac{10^6}{\mathrm{K}}\right]$	$a_{\mathrm{Cu}}\left[\frac{10^6}{\mathrm{K}}\right]$
$3.06 \cdot 10^{-10}$	$3.808 \cdot 10^{-10}$	$7.25 \cdot 10^{-25}$	$3.65 \cdot 10^{-25}$	18.9	16.5

Table 3.1 – Material parameters (taken from [20])

with parameters β_i given in Table 3.3. The splitting (2.2) is chosen according to

$$\Phi(c) = \beta_0 R\theta \left(c \log(c) + (1-c) \log(1-c)\right)$$
$$+ (\beta_4 - \beta_3)c^3 + (\beta_3 - \beta_4)c^2 + (\beta_2 - \beta_1 + \beta_4)c + \beta_1$$
$$\Upsilon(c) = -\beta_4 c^2.$$

$\mathcal{C}^{11}_{\mathrm{Ag}}[\mathrm{GPa}]$	$\mathcal{C}^{12}_{\mathrm{Ag}}[\mathrm{GPa}]$	$\mathcal{C}^{44}_{\mathrm{Ag}}[\mathrm{GPa}]$	$\mathcal{C}^{11}_{\mathrm{Cu}}[\mathrm{GPa}]$	$\mathcal{C}^{12}_{\mathrm{Cu}}[\mathrm{GPa}]$	$\mathcal{C}^{44}_{\mathrm{Cu}}[\mathrm{GPa}]$
168	121	75	124	94	46

Table 3.2 – Entries of the Hooke tensors for pure silver and copper in Voigt notation (taken from [20])

$\beta_0[\frac{\mathrm{mol}}{\mathrm{m}^3}]$	$\beta_1[\frac{\mathrm{GJ}}{\mathrm{m}^3}]$	$\beta_2[\frac{\mathrm{GJ}}{\mathrm{m}^3}]$	$\beta_3[\frac{\mathrm{GJ}}{\mathrm{m}^3}]$	$\beta_4[\frac{\mathrm{GJ}}{\mathrm{m}^3}]$
$1.11248134 \cdot 10^5$	-5.20027	-7.2738	2.96683	3.01417

Table 3.3 – Fitting parameters for Margules ansatz at $\theta = 1000\,\mathrm{K}$ and given material data (taken from [20, 18])

In order to choose a reasonable time step size τ that leads to acceptable discretization errors we performed several computations for the classical Cahn–Hilliardequation with logarithmic potential as model problem, i.e. $c \in [-1, 1]$, $\Gamma(c) = \gamma\mathsf{Id}$, $\mathcal{M}(c) = \mathsf{Id}$, $\mathcal{C} = 0$, in (3.9). As initial value we chose a decomposed "melt", i.e. starting from a random initial distribution of $c_0(x) \in [-0.42 - \delta, -0.42 + \delta]$ where $\delta = 10^{-2}$ we compute a Cahn–Hilliard evolution until grain formation has mostly finished and use that as initial value for the present computations (cf. Figure 3.4). In these computations we chose $\theta = 0.6$ and various values for γ and τ on uniform grids. Assuming the relationship $\tau = \vartheta \cdot \gamma$ the computed mean phase radius evolutions suggest a choice of $\vartheta \approx 5$ (cf. Figure 3.5).

In the following computations we chose L as unit length, $\Psi_0 = 0.1\,\frac{\mathrm{GJ}}{\mathrm{m}^3}$ as unit energy
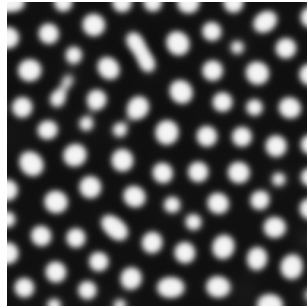

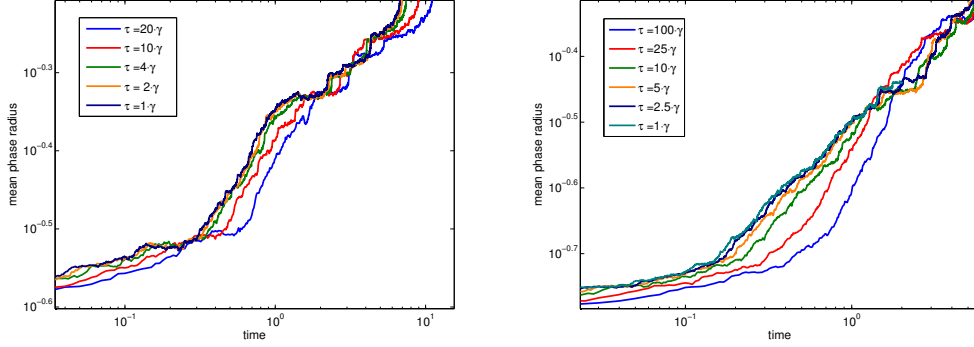*Figure 3.4* – Initial value for timestepsize selection computations.

Figure 3.5 – Simulated mean phase radii vs time for $\gamma = 5 \cdot 10^{-4}$ (left) and $\gamma = 2 \cdot 10^{-4}$ (right)

density, and $10^{-25} \frac{\mathrm{m}^5}{\mathrm{Js}}$ as unit mobility resulting in a unit time of $t_0 = 250\,\mathrm{s}$. After nondimensionalization the interface parameter is roughly $\gamma(c) \approx 1.53 \cdot 10^{-4}$. The above presented numerical tests therefore suggest the choice $\tau = 7.5 \cdot 10^{-4} t_0 = 5 \cdot 10^{-4} T$. The coarsest grid $\mathfrak{T}_0$ consists of a partition of Ω into two congruent subtriangles. In the first time step, we start the derefinement process described in Section 2.2.2 from $\mathfrak{T}^{\mathrm{old}}$ obtained by 8 uniform refinements of $\mathfrak{T}_0$.

3.3.2. Evolution of concentration

In our first simulation, we apply no boundary stress and select the initial condition c^0 as shown in the upper left picture of Figure 3.6. We chose these default data in the sequel, if not otherwise stated. The colors blue and red indicate high concentrations of silver and copper, respectively. The remaining pictures in Figure 3.6 illustrate the evolution of the approximate concentration $c_{\mathfrak{T}}^m$ together with the corresponding final grids of the adaptive procedure over various time steps $m = 50, \ldots, 2000$. Observe that the coarsening significantly slows down during the evolution (see Subsection 3.3.3 for details).

Mass conservation of the constituents is a key feature of the physical process which should be preserved in numerical simulations. In our computation of over 2000 time steps, we found the maximal relative deviation from the initial mass of copper of

$$\max_{m=1,\ldots,2000} \frac{|\int_\Omega c_{\mathfrak{T}}^m - \int_\Omega c^0|}{\int_\Omega c^0} \approx 1.9 \cdot 10^{-11}.$$
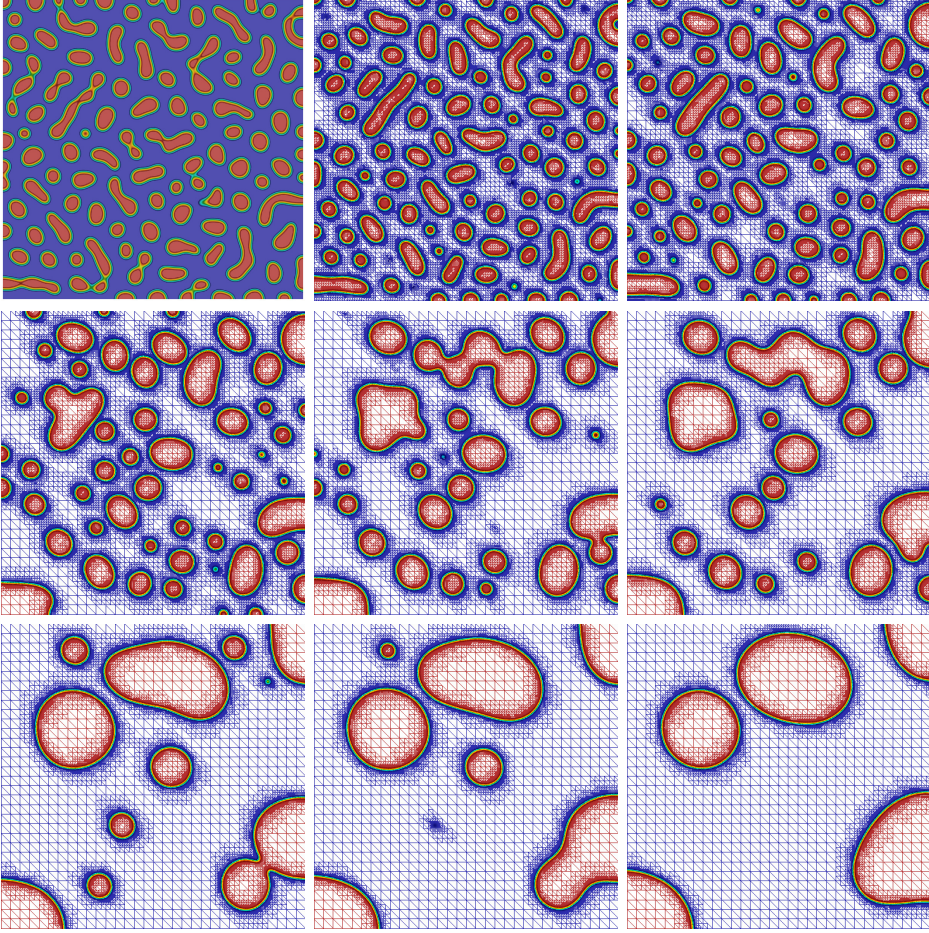
Figure 3.6 – Initial value c^0 and approximation $c_{\mathfrak{T}}^m$ at time steps $m = 50, 100, 200, 300, 400, 800, 1000, 2000$.

The equilibrium concentrations

$$c_\alpha = 0.05096976816135458 \quad \text{and} \quad c_\beta = 0.9460270077128279$$

of the Ag-rich α- and the Cu-rich β-phase are determined from Ψ by the Maxwell-tangent construction (see e.g. [97]). In our computations the phase equilibria are recovered up to about $4 \cdot 10^{-4}$. This is illustrated by Figure 3.7 showing the cross section of the initial condition (black) and of the approximate solution $c_{\mathfrak{T}}^{2000}$ (red) along the y-axis.

In order to study the influence of thermomechanical stress on the evolution of the phase
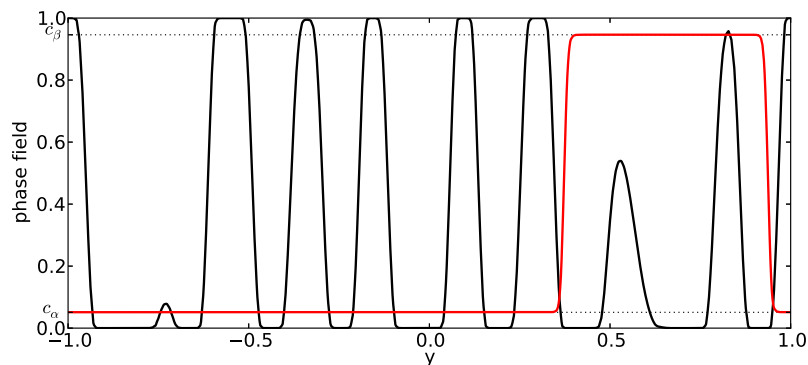
Figure 3.7 – Cross section of the initial condition (black) and of the approximate solution $c_{\mathfrak{T}}^{2000}$ (red) along the y-axis. The dotted lines represent the equilibrium concentrations c_α and c_β.

field we applied boundary stress of the form

$$\boldsymbol{g} = -g\boldsymbol{n} \qquad \text{on } \partial\Omega$$
$$g(x) = g_0 \,\text{GPa, if } x = (x_1, \pm L) \quad \text{and} \quad g(x) = 0 \,\text{GPa, otherwise}$$

(3.28)

with the different values $g_0 = 0, \dots, 20\,\text{GPa}$, but observed only minor changes in the evolution (see also Subsection 3.3.3). In this and the following experiment the error tolerance $\vartheta_{\text{adapt}} = 0.05$ was chosen.

In order to (unphysically!) enhance the influence of thermomechanical stress, the elastic energy density $\mathcal{W}(c, \boldsymbol{\varepsilon}(\boldsymbol{u}))$ is multiplied by a factor of $\omega = 1, 1000, 1 \cdot 10^4, 2 \cdot 10^4, 5 \cdot 10^4, 1 \cdot 10^5, 2 \cdot 10^5, 4 \cdot 10^5$ while zero boundary stress is prescribed. This leads to a significantly faster dynamics and oblong phase shapes oriented along the coordinate directions. This is illustrated in Figure 3.8 that shows the initial condition c^0 and the approximate concentration $c_{\mathfrak{T}}^m$ together with the underlying grids for $\omega = 4 \cdot 10^5$ and the time steps $m = 30, 50, 70, 90, 130$.

Due to the unified grid interface of the numerics library DUNE (cf. Section 2.2.4) and its extensive use of templates, we may switch from 2D to 3D computations by simply resetting a compile-time parameter. All it requires is a little additional care while coding. The numerical solution illustrated in Figure 3.9 have thus been computed by the same code as above but with $\tau = 10^{-4}$.

82
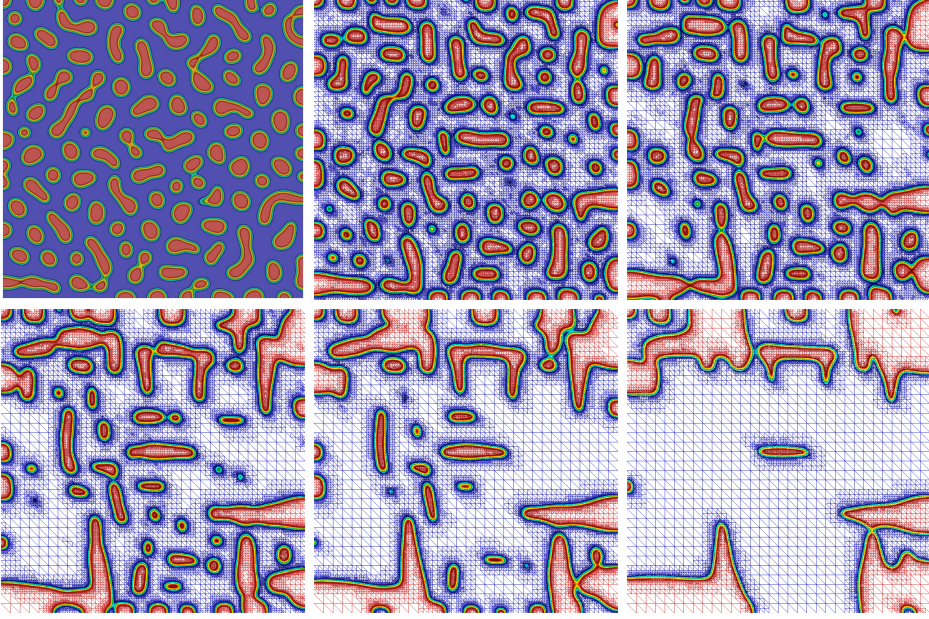
Figure 3.8 – Initial value c^0 and approximation $c_{\overline{\tau}}^m$ at time steps $m = 30, 50, 70, 90, 130$ for (unphysically!) increased elastic energy density $\mathcal{W}(c, \varepsilon(\boldsymbol{u}))$.

3.3.3. Evolution of mean intercept length

In this subsection, we investigate the dynamics of coarsening in terms of the evolution of the mean intercept length in more detail.

In our first experiment we investigate the sensitivity of the evolution of mean intercept length with respect to a smooth approximation of the logarithmic Margules potential Ψ as described in (3.2) with parameters β_i given in Table 3.3. To this end, we consider the quartic Hermite polynomial $P^\Psi(c) = \sum_{i=0}^{4} \alpha_i c^i$ interpolating Ψ at the equilibrium concentrations c_α, c_β, and at the eutectic point c_{eut}, characterized by

$$P^\Psi(c_\alpha) = \Psi(c_\alpha), \qquad P^\Psi(c_\beta) = \Psi(c_\beta), \qquad P^\Psi(c_{\text{eut}}) = \Psi(c_{\text{eut}})$$

$$(P^\Psi)'(c_\alpha) = \Psi'(c_\alpha), \qquad (P^\Psi)'(c_\beta) = \Psi'(c_\beta).$$

The left and the right picture in Figure 3.10 show Ψ (solid), P^Ψ (dashed), and their derivatives, respectively. The splitting (2.2) of P^Ψ is selected according to $P^\Phi = \sum_{\substack{i=0 \\ i \neq 3}}^{4} \alpha_i c^i$ and $P^\Upsilon = \alpha_3 c^3$.
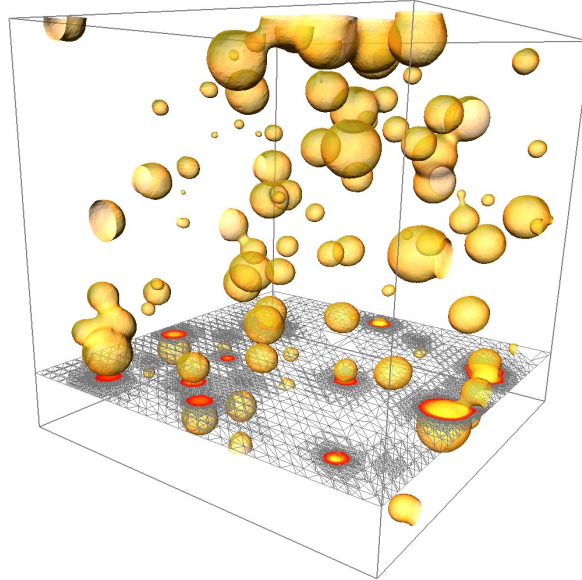
Figure 3.9 – 0.47-levelset and cross-section of the numerical approximation at timestep 5 of the described 3D problem

We prescribe zero boundary stress (see Figure 3.6 for the corresponding evolution of the approximate concentrations). Now Figure 3.11 shows the evolution of the mean intercept length for the Margules potential Ψ (black) and its quartic approximation P^Ψ (red), respectively. It turns out that quartic approximation strongly perturbs the coarsening behavior which is in agreement with the engineering literature [42, 43].

In our next experiment, we investigate the influence of strongly varying boundary pressure $g_0 = 0, 1, 2, 3, 4, 5, 10, 20\,\text{GPa}$ in the boundary condition (3.28). Figure 3.12 shows that even large mechanical stress has only minor influence on the coarsening behavior. This effect has also been observed in previous simulations [43, Section 4.3].

For a qualitative investigation of mechanically induced coarsening, the elastic energy density $\mathcal{W}(c, \boldsymbol{\varepsilon}(\boldsymbol{u}))$ is replaced by $\omega\mathcal{W}(c, \boldsymbol{\varepsilon}(\boldsymbol{u}))$ with (unphysical!) amplification factors $\omega = 1, 1000, 1\cdot10^4, 2\cdot10^4, 5\cdot10^4, 1\cdot10^5, 2\cdot10^5, 4\cdot10^5$. Figure 3.13 shows that the coarsening speed increases with increasing ω, as expected (recall the evolution of concentrations for $\omega = 4 \cdot 10^5$ depicted in Figure 3.8).
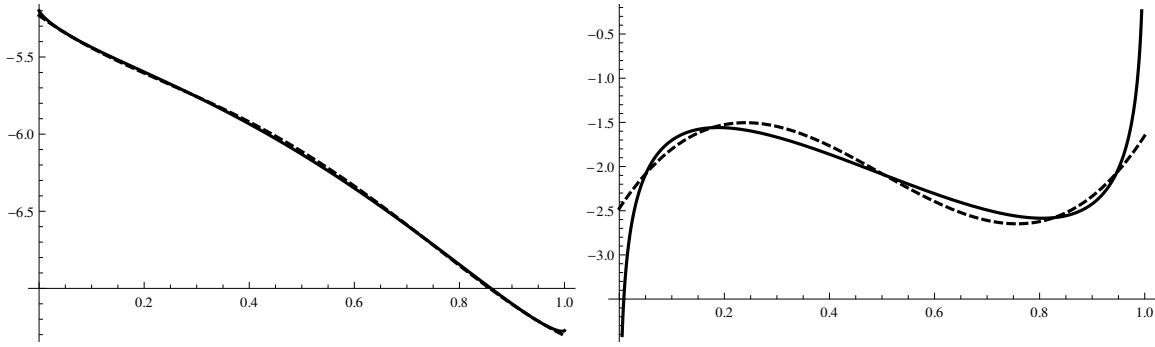
Figure 3.10 – Left: Margules potential Ψ (solid), quartic approximation P^Ψ (dashed). Right: First derivatives.
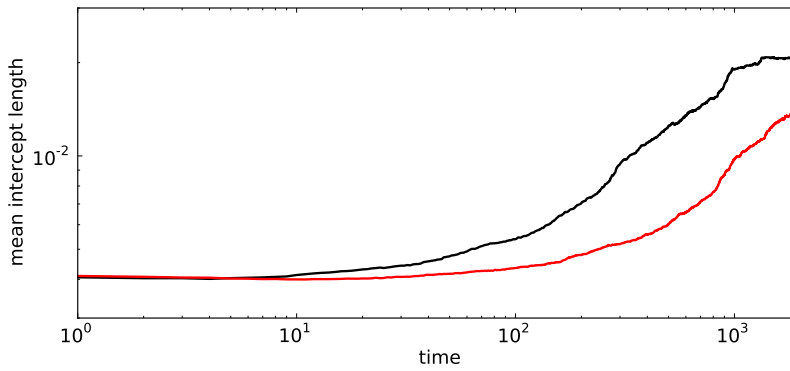
Figure 3.11 – Approximate evolution of mean intercept length for Margules potential Ψ (thin solid) and its quartic approximation P^Ψ (bold solid).

3.3.4. Numerical aspects

We now briefly illustrate the performance of the main building blocks of our numerical solution algorithm. For more detailed numerical experiments, we refer to [66, 61, 67, 68].

We first consider a posteriori error estimation and adaptive mesh refinement as described in Subsections 2.2.2 and 3.2.2. The corresponding adaptive algorithm is applied to the spatial problem arising in the $m = 1^{\text{st}}$ time step of the discretized Cahn–Larché system (3.13) with material data and discretization parameters given in Subsection 3.3.1. The grid $\mathfrak{T}$ satisfying the stopping criterion (2.39) with $\vartheta_{\text{adapt}} = 0.015$ after 9 adaptive refinement steps and a grid detail are shown in Figure 3.14. The final grid contains 2793228 nodes of which 2426748 are nonhanging. Observe how the initial, 8 times uniformly refined grid $\mathfrak{T}^{\text{old}}$ has been adaptively coarsened and then refined according
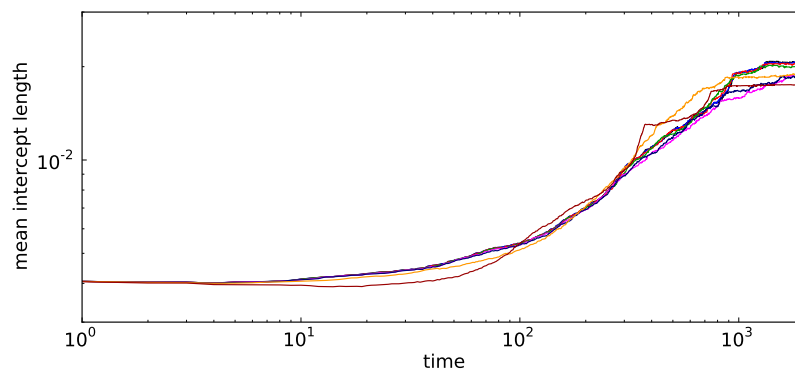
Figure 3.12 – Approximate evolution of mean intercept length for boundary pressure $g_0 = 0\,\text{GPa}$ (black), $1\,\text{GPa}$ (blue), $2\,\text{GPa}$ (red), $3\,\text{GPa}$ (green), $4\,\text{GPa}$ (magenta), $5\,\text{GPa}$ (darkblue), $10\,\text{GPa}$ (orange), and $20\,\text{GPa}$ (brown).

to the new approximation in the new time step. Further note how the regions of high curvature are finely resolved whereas the regions of highest gradients in the middle of the interface are not, as opposed to simple gradient based refinement strategies. Figure 3.15 shows the corresponding estimated error η, as introduced in (3.19), over $\sqrt{n}$, n denoting the corresponding number of unknowns. Note that $h = n^{-1/2}$ is the mesh size in case of uniform refinement. The dashed line indicates $\mathcal{O}(n^{-1/2})$. A comparison suggests that our adaptive refinement algorithm provides approximations with optimal order.

Using the same problem as above, we now illustrate the iterative solution of the discretized phase field system (3.18a), (3.18b). On each computational grid the overall iteration is stopped once the termination criterion (3.26) with $\vartheta_{\text{NSNMG}} = 10^{-12}$ is matched. The initial iterate is selected as the final iterate from the preceding refinement step (nested iteration). The resulting number of *Nonsmooth Schur–Newton Multigrid* (NSNMG) iterations required to reach this tolerance ranges from 5 on the coarser grids to 3 on the finer grids.

Recall that each step of NSNMG is quite expensive (cf. Subsection 3.2.3): It involves the approximate solution of the discrete Allen–Cahn-type system (3.25) by V(3,3) cycles of *truncated nonsmooth Newton multigrid* (TNNMG) and of the linear saddle point problem (3.24) by a GMRES method with a multigrid preconditioner with block Gauß–Seidel smoother. In order to illustrate the share of the numerical solution of each of these two subproblems in the computational effort of an NSNMG iteration step, we consider the discrete spatial problems occurring in the first time step after $j = 0, \ldots, 9$ adaptive refinement cycles. This leads to a minimal mesh size $\sqrt{2} \cdot 2^{-11}$ and 2426748 unknowns
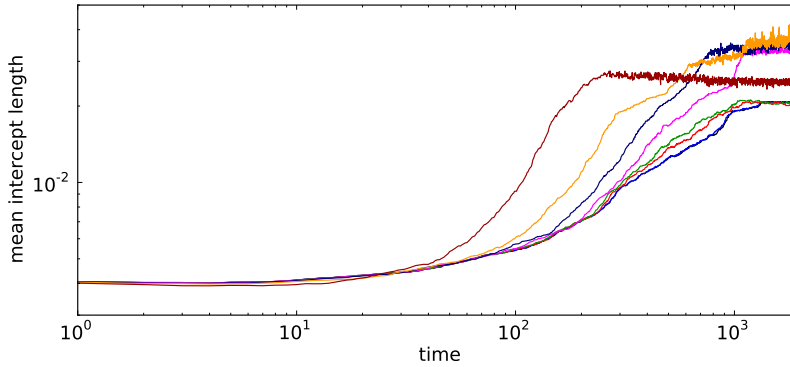
Figure 3.13 – Approximate evolution of mean intercept length for (unphysically!) amplified elastic energy by the factor $\omega = 1$ (black), 1000 (blue), $1 \cdot 10^4$ (red), $2 \cdot 10^4$ (green), $5 \cdot 10^4$ (magenta), $1 \cdot 10^5$ (darkblue), $2 \cdot 10^5$ (orange), $4 \cdot 10^5$ (brown).
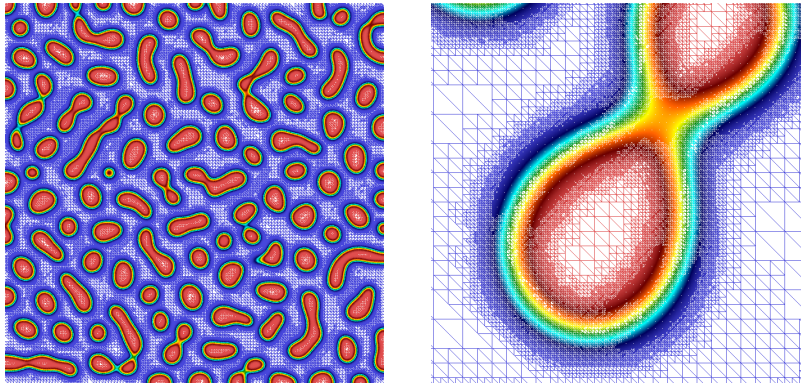
Figure 3.14 – Left: Adaptively refined grid $\mathfrak{T}$. Right: Grid detail.

on the final level.

For a fair comparison, the required computational work is measured in work units rather than iteration steps. One work unit is chosen to be the cpu time for one V(3,3) cycle of TNNMG on the corresponding grid. While the sum of work units for all subproblems on each refinement level is ranging from 12 to 21 for the discrete Allen–Cahn-type system (TNNMG), it reaches values from 753 to 2515 for the linear saddle point problem (preconditioned GMRES). Similarly, for TNNMG the average error reduction over all subproblems occurring on each refinement level $j = 1, \ldots, 9$ never exceeds 0.05, but even reaches values of 0.98 for preconditioned GMRES on finer grids.

Thus, the overall computational work is obviously dominated by the *linear* saddle point
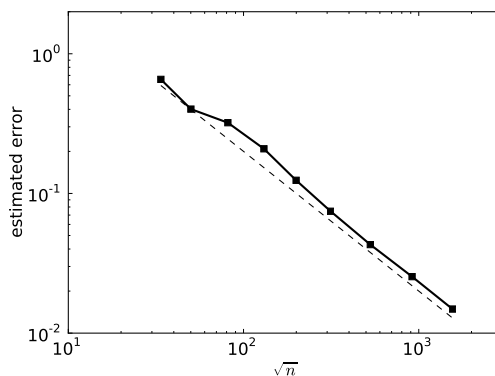
Figure 3.15 – Estimated error η over $n^{1/2}$ (solid) in comparison with $\mathcal{O}(n^{-1/2})$ (dashed).

solver. A first, simple, reason is that the linear saddle point problem (3.24) is larger: It involves twice the number of unknowns of the discrete Allen–Cahn-type system (3.25). Another reason is that an equivalent reformulation of the discrete Allen–Cahn-type system in terms of convex minimization could be directly exploited in the algebraic solution process. This is not the case for linear saddle point problems.

We now consider the (indefinite) linear elasticity problem (3.18c). To that end we perform some numerical tests on a model problem which is illustrated in Figure 3.16 left. We consider the isotropic linear elasticity problem with Young's modulus $\texttt{E} = 1000$ and Poisson's ratio $\nu = 0.3$ and zero eigenstrain on a cube $\Omega = [-1,1]^d$ in two and three space dimensions and prescribe compressing Dirichlet conditions on the top and bottom boundaries and homogeneous Neumann conditions on the remainder:

$$\boldsymbol{u} = \boldsymbol{0} \pm 0.1 \cdot e_d \quad \text{on } (\partial\Omega)_{D\mp}$$
$$\boldsymbol{\sigma} \cdot \boldsymbol{n} = 0 \qquad\qquad \text{on } (\partial\Omega)_N,$$

where e_d is the d-th unit vector and $(\partial\Omega)_{D\mp}$ are the bottom and top boundary respectively. The corresponding Neumann problem is then obtained by calculating its right-hand side according to

$$(\mathcal{C}\boldsymbol{\varepsilon}(\boldsymbol{u}_D), \boldsymbol{\varepsilon}(\boldsymbol{v})) = (\boldsymbol{f}, \boldsymbol{v}) \qquad \forall \boldsymbol{v} \in (H^1(\Omega))^d,$$

with $\boldsymbol{u}_D$ being the solution of the Dirichlet problem.

Figure 3.16 right shows the average error reduction ρ^k per iteration step of the *Quotient Space Multigrid method* (QSMG) described in Subsection 3.2.3 for a Dirichlet problem of linear elasticity (triangles) and the corresponding Neumann problem (circles) in 2D

(solid) and 3D (dashed).The iteration is stopped once the estimated relative accuracy of 10^{-10} is reached and the initial iterates are obtained by nested iteration. The average error reduction ρ^k seems to saturate with increasing refinement level. This is in perfect agreement with theoretical considerations (cf., e.g., [90]).

Finally Figure 3.17 shows the error, measured in the norm of relative corrections, over
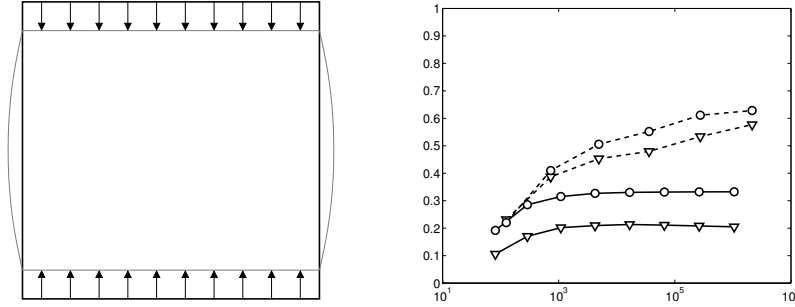
Figure 3.16 – Left: Sketch of the 2D model problem with Dirichlet conditions on the top and bottom boundaries. Right: Averaged error reduction per iteration step of QSMG over number of unknowns for a Dirichlet problem of linear elasticity (triangles) and the corresponding Neumann problem (circles) in 2D (solid) and 3D (dashed).

the iteration step for the indefinite elasticity problem (3.18c) arising in the computation to Figure 3.15 on the finest grid. Here the iteration was stopped when the estimated relative accuracy dropped below 10^{-7}.
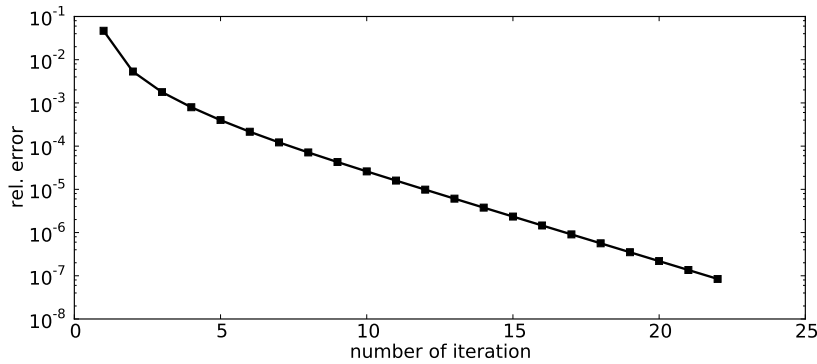
Figure 3.17 – Iteration history of QSMG for the elasticity problem arising in the computation to Figure 3.15 on the finest grid. The graph shows the norm of corrections divided by norm of the iterate over the iteration number.

4. Multicomponent Cahn–Hilliard systems

The key to phase-field simulations of multicomponent alloys is a fast and reliable solver for Cahn–Hilliard-type equations. Hence in our final chapter we consider multicomponent Cahn–Hilliard systems – i.e. Cahn–Hilliard systems with vector-valued order parameter.

While the numerical analysis of multicomponent Cahn–Hilliard systems with logarithmic free energy and the associated deep quench limit model is well developed (cf. [16, 5, 6]), the fast and robust numerical solution of large-scale algebraic systems arising in each time step still seems to be largely open. Existing solvers typically suffer from severe mesh dependance ([16, 5, 6]) or rely on smooth approximations of the free energy ([80, 26]). To our best knowledge, efficient, reliable and robust solvers for multicomponent Cahn–Hilliard systems with logarithmic free energy are previously unknown.

In this work we present the extension of the *Nonsmooth Schur–Newton methods* (see Section 3.2.3 and references therein) to the vector-valued spatial problems arising from the discretizations of multicomponent Cahn–Hilliard systems suggested in [5, 6, 16] up to lumping of lower order terms. Though our approach is applicable to both implicit and semi-implicit time discretizations (see [66, Section 3.4.2]), we concentrate on the semi-implicit variant for ease of presentation.

The chapter is organized as follows. After presentation of the continuous problem and its discretization, Section 4.2.1 concentrates on a unified formulation of the spatial problems as a variational inequality that includes both the logarithmic potential and the deep quench limit. We show existence, uniqueness, and equivalence to a, generally set-valued, nonlinear saddle point problem. In Section 4.2.2 we extend truncated nonsmooth Schur–Newton methods for the iterative solution of an algebraic reformulation of the spatial problem, prove global convergence and discuss some algorithmic issues. Numerical experiments, as reported in Section 4.3, illustrate efficiency and robustness of our

approach.

4.1. Continuous Problem

As before we consider isothermal phase separation in a polyhedral domain $\Omega \subset \mathbb{R}^d$, $d = 1, 2, 3$. The concentrations of the different constituents $i = 1, \ldots, N$ at $(x, t) \in \Omega \times [0, T]$, $T > 0$, are represented by the components $c_i(x, t)$ of the order parameter $\boldsymbol{c} = (c_1, \ldots, c_N)^T$.

Same as earlier, we denote the Euclidean scalar product by $\langle \cdot, \cdot \rangle$ and the $L^2(\Omega)$ scalar product by $(\cdot, \cdot)$. Furthermore we will use the scalar products

$$(\boldsymbol{v}, \boldsymbol{w}) = \int_\Omega \langle \boldsymbol{v}(x), \boldsymbol{w}(x) \rangle \ dx$$

in $L^2(\Omega)^N$ with canonical norm $\| \cdot \|_0$ and

$$(\boldsymbol{v}, \boldsymbol{w})_1 = (\boldsymbol{v}, \boldsymbol{w}) + (\nabla \boldsymbol{v}, \nabla \boldsymbol{w}), \qquad (\nabla \boldsymbol{v}, \nabla \boldsymbol{w}) = \sum_{i=1}^N \int_\Omega \langle \nabla v_i(x), \nabla w_i(x) \rangle \ dx$$

in $H^1(\Omega)^N$ with canonical norm $\| \cdot \|_1$ and semi-norm $| \cdot |_1^2 = (\nabla \cdot, \nabla \cdot)$. Generic constants are denoted by λ, Λ and can have different values at different occurrences.

The order parameter $\boldsymbol{c}$ satisfies the constraints

$$\boldsymbol{c}(x, t) \in G = \{ \boldsymbol{r} \in \mathbb{R}^N \mid \boldsymbol{r} \geqslant 0, \ \textstyle\sum_{i=1}^N r_i = 1 \} \qquad \forall (x, t) \in \Omega \times [0, T_0],$$

because concentrations are non-negative and add up to unity. Here and in the following inequalities of the form $\mathbb{R}^N \ni \boldsymbol{r} \geqslant s \in \mathbb{R}$ are to be understood componentwise. The closed convex set $G \subset \mathbb{R}^N$ is often called *Gibbs simplex*. Note that the indicator function χ_G, defined by $\chi_G(\boldsymbol{r}) = 0$ for $\boldsymbol{r} \in G$ and $\chi_G(\boldsymbol{r}) = +\infty$ for $\boldsymbol{r} \notin G$ can be decomposed according to

$$\chi_G(\boldsymbol{r}) = \sum_{i=1}^N \chi_{[0,\infty)}(r_i) + \chi_{V_1}(\boldsymbol{r})$$

with $\chi_{[0,\infty)}$ and χ_{V_1} denoting the indicator functions of $[0,\infty)$ and V_1, respectively, where

$$V_s = \{ \boldsymbol{r} \in \mathbb{R}^N \mid \textstyle\sum_{i=1}^N r_i = s \}. \tag{4.1}$$

4.1.1. Ginzburg-Landau free energy

We assume that the Ginzburg–Landau total free energy of our system takes the form

$$\mathcal{E}(\boldsymbol{c}) = \int_\Omega \frac{\varepsilon}{2} \sum_{i=1}^N |\nabla c_i|^2 + \frac{1}{\varepsilon} \Psi(\boldsymbol{c}) \, dx \tag{4.2}$$

with fixed interface parameter $\varepsilon > 0$. Here we concentrate on a quadratic interfacial energy and a multi-phase version of the well-known logarithmic free energy (2.5),(2.4) (cf. [5, 16]). More precisely, $\Psi = \Psi_\theta$ is given by

$$\Psi_\theta(\boldsymbol{r}) = \Phi_\theta(\boldsymbol{r}) + \chi_{V_1}(\boldsymbol{r}) + \tfrac{1}{2} \langle K\boldsymbol{r}, \boldsymbol{r} \rangle \tag{4.3}$$

with the convex function

$$\Phi_\theta(\boldsymbol{r}) = \sum_{i=1}^N \theta r_i \ln(r_i) + \sum_{i=1}^N \chi_{[0,\infty)}(r_i) \tag{4.4}$$

and a symmetric interaction matrix $K = (K_{ij})_{i,j=1}^N$ (cf. De Fontaine [51]). Here, as before θ denotes normalized temperature. Note that in slight abuse of previous notation Φ does not represent the (full) convex part of Ψ in the sense of the splitting (2.2), which would be given here by $\Phi_\theta + \chi_{V_1}$. For $\theta < 1$, we assume that Ψ_θ has exactly N distinct local minima on G, corresponding to dominant components $i = 1, \ldots, N$. For example, this is achieved by choosing the interaction matrix

$$K = N(1 - \delta_{ij})_{i,j=1}^N \qquad \text{(Kronecker-}\delta) \tag{4.5}$$

which means that the interaction of all different components is equal and no self-interaction occurs. In the deep quench limit $\theta = 0$, we then obtain the classical obstacle potential (cf. Blowey & Barrett [6])

$$\Psi_0(\boldsymbol{c}) = \chi_G(\boldsymbol{c}) + \tfrac{N}{2} \sum_{i=1}^N c_i(1 - c_i).$$

For $\theta > 0$ and $N = 2$ the well-known scalar logarithmic free energy given by (2.5),(2.4) for the scalar order parameter $\tilde{c} := c_2 - c_1 \in [-1, 1]$ is recovered up to a constant in this way. In the shallow quench, i.e. for $\theta \approx 1$, polynomial free energies generalizing the quartic potential $(1 - \tilde{c}^2)^2$ provide good approximations of Ψ_θ (cf. Steinbach et al. [115]). As polynomials are defined everywhere, the contributions from the non-differentiable indicator function $\chi_{[0,\infty)}$ are usually skipped in this case.

4.1.2. Vector-valued Cahn–Hilliard Equations

For $\theta > 0$ the multicomponent Cahn–Hilliard system

$$
\begin{aligned}
\boldsymbol{c}_t &= L\Delta \boldsymbol{w}, \\
\boldsymbol{w} &= -\varepsilon^2 \Delta \boldsymbol{c} + P\Psi_\theta'(\boldsymbol{c})
\end{aligned}
\tag{4.6}
$$

is obtained by postulating that $\boldsymbol{c}$ satisfies a conservation law with flux $-L\nabla \boldsymbol{w}$ and $\boldsymbol{w}$ is given by the derivative of the total free energy $\mathcal{E}$ defined in (4.2). In this way, the mass of all components c_i is conserved and (4.6) is thermodynamically consistent in the sense that $\mathcal{E}$ decreases monotonically throughout the evolution. We assume that the matrix L is symmetric and positive semi-definite with one-dimensional kernel spanned by $\mathbf{1} = (1, \ldots, 1)^{\mathsf{T}} \in \mathbb{R}^N$. The latter condition accounts for the fact that $\langle \boldsymbol{c}_t, \mathbf{1} \rangle \equiv 0$ and therefore $\langle \boldsymbol{c}, \mathbf{1} \rangle \equiv \langle \boldsymbol{c}^0, \mathbf{1} \rangle$. For ease of presentation, we concentrate on constant mobilities $L \in \mathbb{R}^{N \times N}$. However, all our algorithms and theoretical considerations to be presented below extend to discretizations of solution dependent mobilities as suggested in [8], where $L = L(\boldsymbol{c})$ is replaced by a suitable constant.

The orthogonal projection

$$
P = \mathsf{Id}_N - \tfrac{1}{N}\mathbf{1}\mathbf{1}^{\mathsf{T}} \in \mathbb{R}^{N \times N},
$$

maps $\mathbb{R}^N$ onto the linear subspace $V_0 = \subset \mathbb{R}^N$ (cf. Eq. (4.1)). It accounts for the fact that admissible variations of $\boldsymbol{c}(x, t) \in V_1$ must be in V_0.

The weak formulation of (4.6) is now given by
Find $\boldsymbol{c} \in L^2(0, T; H^1(\Omega)^N) \cap H^1(0, T; (H^1(\Omega)^N)')$ with the property $\boldsymbol{c}(\cdot, 0) = \boldsymbol{c}^0$, $\boldsymbol{w} \in$

$L^2(0, T; H^1(\Omega)^N)$ such that,

$$\langle \boldsymbol{c}_t, \boldsymbol{v} \rangle + (L \nabla \boldsymbol{w}, \nabla \boldsymbol{v}) = 0 \qquad\qquad \forall \boldsymbol{v} \in H^1(\Omega)^N, \qquad (4.7\text{a})$$

$$\varepsilon^2 (\nabla \boldsymbol{c}, \nabla \boldsymbol{v}) + (P \Phi'_\theta(\boldsymbol{c}), \boldsymbol{v}) + (P K \boldsymbol{c}, \boldsymbol{v}) = (\boldsymbol{w}, \boldsymbol{v}) \qquad \forall \boldsymbol{v} \in H^1(\Omega)^N, \qquad (4.7\text{b})$$

holds a.e. in $(0, T]$.

In the singular deep quench limit $\theta = 0$, the second equation in (4.6) becomes

$$\boldsymbol{w} \in -\varepsilon^2 \Delta \boldsymbol{c} + P \partial \Psi_0(\boldsymbol{c}). \qquad (4.8)$$

We assume that the initial condition $\boldsymbol{c}^0 \in H^1(\Omega)$ satisfies $\boldsymbol{c}^0(x) \in V_1$ for almost all $x \in \Omega$ and the componentwise inequality

$$0 < \frac{1}{|\Omega|} \int_\Omega \boldsymbol{c}^0(x) \, dx < \boldsymbol{1} \qquad (4.9)$$

which means that the given problem is non-degenerate in the sense that exactly N different components are actually occurring. We further impose Neumann boundary conditions for $\boldsymbol{c}$ and $\boldsymbol{w}$ so that mass conservation

$$\int_\Omega \boldsymbol{c}(x, t) \, dx = \int_\Omega \boldsymbol{c}^0(x) \, dx,$$

and

$$(\mathsf{Id} - P) \boldsymbol{c}(x, t) = \tfrac{1}{N} \boldsymbol{1}, \qquad (\mathsf{Id} - P) \boldsymbol{w}(x, t) = 0$$

hold for almost all $x \in \Omega$ and $t > 0$.

On these assumptions, existence and uniqueness was shown by Elliott and Luckhaus [91] for $\theta \geqslant 0$. Note that Garcke's existence and uniqueness result ([52, Theroem 3.1]), which is stated here for the binary case as Theorem 3.1, also covers the vector-valued setting. For sharp interface limits, we refer to Bronsard et al. [89].

4.2. Numerical solution

This section introduces a method for the efficient, reliable, and robust numerical approximation of multicomponent Cahn–Hilliard systems. The presentation follows that

of [64] and extends the corresponding scalar version [66, 61]. Again we will employ Rothe's method and finite elements in conjunction with adaptive mesh refinement for discretization and Nonsmooth Schur–Newton Multigrid methods for the solution of the algebraic problems. However, the simplex constraint $c(x,t) \in G$ requires some extra care.

4.2.1. Discretization

Starting out from a fully discrete system for the case $\theta > 0$ we derive a unified formulation of the spatial problems for all $\theta \geqslant 0$ that incorporates a weak form of the simplex constraint and go on to prove an existence and uniqueness theorem for this system. Adaptive mesh refinement is carried out as in the previous chapters. Note that the hierarchical error estimator is derived exactly as in the scalar case (cf. Section 3.2.2).

Semi-implicit time discretization and finite elements

Let us first consider the case $\theta > 0$. Then time discretization of the weak problem (4.7) by the implicit Euler scheme and subsequent finite element discretization leads to spatial problems of the form

(FI) Find $c_{\mathfrak{T}} \in \mathcal{G}_{\mathfrak{T}}, w_{\mathfrak{T}} \in \mathcal{S}_{\mathfrak{T}}^N$ such that

$$\varepsilon^2 \left(\nabla c_{\mathfrak{T}}, \nabla v \right) + (P\Phi'_\theta(c_{\mathfrak{T}}), v)_{\mathfrak{T}} + (PK c_{\mathfrak{T}}, v) = (w_{\mathfrak{T}}, v) \qquad \forall v \in \mathcal{S}_{\mathfrak{T}}^N,$$

$$(c_{\mathfrak{T}}, v) + \tau \left(L\nabla w_{\mathfrak{T}}, \nabla v \right) = \left(c^{\text{old}}, v \right) \qquad \forall v \in \mathcal{S}_{\mathfrak{T}}^N.$$

Again, $\tau > 0$ denotes the uniform time step size and c^{old} denotes the approximate order parameter in the preceding time step while $c_{\mathfrak{T}}$ and $w_{\mathfrak{T}}$ stand for the finite element approximations of the order parameter and chemical potential in the given time step, respectively. If no confusion is likely in the following we drop the subscript $\mathfrak{T}$ for discrete solutions. The finite element space $\mathcal{S}_{\mathfrak{T}}^N$ is the tensor product of scalar, piecewise affine finite elements as defined in (2.32).

As before, we assume that $\mathfrak{T} = \mathcal{L}(\mathfrak{T}_0, \ldots, \mathfrak{T}_j)$ together with an underlying hierarchy $\mathfrak{T}_0, \ldots, \mathfrak{T}_j$ is obtained by successive adaptive refinements of a conforming, intentionally

coarse partition $\mathfrak{T}_0$. Recall that by $\mathfrak{F}_0^\bullet$ we denote the set of nonhanging vertices, i.e. the nodes that define the nodal basis for a conforming finite element space on $\mathfrak{T}$.

Further we used the closed convex subset

$$\mathcal{G}_\mathfrak{T} = \{ \boldsymbol{v} \in \mathcal{S}_\mathfrak{T}^N \mid \boldsymbol{v}(\mathfrak{p}) \in G \ \ \forall \mathfrak{p} \in \mathfrak{F}_0^\bullet \},$$

and the lumped L^2 scalar product

$$(\boldsymbol{c}, \boldsymbol{v})_\mathfrak{T} = \int_\Omega I_\mathfrak{T}(\langle \boldsymbol{c}(x), \boldsymbol{v}(x) \rangle) \, dx$$

induced by canonical nodal interpolation $I_\mathfrak{T} \boldsymbol{v} = \sum_{\mathfrak{p} \in \mathfrak{F}_0^\bullet} \boldsymbol{v}(\mathfrak{p}) b_\mathfrak{p}$. Note that lumping has been applied only to the nonlinear term $(\Phi'_\theta(\boldsymbol{c}), \boldsymbol{v})$ in order to separate the unknowns associated with different nodes with respect to the nonlinearity. Full lumping, i.e., lumping of all other zero-order terms, is quite common in the literature (cf., e.g. [5, 6, 8, 7, 16]) but is avoided here, because it would destroy either symmetry or mass conservation if the underlying grids have changed from the preceding to the given time step (cf. Section 3.2.2).

All reasoning to be presented below extends a fully lumped version of (FI) as proposed and analyzed by Blowey et al. [16] and Barrett and Blowey [5]. Existence and uniqueness of corresponding discrete solutions has been shown in [16, Theorem 2.4] for the fully lumped version on the time step constraint

$$\tau < 4\varepsilon^2/(\lambda_K^2 \|L\|).$$

Here, λ_K denotes the largest positive eigenvalue of K and $\|L\|$ stands for the spectral norm of L. For example, for K taken as in (4.5) the time step τ has to satisfy $\tau < 4\varepsilon^2/(N^2(N-1)^2 \|L\|)$. In order to avoid such severe stability restrictions, the expanding linear part K of $\Psi'_\theta = \Phi'_\theta + K$ on $\mathcal{G}_\mathfrak{T}$ is often discretized explicitly (cf., e.g., [16, 17, 70, 9]). More precisely, $PK\boldsymbol{c}$ is replaced by $K\boldsymbol{c}^{\text{old}} + (P - \mathsf{Id})K\boldsymbol{c}$ providing the unconditionally stable semi-implicit scheme

(SI) Find $\boldsymbol{c} \in \mathcal{G}_\mathfrak{T}, \boldsymbol{w} \in \mathcal{S}_\mathfrak{T}^N$ such that

$$\varepsilon^2 (\nabla \boldsymbol{c}, \nabla \boldsymbol{v}) + (P\Phi'_\theta(\boldsymbol{c}), \boldsymbol{v})_\mathfrak{T} + (K\boldsymbol{c}^{\text{old}} + (P - \mathsf{Id})K\boldsymbol{c}, \boldsymbol{v}) = (\boldsymbol{w}, \boldsymbol{v}) \qquad \forall \boldsymbol{v} \in \mathcal{S}_\mathfrak{T}^N,$$
$$(\boldsymbol{c}, \boldsymbol{v}) + \tau (L\nabla \boldsymbol{w}, \nabla \boldsymbol{v}) = (\boldsymbol{c}^{\text{old}}, \boldsymbol{v}) \qquad \forall \boldsymbol{v} \in \mathcal{S}_\mathfrak{T}^N.$$

By construction $\boldsymbol{c}(\mathfrak{p}) \in G \; \forall \mathfrak{p} \in \mathfrak{F}_0^\bullet$. Orthogonality of P with respect to the Euclidean scalar product immediately provides $(\mathsf{Id} - P)\boldsymbol{w} \equiv 0$ for the fully implicit discretization (FI). For the semi-implicit version (SI), testing with $\boldsymbol{v} = b_\mathfrak{p}\boldsymbol{1}$ and a short calculation shows

$$\left(\langle \boldsymbol{w}, \boldsymbol{1}\rangle, b_\mathfrak{p}\right) = \left(\langle K(\boldsymbol{c}^{\mathrm{old}} - \boldsymbol{c}), \boldsymbol{1}\rangle, b_\mathfrak{p}\right). \tag{4.10}$$

Hence $(\mathsf{Id} - P)\boldsymbol{w} \equiv 0$ is no longer true in general but only holds in special cases, e.g. for the choice (4.5) of K.

Unified formulation of spatial problems for $\theta \geqslant 0$

The occurrence of P in the projected derivative $P\Phi'_\theta(\cdot)$ in the discretizations (FI) and (SI) prevents a direct reformulation as a variational inequality that would allow to pass to the deep quench limit $\theta = 0$. Utilizing $(\mathsf{Id} - P)\boldsymbol{w} \equiv 0$, such a formulation can be easily obtained for the fully implicit version (FI). We therefore concentrate on the semi-implicit variant and first introduce the (affine) subspaces

$$\mathcal{V}_{r,\mathfrak{T}} = \{\boldsymbol{v} \in \mathcal{S}_\mathfrak{T}^N \mid \boldsymbol{v}(\mathfrak{p}) \in V_r \; \forall \mathfrak{p} \in \mathfrak{F}_0^\bullet\}, \qquad r \in \{0, 1\}$$

and the lumped nonlinear functional $\phi_\mathfrak{T}^\theta$, defined analogously to (2.33)

$$\phi_\mathfrak{T}^\theta(\boldsymbol{v}) = \int_\Omega I_\mathfrak{T}\big(\Phi_\theta(\boldsymbol{v})\big)\, dx.$$

Using the reduced test space $\mathcal{V}_{0,\mathfrak{T}} \subset \mathcal{S}_\mathfrak{T}^N$ in the first equation of (SI), we obtain

$$\varepsilon^2 \left(\nabla \boldsymbol{c}, \nabla \boldsymbol{v}\right) + \left(\Phi'_\theta(\boldsymbol{c}), \boldsymbol{v}\right)_\mathfrak{T} + \left(K\boldsymbol{c}^{\mathrm{old}}, \boldsymbol{v}\right) = (\boldsymbol{w}_0, \boldsymbol{v}) \qquad \forall \boldsymbol{v} \in \mathcal{V}_{0,\mathfrak{T}}$$

with the new variable $\boldsymbol{w}_0 = P\boldsymbol{w} \in \mathcal{V}_{0,\mathfrak{T}}$. We now rewrite this equation as a variational inequality and use the reduced test space $\mathcal{V}_{0,\mathfrak{T}} \subset \mathcal{S}_\mathfrak{T}^N$ in the second equation of (SI) to obtain

($\widehat{\text{VI}}$) Find $\boldsymbol{c} \in \mathcal{V}_{1,\mathfrak{T}}, \boldsymbol{w}_0 \in \mathcal{V}_{0,\mathfrak{T}}$ such that

$$\varepsilon^2 \left(\nabla \boldsymbol{c}, \nabla(\boldsymbol{v} - \boldsymbol{c}) \right) + \phi_{\mathfrak{T}}^{\theta}(\boldsymbol{v}) - \phi_{\mathfrak{T}}^{\theta}(\boldsymbol{c})$$

$$- (\boldsymbol{w}_0, \boldsymbol{v} - \boldsymbol{c}) \geqslant - \left(K \boldsymbol{c}^{\text{old}}, \boldsymbol{v} - \boldsymbol{c} \right) \qquad \forall \boldsymbol{v} \in \mathcal{V}_{1,\mathfrak{T}},$$

$$(\boldsymbol{c}, \boldsymbol{v}) + \tau \left(L \nabla \boldsymbol{w}_0, \nabla \boldsymbol{v} \right) = \left(\boldsymbol{c}^{\text{old}}, \boldsymbol{v} \right) \qquad \forall \boldsymbol{v} \in \mathcal{V}_{0,\mathfrak{T}}.$$

The variational problem ($\widehat{\text{VI}}$) has the advantage that it allows for a straightforward extension to the deep quench limit $\theta = 0$. In this case, $\phi_{\mathfrak{T}}^{0}$ just accounts for the inequality constraints $c_i \geqslant 0$. For positive temperature, the variational formulation ($\widehat{\text{VI}}$) is equivalent to (SI) in the following sense.

Proposition 4.1. *Let $\theta > 0$. If $(\boldsymbol{c}, \boldsymbol{w})$ is a solution of (SI) then $(\boldsymbol{c}, P\boldsymbol{w})$ is a solution of ($\widehat{\text{VI}}$), and if $(\boldsymbol{c}, \boldsymbol{w}_0)$ is a solution of ($\widehat{\text{VI}}$), then there is a solution $(\boldsymbol{c}, \boldsymbol{w})$ of (SI) with $\boldsymbol{w}_0 = P\boldsymbol{w}$.*

Proof. Let $(\boldsymbol{c}, \boldsymbol{w})$ be a solution of (SI). Then $(\boldsymbol{c}, P\boldsymbol{w})$ is a solution of ($\widehat{\text{VI}}$) by construction.

Now let $(\boldsymbol{c}, \boldsymbol{w}_0)$ be a solution of ($\widehat{\text{VI}}$). Then we use the decomposition

$$\boldsymbol{v} = P\boldsymbol{v} + (\mathsf{Id} - P)\boldsymbol{v} = \boldsymbol{v}_0 + v_1 \mathbf{1}, \quad \boldsymbol{v}_0 = P\boldsymbol{v} \in \mathcal{V}_{0,\mathfrak{T}}, \quad v_1 = \tfrac{1}{N} \langle \boldsymbol{v}, \mathbf{1} \rangle$$

of all $\boldsymbol{v} \in \mathcal{S}_{\mathfrak{T}}^{N}$ to define (cf. (4.10))

$$\boldsymbol{w} = \boldsymbol{w}_0 + w_1 \mathbf{1}, \qquad (w_1, b_{\mathfrak{p}}) = \tfrac{1}{N} \left(\langle K(\boldsymbol{c}^{\text{old}} - \boldsymbol{c}), \mathbf{1} \rangle, b_{\mathfrak{p}} \right) \quad \forall \mathfrak{p} \in \mathfrak{F}_0^{\bullet}.$$

Note that $\boldsymbol{w}$ is well defined because the mass matrix $\left((b_{\mathfrak{p}}, b_{\mathfrak{q}}) \right)_{\mathfrak{p},\mathfrak{q} \in \mathfrak{F}_0^{\bullet}}$ is invertible. Now, exploiting the orthogonality of P and the properties of L, it is easily checked that $\boldsymbol{c}$, $\boldsymbol{w}$ solve (SI). $\qquad\qquad \square$

Weak formulation of affine constraints

In order to simplify the algebraic solution, we now derive a version of (SI) that incorporates the affine constraints $\langle \boldsymbol{c}(\mathfrak{p}), \mathbf{1} \rangle = 1$ in the weak form

$$(\boldsymbol{c}, \mathbf{1} v) = (\langle \boldsymbol{c}, \mathbf{1} \rangle, v) = (1, v) \qquad\qquad \forall v \in \mathcal{S}_{\mathfrak{T}} \qquad\qquad (4.11)$$

and not in the strong form $\boldsymbol{c} \in \mathcal{V}_{1,\mathfrak{T}}$. Introducing the Lagrange multiplier $\mathbf{1}\eta \in \mathcal{S}_{\mathfrak{T}}^{N}$ associated with (4.11), the solution of $(\widehat{\text{VI}})$ amounts to find $\boldsymbol{c} \in \mathcal{S}_{\mathfrak{T}}^{N}$, $\boldsymbol{w}_0 \in \mathcal{V}_{0,\mathfrak{T}}$, $\eta \in \mathcal{S}_{\mathfrak{T}}$ such that

$$
\begin{aligned}
\varepsilon^2 \left(\nabla \boldsymbol{c}, \nabla(\boldsymbol{v} - \boldsymbol{c})\right) + \phi_{\mathfrak{T}}^{\theta}(\boldsymbol{v}) - \phi_{\mathfrak{T}}^{\theta}(\boldsymbol{c}) & \\
- \left(\boldsymbol{w}_0 + \mathbf{1}\eta, \boldsymbol{v} - \boldsymbol{c}\right) &\geqslant - \left(K\boldsymbol{c}^{\text{old}}, \boldsymbol{v} - \boldsymbol{c}\right) & \forall \boldsymbol{v} \in \mathcal{S}_{\mathfrak{T}}^{N}, \\
- (\boldsymbol{c}, \boldsymbol{v}) - \tau \left(L\nabla \boldsymbol{w}_0, \nabla \boldsymbol{v}\right) &= - \left(\boldsymbol{c}^{\text{old}}, \boldsymbol{v}\right) & \forall \boldsymbol{v} \in \mathcal{V}_{0,\mathfrak{T}} \\
- (\boldsymbol{c}, \mathbf{1}v) &= - \left(\boldsymbol{c}^{\text{old}}, \mathbf{1}v\right) & \forall v \in \mathcal{S}_{\mathfrak{T}}.
\end{aligned}
$$

For the deep quench limit $\theta = 0$ a fully implicit and fully lumped version of this discretization has been suggested and analyzed by Barrett and Blowey [6].

Introducing the new variable $\tilde{\boldsymbol{w}} = \boldsymbol{w}_0 + \mathbf{1}\eta$, adding the last two equations, and using $L\mathbf{1} = 0$, we see that this problem is equivalent to finding $\boldsymbol{c} \in \mathcal{S}_{\mathfrak{T}}^{N}$, $\tilde{\boldsymbol{w}} \in \mathcal{S}_{\mathfrak{T}}^{N}$ such that

$$
\begin{aligned}
\varepsilon^2 \left(\nabla \boldsymbol{c}, \nabla(\boldsymbol{v} - \boldsymbol{c})\right) + \phi_{\mathfrak{T}}^{\theta}(\boldsymbol{v}) - \phi_{\mathfrak{T}}^{\theta}(\boldsymbol{c}) & \\
- \left(\tilde{\boldsymbol{w}}, \boldsymbol{v} - \boldsymbol{c}\right) &\geqslant - \left(K\boldsymbol{c}^{\text{old}}, \boldsymbol{v} - \boldsymbol{c}\right) & \forall \boldsymbol{v} \in \mathcal{S}_{\mathfrak{T}}^{N}, \\
- (\boldsymbol{c}, \boldsymbol{v}) - \tau \left(L\nabla \tilde{\boldsymbol{w}}, \nabla \boldsymbol{v}\right) &= - \left(\boldsymbol{c}^{\text{old}}, \boldsymbol{v}\right) & \forall \boldsymbol{v} \in \mathcal{S}_{\mathfrak{T}}^{N}.
\end{aligned}
$$

In the final step, we enforce coercivity of the primal operator by exploiting mass conservation

$$
\int_{\Omega} c_i(x)\, dx = \int_{\Omega} c_i^{\text{old}}(x)\, dx.
$$

in a similar way as introduced in [60, 66, 63]. More precisely, we add the identity

$$
\varepsilon^2 \left\langle \int_{\Omega} \boldsymbol{c}\, dx, \int_{\Omega} \boldsymbol{v} - \boldsymbol{c}\, dx \right\rangle = \varepsilon^2 \left\langle \int_{\Omega} \boldsymbol{c}^{\text{old}}\, dx, \int_{\Omega} \boldsymbol{v} - \boldsymbol{c}\, dx \right\rangle \qquad \forall \boldsymbol{v} \in \mathcal{S}_{\mathfrak{T}}^{N}.
$$

to the variational inequality above, to obtain the final form of the spatial problem

(VI) Find $(\boldsymbol{c}, \boldsymbol{w}) \in \mathcal{S}_{\mathfrak{T}}^N \times \mathcal{S}_{\mathfrak{T}}^N$ such that

$$\varepsilon^2 \left(\nabla \boldsymbol{c}, \nabla(\boldsymbol{v} - \boldsymbol{c})\right) + \varepsilon^2 \left\langle \int_\Omega \boldsymbol{c} \, dx, \int_\Omega \boldsymbol{v} - \boldsymbol{c} \, dx \right\rangle + \phi_{\mathfrak{T}}^\theta(\boldsymbol{v}) - \phi_{\mathfrak{T}}^\theta(\boldsymbol{c})$$

$$- (\boldsymbol{w}, \boldsymbol{v} - \boldsymbol{c}) \geqslant \varepsilon^2 \left\langle \int_\Omega \boldsymbol{c}^{\mathrm{old}} \, dx, \int_\Omega \boldsymbol{v} - \boldsymbol{c} \, dx \right\rangle - \left(K \boldsymbol{c}^{\mathrm{old}}, \boldsymbol{v} - \boldsymbol{c}\right) \quad \forall \boldsymbol{v} \in \mathcal{S}_{\mathfrak{T}}^N,$$

$$- (\boldsymbol{c}, \boldsymbol{v}) - \tau \left(L \nabla \boldsymbol{w}, \nabla \boldsymbol{v}\right) = - \left(\boldsymbol{c}^{\mathrm{old}}, \boldsymbol{v}\right) \qquad \forall \boldsymbol{v} \in \mathcal{S}_{\mathfrak{T}}^N.$$

In the light of the above considerations and Proposition 4.1, the formulations (SI) and (VI) are equivalent for positive temperature in the following sense.

Proposition 4.2. *Let $\theta > 0$. If $(\boldsymbol{c}, \boldsymbol{w})$ is a solution of (SI) then there is a solution $(\boldsymbol{c}, \tilde{\boldsymbol{w}})$ of (VI) satisfying $P\boldsymbol{w} = P\tilde{\boldsymbol{w}}$ and vice versa.*

The common idea behind the above reformulations is to use the part $(\mathsf{Id} - P)\boldsymbol{w} \in \mathcal{S}_{\mathfrak{T}}$ as a kind of dustbin, e.g., for the Lagrange multiplier in $\eta \in \mathcal{S}_{\mathfrak{T}}$.

Existence and uniqueness of discrete solutions

Analogously to the scalar case (cf. Section 3.2) the variational problem (VI) is equivalent to a saddle point problem for the Lagrangian

$$\mathcal{L}(\boldsymbol{v}, \boldsymbol{z}) = \mathcal{J}(\boldsymbol{v}) + \left(\boldsymbol{c}^{\mathrm{old}} - \boldsymbol{v}, \boldsymbol{z}\right) - \frac{\tau}{2} \left(L \nabla \boldsymbol{z}, \nabla \boldsymbol{z}\right)$$

to find $(\boldsymbol{c}, \boldsymbol{w}) \in \mathcal{S}_{\mathfrak{T}}^N \times \mathcal{S}_{\mathfrak{T}}^N$ such that

$$\mathcal{L}(\boldsymbol{c}, \boldsymbol{w}) = \inf_{\boldsymbol{v} \in \mathcal{S}_{\mathfrak{T}}^N} \sup_{\boldsymbol{z} \in \mathcal{S}_{\mathfrak{T}}^N} \mathcal{L}(\boldsymbol{v}, \boldsymbol{z}) \tag{4.12}$$

This involves the coercive, convex, lower semi-continuous energy functional

$$\mathcal{J}(\boldsymbol{v}) = \frac{\varepsilon^2}{2} \left(\nabla \boldsymbol{v}, \nabla \boldsymbol{v}\right) + \frac{\varepsilon^2}{2} \left| \int_\Omega \boldsymbol{v} - \boldsymbol{c}^{\mathrm{old}} \, dx \right|^2 + \phi_{\mathfrak{T}}^\theta(\boldsymbol{v}) + \left(K \boldsymbol{c}^{\mathrm{old}}, \boldsymbol{v}\right).$$

The Lagrangian $\mathcal{L}$ has finite values on the closed, convex set

$$\mathrm{dom}(\mathcal{J}) \times \mathcal{S}_{\mathfrak{T}}^N = \{\boldsymbol{v} \in \mathcal{S}_{\mathfrak{T}}^N \mid \forall_{i \in \{1 \dots N\}} v_i \geqslant 0\} \times \mathcal{S}_{\mathfrak{T}}^N.$$

4. Multicomponent Cahn–Hilliard systems

The proof of existence of discrete solutions to (4.12) was given in [64] and is based on the same ideas as in the scalar case (cf. e.g. 3.2.2) but requires a little more care in the details, which is why we repeat it here despite a certain redundancy. As before the key ingredient of the proof is the following result.

Lemma 4.3. *The functional $h = -\inf_{\boldsymbol{v} \in \mathsf{dom}(\mathcal{J})} \mathcal{L}(\boldsymbol{v}, \cdot)$ is coercive on $\mathcal{S}_{\mathfrak{T}}^N$.*

Proof. Let $\boldsymbol{z} \in \mathcal{S}_{\mathfrak{T}}^N$ be arbitrary and define a corresponding $\boldsymbol{v}_0 = \boldsymbol{v}^{(1)} + \boldsymbol{v}^{(2)} \in \mathcal{S}_{\mathfrak{T}}^N$ with $\boldsymbol{v}^{(1)}, \boldsymbol{v}^{(2)} \in \mathcal{S}_{\mathfrak{T}}^N$ given by the nodal values

$$\boldsymbol{v}^{(1)}(\mathfrak{p}) = \tfrac{1}{2}\big(1 + \mathsf{sgn}(\boldsymbol{z}^{(1)})\big), \qquad \boldsymbol{v}^{(2)}(\mathfrak{p}) = \rho\big(1 + \mathsf{sgn}(\langle \mathbf{1}, \boldsymbol{z}(\mathfrak{p})\rangle)\big)\mathbf{1}, \qquad \forall \mathfrak{p} \in \mathfrak{F}_0^\bullet.$$

Here we have used the componentwise mean value of $\boldsymbol{z}$,

$$\boldsymbol{z}^{(1)} = |\Omega|^{-1} \int_\Omega \boldsymbol{z} \, dx, \qquad |\Omega| = \int_\Omega dx,$$

and some positive $\rho \in \mathbb{R}$ to be specified later. In the light of

$$-\inf_{\boldsymbol{v} \in \mathsf{dom}(\mathcal{J})} \mathcal{L}(\boldsymbol{v}, \boldsymbol{z}) \geqslant -\mathcal{L}(\boldsymbol{v}_0, \boldsymbol{z}) = -\mathcal{J}(\boldsymbol{v}_0) - (\boldsymbol{c}^{\mathrm{old}} - \boldsymbol{v}_0, \boldsymbol{z}) + \frac{\tau}{2}(L\nabla \boldsymbol{z}, \nabla \boldsymbol{z}) \qquad (4.13)$$

we now derive an upper bound for $(\boldsymbol{c}^{\mathrm{old}} - \boldsymbol{v}_0, \boldsymbol{z})$. To this end, we first decompose $\boldsymbol{z}$ according to

$$\boldsymbol{z} = \boldsymbol{z}^{(0)} + \boldsymbol{z}^{(1)}, \qquad \boldsymbol{z}^{(0)} = \boldsymbol{z} - \boldsymbol{z}^{(1)} = \boldsymbol{z} - |\Omega|^{-1} \int_\Omega \boldsymbol{z} \, dx.$$

Utilizing $\boldsymbol{c}^{\mathrm{old}}(\mathfrak{p}) \in V_1$ and the definition of $\boldsymbol{z}^{(0)}$ and $\boldsymbol{v}^{(1)}$, we then have

$$(\boldsymbol{c}^{\mathrm{old}}, (\mathsf{Id} - P)\boldsymbol{z}^{(0)}) = \frac{1}{N}(\mathbf{1}, \boldsymbol{z}^{(0)}) = 0 = \rho(\mathbf{1}, \boldsymbol{z}^{(0)}), \qquad (\boldsymbol{v}^{(1)}, \boldsymbol{z}^{(0)}) = 0.$$

These identities and the properties of P provide

$$\begin{aligned}
(\boldsymbol{c}^{\mathrm{old}} - \boldsymbol{v}_0, \boldsymbol{z}) &= (\boldsymbol{c}^{\mathrm{old}}, P\boldsymbol{z}^{(0)}) + (\boldsymbol{c}^{\mathrm{old}}, (\mathsf{Id} - P)\boldsymbol{z}^{(0)}) - (\boldsymbol{v}_0, \boldsymbol{z}^{(0)}) \\
&\qquad\qquad\qquad + (\boldsymbol{c}^{\mathrm{old}} - \boldsymbol{v}^{(1)}, \boldsymbol{z}^{(1)}) - (\boldsymbol{v}^{(2)}, \boldsymbol{z}^{(1)}) \\
&= (\boldsymbol{c}^{\mathrm{old}}, P\boldsymbol{z}^{(0)}) + (\rho\mathbf{1}, \boldsymbol{z}^{(0)}) + (\boldsymbol{c}^{\mathrm{old}} - \boldsymbol{v}^{(1)}, \boldsymbol{z}^{(1)}) - (\boldsymbol{v}^{(2)}, \boldsymbol{z}) \\
&= (\boldsymbol{c}^{\mathrm{old}}, P\boldsymbol{z}^{(0)}) + (\boldsymbol{c}^{\mathrm{old}} - \rho\mathbf{1} - \boldsymbol{v}^{(1)}, \boldsymbol{z}^{(1)}) + (\rho\mathbf{1} - \boldsymbol{v}^{(2)}, \boldsymbol{z}).
\end{aligned}$$

Using the Poincaré inequality, the first term can be estimated by

$$\left(\boldsymbol{c}^{\text{old}}, P\boldsymbol{z}^{(0)}\right) \leqslant \left\|\boldsymbol{c}^{\text{old}}\right\|_0 \left\|P\boldsymbol{z}^{(0)}\right\|_0 \leqslant \Lambda_0 \left|P\boldsymbol{z}^{(0)}\right|_1 = \Lambda_0 \left|P\boldsymbol{z}\right|_1 \qquad (4.14)$$

with Λ_0 independent of $\boldsymbol{z}$. In order to estimate the second term, we now select

$$\rho = \frac{1}{2|\Omega|} \min_{i=1,\ldots,N} \int_\Omega c_i^{\text{old}}\, dx > 0$$

and set $\mu_i = |\Omega|^{-1} \int_\Omega c_i^{\text{old}} - \rho\, dx$. Note that $0 < \mu_i < 1$. Investigating the three cases $\boldsymbol{v}_i^{(1)} \in \{0, \frac{1}{2}, 1\}$, using the equivalence of norms on $\mathbb{R}^N$, and that the orthogonal projection has unit norm, we obtain

$$\left(\boldsymbol{c}^{\text{old}} - \rho\boldsymbol{1} - \boldsymbol{v}, \boldsymbol{z}^{(1)}\right) = \sum_{i=1}^N (\mu_i - v_i^{(1)}) \int_\Omega z_i\, dx = -\sum_{i=1}^N |\mu_i - v_i^{(1)}| \left|\int_\Omega z_i\, dx\right|$$

$$\leqslant -\lambda_0 \sum_{i=1}^N \left|\int_\Omega z_i\, dx\right| \leqslant -\lambda_0 \sqrt{N} \left|\int_\Omega \boldsymbol{z}\, dx\right| \leqslant -\lambda_0 \sqrt{N} \left|\int_\Omega P\boldsymbol{z}\, dx\right|$$

Here, λ_0 is defined by

$$\lambda_0 = \min_{\substack{i=1,\ldots,N \\ z_i^{(1)} \neq 0}} |\mu_i - v_i^{(1)}| > 0$$

if there is at least one i such that $\boldsymbol{z}_i^{(1)} = |\Omega|^{-1}|\int_\Omega z_i\, dx| \neq 0$ and $\lambda_0 = 1$ otherwise. In order to treat the third term $\left(\rho\boldsymbol{1} - \boldsymbol{v}^{(2)}, \boldsymbol{z}\right)$, we utilize the identities

$$\left\langle (\rho\boldsymbol{1} - \boldsymbol{v}^{(2)}(\mathfrak{p})), \boldsymbol{z}(\mathfrak{p})\right\rangle = -\rho\, \mathsf{sgn}(\langle \boldsymbol{1}, \boldsymbol{z}(\mathfrak{p})\rangle) \langle \boldsymbol{1}, (\mathsf{Id} - P)\boldsymbol{z}(\mathfrak{p})\rangle = -\rho| \langle \boldsymbol{1}, \boldsymbol{z}(\mathfrak{p})\rangle |$$

$$|(\mathsf{Id} - P)\boldsymbol{z}(\mathfrak{p})| = \frac{1}{\sqrt{N}}| \langle \boldsymbol{1}, \boldsymbol{z}(\mathfrak{p})\rangle |$$

to obtain

$$\left(\rho\boldsymbol{1} - \boldsymbol{v}^{(2)}, \boldsymbol{z}\right) = -\rho \int_\Omega | \langle \boldsymbol{1}, \boldsymbol{z}\rangle |\, dx = -\rho\sqrt{N} \int_\Omega |(\mathsf{Id} - P)\boldsymbol{z}|\, dx.$$

Inserting these three estimates and the identity $(L\nabla\boldsymbol{z}, \nabla\boldsymbol{z}) = |P\boldsymbol{z}|_1^2$ into (4.13), we have

$$-\mathcal{L}(\boldsymbol{v}_0, \boldsymbol{z}) \geqslant \Lambda \left(|P\boldsymbol{z}|_1^2 - |P\boldsymbol{z}|_1 + \left|\int_\Omega P\boldsymbol{z}\, dx\right| + \int_\Omega |(\mathsf{Id} - P)\boldsymbol{z}|\, dx - 1\right) \qquad (4.15)$$

with a constant Λ independent of $\boldsymbol{z}$. In order to show that the right hand side of this

inequality tends to infinity, if (a suitable norm of) $\boldsymbol{z}$ tends to infinity, observe that Poincaré's inequality yields

$$|P\boldsymbol{z}|_1^2 - |P\boldsymbol{z}|_1 + \left|\int_\Omega P\boldsymbol{z}\,dx\right| \geqslant |P\boldsymbol{z}|_1 + \left|\int_\Omega P\boldsymbol{z}\,dx\right| - 1$$

$$\geqslant \lambda\left(|P\boldsymbol{z}|_1 + \|P\boldsymbol{z}\|_0 - 1\right) \geqslant \lambda(\|P\boldsymbol{z}\|_1 - 1)$$

with positive λ independent of $\boldsymbol{z}$. Inserting this estimate into (4.15), we finally get

$$-\mathcal{L}(\boldsymbol{v}_0, \boldsymbol{z}) \geqslant \Lambda\left(\|P\boldsymbol{z}\|_1 + \int_\Omega |(\mathsf{Id} - P)\boldsymbol{z}| - 1\right). \tag{4.16}$$

with a constant Λ independent of $\boldsymbol{z}$. This concludes the proof. $\qquad\square$

Now we are ready to show existence and uniqueness. Here, the condition

$$0 < \int_\Omega \boldsymbol{c}^{old}\,dx. \tag{4.17}$$

follows from the non-degeneracy condition (4.9) by componentwise mass conservation of (VI).

Theorem 4.4. *Assume that $\boldsymbol{c}^{old}$ satisfies the non-degeneracy condition (4.17). Then (VI) has a solution $(\boldsymbol{c}, \boldsymbol{w})$.*

Proof. Later, we will show in Proposition 4.10 that (i) the functional h defined in Lemma 4.3 is convex, continuous, and finite and (ii) that minimizing h over $\mathcal{S}_{\mathfrak{X}}^N$ is equivalent to (VI). Hence existence of a minimizer $\boldsymbol{w}$ of h and thus of a solution $(\boldsymbol{c}, \boldsymbol{w})$ of (VI) follows from convexity and continuity stated in Proposition 4.10 together with coercivity stated in Lemma 4.3, see, e.g., [45, Chapter II, Proposition 1.2]. $\qquad\square$

An important feature of (VI) is that it provides a unified formulation for $\theta > 0$ and $\theta = 0$. The following results show that (VI) is robust in the sense that solutions $(\boldsymbol{c}, \boldsymbol{w})$ depend continuously on θ for all $\theta \geqslant 0$.

Theorem 4.5. *Assume that $\boldsymbol{c}^{old}$ satisfies the non-degeneracy condition (4.17) and let $(\boldsymbol{c}, \boldsymbol{w})$ be a solution of (VI). Then $\boldsymbol{c}$ and $\nabla P\boldsymbol{w}$ depend Hölder continuously on θ with Hölder exponent 0.5 and a constant only depending on Ω and L. Particularly, $\boldsymbol{c}$ and $\nabla P\boldsymbol{w}$ are unique for each $\theta \geqslant 0$.*

Proof. Let $(\boldsymbol{c}^1, \boldsymbol{w}^1) \in \mathcal{S}_{\mathfrak{T}}^N \times \mathcal{S}_{\mathfrak{T}}^N$ and $(\boldsymbol{c}^2, \boldsymbol{w}^2) \in \mathcal{S}_{\mathfrak{T}}^N \times \mathcal{S}_{\mathfrak{T}}^N$ be solutions of (VI) for $\theta_1 \geqslant 0$ and $\theta_2 \geqslant 0$, respectively. Testing the variational inequalities for $(\boldsymbol{c}^1, \boldsymbol{w}^1)$ with $\boldsymbol{c}^2$ and vice versa and adding the inequalities yields

$$\varepsilon^2 |\boldsymbol{c}^1 - \boldsymbol{c}^2|_1^2 + \varepsilon^2 \left| \int_\Omega \boldsymbol{c}^1 - \boldsymbol{c}^2 \, dx \right|^2 + \left(\boldsymbol{w}^1 - \boldsymbol{w}^2, \boldsymbol{c}^2 - \boldsymbol{c}^1 \right)$$
$$\leqslant \phi_{\theta_1}^{\mathfrak{T}}(\boldsymbol{c}^2) - \phi_{\theta_1}^{\mathfrak{T}}(\boldsymbol{c}^1) + \phi_{\theta_2}^{\mathfrak{T}}(\boldsymbol{c}^1) - \phi_{\theta_2}^{\mathfrak{T}}(\boldsymbol{c}^2). \quad (4.18)$$

Similarly testing the variational equation with $\boldsymbol{w}^1 - \boldsymbol{w}^2$ yields

$$\left(\boldsymbol{c}^1 - \boldsymbol{c}^2, \boldsymbol{w}^1 - \boldsymbol{w}^2 \right) + \tau \left(L\nabla(\boldsymbol{w}^1 - \boldsymbol{w}^2), \nabla(\boldsymbol{w}^1 - \boldsymbol{w}^2) \right) = 0.$$

Inserting this in (4.18) and using the Poincaré inequality, properties of L, the definition of Φ_θ, and boundedness $-\frac{1}{e} \leqslant \Phi_1 \leqslant 0$ on $[0, 1]$ then gives

$$\varepsilon^2 \left\| \boldsymbol{c}^1 - \boldsymbol{c}^2 \right\|_1^2 + \tau |P(\boldsymbol{w}^1 - \boldsymbol{w}^2)|_1^2$$
$$\leqslant \Lambda \left(\phi_{\theta_1}^{\mathfrak{T}}(\boldsymbol{c}^2) - \phi_{\theta_1}^{\mathfrak{T}}(\boldsymbol{c}^1) + \phi_{\theta_2}^{\mathfrak{T}}(\boldsymbol{c}^1) - \phi_{\theta_2}^{\mathfrak{T}}(\boldsymbol{c}^2) \right)$$
$$= \Lambda(\theta_1 - \theta_2) \left(\phi_1^{\mathfrak{T}}(\boldsymbol{c}^2) - \phi_1^{\mathfrak{T}}(\boldsymbol{c}^1) \right) \leqslant \Lambda \frac{N|\Omega|}{e} |\theta_1 - \theta_2|$$

with Λ being the maximum of the Poincaré constant and the smallest nonzero eigenvalue of L. Using $\theta_1 = \theta_2$ shows uniqueness of $\boldsymbol{c}$ and $\nabla P\boldsymbol{w}$. $\qquad\square$

For the chemical potential $\boldsymbol{w}$ uniqueness and continuous dependence on θ are available on additional conditions.

Theorem 4.6. *Denote by $(\boldsymbol{c}^\theta, \boldsymbol{w}^\theta)$ a solution of (VI) for $\theta \geqslant 0$. In addition to the non-degeneracy condition (4.17) of Theorem 4.5, assume that for some fixed $\theta_0 \geqslant 0$ there is a subset*

$$\mathcal{B} = \{\eta_{i,j} = e^i - e^j \mid i \neq j \text{ and } \exists \mathfrak{p} \in \mathfrak{F}_0^\bullet : \ c_i^{\theta_0}(\mathfrak{p}), c_j^{\theta_0}(\mathfrak{p}) > 0\} \subset V_0 \qquad (4.19)$$

such that $\text{span } \mathcal{B} = V_0$. *Then there is a relatively open neighborhood of θ_0 in $\mathbb{R}_0^+$ where $(\boldsymbol{c}^\theta, \boldsymbol{w}^\theta)$ is unique and depends continuously on θ.*

Proof. By continuity of $\theta \mapsto \boldsymbol{c}^\theta$ there is a relatively open neighborhood U of θ_0 in $\mathbb{R}_0^+$ and $\alpha > 0$ such that for all $\eta_{i,j} \in \mathcal{B}$ there is a $\mathfrak{p} \in \mathfrak{F}_0^\bullet$ with $c_i^\theta(\mathfrak{p}), c_j^\theta(\mathfrak{p}) \geqslant \alpha > 0$ for all

4. Multicomponent Cahn–Hilliard systems

$\theta \in U$. To show continuity of $\theta \mapsto \boldsymbol{w}^\theta$ in U let (in abuse of notation) $\theta_0 \in U$ be arbitrary and fixed and $\theta \in U$ arbitrary.

First we show $P\boldsymbol{w}^\theta \to P\boldsymbol{w}^{\theta_0}$ as $\theta \to \theta_0$. To this end, we consider some arbitrary $\eta_{i,j} \in \mathcal{B}$ with associated vertex $\mathfrak{p} \in \mathfrak{F}_0^\bullet$ such that $c_i^\theta(\mathfrak{p}), c_j^\theta(\mathfrak{p}) \geqslant \alpha > 0$ for all $\theta \in U$. Then $\boldsymbol{v}_\pm^\theta = \boldsymbol{c}^\theta \pm \delta \boldsymbol{v} \geqslant 0$ with $\boldsymbol{v} = \eta_{i,j} b_\mathfrak{p}$ holds for $\delta < \alpha$ and all $\theta \in U$. Testing the variational inequality for θ with $\boldsymbol{v}_+^\theta$ and for θ_0 with $\boldsymbol{v}_-^{\theta_0}$, adding both, and dividing by δ yields

$$
\begin{aligned}
\left(\boldsymbol{w}^\theta - \boldsymbol{w}^{\theta_0}, \boldsymbol{v}\right) &\leqslant \varepsilon^2 \left(\nabla(\boldsymbol{c}^\theta - \boldsymbol{c}^{\theta_0}), \nabla \boldsymbol{v}\right) + \varepsilon^2 \left\langle \int_\Omega \boldsymbol{c}^\theta - \boldsymbol{c}^{\theta_0} \, dx, \int_\Omega \boldsymbol{v} \, dx \right\rangle \\
&\quad + \theta \frac{\phi_{\mathfrak{T}}^1(\boldsymbol{c}^\theta + \delta \boldsymbol{v}) - \phi_{\mathfrak{T}}^1(\boldsymbol{c}^\theta)}{\delta} - \theta_0 \frac{\phi_{\mathfrak{T}}^1(\boldsymbol{c}^{\theta_0}) - \phi_{\mathfrak{T}}^1(\boldsymbol{c}^{\theta_0} - \delta \boldsymbol{v})}{\delta}.
\end{aligned}
$$

As $c_i^\theta(\mathfrak{p}), c_j^\theta(\mathfrak{p}), c_i^{\theta^0}(\mathfrak{p}), c_j^{\theta_0}(\mathfrak{p}) > 0$, the scalar functions $\xi \mapsto \phi_{\mathfrak{T}}^\theta(\boldsymbol{c}^\theta + \xi \boldsymbol{v})$ and $\xi \mapsto \phi_{\mathfrak{T}}^\theta(\boldsymbol{c}^{\theta_0} - \xi \boldsymbol{v})$ are differentiable in $\xi = 0$. Hence, we can pass to the limit $\delta = 0$ and use the Hölder continuity of Theorem 4.5 to get

$$
\left(\boldsymbol{w}^\theta - \boldsymbol{w}^{\theta_0}, \boldsymbol{v}\right) \leqslant \Lambda \left(|\theta - \theta_0|^{\frac{1}{2}} \|\boldsymbol{v}\|_1 + \theta \Phi_1'(\boldsymbol{c}^\theta) + \theta_0 \Phi_1'(\boldsymbol{c}^{\theta_0})\right) \xrightarrow[\theta \to \theta_0]{} 0.
$$

Exchanging the role of θ_1 and θ_2 and using $P\boldsymbol{v} = \boldsymbol{v}$ we finally get

$$
\left| \left(\left\langle P(\boldsymbol{w}^\theta - \boldsymbol{w}^{\theta_0}), \eta_{i,j}\right\rangle, b_\mathfrak{p}\right) \right| = \left| \left(\boldsymbol{w}^\theta - \boldsymbol{w}^{\theta_0}, \boldsymbol{v}\right) \right| \xrightarrow[\theta \to \theta_0]{} 0. \tag{4.20}
$$

In combination with $\nabla P(\boldsymbol{w}^\theta - \boldsymbol{w}^{\theta_0}) \to 0$, (4.20) provides $\left\langle P(\boldsymbol{w}^\theta - \boldsymbol{w}^{\theta_0}), \eta_{i,j}\right\rangle \to 0$, since $|\cdot|_1 + \left|(\cdot, b_\mathfrak{p})\right|$ is a norm on $\mathcal{S}_\mathfrak{T}$. As $\eta_{i,j} \in \mathcal{B}$ was arbitrarily chosen, we have shown $P(\boldsymbol{w}^\theta - \boldsymbol{w}^{\theta_0}) \to 0$. This holds for all solutions $\boldsymbol{w}^{\theta_0}$. Hence, $P\boldsymbol{w}^{\theta_0}$ must be unique.

Finally we show $\boldsymbol{w}^\theta \to \boldsymbol{w}^{\theta_0}$ as $\theta \to \theta_0$. To this end, we select for each node $\mathfrak{p} \in \mathfrak{F}_0^\bullet$ some $1 \leqslant i_\mathfrak{p} \leqslant N$ such that $\boldsymbol{c}_{i_\mathfrak{p}}^{\theta_0}(\mathfrak{p}) \geqslant 2\beta > 0$ for some $\beta > 0$. This is possible, because $\left\langle \boldsymbol{c}^{\theta_0}(\mathfrak{p}), \mathbf{1}\right\rangle = 1$ holds for all nodes $\mathfrak{p} \in \mathfrak{F}_0^\bullet$. By continuity of $\theta \mapsto \boldsymbol{c}^\theta$, we also have $\boldsymbol{c}_{i_\mathfrak{p}}^\theta(\mathfrak{p}) \geqslant \beta > 0$ for all $\theta \in U' \subset U$ with a possibly smaller neighborhood U' of θ_0.

For any $\mathfrak{p} \in \mathfrak{F}_0^\bullet$, $\theta \in U'$, and $\delta < \beta$ we then have $\boldsymbol{v}_\pm^\theta = \boldsymbol{c}^\theta \pm \delta \boldsymbol{v} > 0$ with $\boldsymbol{v} = e^{i_\mathfrak{p}} b_\mathfrak{p}$. Proceeding literally as above, we get

$$
\left| \left((\boldsymbol{w}^\theta - \boldsymbol{w}^{\theta_0})_{i_\mathfrak{p}}, b_\mathfrak{p}\right) \right| = \left| \left(\boldsymbol{w}^\theta - \boldsymbol{w}^{\theta_0}, \boldsymbol{v}\right) \right| \xrightarrow[\theta \to \theta_0]{} 0. \tag{4.21}
$$

Since $\boldsymbol{v} \mapsto \|P\boldsymbol{v}\|_1 + \sum_{\mathfrak{p} \in \mathfrak{F}_0^\bullet} \left|(\boldsymbol{v}_{i_\mathfrak{p}}, b_\mathfrak{p})\right|$ is a norm on $\mathcal{S}_\mathfrak{T}^N$, (4.21) in conjunction with

$P(\boldsymbol{w}^\theta - \boldsymbol{w}^{\theta_0}) \to 0$ gives $\boldsymbol{w}^\theta - \boldsymbol{w}^{\theta_0} \to 0$. Again this implies uniqueness of $\boldsymbol{w}^{\theta_0}$. $\qquad\qquad\square$

The assumption on $\mathfrak{F}_0^\bullet$ in Theorem 4.6 essentially means that the discrete interfacial region is rich enough to contain a suitable set of nodal basis functions. This assumption can be replaced by the more instructive, but much stronger condition that at least one of the components that are present at a certain vertex must also be present at each neighboring one. This property can always be achieved by resolving the diffuse interface sufficiently well.

Lemma 4.7. *Assume that for some fixed $\theta_0 \geqslant 0$ the given $\boldsymbol{c}^{old}$ satisfies the non-degeneracy condition* (4.17) *and that for any pair* $(\mathfrak{p}, \mathfrak{q})$ *of neighboring vertices we have*

$$\{1 \leqslant i \leqslant N \mid c_i(\mathfrak{p}) > 0\} \cap \{1 \leqslant i \leqslant N \mid c_i(\mathfrak{q}) > 0\} \neq \varnothing. \qquad (4.22)$$

Then there is a set $\mathcal{B} \subset V_0$ of vertices satisfying the assumption in Theorem 4.6.

Proof. It is sufficient to construct subsets $\mathcal{B}_i$, $i = 1, \ldots, N$, of the form (4.19), i.e.,

$$\mathcal{B}_i = \{\eta_{k,j} \mid \eta_{k,j} = e^k - e^j \text{ with } k \neq j \text{ and } c_k(\mathfrak{p}), c_j(\mathfrak{p}) > 0 \text{ for some } \mathfrak{p} \in \mathfrak{F}_0^\bullet\}$$

such that $e^i - e^1 \in \text{span } \mathcal{B}_i$, because then the vectors $e^i - e^1$, $i = 1, \ldots, N$, spanning V_0, are contained in the span of

$$\mathcal{B} := \bigcup_{i=1}^N \mathcal{B}_i.$$

Let us consider some fixed $i \in \{1, \ldots, N\}$. By the degeneracy condition (4.17) there are vertices $\mathfrak{q}_1$, $\mathfrak{q}_i \in \mathfrak{F}_0^\bullet$ such that $c_1(\mathfrak{q}_1) > 0$, $c_i(\mathfrak{q}_i) > 0$. Since the grid $\mathfrak{T}$ is a connect graph, there is a path $\mathfrak{p}^1, \ldots, \mathfrak{p}^K$ of neighboring vertices with $\mathfrak{p}^1 = \mathfrak{q}_1$ and $\mathfrak{p}^K = \mathfrak{q}_i$.

We now assign a component $j_k \in \{1, \ldots, N\}$ to each $\mathfrak{p}^k$ in the following way. We start by setting $j_1 = 1$ so that $c_{j_1}(\mathfrak{p}^1) > 0$ and assume $c_{j_{k-1}}(\mathfrak{p}^{k-1}) > 0$ for some $k > 1$. Then we keep $j_k := j_{k-1}$, if $c_{j_{k-1}}(\mathfrak{p}^k) > 0$, i.e., if the component j_{k-1} is still present at the neighboring vertex $\mathfrak{p}^k$. If this is not the case, then we switch to a new component j_k with $c_{j_k}(\mathfrak{p}^k) > 0$ and $c_{j_k}(\mathfrak{p}^{k-1}) > 0$, i.e. to a new component which is present in both vertices $\mathfrak{p}^k$ and $\mathfrak{p}^{k-1}$. This is possible due to assumption (4.22). Finally we formally set $j_{K+1} = i$ and define

$$\mathcal{B}_i = \{e^{j_k} - e^{j_{k-1}} \mid j_k \neq j_{k-1}, k = 2, \ldots, K+1\}$$

By construction, $c_{j_k}(\mathfrak{p}^{k-1})$, $c_{j_{k-1}}(\mathfrak{p}^{k-1}) > 0$ holds for all $k = 2, \ldots, K+1$ so that $\mathcal{B}_i$ is of the desired form. Moreover, we have $e^i - e^1 \in \operatorname{span} \mathcal{B}_i$ using the telescope sum

$$e^i - e^1 = \sum_{k=2}^{K+1} e^{j_k} - e^{j_{k-1}} \in \operatorname{span} \mathcal{B}_i.$$

$\square$

Obviously, the assumption in Lemma 4.7 can be weakened by applying the same arguments to certain paths of not necessarily neighboring vertices. However, this essentially amounts to a reformulation of the abstract assumption of Theorem 4.6 again.

Algebraic formulation

Similar to Section 3.2.2 we rewrite the discrete problem (VI) in an algebraic fashion. This will simplify the derivation and convergence analysis of nonsmooth Schur–Newton methods for the iterative solution of (VI) to be presented in the next section. Certain redundancies are intended for compactness of presentation. Starting from an enumeration $\mathfrak{F}_0^\bullet = \{\mathfrak{p}_1, \ldots, \mathfrak{p}_m\}$ of the $m = |\mathfrak{F}_0^\bullet|$ vertices, here we enumerate the $n = mN$ nodal basis functions of $\mathcal{S}_{\mathfrak{T}}^N$ according to

$$\{b^1, b^2, \ldots, b^n\}, \qquad b^{\pi(i,k)} = e^i b_{\mathfrak{p}_k}, \ i = 1, \ldots, N, \ k = 1, \ldots m,$$

utilizing the bijective index map $\pi : \{1, \ldots, N\} \times \{1, \ldots, m\} \to \{1, \ldots, n\}$ defined by $\pi(i, k) = i + N(k-1)$. Utilizing the canonical isomorphism $\mathcal{S}_{\mathfrak{T}}^N \ni \boldsymbol{v} \mapsto \mathbf{v} = (\mathrm{v}_i) \in \mathbb{R}^n$ induced by the basis representation

$$\boldsymbol{v} = \sum_{i=1}^n \mathrm{v}_i b^i, \qquad \boldsymbol{v} \in \mathcal{S}_{\mathfrak{T}}^N,$$

we arrive at the vector-valued analogue of (3.20), to find $\mathbf{c}, \mathbf{w} \in \mathbb{R}^n$ such that

$$\langle A\mathbf{c}, (\mathbf{v} - \mathbf{c})\rangle + \varphi(\mathbf{v}) - \varphi(\mathbf{c}) - \langle B\mathbf{w}, (\mathbf{v} - \mathbf{c})\rangle \geqslant \langle \mathbf{f}, (\mathbf{v} - \mathbf{c})\rangle \quad \forall \mathbf{v} \in \mathbb{R}^n \tag{4.23}$$

$$B\mathbf{c} + C\mathbf{w} = -g.$$

Here we have used the matrices $A = (A_{ij})$, $B = (B_{ij})$, $C = (C_{ij}) \in \mathbb{R}^{n,n}$ given by

$$A_{ij} = \varepsilon^2 \left(\nabla b^j, \nabla b^i \right) + (M^{\mathsf{T}} M)_{ij}, \quad B_{ij} = \left(b^j, b^i \right), \quad C_{ij} = \tau \left(L \nabla b^j, \nabla b^i \right), \qquad (4.24)$$

where the definition

$$M_{i,j} = \varepsilon \left(\int_{\Omega} b^j \right)_i, \qquad i = 1, \dots, N, \quad j = 1, \dots n, \qquad (4.25)$$

of $M = (M_{ij}) \in \mathbb{R}^{N,n}$ provides $\left\langle M^{\mathsf{T}} M \mathbf{c}, \mathbf{v} \right\rangle = \varepsilon^2 \left\langle \int_{\Omega} \mathbf{c} \, dx, \int_{\Omega} \mathbf{v} \, dx \right\rangle$. The algebraic representation

$$\varphi(\mathbf{v}) = \sum_{i=1}^{n} \varphi_i(\mathbf{v}_i), \quad \text{with} \quad \varphi_i(\xi) = \Phi_\theta(\xi) \int_{\Omega} b^i \, dx \qquad (4.26)$$

of the nonlinearity ϕ_θ satisfies $\varphi(\mathbf{v}) = \phi_\theta(\mathbf{v})$ and the right-hand sides $\mathbf{f} = (\mathbf{f}_i)$, $\mathbf{g} = (\mathbf{g}_i) \in \mathbb{R}^n$ are given by

$$\mathbf{f}_i = - \left(K \mathbf{c}^{\mathrm{old}}, b^i \right) + \left(M^{\mathsf{T}} M \int_{\Omega} \mathbf{c}^{\mathrm{old}} \, dx \right)_i, \qquad \mathbf{g}_i = - \left(\mathbf{c}^{\mathrm{old}}, b^i \right). \qquad (4.27)$$

In analogy to (4.12) the variational problem (4.23) can be reformulated as the saddle point problem

$$\mathcal{L}(\mathbf{c}, \mathbf{w}) = \inf_{\mathbf{v} \in \mathbb{R}^n} \sup_{Z \in \mathcal{S}_{\mathfrak{T}}^N} \mathcal{L}(\mathbf{v}, Z) \qquad (4.28)$$

for the Lagrangian

$$\mathcal{L}(\mathbf{c}, \mathbf{w}) = \frac{1}{2} \langle A \mathbf{c}, \mathbf{c} \rangle - \langle \mathbf{f}, \mathbf{c} \rangle + \varphi(\mathbf{c}) - \langle (B \mathbf{c} + \mathbf{g}), \mathbf{w} \rangle - \frac{1}{2} \langle C \mathbf{w}, \mathbf{w} \rangle.$$

The construction and convergence analysis of nonsmooth Schur–Newton methods to be presented below will rely on the following reformulation.

Proposition 4.8. *The discrete spatial problem (VI) is equivalent to the set-valued saddle point problem*

(VIA) Find $\mathbf{c}$, $\mathbf{w} \in \mathbb{R}^n$ *such that*

$$\begin{pmatrix} A + \partial\varphi & -B^{\mathsf{T}} \\ -B & -C \end{pmatrix} \begin{pmatrix} \mathbf{c} \\ \mathbf{w} \end{pmatrix} \ni \begin{pmatrix} \mathbf{f} \\ \mathbf{g} \end{pmatrix}$$

with the symmetric, positive definite matrix $A \in \mathbb{R}^{n,n}$, $B \in \mathbb{R}^{n,n}$, the symmetric, positive semi-definite matrix $C \in \mathbb{R}^{n,n}$, the subdifferential $\partial\varphi$ of the lower semi-continuous, proper convex functional $\varphi : \mathbb{R}^n \to \mathbb{R}$ and $\mathbf{f}$, $\mathbf{g} \in \mathbb{R}^n$ given in (4.24) – (4.27).

4.2.2. Nonsmooth Schur–Newton methods

In this section we consider the efficient algebraic solution of set-valued saddle point problems of the form (VIA) with a symmetric, positive definite matrix $A \in \mathbb{R}^{n,n}$, some matrix $B \in \mathbb{R}^{n,n}$, a symmetric, positive semi-definite matrix $C \in \mathbb{R}^{n,n}$, the subdifferential $\partial\varphi$ of a lower semi-continuous, proper convex functional $\varphi : \mathbb{R}^n \to \mathbb{R}$, and $\mathbf{f}$, $\mathbf{g} \in \mathbb{R}^n$ by nonsmooth Schur–Newton methods. This approach has been introduced and applied to discretized binary Cahn–Hilliard equations with obstacle potential in [63]. It was extended to more general nonsmooth nonlinearities and applied to a binary Cahn–Hilliardequation with logarithmic potential in [66, 61]. For completeness, we present the basic ideas and convergence results, referring to [61, 63] for details.

Nonlinear Schur complement and unconstrained minimization

Nonsmooth Schur–Newton methods are based on the reformulation of the set-valued saddle point problem (VIA) as a dual, unconstrained minimization problem. In a first step, we eliminate the primal variable $\mathbf{c}$ from (VIA).

Lemma 4.9. *The set-valued saddle point problem (VIA) is equivalent to the nonlinear system*

$$H(\mathbf{w}) = 0 \tag{4.29}$$

with the single-valued, Lipschitz continuous nonlinear Schur complement

$$H(\mathbf{w}) = B(A + \partial\varphi)^{-1}(\mathbf{f} + B^\mathsf{T}\mathbf{w}) + C\mathbf{w} + \mathbf{g} \tag{4.30}$$

in the sense that $(\mathbf{c}, \mathbf{w})$ is a solution of (VIA) if and only if $\mathbf{w}$ solves (4.29) and $\mathbf{c} = (A + \partial\varphi)^{-1}(\mathbf{f} + B^\mathsf{T}\mathbf{w})$.

Proof. The inverse $(A + \partial\varphi)^{-1}$ of $A + \partial\varphi$ is single-valued and Lipschitz continuous with Lipschitz constant given by the inverse of the coercivity constant of A, because A is

s.p.d. and φ is lower semi-continuous, proper convex [45, Part One, Chapter II]. Now the assertion follows from straightforward computation. $\qquad\square$

In the linear case $\partial\varphi \equiv 0$, it is well-known that the Schur complement $BA^{-1}B^{\mathsf{T}} + C$ is symmetric and positive definite. We now provide an extension of this property to the present nonlinear case.

Proposition 4.10. *There is a Fréchet-differentiable convex functional $h : \mathbb{R}^n \to \mathbb{R}$ such that $H = \nabla h$.*

Proof. Using Corollary 5.2 in [45, p. 22], it follows that $H = \partial h$ is the subdifferential of

$$h(\mathbf{w}) = - \inf_{\mathbf{v}\in\mathbb{R}^n} \mathcal{L}(\mathbf{v}, \mathbf{w}) = -\mathcal{L}((A + \partial\varphi)^{-1}(\mathbf{f} + B^{\mathsf{T}}\mathbf{w}), \mathbf{w}).$$

As $\partial h = H$ is single-valued and continuous, h is even Fréchet-differentiable and $H = \nabla h$ is the Fréchet derivative of h. $\qquad\square$

As a direct consequence of Lemma 4.9 and Proposition 4.10, the set-valued saddle point problem (VIA) is equivalent to find $\mathbf{w} \in \mathbb{R}^n$ such that

$$h(\mathbf{w}) \leqslant h(\mathbf{v}) \qquad \forall \mathbf{v} \in \mathbb{R}^n \tag{4.31}$$

and then solve $A\mathbf{c} + \partial\varphi(\mathbf{c}) \ni \mathbf{f} + B^{\mathsf{T}}\mathbf{w}$. We emphasize that (4.31) now is an unconstrained convex minimization problem for a $C^{1,1}$ function to which classical gradient-related descent methods can be applied.

Gradient-related descent methods

We give a short summary of this approach referring to text books like, e.g., [104] for the general theory or to [66, 63] for a more specific presentation.

We consider iterative methods for the approximation of minimizers of a given functional $h : \mathbb{R}^n \to \mathbb{R}$ of the form

$$\mathbf{w}^{\nu+1} = \mathbf{w}^\nu + \rho_\nu \mathbf{d}^\nu. \tag{4.32}$$

The search directions $\mathbf{d}^\nu \in \mathbb{R}^n$ are called *gradient-related*, if for any sequence $(\mathbf{w}^\nu) \subset \mathbb{R}^n$ the conditions

$$\nabla h(\mathbf{w}^\nu) = 0 \quad \Longleftrightarrow \quad \mathbf{d}^\nu = 0$$

and

$$-\langle \nabla h(\mathbf{w}^\nu), \mathbf{d}^\nu \rangle \geqslant \lambda_{\mathbf{d}} |\nabla h(\mathbf{w}^\nu)| |\mathbf{d}^\nu|$$

hold for all $\nu \in \mathbb{N}$ with a constant $\lambda_{\mathbf{d}} > 0$ independent of ν. For example, the gradients $\mathbf{d}^\nu = -\nabla h(\mathbf{w}^\nu)$ are gradient-related, and we obtain the classical gradient method for this choice. Faster convergence speed can be expected for preconditioned gradient methods as resulting from search directions of the form

$$\mathbf{d}^\nu = -S_\nu^{-1} \nabla h(\mathbf{w}^\nu) \tag{4.33}$$

with a sequence $(S_\nu) \subset \mathbb{R}^{n,n}$ of suitable symmetric, positive definite preconditioners. Such search directions are gradient-related, if there are constants $\lambda, \Lambda > 0$ such that

$$\lambda |\mathbf{v}|^2 \leqslant \langle S_\nu \mathbf{v}, \mathbf{v} \rangle \leqslant \Lambda |\mathbf{v}|^2 \tag{4.34}$$

holds uniformly in $\nu \in \mathbb{N}$.

While the search directions $\mathbf{d}^\nu$ are constructed to allow for suitable descent of the functional h, the step sizes ρ_ν should guarantee that this descent is actually realized. A sequence $(\rho_\nu) \subset \mathbb{R}$ of step sizes is called *efficient*, if

$$h(\mathbf{w}^\nu + \rho_\nu \mathbf{d}^\nu) \leqslant h(\mathbf{w}^\nu) - \lambda_S \left(\frac{\langle \nabla h(\mathbf{w}^\nu), \mathbf{d}^\nu \rangle}{|\mathbf{d}^\nu|} \right)^2 \tag{4.35}$$

holds with a constant $\lambda_S > 0$ independent of ν.

Theorem 4.11. *Assume that the search directions take the form $\mathbf{d}^\nu = -S_\nu^{-1} \nabla h(\mathbf{w}^\nu)$ with symmetric, positive definite preconditioners $S_\nu \in \mathbb{R}^{n,n}$ satisfying (4.34), that the step sizes ρ_ν are efficient in the sense of (4.35), and that h has a unique minimizer. Then the sequence $(\mathbf{w}^\nu)$ produced by (4.32) converges to the minimizer of h for $\nu \to \infty$.*

Proof. See Theorem 5.2 and Theorem 5.7 in [66]. The proof presented there is based on the fact that uniqueness of the minimizer implies compactness of the sublevel set $\{\mathbf{w} \in \mathbb{R}^n \mid h(\mathbf{w}) \leqslant h(\mathbf{w}^0)\}$. Using this the rest can essentially be shown with standard arguments as, e.g. in, [104]. $\qquad \square$

Efficiency of the step sizes ρ_ν can be guaranteed by various strategies such as, e.g., the Armijo rule (see, e.g., [38, Chapter 3] for a detailed discussion). In order to reduce the number of tuning parameters involved, we propose a strategy that approximates the minimizer of h along $\mathbf{w}^\nu + \rho \mathbf{d}^\nu$, $\rho \in \mathbb{R}$.

Proposition 4.12. *Assume that the search directions in the descent method (4.32) take the form $\mathbf{d}^\nu = -S_\nu^{-1} \nabla h(\mathbf{w}^\nu)$ and that*

$$\langle \nabla h(\mathbf{w}^\nu + \rho_\nu \mathbf{d}^\nu), \mathbf{d}^\nu \rangle \in \left[\, \alpha \, \langle \nabla h(\mathbf{w}^\nu), \mathbf{d}^\nu \rangle, 0 \,\right]$$

holds for all $\nu \in \mathbb{N}$ with some $\alpha \in [0, 1)$ independent of ν. Then the step sizes ρ_ν are efficient.

Proof. See Proposition 5.4 in [66]. $\qquad\square$

Remark 4.1. *Utilizing Proposition 4.12 with fixed $\alpha \in (0, 1)$, efficient step sizes ρ_ν can be computed by a simple bisection algorithm. However, as each iteration step requires the evaluation of $H = \nabla h$ and thus of $(A + \varphi)^{-1}$, this procedure might be quite costly. The actual computation of ρ_ν can be avoided, if the monotonicity test*

$$|\mathbf{d}^\nu| \leqslant \sigma |\mathbf{d}^{\nu-1}| \tag{4.36}$$

holds with some fixed $\sigma < 1$. In this case, convergence is preserved for $\rho_\nu = 1$. We refer to [66, Theorem 5.4] for details.

Remark 4.2. *The above convergence results also remain valid, if the descent directions $\mathbf{d}^\nu$ are replaced by approximations $\tilde{\mathbf{d}}^\nu$ which are sufficiently accurate in the sense that the conditions*

$$\left\langle \tilde{\mathbf{d}}^\nu, \nabla h(\mathbf{w}^\nu) \right\rangle < 0, \qquad\qquad |\mathbf{d}^\nu - \tilde{\mathbf{d}}^\nu| / |\tilde{\mathbf{d}}^\nu| \to 0$$

are satisfied. For a detailed analysis of such inexact versions we refer to [66].

In particular, Remark 4.2 allows for inexact evaluation of the preconditioner S_ν^{-1}.

Nonsmooth Newton-like descent directions

In the light of Theorem 4.11 the gradient-related descent method (4.32) with search directions of the form (4.33) converges globally for any sequence of symmetric positive

definite preconditioners S_ν with the property (4.34). We now aim at selecting S_ν in such a way that the convergence is locally fast. For a sufficiently smooth functional h, the Jacobian $S_\nu = \nabla^2 h(\mathbf{w}^\nu)$ would clearly be a desirable choice, because it leads to the classical Newton method with asymptotically quadratic convergence. Since for the given problem we cannot expect $\nabla h = H$ to be differentiable but only to be Lipschitz, the choice $S_\nu \in \partial_C H(\mathbf{w}^\nu)$ with ∂_C denoting the generalized Jacobian in the sense of Clarke [35] would be a natural generalization. However, an element of $\partial_C H(\mathbf{w}^\nu)$ is difficult to obtain, since, in general, we cannot make use of the chain rule. Following [66, 63], we will therefore construct related nonsmooth Newton-like preconditioners S_ν by *postulating* the chain rule. We will focus on the basic ideas of construction and present the resulting preconditioner for the given problem (4.29), referring to [66, 63] for details.

Our starting point is the observation that some of the components of $(A + \partial\varphi)^{-1}$ are smooth in a given $\mathbf{y} \in \mathbb{R}^n$ while the others are not. To be precise, we introduce the inactive set

$$\mathcal{I}(\mathbf{y}) := \{1 \leqslant i \leqslant n \mid \partial\varphi_i \text{ is single-valued and differentiable in } y_i\}.$$

For the given φ defined in (4.26), we obtain

$$\mathcal{I}(\mathbf{y}) = \{1 \leqslant i \leqslant n \mid y_i > 0\}. \tag{4.37}$$

It turns out that the i-th component of the inverse $(A + \partial\varphi)^{-1}$ is differentiable in $\mathbf{y}$, if $i \in \mathcal{I}((A + \partial\varphi)^{-1}\mathbf{y})$. This observation motivates the linearization

$$\partial(A + \partial\varphi)^{-1}(\mathbf{y}) := (A + \varphi''(\mathbf{x}))^+_{\mathcal{I}(\mathbf{x})} \tag{4.38}$$

of $(A + \partial\varphi)^{-1}$ at a given $\mathbf{y} \in (A + \partial\varphi)(\mathbf{x})$. Here, $\varphi''(\mathbf{x})$ denotes the diagonal matrix with diagonal entries $\varphi_i''(x_i)$, the matrix $M^+ \in \mathbb{R}^{n,n}$ stands for the Moore–Penrose pseudoinverse of $M \in \mathbb{R}^{n,n}$, and $M_\mathcal{I} \in \mathbb{R}^{n,n}$ again denotes the truncated matrix as in (2.54). Recall that truncation of a matrix means that certain lines and columns defined by the index set $\mathcal{I}$ are set to zero. Note that the multiplication of the matrix $(A + \varphi''(\mathbf{x}))^+_{\mathcal{I}(\mathbf{x})}$ with a vector amounts to the solution of a *truncated linear system*, i.e., of a reduced linear system with a coefficient matrix consisting of the i-th row and column unit vector in $\mathbb{R}^n$, if $i \notin \mathcal{I}(\mathbf{x})$ and remaining entries taken from $A + \varphi''(\mathbf{x})$, respectively.

The definition (4.37) of inactive sets is well-suited for the deep quench limit $\theta = 0$,

because then the second derivatives of $\varphi_i(y_i)$ are uniformly bounded, in fact equal to zero. This is different for the logarithmic potential, where the property $\varphi''(y_i) \to \infty$ for $y_i \to 0$ might lead to badly scaled linearizations of the form (4.38). As a remedy we modify the definition of the inactive set according to

$$\mathcal{I}''(\mathbf{y}) := \{1 \leqslant i \leqslant n \mid y_i > \delta\} \tag{4.39}$$

with some fixed $\delta > 0$ such that $\varphi_i(y_i) \leqslant \lambda_T$ holds with a corresponding fixed constant λ_T. We will use $\lambda_T = 10^8$ in our numerical computations. On this background, we finally define the linearization

$$\partial(A + \partial\varphi)^{-1}(\mathbf{y}) = (A + \varphi''(\mathbf{x}))^+_{\mathcal{I}''(\mathbf{x})}, \qquad \mathbf{x} = (A + \partial\varphi)^{-1}(\mathbf{y}),$$

of $(A + \partial\varphi)^{-1}$ at some given $\mathbf{y} \in \mathbb{R}^n$. Now, postulating the chain rule with $\partial(A + \partial\varphi)^{-1}$ as inner derivative, we obtain the nonsmooth Newton-like linearization

$$\partial H(\mathbf{y}) = B(A + \varphi''(\mathbf{x}))^+_{\mathcal{I}''(\mathbf{x})} B^\mathsf{T} + C, \qquad \mathbf{x} = (A + \partial\varphi)^{-1}(\mathbf{f} + B^\mathsf{T}\mathbf{y}),$$

of H defined in (4.30) at some given $\mathbf{y} \in \mathbb{R}^n$.

The candidate $\partial H(\mathbf{w}^\nu)$ for a preconditioner S_ν is symmetric and positive definite, if and only if $\mathcal{I}''(\mathbf{c}^\nu) \neq \varnothing$ holds with $\mathbf{c}^\nu = (A + \partial\varphi)^{-1}(\mathbf{w}^\nu)$, because we get $\partial H(\mathbf{w}^\nu) = C$ otherwise, and C is only positive semi-definite. Hence, in the non-generic case $\mathcal{I}''(\mathbf{c}^\nu) = \varnothing$, we regularize $\partial H(\mathbf{w}^\nu)$, e.g., by adding the scaled mass matrix τB to obtain

$$S_\nu = \begin{cases} \partial H(\mathbf{w}^\nu) & \text{if } \mathcal{I}''(\mathbf{c}^\nu) \neq \varnothing, \\ \partial H(\mathbf{w}^\nu) + \tau B & \text{else.} \end{cases} \tag{4.40}$$

Definition 4.1: The gradient-related descent method (4.32) with search directions $\mathbf{d}^\nu = -S_\nu^{-1}H(\mathbf{w}^\nu)$, preconditioners $S_\nu \in \mathbb{R}^{n,n}$ defined in (4.40), and efficient step sizes ρ_ν is called *nonsmooth Schur–Newton iteration* for the set-valued saddle point problem (VIA). $\triangle$

Recall that efficient step sizes ρ_ν can be computed utilizing Proposition 4.12.

4. Multicomponent Cahn–Hilliard systems

Theorem 4.13. *Assume that (VIA) has a unique solution* $(\mathbf{c}, \mathbf{w})$. *Then, for any initial iterate* $\mathbf{w}^0 \in \mathbb{R}^n$, *the nonsmooth Schur–Newton iteration converges to the solution* $\mathbf{w}$ *and* $\mathbf{c} = (A + \partial\varphi)^{-1}(\mathbf{f} + B^\mathsf{T}\mathbf{w})$.

Proof. In the light of Theorem 4.11, it only remains to show that the preconditioners S_ν, defined in (4.40) are s.p.d. and satisfy condition (4.34). We refer to Theorem 5.7 in [66]. □

Recall that sufficient conditions for uniqueness are given in Theorem 4.6. Global convergence also holds for suitable inexact versions of (4.32) according to Remark 4.2.

By construction, we generally cannot expect $\partial H(\mathbf{w}^\nu)$ to be contained in the set of generalized Jacobians in the sense of Clarke. Hence, the general theory of semi-smooth Newton methods cannot be applied to show local quadratic convergence. However, exploiting that the underlying solution space is finite dimensional, related results can easily be shown directly.

Remark 4.3. *Assume that the parameter* $\delta > 0$ *in* (4.39) *is sufficiently small and that the monotonicity test in* (4.36) *is not used. Then the nonsmooth Schur–Newton method as applied to the set-valued saddle point problem (VIA) locally reduces to a classical Newton iteration in case of the logarithmic potential* $\theta > 0$, *and is even locally exact in the deep quench limit* $\theta = 0$.

The numerical relevance of these asymptotic results is limited: For $\theta > 0$ sufficiently small parameters $\delta > 0$ typically lead to severe ill-conditioning of the arising Hessian matrices and to convergence radii of the Newton iteration that are smaller than machine precision.

The general convergence analysis of nonsmooth Schur–Newton methods is based on arguments restricted to finite dimensional spaces (see [66, 63] for a detailed discussion). Convergence results in function spaces are available only in special cases [76]. However, numerical computations indicate mesh-independent convergence speed for initial iterates provided by nested iteration (cf. [66, 63] and the numerical experiments to be reported below). Theoretical validation of such kind of local mesh independence is still open.

Algorithmic aspects

Rewriting the nonsmooth Schur–Newton iteration introduced in Definition 4.1 in primal-dual form

$$\mathbf{c}^\nu = (A + \partial\varphi)^{-1}(\mathbf{f} + B^\mathsf{T}\mathbf{w}^\nu)$$
$$\mathbf{w}^{\nu+1} = \mathbf{w}^\nu + \rho_\nu S_\nu^{-1}(-B\mathbf{c}^\nu + C\mathbf{w}^\nu + \mathbf{g}),$$

we obtain a preconditioned Uzawa method. Each iteration step amounts to the update of the primal variable $\mathbf{c}^\nu$, the evaluation of the preconditioned residual $S_\nu^{-1}(-B\mathbf{c}^\nu + C\mathbf{w}^\nu + \mathbf{g})$, and the selection of a suitable step size ρ_ν.

The first substep is equivalent to the solution of the minimization problem

$$\mathbf{c}^\nu = \arg\min_{\mathbf{v}\in\mathbb{R}^n} \tfrac{1}{2}\langle A\mathbf{v}, \mathbf{v}\rangle + \varphi(\mathbf{v}) - \langle(\mathbf{f} + B^\mathsf{T}\mathbf{w}^\nu), \mathbf{v}\rangle. \tag{4.41}$$

While there is a vast literature about elliptic obstacle problems emerging in the deep quench limit $\theta = 0$ (cf., e.g., [41, 62] and the references cited therein), fast solvers for the logarithmic potential $\theta > 0$ that show a robust convergence behavior for $\theta \to 0$ are still rare (see, however, [85, 86]). In the numerical experiments to be reported below, we apply the *truncated nonsmooth Newton method* (TNNMG) [66, 62, 65] that combines robustness for $\theta \to 0$ with similar efficiency as observed for classical multigrid methods in the linear self-adjoint case. Note that optimal complexity of each iteration step even for the dense matrix A is achieved by exploiting that A is the sum of a sparse matrix and a dense low-rank matrix with a known product representation [60].

The preconditioned residual $\mathbf{w}^{\nu+1/2} = S_\nu^{-1}(-B\mathbf{c}^\nu + C\mathbf{w}^\nu + \mathbf{g})$ can be computed by (approximately) solving a truncated linear saddle point problem of the form

$$\begin{pmatrix} \hat{A} & -\hat{B}^\mathsf{T} \\ -\hat{B} & -\hat{C} \end{pmatrix} \begin{pmatrix} \hat{\mathbf{c}} \\ \mathbf{w}^{\nu+1/2} \end{pmatrix} = \begin{pmatrix} \hat{\mathbf{f}} \\ \mathbf{g} \end{pmatrix} \tag{4.42}$$

with the symmetric, positive definite matrix $\hat{A} \in \mathbb{R}^{\hat{n},\hat{n}}$, $\hat{n} = |\mathcal{I}''(\mathbf{c}^\nu)|$, obtained by eliminating the i-th row and column of A for all $i \notin \mathcal{I}''(\mathbf{c}^\nu)$, the matrix $\hat{B} \in \mathbb{R}^{\hat{n},n}$ obtained by eliminating the i-th column of B for all $i \notin \mathcal{I}''(\mathbf{c}^\nu)$, and $\hat{C} = C$, if $\hat{n} > 0$ or $C = C + \tau B$ otherwise. In the numerical experiments to be reported below, we use a preconditioned

GMRES iteration with a truncated version of the multigrid method with successive Vanka smoother suggested by Schöberl and Zulehner [113] as a preconditioner. For an overview on other methods for the numerical solution of linear saddle point problems, we refer to [14].

Efficient step sizes ρ^ν can be computed utilizing Remark 4.1 which requires the evaluation of $\nabla h(\mathbf{w}^\nu + \rho \mathbf{d}^\nu) = H(\mathbf{w}^\nu + \rho \mathbf{d}^\nu)$ and thus the solution of a minimization problem of the form (4.41) in each bisection step. Recall that this costly procedure can be avoided for iterates that are sufficiently accurate in the sense that the monotonicity test (4.36) is passed.

4.3. Numerical Results

4.3.1. Problem, discretization and subproblem solvers

We consider the multicomponent Cahn–Hilliard system (4.6) on the computational domain $\Omega = [-1, 1]^d$ with $L = P = \mathsf{Id} - \frac{1}{N}(\mathbf{1}, \ldots, \mathbf{1})$, $\varepsilon^2 = 5 \cdot 10^{-3}$ for the 2D computations and $2 \cdot 10^{-2}$ for the 3D computation. We use the logarithmic potential Ψ_θ defined by (4.3), where K is given by (4.5). We select $N = 4$ components and the temperature $\theta = 0.1$, if not stated otherwise. To obtain initial conditions with similar granularity for varying N, 200 circles with radius $0.1 - 0.15$ are randomly distributed over Ω and randomly assigned to the different components. For the 3D computation we used 150 balls with radii ranging from 0.1 to 0.5.

Throughout the following, we use the uniform time step size $\tau = 10^{-3}$ and a grid hierarchy $\mathfrak{T}_0, \ldots, \mathfrak{T}_j$ as obtained by successive refinement of the initial triangulation $\mathfrak{T}_0$ consisting of two triangles resp. five tetrahedra. Again adaptivity is clearly mandatory in practical applications due to the strongly locally varying solutions. However, in order not to introduce any effects due to differing grids we avoid adaptivity in all but the 3D computation and the final 2D experiment that focusses on adaptivity. If not stated otherwise, we select $j = 8$ uniform refinement steps, providing the triangulation $\mathfrak{T}_8$ with $m_8 = 66049$ vertices and the mesh size $h_8 = 2^{-7} \approx \varepsilon/9$. In this case, we found that the interface is resolved by about 11 grid points.

For the iterative solution of the resulting algebraic subproblems, we consider the non-

smooth Schur–Newton method (NSNMG) presented in Section 4.2.2 with a multigrid solver for the nonlinear non-smooth minimization problems (4.41) and a preconditioned GMRES iteration for the linearized saddle point problems (4.42).

More precisely, non-smooth subproblems (4.41) are solved by a truncated nonsmooth Newton multigrid method (TNNMG) [66, 62, 65]. Throughout the following, the iteration is executed almost up to machine precision, i.e., we use the stopping criterion

$$\left\|\mathbf{c}^{\nu,k+1} - \mathbf{c}^{\nu,k}\right\|_A < \vartheta_{\mathrm{TNNMG}} \tag{4.43}$$

for the iterates $\mathbf{c}^{\nu,k}$, $k = 1, \dots$, with $\|\cdot\|_A$ denoting the energy norm induced by the matrix A. In the computations reported on below we chose $\vartheta_{\mathrm{TNNMG}} = 10^{-13}$.

The linear saddle point problems (4.42) are solved by a preconditioned GMRES iteration with restart after 50 steps. The preconditioner is based on a straightforward extension of a truncated multigrid method with block-Gauß-Seidel smoother as suggested in [85, 113] to the case of vector-valued order parameters. In the light of Remark 4.2 the iteration is stopped, if the ratio of the Euclidean norms of the preconditioned residual and the actual iterate is less than $\min\left(\zeta_1^\nu,\ \zeta_2 \left\|\mathbf{w}^\nu - \mathbf{w}^{\nu-1}\right\|_{C,B}^2\right)$. Here, we chose $\zeta_1 = 10^{-1}$ and $\zeta_2 = 10^{-2}$ and the corrections $\mathbf{w}^\nu - \mathbf{w}^{\nu-1}$ of the overall NSNMG iteration are measured in the norm

$$\|\mathbf{v}\|_{C,B} = \|\mathbf{v}\|_C + \tau \|\mathbf{v}\|_B\,, \qquad \mathbf{v} \in \mathbb{R}^n, \tag{4.44}$$

generated by the positive semi-definite matrix C and the mass matrix B defined in (4.24).

The step sizes ρ^ν are computed according to Proposition 4.12.

The overall NSNMG iteration is terminated once its target, the dual variable $\mathbf{w}$, is approximated sufficiently well, i.e. once the stopping criterion

$$\left\|\mathbf{w}^{\nu+1} - \mathbf{w}^\nu\right\|_{C,B} < \vartheta_{\mathrm{NSNMG}} = \kappa \cdot 10^{-11}. \tag{4.45}$$

is satisfied with some $\kappa > 0$. We chose the default value $\kappa = 1$, if not stated otherwise.

4.3.2. Evolution and distribution of computational work

In our first experiment, we consider the evolution of $N = 6$ components. Here, we chose $\kappa = 2$ in the stopping criterion (4.45) in order to avoid the influence of round-off errors

in our linear saddle point solver. The evolution over 1000 time steps is illustrated in Figure 4.2. As expected, we observe fast separation in the beginning and slower dynamics in course of the evolution. It is interesting to see that the evolution tends to a hexagonal structure of grains with equilibrated mass. Mass conservation is fulfilled up to 0.0053% over all time steps, which is in good accordance with our prescribed algebraic accuracy. In a second computation we consider $N = 4$ components in 3D with $\kappa = 10$ over 100 timesteps. The evolution is illustrated in Figure 4.3. In this case mass is conserved up to 0.0024% over all time steps.
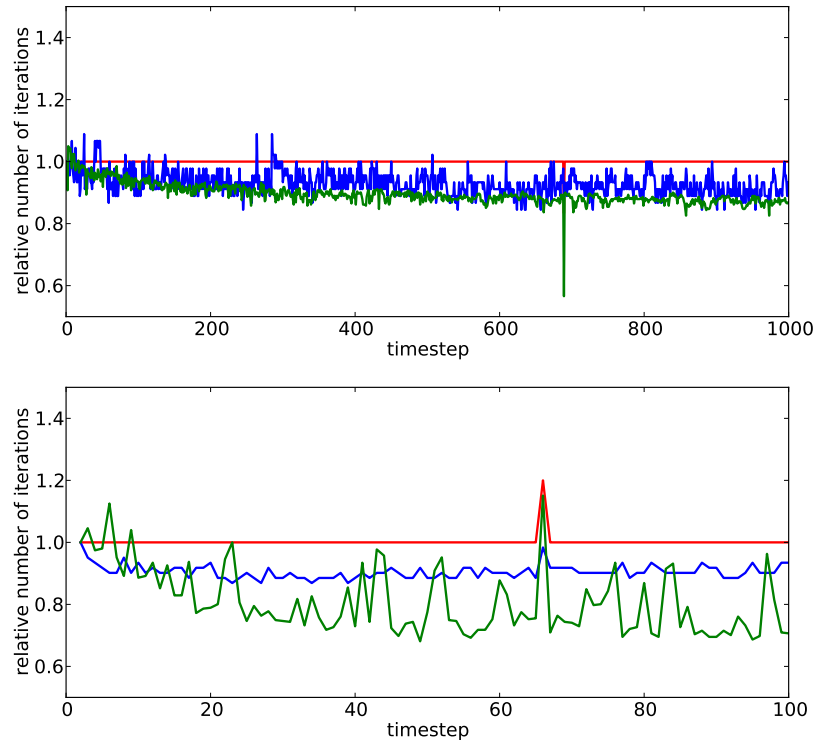
Figure 4.1 – Total number of iterations by NSNMG (red), TNNMG (blue), and preconditioned GMRES (green) for the described 2D (top) and 3D (bottom) evolutions, scaled by their value in the first timestep 6 (NSNMG), 45 (TNNMG), and 281 (preconditioned GMRES) resp. 5, 61, 351, over the number of time steps.

To illustrate the amount of computational work, Figure 4.1 shows the total number of iterations by NSNMG (red), TNNMG (blue), and preconditioned GMRES (green) for each spatial problem for the 2D (top) and 3D computation (bottom), scaled by their respective values in the first timestep (6 (NSNMG), 45 (TNNMG), and 281 (preconditioned GMRES) for 2D and 5, 61, 351 for 3D), over the number of time steps. The initial iterate is
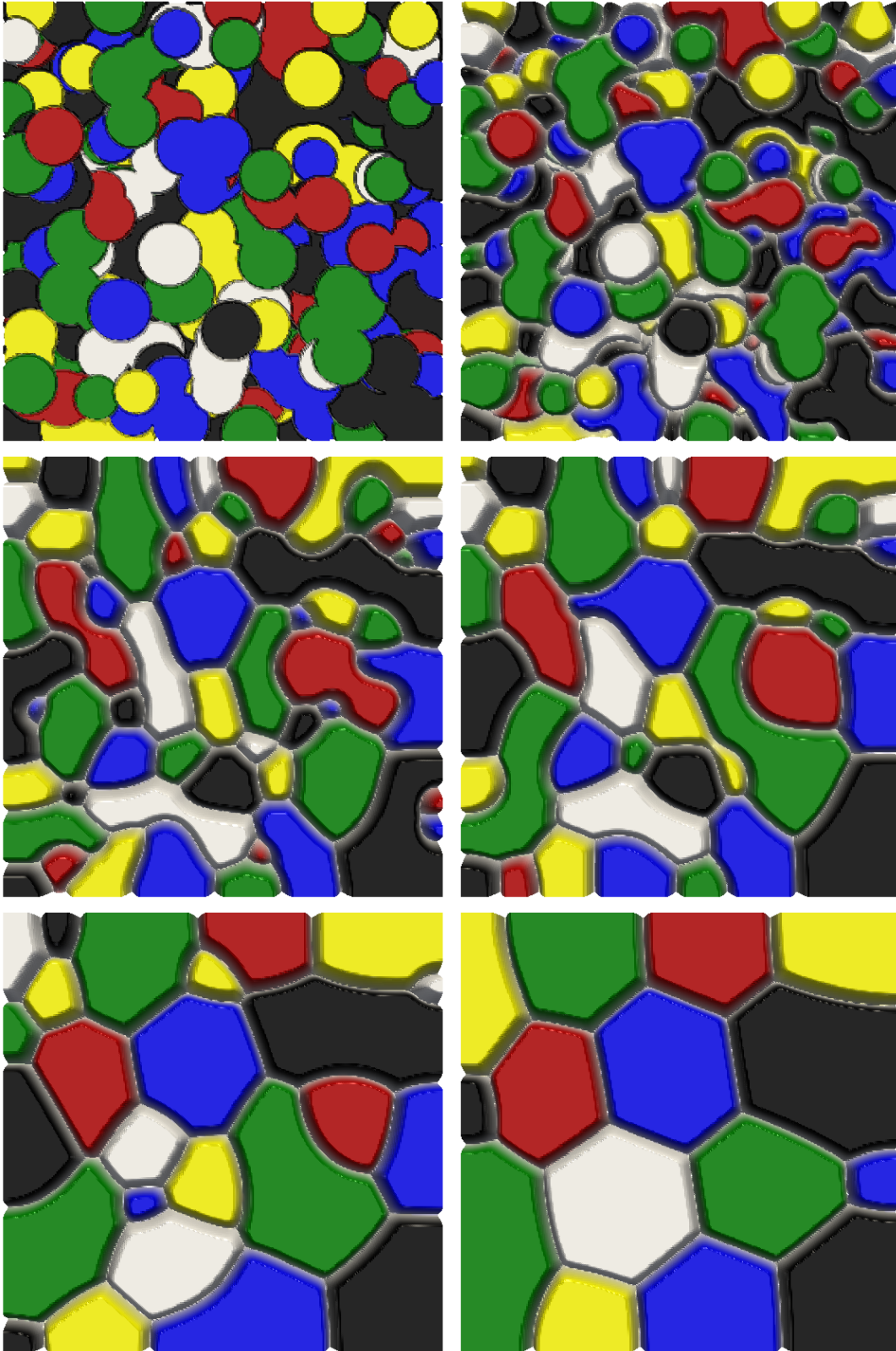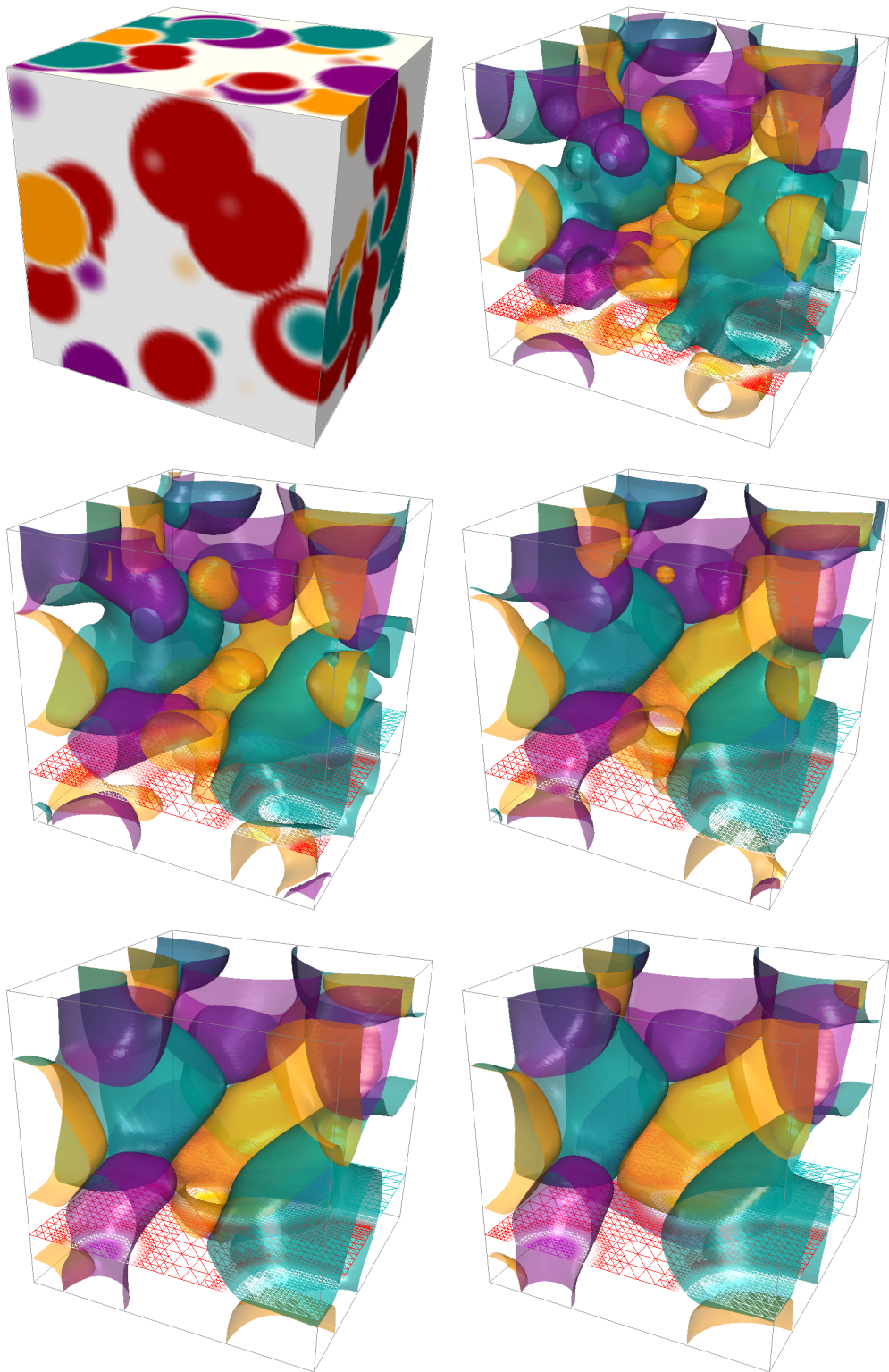
Figure 4.2 – Initial condition $\boldsymbol{c}^0$ and approximate order parameter $\boldsymbol{c}(\cdot, t)$ at time $t = 1\tau,\ 20\tau,\ 50\tau,\ 200\tau,\ 1000\tau$.

Figure 4.3 – The initial value of the phase-field on the surface of the computational domain and 0.51-levelsets of 3 phases in a 4-phase computation at timesteps 1, 5, 20, 40, 80 together with a grid cross-section. Note that white in the initial value is a homogeneous mixed state and the red phase has been rendered invisible in the latter images.

obtained by nested iteration in each case. We observe exactly 6 resp. 5 NSNMG iterations in the 2D resp. 3D case for all but one spatial problems and only slight changes in the performance of TNNMG and preconditioned GMRES. No damping was needed throughout the evolutions. Hence, the solution of each subproblem (4.41) only required about 7 resp. 12 iterations of TNNMG. This is in accordance with previous computations, where TNNMG exhibited linear multigrid efficiency and mesh-independent convergence rates for initial iterates provided by nested iteration [66, 65]. The preconditioned GMRES needed more than 40 resp. 70 iterations for each linear solve and thus strongly dominates the overall computational work. Moreover, we found that our straightforward multigrid preconditioning did not provide mesh independence. Hence, the overall efficiency of NSNMG will benefit from more sophisticated linear saddle point solvers as have been studied elsewhere (see, e.g.,[98]).

4.3.3. Influence of initial iterate, temperature, number of components, and spatial mesh size on the convergence speed

In our next experiment, we come back to $N = 4$ components and study the influence of initial iterates $\mathbf{w}^0$ and temperature θ on the convergence speed of NSNMG. As the
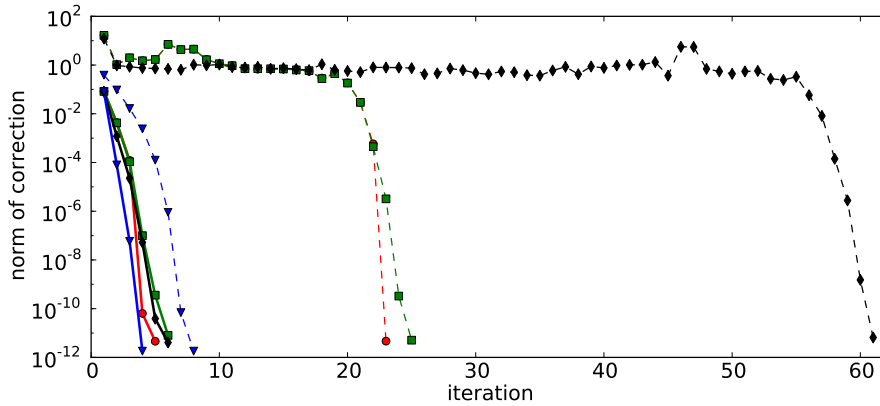

Figure 4.4 – Approximate algebraic error $\left\|\mathbf{w}^\nu - \mathbf{w}^{\nu-1}\right\|_{C,B}$ over the number of NSNMG iterations for the temperatures $\theta = 0.0$ (red ●), 0.001 (green ■), 0.1 (black ◆), 0.5 (blue ▼) with initial iterates $\mathbf{w}^0 = 0$ (dashed lines) and nested iteration (solid lines) for the first spatial problem.

performance of NSNMG hardly changed for different spatial problems (cf. Section 4.3.2),

we concentrate on the first one. Figure 4.4 shows the approximate algebraic error $\|\mathbf{w}^\nu - \mathbf{w}^{\nu-1}\|_{C,B}$ over the number of NSNMG iterations for the temperatures $\theta = 0.5$ (blue), 0.1 (black), 0.001 (green), 0 (red) with "bad" initial iterates $\mathbf{w}^0 = 0$ (dashed lines) and "good" initial iterates obtained by nested iteration (solid lines). For bad initial iterates, the iteration history can be separated into a preasymptotic phase with slow convergence and step sizes $\rho^\nu < 1$ and into an asymptotic phase with superlinear convergence speed. The asymptotic phase is entered immediately for initial iterates obtained by nested iteration. While we observe a strong influence of the temperature θ on the duration of the preasymptotic phase, it hardly seems to affect the asymptotic superlinear convergence speed.

This suggests robustness of NSNMG with respect to temperature θ for initial iterates as obtained by nested iteration, which is confirmed by our next experiment, as illustrated in Figure 4.5. The left picture shows the number of iterations as required to meet the stopping criterion (4.45) with $\kappa = 1$ over the inverse temperature $1/\theta$. We chose the values $\theta = i \cdot 10^{-1}$, $i = 1, \ldots 9$, and $\theta = 10^{-i}$, $i = 2, \ldots 10$. The corresponding averaged
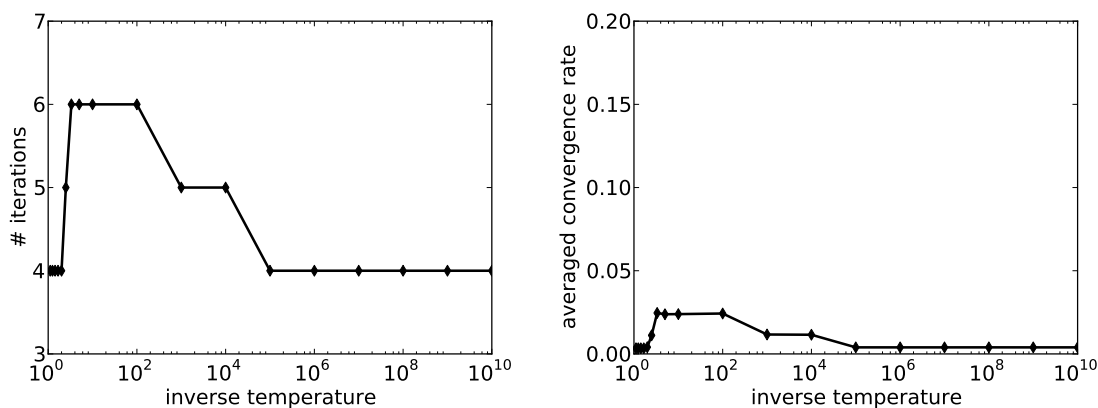

Figure 4.5 – Number of NSNMG iterations over inverse temperature $1/\theta$ (left) and averaged convergence rates of NSNMG over $1/\theta$ (right).

convergence rates are shown in the picture on the right. In a sense, problems with $\theta \approx 1$ and $\theta \approx 0$ seem to be a little bit easier to solve than problems with medium temperatures, such as, e.g. $\theta = 0.1$. Observe that the convergence behavior for $\theta = 10^{-5}$ can not be distinguished from the deep quench limit $\theta = 0$. At most 6 NSNMG iterations were required to reduce the approximate error by 10 orders of magnitude. The averaged NSNMG convergence rate is always far below 0.05 so that usually one or two NSNMG steps would be enough to reduce the algebraic error below discretization accuracy. Each

NSNMG step amounts to the total number of at most 23 TNNMG iterations and one inexact linear saddle point solution. This means that the average number of TNNMG iterations for each occurring subproblem (4.41) is less than 6, which nicely confirms efficiency and robustness of this method [66, 65]. Again the overall computational work is strongly dominated by the inexact linear saddle point solution which is partly due to the larger number of unknowns.
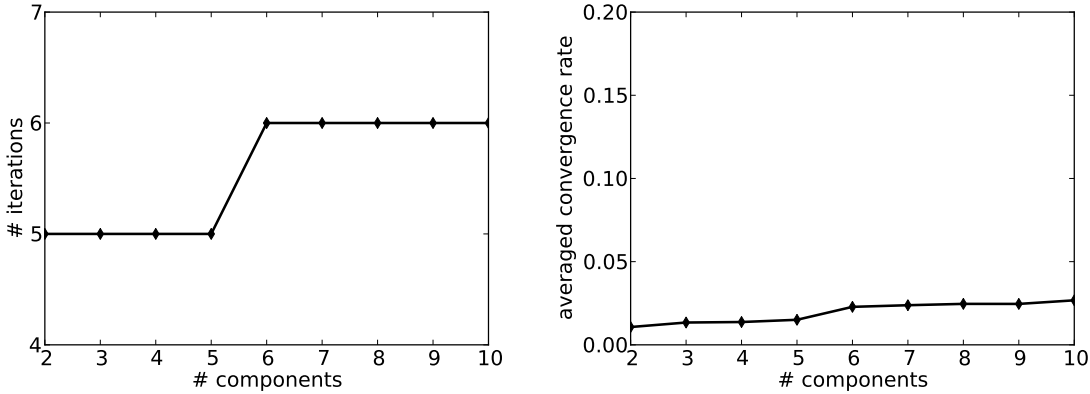

Figure 4.6 – Number of NSNMG iterations over the number N of components (left) and averaged convergence rates of NSNMG over N (right).

In the next experiment, we assess the influence of the number N of components on the convergence speed of NSNMG. Here, we had to chose $\kappa = 7$ in the stopping criterion (4.45) in order to avoid the influence of round-off errors in our linear saddle point solver. The left picture of Figure 4.6 shows the number of NSNMG iterations over N, while the right picture shows the corresponding averaged convergence rates. Again, the initial iterates are obtained by nested iteration. The number of NSNMG iterations is varying between 5 and 6 over $N = 2, \ldots, 10$ components, indicating considerable robustness of the convergence speed of NSNMG with respect to the number of components. This robustness is preserved by TNNMG, which required less than a total number of 45 TNNMG iterations in each NSNMG step to solve the nonlinear nonsmooth subproblems (4.41) almost up to machine accuracy.

As the convergence theory presented in Section 4.2.2 is partly based on arguments that are restricted to finite dimensional spaces, we now investigate the mesh dependence of NSNMG. As we are interested in the local asymptotic convergence speed, the initial iterates are obtained by nested iteration. The left picture of Figure 4.7 shows the number of NSNMG iterations over the number m_j of vertices of the triangulations $\mathfrak{T}_j$ for two
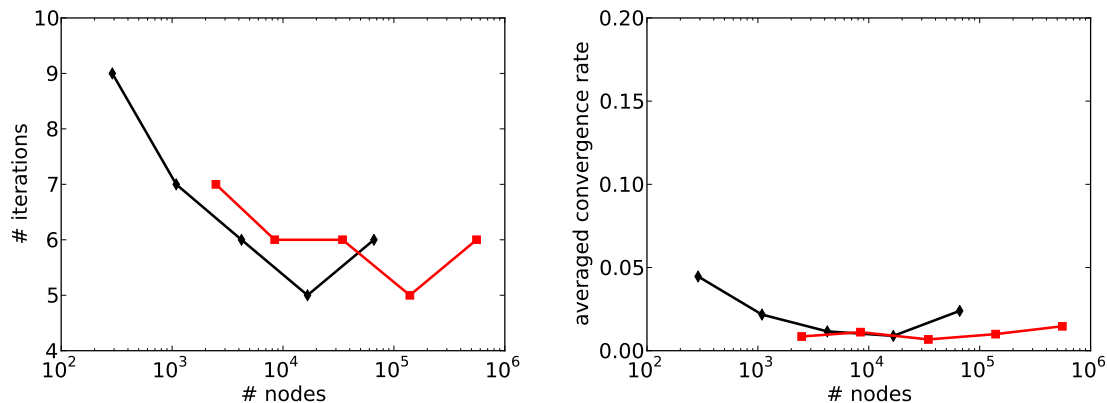
Figure 4.7 – Number of NSNMG iterations over the number of vertices m (left) and averaged convergence rates of NSNMG over m (right) in 2D (black) and 3D (red).

(black) and three (red) space dimensions, while the right picture shows the corresponding averaged convergence rates. The 3D data stems from the computation already described above. The plotted data is taken from the first timestep. For the mesh size ranging from $h_4 = 2^{-3}$ to $h_8 = 2^{-7}$, the number of NSNMG iterations is bounded by 9 in 2D and similarly for 3D. This suggests local mesh-independent convergence of NSNMG and even local convergence of a related approach in function space (see [76] for a first result in this direction). Theoretical justification will be the subject of future research.

4.3.4. Adaptive mesh refinement and order of convergence

The final experiment addresses the order of convergence of the adaptive refinement algorithm. We chose a checkerboard pattern as initial value for adaptive computations in order to have comparable overall interface lengths for different $N \in \{2, 4, 6\}$ (cf. Figure 4.9 left). We consider the second timestep in order to avoid artifacts that may arise due to the sharp interfaces of the initial values. The tolerances in the termination criterion (2.39) were chosen as $\vartheta_{\text{adapt}}(N = 2) = 2 \cdot 10^{-2}$, $\vartheta_{\text{adapt}}(4) = 2.5 \cdot 10^{-2}$, $\vartheta_{\text{adapt}}(6) = 3 \cdot 10^{-2}$ such that the resulting numbers of (nonhanging) nodes in the final grids are roughly of the same size $m(N = 2, 4, 6) = (136790, 133727, 112377)$. All other parameters of our refinement cycle were chosen as in previous chapters. Figure 4.8 shows the corresponding estimated errors η, as introduced in (3.19), over $\sqrt{m}$. Note that $h = m^{-1/2}$ is the mesh size in case of uniform refinement. The dashed line indicates $\mathcal{O}(m^{-1/2})$. A comparison

suggests that our adaptive refinement algorithm provides approximations with optimal order independently of the number of components.
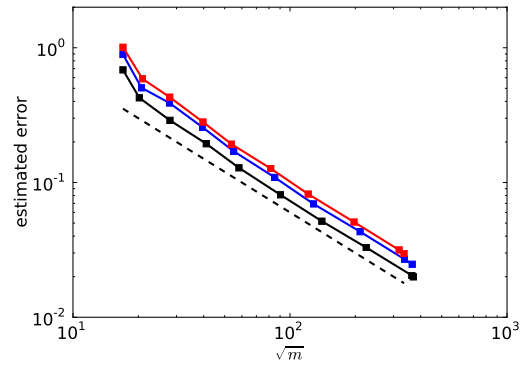

Figure 4.8 – Estimated error η over $m^{1/2}$ for $N = 2$ (black), $N = 4$ (blue), $N = 6$ (red) in comparison with $\mathcal{O}(m^{-1/2})$ (dashed).
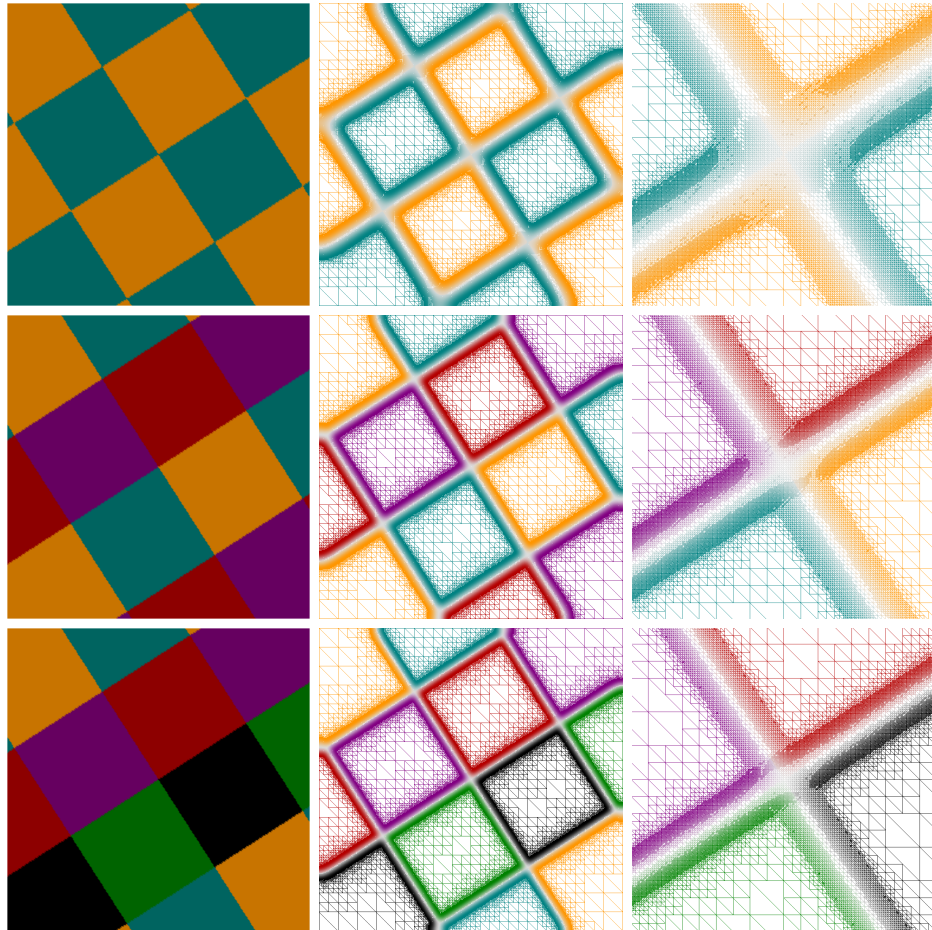
Figure 4.9 – Initial values (left), final grids (middle), and grid details (right) for adaptive computations with $N = 2, 4, 6$

A. Appendices

Appendix A.2 is a loose collection of a few functional analytic results which are used in the proofs given in Chapters 2-4. The crucial theorem of monotone operator theory, on which the existence and uniqueness proof in Chapter 2 is based, is given and developed in Appendix A.1.

A.1. Maximal Monotone Operators

In this section we will state the definition of maximal monotone operators on a Hilbert space $\mathcal{H}$ and collect some important examples, lemmata, and theorems. The contents of this section are taken from the monograph by Brézis [27] with some elaboration of proofs. Subject of study are (set-valued) mappings $A : \mathcal{H} \to \mathfrak{P}(\mathcal{H})$ from a Hilbert space into its powerset.

Definition A.1: The set $\mathrm{dom}(A) = \{x \in \mathcal{H} \mid Ax \neq \varnothing\}$ is called the *domain* of A and $\mathrm{range}(A) = \bigcup_{x \in \mathcal{H}} Ax$ its *range*. The set $\mathrm{graph}(A) = \{(x; y) \in \mathcal{H} \times \mathcal{H} \mid y \in Ax\}$ will be called the *graph* of A. The *inverse* operator A^{-1} is defined by $y \in A^{-1}x \Leftrightarrow x \in Ay$. $\triangle$

Definition A.2: An operator $A : \mathcal{H} \to \mathfrak{P}(\mathcal{H})$ is called *monotone* iff

$$\forall_{x_1, x_2 \in \mathrm{dom}(A)} \forall_{y_1 \in Ax_1} \forall_{y_2 \in Ax_2} (y_1 - y_2, x_1 - x_2)_{\mathcal{H}} \geqslant 0$$

A monotone operator is called *maximal monotone*, if it is maximal in the set of monotone operators on $\mathcal{H}$ wrt to the subset relation on their graphs; or more explicitly, for all $(x; y) \in \mathcal{H} \times \mathcal{H}$ with $(y - \eta, x - \xi)_{\mathcal{H}} \geqslant 0$ for all $\xi \in \mathrm{dom}(A)$, $\eta \in A\xi$ it follows $y \in Ax$, i.e. $(x; y) \in \mathrm{graph}(A)$. $\triangle$

The set of monotone operators on $\mathcal{H}$ is inductively ordered, which together with Zorn's lemma guarantees the existence of a maximal extension of any monotone operator (cf. [27,

A. Appendices

Corollaire 2.1]). The following lemma ([27, Proposition 2.2]) states criteria for maximal monotonicity which may be easier to verify.

Lemma A.1. *Let A be an operator on $\mathcal{H}$, then the following properties of A are equivalent*

1. *A is maximal monotone*

2. *A is monotone and* $\mathrm{range}(\mathsf{Id} + A) = \mathcal{H}$

3. $(\mathsf{Id} + \lambda A)^{-1}$ *is a contraction defined everywhere on $\mathcal{H}$, for all $\lambda > 0$*

Given a maximal monotone operator one can construct others from it:

Lemma A.2. *Let A be a maximal monotone operator, then λA for $\lambda > 0$ and A^{-1} are maximal monotone. If B is a maximal monotone operator such that $\overset{\circ}{\mathrm{dom}}(A) \cap \mathrm{dom}(B) \neq \varnothing$ then $A + B$ is maximal monotone and $\overline{\mathrm{dom}(A) \cap \mathrm{dom}(B)} = \overline{\mathrm{dom}(A)} \cap \overline{\mathrm{dom}(B)}$.*

The proof of the latter result can be found in [27, Corollaire 2.7], the former are immediate.

The following important result was proven by Moreau [96] and extended to general Banach spaces by Rockafellar [110]. We give the proof from [27, Exemple 2.3.4] in a slightly more elaborate version.

Theorem A.3. *Let ϕ be a proper convex and lower semicontinuous functional on $\mathcal{H}$, then the subdifferential $\partial\phi$ is a maximal monotone operator on $\mathcal{H}$ (identifying $\mathcal{H}$ with its dual $\mathcal{H}'$ via the Riesz isomorphism).*

Proof. Monotonicity of the subdifferential follows directly from the definition. We have for any $x_1, x_2 \in \mathcal{H}$ and $y_1 \in \partial\phi(x_1)$, $y_2 \in \partial\phi(x_2)$

$$\phi(x_1) \geqslant \phi(x_2) + (y_2, x_1 - x_2) \qquad \text{and}$$
$$\phi(x_2) \geqslant \phi(x_1) + (y_1, x_2 - x_1).$$

Addition of the inequalities yields $(y_1 - y_2, x_1 - x_2) \geqslant 0$.

In order to prove maximality we will use Lemma A.1 and the following result: For a proper convex function ϕ on $\mathcal{H}$, $y \in \mathcal{H}$ and $\alpha > 0$ the convex function $\psi_\alpha(x) = \phi(x) + \frac{\alpha}{2} \|x - y\|_{\mathcal{H}}^2$ takes on its minimum in $x_0 \in \mathcal{H}$ iff $\alpha(y - x_0) \in \partial\phi(x_0)$. Indeed if $\alpha(y - x_0) \in \partial\phi(x_0)$ we have $\phi(x_0) < +\infty$. The definition of the subgradient and a simple computation yield

$$\phi(\xi) - \phi(x_0) \geqslant \alpha(y - x_0, \xi - x_0) \geqslant \frac{\alpha}{2} \left(\|x_0 - y\|^2 - \|\xi - y\|^2 \right), \quad \forall \xi \in \mathcal{H}$$

and thus

$$\phi(x_0) + \frac{\alpha}{2}\|x_0 - y\|^2 \leqslant \phi(\xi) + \frac{\alpha}{2}\|\xi - y\|^2 \quad \forall \xi \in \mathcal{H}$$

Conversely taking $\xi = (1-t)x_0 + t\eta$ with $t \in (0,1)$ and some $\eta \in \mathcal{H}$ we have

$$
\begin{aligned}
t\left(\phi(\eta) - \phi(x_0)\right) &\geqslant \phi(\xi) - \phi(x_0) \\
&\geqslant \frac{\alpha}{2}\left(\|x_0 - y\|^2 - \|(1-t)x_0 + t\eta - y\|^2\right) \\
&= t\frac{\alpha}{2}\left(2(x_0 - y) + t(\eta - x_0), x_0 - \eta\right)
\end{aligned}
$$

where the first inequality is due to convexity of ϕ, and the second to the minimizing quality of x_0. The equality is a simple application of the binomial rule. Division by t and passing to the limit yields

$$\phi(\eta) - \phi(x_0) \geqslant \alpha(y - x_0, \eta - x_0)$$

i.e. $\alpha(y - x_0)$ is a subgradient of ϕ at x_0.

Now observe that for any $y \in \mathcal{H}$ ψ_1 is convex, lsc and - by virtue of the Hahn-Banach theorem - coercive. Hence ψ_1 takes on its minimum $x_0 \in \mathcal{H}$ and by the preceding result we have $y \in x_0 + \partial\phi(x_0)$. Thus we have shown range$(\mathsf{Id} + \partial\phi) = \mathcal{H}$ which yields maximal monotonicity of $\partial\phi$ by Lemma A.1. □

In the following we state without further proof some important results concerning evolution equations of maximal monotone operators $\frac{du}{dt} + Au \ni f$, $u(0) = u_0$. We begin by stating the definitions of strong and weak solutions to the evolution equation.

Definition A.3: Let A be an operator on $\mathcal{H}$ and $f \in L^1(0, T; \mathcal{H})$. A function $u \in \mathcal{C}([0, T]; \mathcal{H})$ that is absolutely continuous on each compact subset of $(0, T)$ is a *(strong) solution* of $f \in \frac{du}{dt} + Au$ iff $u(t) \in \mathrm{dom}(A)$ and $\frac{du}{dt}(t) + Au(t) \ni f(t)$ for a.e. $t \in (0, T)$.

We call $u \in \mathcal{C}([0, T]; \mathcal{H})$ a *weak solution* iff there exist sequences $f_n \in L^1(0, T; \mathcal{H})$ and $u_n \in \mathcal{C}([0, T]; \mathcal{H})$ with $f_n \to f$ in $L^1(0, T; \mathcal{H})$ and $u_n \to u$ uniformly in $\mathcal{C}([0, T]; \mathcal{H})$ and u_n is a strong solution to $\frac{du_n}{dt} + Au_n \ni f_n$. △

For the weak solutions of evolution equations we state some useful estimates:

Lemma A.4 ([27], Lemme 3.1). *Let A be a maximal monotone operator on $\mathcal{H}$, f and $g \in L^1(0, T; \mathcal{H})$, u and v weak solutions to $\frac{du}{dt} + Au \ni f$ and $\frac{dv}{dt} + Au \ni g$ respectively.*

A. Appendices

Then we have the estimates

$$\|u(t) - v(t)\| \leqslant \|u(s) - v(s)\| + \int_s^t \|f(r) - g(r)\| \, dr \quad \forall 0 \leqslant s \leqslant t \leqslant T \quad \text{(A.1)}$$

$$(u(t) - u(s), u(s) - x) \leqslant \frac{1}{2} \|u(t) - x\|^2 - \frac{1}{2} \|u(s) - x\|^2$$

$$\leqslant \int_s^t (f(r) - y, u(r) - x) \, dr \quad \forall 0 \leqslant s \leqslant t \leqslant T; \ \forall x, y \in A$$

(A.2)

The following theorem ensures existence of unique weak solutions under certain conditions on the right hand side and the initial conditions.

Theorem A.5 ([27], Theorème 3.4). *Let A be a maximal monotone operator on $\mathcal{H}$. For every $f \in L^1(0, T; \mathcal{H})$ and every $u_0 \in \overline{\text{dom}(A)}$ there is a unique weak solution u to the inclusion $\frac{du}{dt} + Au \ni f$ with $u(0) = u_0$.*

In the case of A being a subdifferential of a proper convex lsc function, and f an L^2 right hand side, weak solutions are in fact strong solutions as stated by the following theorem.

Theorem A.6 ([27], Theorème 3.6). *Let $f \in L^2(0, T; \mathcal{H})$ and $u_0 \in \overline{\text{dom}(\phi)}$ then every weak solution to $\frac{du}{dt} + \partial\phi(u) \ni f$ is a strong solution and $\sqrt{t} \frac{du}{dt} \in L^2(0, T; \mathcal{H})$. $\phi(u(\cdot))$ is in $L^1(0, T)$ and absolutely continuous on every interval $[\delta, T]$, $\delta \in (0, T)$ with $\left\| \frac{du}{dt}(t) \right\|^2 + \frac{d}{dt} \phi(u(t)) = \left(f(t), \frac{du}{dt}(t) \right)$ a.e. in $(0, T)$.*
If $u_0 \in \text{dom}(\phi)$ we have $\frac{du}{dt} \in L^2(0, T; \mathcal{H})$ with

$$\left(\int_0^T \left\| \frac{du}{dt}(t) \right\|^2 dt \right)^{\frac{1}{2}} \leqslant \left(\int_0^T \|f(t)\|^2 \right)^{\frac{1}{2}} + \phi(u_0)^{\frac{1}{2}}$$

and $\phi(u(\cdot))$ is absolutely continuous on $[0, T]$.

We are now ready to state the final result of this section. The proof is not omitted in this case as it plays an essential role in the existence proof of chapter 2.

Theorem A.7 ([27], Proposition 3.12). *Let ϕ be a proper convex and lsc function on $\mathcal{H}$ and $B : [0, T] \times \overline{\text{dom}(\phi)} \to \mathcal{H}$ such that*

    1. $\exists_{\omega \geqslant 0} \forall_{x,y \in \mathcal{H}} \forall_{t \in [0,T]} \ \|B(t, x) - B(t, y)\| \leqslant \omega \|x - y\|$

2. $\forall_{x \in \overline{\text{dom}(\phi)}} \ B(\cdot, x) \in L^2(0, T; \mathcal{H})$

Then for every $u_0 \in \overline{\text{dom}(\phi)}$ there exists a unique solution to

$$\frac{du}{dt}(t) + \partial\phi(u(t)) + B(t, u(t)) \ni 0 \quad \text{for a.e. } t \in (0, T), \ u(0) = u_0$$

and

$$\sqrt{t}\frac{du}{dt} \in L^2(0, T; \mathcal{H})$$

If $u_0 \in \text{dom}(\phi)$ then $\frac{du}{dt} \in L^2(0, T; \mathcal{H})$.

Proof. For each $u \in \mathcal{C}([0, T]; \mathcal{H})$ with values in $\overline{\text{dom}(\phi)}$ the function $B(\cdot, u(\cdot))$ is in $L^2(0, T; \mathcal{H})$ which is verified by an easy calculation. Hence the following sequence is well defined by theorems A.5 and A.6: Let u_n be the solution of

$$\frac{du_n}{dt}(t) + \partial\phi(u_n(t)) \ni -B(t, u_{n-1}(t)), \ u_n(0) = u_0$$

From Lemma A.4 and the assumptions on B follow

$$\|u_{n+1}(t) - u_n(t)\| \leqslant \int_0^t \|B(s, u_n(s)) - B(s, u_{n-1}(s))\| \ ds \leqslant \omega \int_0^t \|u_n(s) - u_{n-1}(s)\| \ ds$$

and then by recursion

$$\|u_{n+1}(t) - u_n(t)\| \leqslant \frac{(\omega t)^n}{n!} \|u_1 - u_0\|_{L^\infty}$$

Hence we have uniform convergence of u_n on $[0, T]$ towards some u and by continuity of B in the second argument we have $B(t, u_n(t)) \to B(t, u(t))$. Therefore u is a weak solution to $\frac{du}{dt} + \partial\phi(u) \ni -B(t, u(t))$ and by Theorem A.6 a strong solution with $\sqrt{t}\frac{du}{dt} \in L^2(0, T; \mathcal{H})$ respectively $\frac{du}{dt} \in L^2(0, T; \mathcal{H})$ if $u_0 \in \text{dom}(\phi)$. $\qquad\square$

A.2. Miscellaneous

An important tool to deduce lower semicontinuity of integral operators from the lower semicontinuity of the integrand is known by the name of *Fatou's lemma*.

Lemma A.8 (Fatou)**.** *Let $(f_n) \in L^1(\Omega)$ be a sequence of integrable functions uniformly*

bounded from below. Then the pointwise limes inferior is in $L^1(\Omega)$ and

$$\liminf_{n \longrightarrow \infty} \int_\Omega f_n(x)\,dx \geqslant \int_\Omega \liminf_{n \longrightarrow \infty} f_n(x)\,dx.$$

That a converging L^2-sequence also converges pointwise almost everywhere is in general not true, but holds for a subsequence as stated by the following theorem.

Theorem A.9 ([48], Korollar 2.7)**.** *Let v_n be a sequence converging in $L^2(\Omega)^N$ towards v. Then there is a subsequence v_{n_k} converging towards v almost everywhere.*

Definition A.4 (Carathéodory function)**:**   Let Ω be an open subset of $\mathbb{R}^d$. A function $f : \Omega \times \mathbb{R}^N \to \mathbb{R}$ is called a *Carathéodory function* if

  (*i*) $f(\cdot, \xi)$ is measurable for each $\xi \in \mathbb{R}^N$

  (*ii*) $f(x, \cdot)$ is continuous on $\mathbb{R}^N$ for a.e. $x \in \Omega$

$\triangle$

Definition A.5 (Superposition operator)**:**   Let $f : \Omega \times \mathbb{R}^N \to \mathbb{R}$. The operator mapping $\mathbb{R}^N$-valued functions on Ω to scalar functions defined by

$$F(v)(x) = f(x, v(x))$$

is called *superposition operator* or *Nemytskij operator*. $\triangle$

The following theorem provides continuity of such superposition operators and integrability of composed functions under few assumptions.

Theorem A.10 ([111], Sect. 5.2.2, Propositions 2 & 3)**.** *Let $\Omega \subset \mathbb{R}^d$ be a non-empty, open, bounded domain and $f : \Omega \times \mathbb{R}^N \to \mathbb{R}$ a Carathéodory function satisfying for some constant $c \in \mathbb{R}$ and some $a \in L^q(\Omega)$*

$$|f(x,\xi)| \leqslant a(x) + c \sum_{i=0}^{N} |\xi_i|^{\frac{p}{q}} \quad \text{for a.e. } x \in \Omega,\ \forall \xi \in \mathbb{R}^N.$$

Furthermore let $1 \leqslant p, q < \infty$. Then the superposition operator F induced by f maps $L^p(\Omega)^N$ into $L^q(\Omega)$ and F is continuous and bounded.

Lemma A.11. *Let $\mathcal{H}$ be a Hilbert space and $T : \mathcal{H} \to \mathbb{R}$ be differentiable in $\mathcal{H}$ such that is T' Lipschitz continuous with Lipschitz constant L. Then*

$$|T(x) - T(x_0) - \langle T'(x_0), x - x_0 \rangle| \leqslant \frac{L}{2} \|x - x_0\|_{\mathcal{H}}^2 \qquad \forall x, x_0 \in \mathcal{H}$$

Proof. Let $x, x_0 \in \mathcal{H}$ be arbitrary but fixed and define $g : \mathbb{R} \to \mathbb{R}$, $s \mapsto T(x_0 + s(x - x_0))$. Then by the chain rule $g'(s) = \langle T'(x_0 + s(x - x_0)), x - x_0 \rangle$. By the fundamental theorem of calculus, the Cauchy–Schwarz inequality, and the Lipschitz continuity of T' we now have

$$
\begin{aligned}
|T(x) - T(x_0) - \langle T'(x_0), x - x_0 \rangle| &= |g(1) - g(0) - g'(0)| \\
&= \left| \int_0^1 g'(s)\, ds - g'(0) \right| \\
&= \left| \int_0^1 g'(s) - g'(0)\, ds \right| \\
&= \left| \int_0^1 \langle T'(x_0 + s(x - x_0)) - T'(x_0), x - x_0 \rangle\, ds \right| \\
&\leqslant \int_0^1 |\langle T'(x_0 + s(x - x_0)) - T'(x_0), x - x_0 \rangle|\, ds \\
&\leqslant \int_0^1 \|T'(x_0 + s(x - x_0)) - T'(x_0)\|_{\mathcal{H}'} \|x - x_0\|_{\mathcal{H}}\, ds \\
&\leqslant \int_0^1 sL \|x - x_0\|_{\mathcal{H}}^2\, ds \\
&= \frac{L}{2} \|x - x_0\|_{\mathcal{H}}^2
\end{aligned}
$$

$\square$

Bibliography

[1]   M. Alfaro, H. Garcke, D. Hilhorst, H. Matano, and R. Schätzle. "Motion by anisotropic mean curvature as sharp interface limit of an inhomogeneous and anisotropic Allen–Cahn equation". *Proc. Roy. Soc. Edinburgh Sect. A* 140 (2010), pp. 673–706.

[2]   S. Allen and J. Cahn. "A Microscopic Theory for Antiphase Boundary Motion and its Application to Antiphase Domain Coarsening". *Acta Metallurgica* 27 (1979), pp. 1085–1095.

[3]   *Amira*®. URL: http://www.vsg3d.com/amira/overview (visited on 03/23/2014).

[4]   *Asymptote*. URL: http://asymptote.sourceforge.net/ (visited on 01/28/2014).

[5]   J. W. Barrett and J. F. Blowey. "An error bound for the finite element approximation of a model for phase separation of a multi-component alloy". *IMA J. Numer. Anal.* 16 (1996), pp. 257–287.

[6]   J. W. Barrett and J. F. Blowey. "Finite element approximation of a model for phase separation of a multi-component alloy with non-smooth free energy". *Numer. Math.* 77 (1997), pp. 1–34.

[7]   J. W. Barrett and J. F. Blowey. "An optimal error bound for a finite element approximation of a model for phase separation of a multi-component alloy with non-smooth free energy." *M2AN, Math. Model. Numer. Anal.* 33.5 (1999), pp. 971–987.

[8]   J. W. Barrett and J. F. Blowey. "An improved error bound for a finite element approximation of a model for phase separation of a multi-component alloy with a concentration dependent mobility matrix". *Numer. Math.* 88 (2001), pp. 255–297.

[9]   J. W. Barrett, R. Nürnberg, and V. Styles. "Finite element approximation of a phase field model for void electromigration". *SIAM J. Numer. Anal.* 42 (2004), pp. 738–772.

[10]   P. Bastian, M. Blatt, A. Dedner, C. Engwer, R. Klöfkorn, M. Ohlberger, and O. Sander. "A Generic Interface for Adaptive and Parallel Scientific Computing. Part I: Abstract Framework". *Computing* 82.2–3 (2008), pp. 103–119.

[11]   P. Bastian et al. "A Generic Interface for Adaptive and Parallel Scientific Computing. Part II: Implementation and Tests in DUNE". *Computing* 82.2–3 (2008), pp. 121–138.

[12] G. Bellettini and M. Paolini. "Anisotropic motion by mean curvature in the context of Finsler geometry". *Hokkaido Math. J.* 25 (1996), pp. 537–566.

[13] M. Beneš, V. Chalupecký, and K. Mikula. "Geometrical image segmentation by the Allen–Cahn equation". *Applied Numerical Mathematics* 51.2-3 (2004), pp. 187–205. DOI: `DOI:10.1016/j.apnum.2004.05.001`.

[14] M. Benzi, G. Golub, and J. Liesen. "Numerical solution of saddle point problems". *Acta Numerica* 14 (2005), pp. 1–137.

[15] L. Blank, H. Garcke, L. Sarbu, and V. Styles. "Primal–dual active set methods for Allen–Cahn variational inequalities with nonlocal constraints". *Numerical Methods for Partial Differential Equations* 29.3 (2013), pp. 999–1030.

[16] J. F. Blowey, M. I. M. Copetti, and C. M. Elliott. "Numerical analysis of a model for phase separation of a multi-component alloy." *IMA J. Numer. Anal.* 16.1 (1996), pp. 111–139.

[17] J. F. Blowey and C. M. Elliott. "The Cahn-Hilliard gradient theory for phase separation with non–smooth free energy II: Numerical analysis". *Euro. J. Appl. Math.* 3 (1992), pp. 147–179.

[18] T. Böhme. private communication. 2008.

[19] T. Böhme. "Investigations of Microstructural Changes in Lead-Free Solder Alloys by Means of Phase Field Theories". PhD thesis. Technische Universität Berlin, 2008.

[20] T. Böhme, W. Dreyer, F. Duderstadt, and W. H. Müller. "A higher gradient theory of mixtures for multi-component materials with numerical examples for binary alloys". Preprint 1286. WIAS Berlin, 2007.

[21] E. Bonetti, W. Dreyer, and G. Schimperna. "Global solutions to generalized Cahn–Hilliard equation with viscosity". *Advances in Differential Equations* 8.2 (2003), pp. 231–256.

[22] E. Bonetti, P. Colli, W. Dreyer, G. Gilardi, G. Schimperna, and J. Sprekels. "On mathematical models for phase separation in elastically stressed solids". *Physica D* 165 (2002), pp. 48–65.

[23] F. Bornemann. "An adaptive multilevel approach to parabolic equations in two space dimensions". PhD thesis. Freie Universität Berlin, 1991.

[24] F. Bornemann, B. Erdmann, and R. Kornhuber. "A Posteriori Error Estimates for Elliptic Problems in Two and Three Space Dimensions". *SIAM J. Numer. Anal.* 33 (1996), pp. 1188–1204.

[25] J. C. Bowman and A. Hammerlindl. "Asymptote: A vector graphics language". *TUGBOAT: The Communications of the TeX Users Group* 29.2 (2008), pp. 288–294.

[26] P. Boyanova and M. Neytcheva. "Efficient Numerical Solution of Discrete Multi-Component Cahn-Hilliard Systems". Preprint 09. Department of Information Technology, Uppsala Universitet, 2012.

[27] H. Brézis. *Opérateurs maximaux monotones et semi-groupes des contractions dans les espace de Hilbert.* Vol. 50. Notas de Matemática. Amsterdam: North Holland, 1973.

[28] E. Burman, D. Kessler, and J. Rappaz. "Convergence of the finite element method applied to an anisotropic phase-field model". *Ann. Math. Blaise Pascal* 11 (2004), pp. 67–94.

[29] E. Burman and J. Rappaz. "Existence of solutions to an anisotropic phase-field model". *Math. Meth. Appl. Sc.* 26 (2003), pp. 1137–1160.

[30] A. Burri, A. Dedner, R. Klöfkorn, and M. Ohlberger. "An efficient implementation of an adaptive and parallel grid in DUNE". In: *Proc. of the 2nd Russian-German Advanced Research Workshop on Computational Science and High Performance Computing.* 2005.

[31] J. Cahn and J. Hilliard. "Free energy of a non-uniform system. I. Interfacial free energy". *The Journal of Chemical Physics* 28 (1958), 258–267.

[32] J. Cahn and F. Larché. "Thermochemical equilibrium of multiphase solids under stress." *Acta Metallurgica* 26 (1978), 1579–1589.

[33] R. Cerf. *The Wulff Crystal in Ising and Percolation Models. Ecole d'Eté de Probabilités de Saint-Flour XXXIV - 2004.* Vol. 1878. Lecture Notes in Mathematics. Berlin, Heidelberg: Springer, 2006.

[34] X. Chen. "Global asymptotic limit of solutions of the Cahn–Hilliard equation". *J. Differential Geometry* 44 (1996), pp. 262–311.

[35] F. Clarke. *Optimization and nonsmooth analysis.* New York: Wiley, 1983.

[36] S. Conti, B. Niethammer, and F. Otto. "Coarsening in off-critical mixtures". *SIAM J. Math. Anal.* 37.6 (2006), pp. 1732–1741.

[37] K. Deckelnick, G. Dziuk, and C. M. Elliott. "Computation of geometric partial differential equations and mean curvature flow". *Acta Numerica* 14 (2005), pp. 139–232.

[38] P. Deuflhard. *Newton Methods for Nonlinear Problems.* Berlin, Heidelberg: Springer, 2004.

[39] P. Deuflhard, P. Leinen, and H. Yserentant. "Concepts of an adaptive hierarchical finite element code". *IMPACT Comput. Sci. Engrg.* 1 (1989), pp. 3–35.

[40] W. Dörfler. "A convergent adaptive algorithm for Poisson's equation". *SIAM Journal of Numerical Analysis* 33 (1996), pp. 1106–1124.

[41] Z. Dostál. *Optimal Quadratic Programming Algorithms.* Springer, 2009.

[42] W. Dreyer and W. H. Müller. "A study of the coarsening in tin/lead solders". *Int. J. Solid Struct.* 37 (2000), pp. 3841–3871.

[43] W. Dreyer and W. H. Müller. "Modeling diffusional coarsening in eutectic tin/lead solders: a quantitative approach". *Int. J. Solid Struct.* 38 (2001), pp. 1433–1458.

[44]   *Dune-fufem Infoseite*. URL: http : / / lists . spline . inf . fu - berlin . de / mailman/listinfo/dune-fufem (visited on 01/28/2014).

[45]   I. Ekeland and R. Temam. *Convex Analysis and Variational Problems*. SIAM, 1999.

[46]   C. M. Elliott and R. Schätzle. "The limit of the anisotropic double-obstacle Allen–Cahn equation". *Proc. Roy. Soc. Edinburgh Sect. A* 126 (1996), pp. 1217–1234.

[47]   C. M. Elliott and R. Schätzle. "The limit of the fully anisotropic double-obstacle Allen–Cahn equation in the nonsmooth case". *SIAM J. Math. Anal.* 28 (1997), pp. 274–303.

[48]   J. Elstrodt. *Maß- und Integrationstheorie*. 5th edition. Berlin, Heidelberg, New York: Springer, 2006.

[49]   L. C. Evans, H. M. Soner, and P. E. Souganidis. "Phase transitions and generalized motion by mean curvature". *Communications on Pure and Applied Mathematics* 45.9 (1992), pp. 1097–1123.

[50]   X. Feng and A. Prohl. "Numerical analysis of the Allen-Cahn equation and approximation for mean curvature flows". *Num. Math.* 94 (2003), pp. 33–65.

[51]   D. D. Fontaine. "An analysis of clustering and ordering in multicomponent solid solutions I. Stability criteria." *J. Phys. Chem. Solids* 33 (1972), pp. 287–310.

[52]   H. Garcke. "On mathematical models for phase separation in elastically stressed solids". Habilitation Thesis. Universität Bonn, 2000.

[53]   H. Garcke, M. Rumpf, and U. Weikard. "The Cahn–Hilliard equation with elasticity: Finite element approximation and qualitative studies." *Interfaces Free Bound.* 3 (2001), pp. 101–118.

[54]   H. Garcke and D. J. C. Kwak. "On asymptotic limits of Cahn–Hilliard systems with elastic misfit". In: *Analysis, modeling and simulation of multiscale problems*. Ed. by A. Mielke. Berlin, Heidelberg, New York: Springer, 2006, pp. 87–111.

[55]   H. Garcke, B. Niethammer, M. Rumpf, and U. Weikard. "Transient coarsening behaviour in the Cahn–Hilliard model". *Acta Materialia* 51 (2003), pp. 2823–2830.

[56]   G. Giacomin and J. L. Lebowitz. "Phase segregation dynamics in particle systems with long range interactions I: macroscopic limits". *J. Statist. Phys.* 87 (1998), pp. 37–61.

[57]   G. Giacomin and J. L. Lebowitz. "Phase segregation dynamics in particle systems with long range interactions II: interface motion". *SIAM J. Appl. Math.* 58 (1998), pp. 1707–1729.

[58]   Y. Giga. *Surface Evolution Equations*. Basel: Birkhäuser, 2006.

[59]   R. Glowinski. *Numerical Methods for Nonlinear Variational Problems*. Springer, 1984.

[60] C. Gräser. "Analysis und Approximation der Cahn–Hilliard Gleichung mit Hindernispotential". Diplomarbeit. Freie Universität Berlin, 2004.

[61] C. Gräser. "Nonsmooth Schur–Newton methods for nonsmooth saddle point problems". Preprint 1004. Matheon Berlin, 2013.

[62] C. Gräser and R. Kornhuber. "Multigrid Methods for Obstacle Problems". *J. Comp. Math.* 27.1 (2009), pp. 1–44.

[63] C. Gräser and R. Kornhuber. "Nonsmooth Newton Methods for Set-Valued Saddle Point Problems". *SIAM J. Numer. Anal.* 47.2 (2009), pp. 1251–1273.

[64] C. Gräser, R. Kornhuber, and U. Sack. "Nonsmooth Schur–Newton methods for vector-valued Cahn–Hilliard equations". Preprint, Serie A 01/2013. Freie Universität Berlin, 2013. URL: http://page.mi.fu-berlin.de/graeser/public_files/paper/graeser_kornhuber_sack_schur_newton_vvch.pdf.

[65] C. Gräser, U. Sack, and O. Sander. "Truncated Nonsmooth Newton Multigrid Methods for Convex Minimization Problems". In: *Domain Decomposition Methods in Science and Engineering XVIII.* Ed. by M. Bercovier, M. Gander, R. Kornhuber, and O. Widlund. LNCSE. Springer, 2009, pp. 129–136.

[66] C. Gräser. "Convex Minimization and Phase Field Models". PhD thesis. Freie Universität Berlin, 2011.

[67] C. Gräser and R. Kornhuber. "On preconditioned Uzawa-type iterations for a saddle point problem with inequality constraints". In: *Domain Decomposition Methods in Science and Engineering XVI.* Ed. by O. Widlund and D. Keyes. Springer, 2006, pp. 91–102.

[68] C. Gräser, R. Kornhuber, and U. Sack. "On Hierarchical Error Estimators for Time-discretized Phase Field Models". In: *Proceedings of ENUMATH 2009.* Ed. by G. Kreiss, P.Lötstedt, A. Malqvist, and M. Neytcheva. Springer, 2010, pp. 397–406.

[69] C. Gräser, R. Kornhuber, and U. Sack. "Numerical simulation of coarsening in binary solder alloys". Preprint 1041. MATHEON, 2013.

[70] C. Gräser, R. Kornhuber, and U. Sack. "Time discretizations of anisotropic Allen–Cahn equations". *IMA Journal of Numerical Analysis* (2013). DOI: 10.1093/imanum/drs043.

[71] C. Gräser and O. Sander. *The dune-solvers Module.* URL: http://numerik.mi.fu-berlin.de/dune-solvers/index.php (visited on 01/28/2014).

[72] C. Gräser and O. Sander. *The Dune-Subgrid Module.* URL: http://numerik.mi.fu-berlin.de/dune-subgrid/index.php (visited on 10/21/2013).

[73] C. Gräser and O. Sander. "The dune-subgrid Module and Some Applications". *Computing* 8.4 (2009), pp. 269–290.

[74] C. Gräser and O. Sander. "Polyhedral Gauss–Seidel converges". *J. Numer. Math.* (2013). to appear.

Bibliography

[75] M. Gurtin. *Thermomechanics of evolving phase boundaries in the plane.* Oxford Mathematical Monographs. Oxford: Oxford University Press, 1993.

[76] M. Hinze and M. Vierling. "Variational discretization and semi-smooth Newton methods; implementation, convergence and globalization in pde constrained optimzation with control constraints". *Optim. Meth. Software* 27 (2012), pp. 933–950.

[77] G. Huisken. "Flow by mean curvature of convex surfaces into spheres". *J. Differential Equations* 77 (1984), pp. 369–378.

[78] J. D. Hunter. "Matplotlib: A 2D graphics environment". *Computing In Science & Engineering* 9.3 (2007), pp. 90–95.

[79] D. Kay and A. Tomasi. "Color Image Segmentation by the Vector-Valued Allen–Cahn Phase-Field Model: A Multigrid Solution". *IEEE Transaction on Image Processing* 18.10 (2009), pp. 2330–2339. DOI: 10.1109/TIP.2009.2026678.

[80] J. Kim and K. Kang. "A numerical method for a ternary Cahn–Hilliard system with degenerate mobility". *Appl. Numer. Math.* 59 (2009), pp. 1029–1042.

[81] R. Kobayashi. "Modeling and numerical simulations of dendritic crystal growth". *Physica D* 63 (1993), pp. 410–423.

[82] R. Kohn and F. Otto. "Upper bounds for coarsening rates". *Comm. Math. Phys.* 229 (2002), pp. 375–395.

[83] R. Kornhuber. "A Posteriori Error Estimates for Elliptic Variational Inequalities". *Comput. Math. Appl.* 31 (1996), pp. 49–60.

[84] R. Kornhuber. *Adaptive monotone multigrid methods for nonlinear variational problems.* Stuttgart: B.G. Teubner, 1997.

[85] R. Kornhuber. "On constrained Newton linearization and multigrid for variational inequalities". *Numer. Math.* 91 (2002), pp. 699–721.

[86] R. Kornhuber and R. Krause. "Robust multigrid methods for vector-valued Allen–Cahn equations with logarithmic free energy". *Comput Visual Sci* 9 (2006), pp. 103–116. DOI: 10.1007/s00791-006-0020-2.

[87] R. Kornhuber and Q. Zou. "Efficient and Reliable Hierarchical Error Estimates for the Discretization Error of Elliptic Obstacle Problems". *Math. Comp.* 80 (2011), pp. 69–88.

[88] D. J. C. Kwak. "The sharp-interface limit of the Cahn–Hilliard system with elasticity". PhD thesis. Universität Regensburg, 2007.

[89] L. Bronsard, H. Garcke, and B. Stoth. "A multi-phase Mullins-Sekerka system: Matched asymptotic expansions and an implicit time discretisation for the geometric evolution problem." *Proc. R. Soc. Edinb., Sect. A, Math.* 128.3 (1998), pp. 481–506.

[90] Y.-L. Lee, J. Wu, J. Xu, and L. Zikatanov. "A sharp convergence estimate for the method of subspace corrections for singular systems of equations". *Math. Comp.* 77.262 (2008), pp. 831–850.

[91] C. M. M. Elliott and S. Luckhaus. "A generalised diffusion equation for phase separation of a multicomponent mixture with interfacial free energy". Preprint 887. University of Minnesota: IMA, 1991.

[92] *Mathematica*®. URL: http://www.wolfram.com/mathematica/ (visited on 03/23/2014).

[93] *Matlab*®. URL: http://www.mathworks.de/products/matlab/index.html (visited on 03/23/2014).

[94] *matplotlib: Python plotting – Matplotlib 1.3.1 documentation*. URL: http://matplotlib.org/ (visited on 01/28/2014).

[95] T. Merkle. "The Cahn–Larché system: A model for spinodal decomposition in eutectic solder". PhD thesis. Universität Stuttgart, 2005.

[96] J.-J. Moreau. "Proximité et dualité dans un espace Hilbertien". *Bull. Soc. Math. France* 93 (1965), pp. 273–299.

[97] I. Müller and W. H. Müller. *Fundamentals of Thermodynamics and Applications*. Berlin, Heidelberg: Springer, 2009.

[98] M. F. Murphy, G. H. Golub, and A. Wathen. "A note on preconditioning for indefinite linear systems". *SIAM J. Sci. Comput.* 21 (2000), pp. 1969–1972.

[99] National Institute of Standards and Technology, Metallurgy Division. *Ag-Cu Phase Diagram & Computational Thermodynamics*. URL: http://www.metallurgy.nist.gov/phase/solder/agcu.html (visited on 10/23/2013).

[100] J. Nečas and I. Hlaváček. *Mathematical Theory of Elastic and Elastico-Plastic Bodies: An Introduction*. Amsterdam: Elsevier, 1981.

[101] A. Novick-Cohen. "Upper bounds for coarsening for the deep quench obstacle problem". *J. Stat. Phys.* 141.1 (2010), pp. 142–157.

[102] A. Novick-Cohen and A. Shishkov. "Upper bounds for coarsening for the degenerate Cahn–Hilliard equation". *Disc Cont Dyn Syst A* 25.1 (2009), pp. 251–272.

[103] D. W. K. Olgierd C. Zienkiewicz J.P. De S.R. Gago. "The hierarchical concept in finite element analysis". *Computers & Structures* 16 (1983), pp. 53–65.

[104] J. M. Ortega and W. C. Rheinboldt. *Iterative Solution of Nonlinear Equations in Several Variables*. New York: Academic Press, 1970.

[105] *ParaView – Open source scientific visualization*. URL: http://paraview.org/ (visited on 01/28/2014).

[106] E. Parliament and Council. "Directive 2002/95/EC of the European Parliament and of the Council of 27 January 2003 on the restriction of the use of certain hazardous substances in electrical and electronic equipment". *Official Journal of the European Union* 46.L 37 (2003).

Bibliography

[107] E. Parliament and Council. "Directive 2002/96/EC of the European Parliament and of the Council of 27 January 2003 on waste electrical and electronic equipment (WEEE)". *Official Journal of the European Union* 46.L 37 (2003).

[108] E. Parliament and Council. "Directive 2011/65/EU of the European Parliament and of the Council of 8 June 2011 on the restriction of the use of certain hazardous substances in electrical and electronic equipment". *Official Journal of the European Union* 54.L 174 (2011).

[109] E. Parliament and Council. "Directive 2012/19/EU of the European Parliament and of the Council of 4 July 2012 on waste electrical and electronic equipment (WEEE)". *Official Journal of the European Union* 55.L 197 (2012).

[110] R. T. Rockafellar. "Characterization of the subdifferentials of convex functions". *Pacific J. Math.* 17.3 (1966), pp. 497–510.

[111] T. Runst and W. Sickel. *Sobolev spaces of fractional order, Nemytskij operators, and nonlinear partial differential equations.* Vol. 3. Nonlinear Analysis and Applications. Berlin, New York: Walter de Gruyter, 1996.

[112] Y. Saad and M. H. Schultz. "GMRES: A generalized minimal residual algorithm for solving nonsymmetric linear systems". *SIAM J. Sci. Stat. Comput.* 7.3 (1986), pp. 856–869.

[113] J. Schöberl and W. Zulehner. "On additive Schwarz-type smoothers for saddle point problems". *Numer. Math.* 95.2 (2003), pp. 377–399.

[114] H. M. Soner. "Motion of a Set by the Curvature of Its Boundary". *J. Differential Equations* 101 (1993), pp. 313–372.

[115] I. Steinbach, F. Pezolla, B. Nestler, M. Seeßelberg, R. Prieler, G. J. Schmitz, and J. L. L. Rezende. "A phase-field concept for multiphase systems". *Physica D* 94 (1996), pp. 135–147.

[116] *The ALUGrid Library.* URL: http://aam.mathematik.uni-freiburg.de/IAM/Research/alugrid/ (visited on 01/28/2014).

[117] *The Distributed and Unified Numerics Environment - DUNE.* URL: http://dune-project.org (visited on 01/19/2014).

[118] E. E. Underwood. *Quantitative Stereology.* Metallurgy and Materials. Reading, Mass.: Addison-Wesley, 1970.

[119] S. P. Vanka. "Block-implicit multigrid solution of Navier–Stokes equations in primitive variables". *J. Comput. Phys.* 65 (1986), pp. 138–158.

[120] F. Vogel, N. Wanderka, Z. Balogh, M. Ibrahim, P. Stender, G. Schmitz, and J. Banhart. "Mapping the evolution of hierarchical microstructures in a Ni-based superalloy". *Nature Communications* 4 (2013). DOI: 10.1038/ncomms3955.

[121] U. Weikard. "Numerische Lösungen der Cahn–Hilliard-Gleichung und der Cahn–Larché Gleichung". PhD thesis. Rheinische Friedrich-Wilhelms-Universität Bonn, 2002.

[122] F. Wendler, J. K. Becker, B. Nestler, P. D. Bons, and N. P. Walte. "Phase–field simulations of partial melts in geological materials". *Computers & Geosciences* 35.9 (2009), pp. 1907–1916.

[123] G. Wulff. "Zur Frage der Geschwindigkeit des Wachstums und der Auflösung von Krystallflächen". *Zeitschrift fur Krystallographie und Mineralogie* 34 (1901), pp. 449–530.

[124] C. Xinfu, C. M. Elliot, G. Andy, and J. J. Zhao. "Convergence of numerical solutions to the Allen–Cahn equation". *Applicable Analysis* 69.1-2 (1998), pp. 95–108.

[125] Q. Zou, A. Veeser, R. Kornhuber, and C. Gräser. "Hierarchical error estimates for the energy functional in obstacle problems". *Numerische Mathematik* 117.4 (2011), pp. 653–677.

[126] W. Zulehner. "A class of smoothers for saddle point problems". *Computing* 65.3 (2000), pp. 227–246.

Zusammenfassung

Mit dem EU weiten Verbot von bleihaltigen Loten in elektronischen Bauteilen ergibt sich die Notwendigkeit, Ersatzlegierungen mit vergleichbaren Verarbeitungseigenschaften und vergleichbarer Lebensdauer zu entwickeln. Numerische Simulationen der Evolution der Mikrostruktur können dazu beitragen, geeignete Kandidaten auszuwählen und damit den großen experimentellen Aufwand zu verringern bzw. zu fokussieren. Als Standardmodell der Phasenseparation und Vergröberung unter mechanischen Spannungen hat sich das Cahn–Larché Modell herauskristallisiert. Es koppelt das nichtlineare Cahn–Hilliard Modell der Phasenseparation mit der Gleichung der linearen Elastostatik. Es existieren schnelle Löser sowohl für linearen mechanischen Teilprobleme als auch die skalare Cahn–Hilliard-Gleichung. Publizierte numerische Löser für die Cahn–Larché Gleichung sind jedoch typischerweise beschränkt auf periodische Randbedingungen und uniforme Gitter [42, 43, 20] oder auf glatte Potentiale [121, 95]. Schnelle Löser für die mehrkomponentige Cahn–Hilliard Gleichung mit logarithmischem Potential sind bislang nicht bekannt.

Ziel dieser Arbeit ist zum einen ein numerisches Framework zur effizienten und robusten Lösung der Cahn–Larché Gleichung mit reellen Materialparametern zu erarbeiten. Dieses soll adaptive Finite-Elemente-Verfahren mit den schnellen Lösern für die Cahn–Hilliard-Gleichung und die elastischen Teilprobleme kombinieren. Zum anderen sollen die Nichtglatten Schur-Newton Verfahren [63, 61] zur Lösung der diskreten skalaren Cahn–Hilliard Gleichung auf den mehrkomponentigen Fall, d.h. mit vektorwertigem Ordnungsparameter, erweitert werden.

Nach einführenden Bemerkungen zu Phasendiagrammen, Phasenseparation und Phasenfeldmodellen in Kapitel 1 wird in Kapitel 2 zunächst die anisotrope Allen–Cahn-Gleichung untersucht. Allen–Cahn-artige Probleme treten als Teilprobleme bei der Lösung der Cahn–Hilliard Gleichung in den Kapiteln 3 und 4 auf. Hier werden Existenz- und Eindeutigkeit von Lösungen mithilfe der Theorie maximal monotoner Operatoren bewiesen. Für die numerische Lösung werden ein adaptiver Ortsgitter-Verfeinerungszyklus für zeitabhängige Probleme und mehrere Varianten impliziter Euler-Zeitdiskretisierung eingeführt. Für letztere wird Stabilität bewiesen und numerische Experimente illustrieren die Genauigkeit der Diskretisierungen sowie den Verlust der Rotationsinvarianz unter Anisotropie.

Kapitel 3 fügt bereits existierende und neu entwickelte numerische Werkzeuge zu einem Simulationstool für Mikrostrukturevolutionen in binären Legierungen zusammen. Wesentliche Bausteine sind dabei der adaptive Gitterverfeinerungszyklus aus Kapitel 2, der NSNMG Löser [61], ein Quantifizierungsalgorithmus für den Grad der Vergröberung der Mikrostruktur und ein Quotientenraum-Mehrgitterverfahren für die indefiniten Elastizitätsprobleme. Die Anwendung dieses Simulationstools für eine eutektische AgCu-Legierung zeigt nur marginalen Einfluss der Elastizität auf die Vergröberung im betrachteten Setting. Die Verwendung eines glatten Potentials anstelle des logarithmischen verfälscht die Vergröberungsdynamik hingegen erheblich.

Im letzten Kapitel wird für die vektorwertige Cahn–Hilliard-Gleichung eine vereinheitlichende Formulierung für die diskretisierten Ortsprobleme hergeleitet, welche die direkte Anwendung des NSNMG Verfahrens erlaubt. Existenz und Eindeutigkeit von diskreten Lösungen werden gezeigt und numerische Beispiele illustrieren die Robustheit des Verfahrens bzgl. Temperatur und Anzahl der Komponenten.